# Spectro-spatial Efficiency Profiling of Volume Phase Holographic Gratings and the Detection of Intermediate Mass Black Holes with HARMONI on the E-ELT

David J. Gooding

Christ Church College
University of Oxford

*A thesis submitted for the degree of*
*Doctor of Philosophy Astrophysics*

Michaelmas 2024

## Abstract

This thesis explores two interconnected areas of astrophysical research: the characterisation of volume phase holographic gratings (VPHGs) for use in the "high angular resolution monolithic optical and near-infrared integral field spectrograph" (HARMONI) and the detection of intermediate mass black holes (IMBHs) using the HARMONI instrument on the European Extremely Large Telescope (E-ELT). The first part of this research provides the most detailed measurements of spatial variations in VPHG transmission efficiency currently available, which is crucial for ensuring optimal performance of the HARMONI spectrograph. These measurements help to refine the design and application of VPHGs, contributing to improved data quality in upcoming observational campaigns.

The second part of the thesis focuses on a promising science case for HARMONI: the detection and observation of IMBHs in star clusters. IMBHs, hypothesised to bridge the gap between stellar-mass and supermassive black holes, remain an elusive component of the black hole population. Using high angular and spectral resolution integral field spectroscopy, this work aims to probe the line-of-sight velocity distributions of stars in the central regions of star clusters to identify kinematic signatures indicative of IMBHs. Simulations and observational strategies are presented to assess the capabilities of HARMONI in identifying IMBHs, with a focus on enhancing our understanding of black hole growth pathways and the role of IMBHs in galactic evolution.

This comprehensive investigation not only characterises key technological components for astronomical spectroscopy but also applies these advancements to pressing questions in black hole astrophysics, pushing the limits of our current observational capabilities.

# Spectro-spatial Efficiency Profiling of Volume Phase Holographic Gratings and the Detection of Intermediate Mass Black Holes with HARMONI on the E-ELT


David J. Gooding

Christ Church College

University of Oxford

A thesis submitted for the degree of

*Doctor of Philosophy Astrophysics*

Michaelmas 2024

# Acknowledgements


## Personal

I am deeply grateful to my supervisor, Prof. Niranjan Thatte, for his exceptional mentorship, insightful feedback, and unwavering support throughout this doctoral journey. His profound knowledge and dedication to the field have provided invaluable learning opportunities, and his ability to explain complex concepts with clarity and precision has been instrumental in my understanding and growth as a researcher. I also extend my sincere appreciation to my co-supervisor, Prof. Michele Cappellari, whose expertise and constructive suggestions have played a pivotal role in shaping both my research and my professional development. It was a privilege to benefit from their immense combined experience.

I owe an immense debt of gratitude to my wife, Carla, whose constant support, patience, and encouragement have been instrumental in keeping me motivated during challenging times. Her belief in me never wavered and truly carried me through this journey. I am forever thankful for the personal sacrifices she has made to enable my pursuit of this doctorate.

My parents and sister have provided unwavering reassurance and practical support across all aspects of my life. Their confidence in me has been a bedrock of strength, reminding me why I chose to pursue this path in the first place.

Lastly, I dedicate this thesis to my late grandfather, Dr. Hedley John Gooding. He was the one who inspired me to embark on this academic adventure with his passion for learning and curiosity about the world. This work stands as a testament to his enduring influence.

## Institutional

I received the Wetton Scholarship, made possible through the generosity of Philip and Roswitha Wetton, whose philanthropic donation helped support the work carried out in this thesis. Their kindness allowed me the freedom to focus on my research and hone my skills under the guidance of my supervisors. I also acknowledge the funding provided by UK Research and Innovation (UKRI) Science and Technology Facilities Council (STFC) grants ST/S001409/1, ST/X002322/1, and ST/X004775/1, which further enabled the successful completion of my doctoral studies.

# Abstract

This thesis explores two interconnected areas of astrophysical research: the characterisation of volume phase holographic gratings (VPHGs) for use in the "high angular resolution monolithic optical and near-infrared integral field spectrograph" (HARMONI) and the detection of intermediate mass black holes (IMBHs) using the HARMONI instrument on the European Extremely Large Telescope (E-ELT). The first part of this research provides the most detailed measurements of spatial variations in VPHG transmission efficiency currently available, which is crucial for ensuring optimal performance of the HARMONI spectrograph. These measurements help to refine the design and application of VPHGs, contributing to improved data quality in upcoming observational campaigns.

The second part of the thesis focuses on a promising science case for HARMONI: the detection and observation of IMBHs in star clusters. IMBHs, hypothesised to bridge the gap between stellar-mass and supermassive black holes, remain an elusive component of the black hole population. Using high angular and spectral resolution integral field spectroscopy, this work aims to probe the line-of-sight velocity distributions of stars in the central regions of star clusters to identify kinematic signatures indicative of IMBHs. Simulations and observational strategies are presented to assess the capabilities of HARMONI in identifying IMBHs, with a focus on enhancing our understanding of black hole growth pathways and the role of IMBHs in galactic evolution.

This comprehensive investigation not only characterises key technological components for astronomical spectroscopy but also applies these advancements to pressing questions in black hole astrophysics, pushing the limits of our current observational capabilities.

# Contents

# List of Figures

# List of Abbreviations

**AO** . . . . . Adaptive Optics

**CCD** . . . . . Charge-Coupled Device

**CMOS** . . . . . Complementary Metal-Oxide Semiconductor

**E-ELT** . . . . . European Extremely Large Telescope

**FWHM** . . . . Full Width Half Maximum

**HARMONI** . High Angular Resolution Monolithic Optical Near-infrared Integral field Spectrograph

**HR** . . . . . High Resolution

**HSIM** . . . . . HARMONI Simulation Pipeline

**IFS** . . . . . Integral Field Spectroscopy

**IMBH** . . . . . Intermediate Mass Black Hole

**LR** . . . . . Low Resolution

**LSF** . . . . . Line Spread Function

**LTAO** . . . . . Laser Tomography Adaptive Optics

**MICADO** . . . Multi-AO Imaging Camera for Deep Observations

**MR** . . . . . Medium Resolution

**MUSE** . . . . . Multi Unit Spectroscopic Explorer

**pPXF** . . . . . Penalized Pixel-Fitting

**PSF** . . . . . Point Spread Function

**SCAO** . . . . . Single Conjugate Adaptive Optics

**SMBH** . . . . . Supermassive black hole

**SNR** . . . . . Signal-to-Noise Ratio

**VLT** . . . . . Very Large Telescope

**VPHG** . . . . . Volume Phase Holographic Grating

# 1 Introduction

## Contents



## 1.1 Integral field spectroscopy for astronomy

The journey of astronomy is a story of human curiosity and technological evolution. From the ancient stargazers to the pioneers of modern astronomy, the field has continually expanded our understanding of the Universe. One of the oldest sciences, astronomy has been intertwined with human curiosity about the cosmos since ancient

times. The advent of telescope technology, pioneered by figures like the lesser-known spectacle-maker Hans Lippershey in the early 17$^{\text{th}}$century and significantly advanced by the great Galileo Galilei, revolutionised our understanding of the Universe. These early telescopes, providing the first detailed views of celestial bodies, opened the door to a Universe that was far more complex and wondrous than previously imagined.

As telescopes evolved, so did the techniques to analyse the light from the stars. Spectroscopy, the study of the interaction between matter and electromagnetic radiation, emerged as a cornerstone of astronomical discovery. Humanity began to unravel the composition, temperature, motion, and other properties of celestial objects. In 1814 Joseph von Fraunhofer invented the modern spectroscope, leading him to discover hundreds of absorption lines from the Sun and bright stars, thus founding the field of stellar spectroscopy. The 19$^{\text{th}}$century also saw critical developments with fellow German scientists Gustav Kirchhoff and Robert Bunsen demonstrating that each element has a unique spectral fingerprint [58]. Earlier work had taken place on the characteristic colours associated with the heating of elements, but not in a systematic way. They built the first prototype of their spectroscope in 1859 and were able to identify the characteristic spectra of sodium, lithium, and potassium. This foundational work led to monumental discoveries such as the identification of helium in the sun before it was found on Earth, arguably by Pierre-Jules-César Janssen, a French astronomer, alongside English scientist Joseph Norman Lockyer who, whilst studying a total solar eclipse in 1868, noticed a yellow line in the Sun's spectrum [65].

Following these breakthroughs, spectroscopy became increasingly sophisticated. The introduction of photographic plates in the late 19$^{\text{th}}$century allowed astronomers such as William and Margaret Huggins [51] to systematically record and study stellar and nebular spectra, revealing that some nebulae consisted of glowing gas rather than unresolved stars. At Harvard College Observatory, Edward C. Pickering initiated extensive spectroscopic surveys, leading to Annie Jump Cannon's [21] development of the stellar classification system still in use today. This work culminated in Cecilia Payne-Gaposchkin's [78] landmark discovery in the 1920s that stellar spectra are

determined primarily by surface temperature, rather than chemical abundance, a finding that fundamentally reshaped astrophysics.

Instrumentation also improved considerably during this period, with innovations such as diffraction gratings pioneered by Henry Rowland [84], which enhanced spectral resolution. Spectroscopy became a fully quantitative tool, enabling measurements of line-of-sight velocities through Doppler shifts, detections of magnetic fields via the Zeeman effect, and studies of gravitational redshifts. By the early $20^{\text{th}}$ century, spectroscopy had evolved from a qualitative observational technique into a powerful method for probing the physical conditions of astronomical objects.

In the 1960s, Willard Boyle and George E. Smith invented the charge-coupled device (CCD) at Bell Labs [16] which prompted a revolution in digital imaging technology. Not long after, the complementary metal-oxide semiconductor (CMOS) based image sensor was developed, based on photodiode technology. Whilst most CCD and CMOS sensors are Silicon-based and sensitive to the visible spectrum, evolutions of this technique using InGaAs or HgCdTe chips emerged in the 1980s[1] which, when used at cryogenic temperatures, opened up the infrared part of the spectrum to digital imaging.

Despite these advancements, a gap remained in our ability to simultaneously obtain high-resolution images and spectral data. This limitation spurred the development of integral field spectroscopy (IFS), also known as hyperspectral imaging.

IFS represented a paradigm shift in observational astronomy, enabling the acquisition of both spatial and spectral data simultaneously. IFS works by splitting the incoming light from a celestial object into its constituent spectra while preserving the spatial information. This technique creates a data cube with two spatial dimensions and one spectral dimension.

The pioneer of IFS, Roland Bacon designed the first astronomical IFS called TIGER[2] [3] which was first used on the Canada-France-Hawaii Telescope (CFHT) in 1987. TIGER used a lenslet array to divide up the light from the source in

[1]The exact date of their first use is classified.

[2]The french acronym is "Traitement Intégral des Galaxies par l'Étude de leurs Raies"

the sky, whilst retaining the information from all wavelengths. Then came MPE 3D[3] by L. Weitzel and R. Genzel [106] which, using an image slicer, worked in near-infrared wavelengths motivated by the desire to study the Galactic Centre, which is heavily obscured and thus cannot be observed at visible wavelengths. Early users of this type of IFS technology such as James E. Gunn and Jeremy R. Allington-Smith, were also instrumental in its development. They recognized the potential of IFS in addressing complex astronomical questions, such as the dynamics of galactic cores or the composition of nebulae.

IFS is a branch of the technique known as hyperspectral imaging, which can be divided into two types; scanning and non-scanning. The former uses 2D detectors and scans through the third dimension, whether spectral or spatial, over time. This has advantages including simplicity of optical design and cost. The main disadvantage is the introduction of temporal variations in the output datacube, which is a concern for ground-based astronomy due to atmospheric turbulence and the resulting variation in the point spread function (PSF). Also an issue is the observing efficiency, as telescopes collect all the photons all the time which are then wasted with scanning techniques. Non-scanning hyperspectral imaging, of which IFS was the first to be developed, simultaneously captures all three dimensions of the datacube providing temporal homogeneity and highly sensitive detection, at the cost of a smaller field of view.

The implementation of IFS can be achieved through various methods, each with its own set of advantages and limitations. The most common approaches, visualised in Figure 1.1 (courtesy of NASA), are:

- **Lenslet Arrays**: (e.g. TIGER [3], SAURON [4], and OSIRIS [62]) These systems use an array of tiny lenses to focus different parts of the field of view onto a detector. They provide high spatial resolution with moderate optical efficiency, typically around 60–80%, although they can suffer from reduced

[3]Named after the Max-Planck-Institute for extraterrestrial physics (MPE) where it was built, the 3D refers to the 3-dimensional datacubes produced by the IFS technique.

instantaneous wavelength coverage due to the way spectra are packed onto the detector.

- **Fibre-fed Systems**: (e.g. VIMOS [63], SAMI [33], and MaNGA [20]) These use bundles of optical fibres to relay different parts of the field of view to a spectrograph. This provides flexibility in instrument design by allowing the spectrograph to be placed remotely from the telescope's focal plane, thus reducing mechanical and thermal stress. However, they struggle with efficiency of light collection due to the fibre-coupling and focal-plane fill factor efficiency and can lose some spatial information.

- **Image Slicers**: (e.g. MUSE [6], NIRSpec [53], SINFONI [98], ERIS [35], and HARMONI [99]) This method involves slicing the incoming image into strips that are then rearranged to form a pseudo-slit. Image slicers offer a good balance between spatial and spectral resolution and generally achieve high optical efficiency (often 70–90%), although they are complex and costly to build and require careful optical alignment to minimise aberrations and scattering.

- **Imaging Fourier Transform Spectrographs (iFTS)**: (e.g. SITELLE [37]) These instruments use interferometric techniques to acquire spectral information by recording multiple interferograms at different optical path differences. iFTS systems offer full spatial and spectral coverage across a broad field of view with high throughput, particularly effective for emission-line studies. However, they are less efficient for faint continuum sources due to the multiplex disadvantage, where the noise from the entire spectral range contributes to each pixel.

Each method has been refined over the years, with advancements in optical engineering and digital processing significantly enhancing their capabilities. The choice of IFS method often depends on the specific scientific goals, observational conditions, and the nature of the target objects. A critical evaluation of these

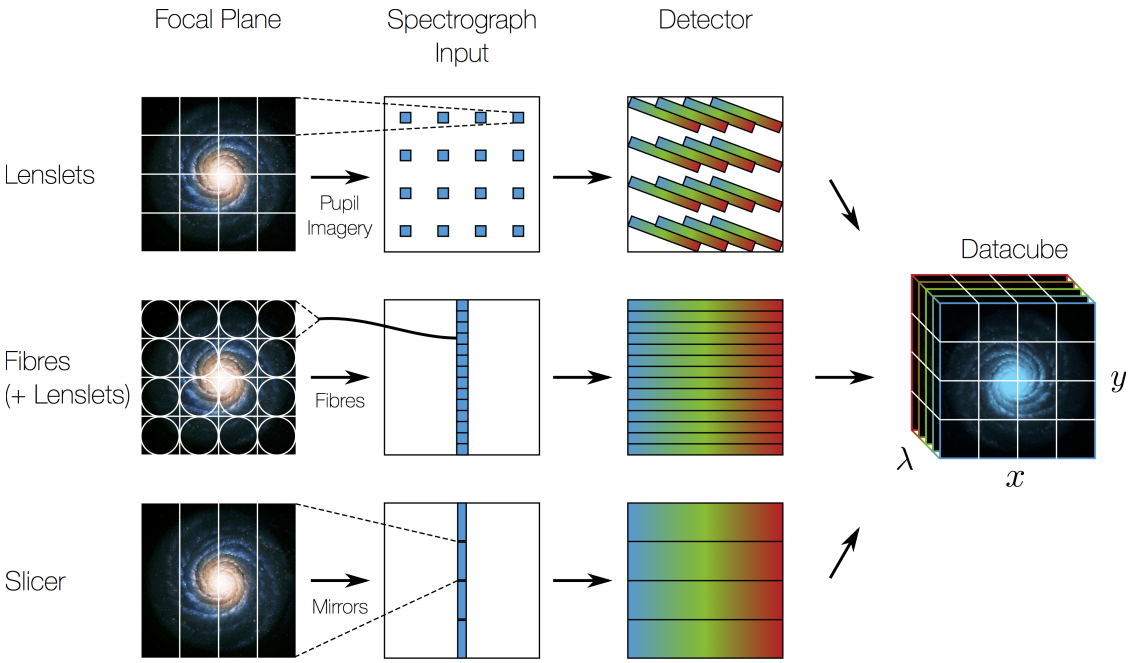


**Figure 1.1:** Types of integral field units: lenslets, fibres, and slicer-based (credit: JWST/STScI/NASA).

methods reveals a continuous trend towards improving sensitivity, spatial resolution, and ease of data interpretation.

The current landscape of IFS is marked by a diverse array of sophisticated instruments and technologies, each contributing uniquely to the field of astronomy. Some examples include:

- **MUSE (Multi Unit Spectroscopic Explorer) [6]**: Mounted on the Very Large Telescope (VLT), MUSE is a prime example of cutting-edge IFS technology, it is seeing limited and benefits from ground-layer adaptive optics (GLAO) and a narrow-field mode which uses LTAO[4]. It operates in the visible wavelength range and offers a wide field of view combined with high spatial and spectral resolution. MUSE has been instrumental in a variety of groundbreaking studies, including the detailed mapping of gas flows in galaxies, the study of the formation and evolution of galactic structures, and the detection of faint galaxies in the early Universe.

[4]Laser tomography adaptive optics (LTAO) is an advanced adaptive optics technique, utilising multiple laser guide stars to sample the turbulence in the atmosphere at different altitudes.

- **NIFS (Near-infrared Integral Field Spectrometer) [71]**: Installed on the Gemini North Telescope, NIFS specialises in the near-infrared spectrum. Its design is optimised for high spatial resolution, making it particularly effective for studying the centres of galaxies, including the regions around supermassive black holes (SMBHs). NIFS has provided critical insights into the dynamics of stars and gas in these extreme environments.

- **KMOS (K-band Multi-Object Spectrometer)[86]**: Located on the VLT, KMOS is unique for its ability to observe multiple objects simultaneously in the near-infrared. It consists of 24 independent deployable integral field units that can target different objects within a large field of view. This capability makes KMOS highly efficient for large surveys, such as studying the properties of intermediate-redshift galaxies.

- **ERIS (Enhanced Resolution Imager and Spectrograph) [35]**: ERIS is the next-generation adaptive optics instrument installed on the VLT. It is designed to replace and enhance the capabilities of earlier instruments like SINFONI (Spectrograph for INtegral Field Observations in the Near Infrared). Operating in the near-infrared, ERIS combines high spatial resolution imaging with integral field spectroscopy across J, H, and K bands. ERIS replaces the functionality previously provided by NaCo[5] and SINFONI.

The next generation of IFS instruments will be bigger and better, none more so than HARMONI, the High Angular Resolution Monolithic Optical and Near-infrared Integral field spectrograph. This instrument is currently being built and is the context of this thesis, further introduced in Section 1.3.

The IFS instruments mentioned above employ various techniques to split the light from the sky and analyse the light from astronomical objects. They also need to divide up the light spectrally. A critical component of these instruments is the disperser, which separates the spectral components of the incoming light, allowing

[5]A combination of Nasmyth Adaptive Optics System (NAOS) – Near-Infrared Imager and Spectrograph (CONICA)

for detailed spectroscopic analysis. Dispersers come in several forms, each with its own set of characteristics and advantages. The most common types include prisms, diffraction gratings, and grisms.

**Prisms** are among the simplest dispersers, refracting light into its constituent colours based on the material's dispersion properties. They offer a continuous spectrum but generally have lower dispersion compared to other types, making them suitable for applications requiring moderate spectral resolution.

**Diffraction gratings** use the interference of light waves to disperse light into its component wavelengths. They can provide high spectral resolution and are widely used in astronomical spectroscopy due to their ability to efficiently separate a wide range of wavelengths. Diffraction gratings can be either ruled or holographic, each with specific advantages in terms of efficiency and resolution.

**Grisms**, a combination of prisms and gratings, provide the dual function of dispersion and spectral coverage without altering the optical path, making them highly versatile. They are particularly useful in instruments that require easy switching between imaging and spectroscopy modes, offering a balance between spectral resolution and simplicity.

Each of these dispersers plays a vital role in the functioning of IFS instruments, ensuring that the spectral information from celestial sources is accurately captured and analysed. In the following section, we will explore diffraction gratings in more detail as the subject of Chapter 2.4.3 and 3.5.3 of this thesis.

## 1.2 Diffraction gratings

### 1.2.1 History

Credited with the first observation in nature, the Scottish astronomer James Gregory [82] observed a diffraction pattern emerging from the use of a bird feather in the $17^{th}$ century. The American astronomer, David Rittenhouse, is believed to have invented the first diffraction grating in 1785 with a series of 50 or 60 hairs held between two finely threaded screws. He performed this experiment in response to a request by a friend to explain a phenomenon he had observed by holding a

handkerchief up to his eye and viewing a distant street lamp [93]. Independently, and some years later, Joseph von Fraunhofer developed a similar system using thin wires, which ultimately led to the first spectrograph.

These early designs were all made by hand and were often transmission gratings but it wasn't long before reflective gratings, surfaces with small grooves etched into them, became mainstream. The late $19^{th}$ and early $20^{th}$ centuries saw the advent of mechanically ruled gratings, where precise grooves were engraved on a reflective surface. These gratings significantly improved spectral resolution.

Holographic gratings were developed in the mid-$20^{th}$ century, these are produced using laser interference patterns, resulting in a grating without the physical errors of ruling.

### 1.2.2 Grating theory

A diffraction grating can be defined as *"a mirror or window with a periodic structure (grooves), which diffracts polychromatic input light into monochromatic beams travelling in different directions"* [5].

The diffraction pattern arises from the periodic alterations of the phase and/or amplitude of an emergent wave. The early prototypes using hair or wire were *transmission amplitude gratings*, as the patterns produced alternate transparent and opaque regions, causing amplitude modulation in the wave. On the other hand, a transmissive element with regular grooves causing an optical thickness variation causes phase modulation, and so are known as *transmission phase gratings*. Alternatively, one can have *reflective* variations of the above when using, for example, a metal surface with a periodic structure.

Incident light waves strike the grating and interact with the slits/grooves. Each groove acts as a secondary source of light waves. The light is diffracted, with each groove producing its own set of wavelets. These wavelets interfere with each other. Constructive interference (where wave peaks align) leads to bright lines, while destructive interference (where peaks and troughs align) results in dark

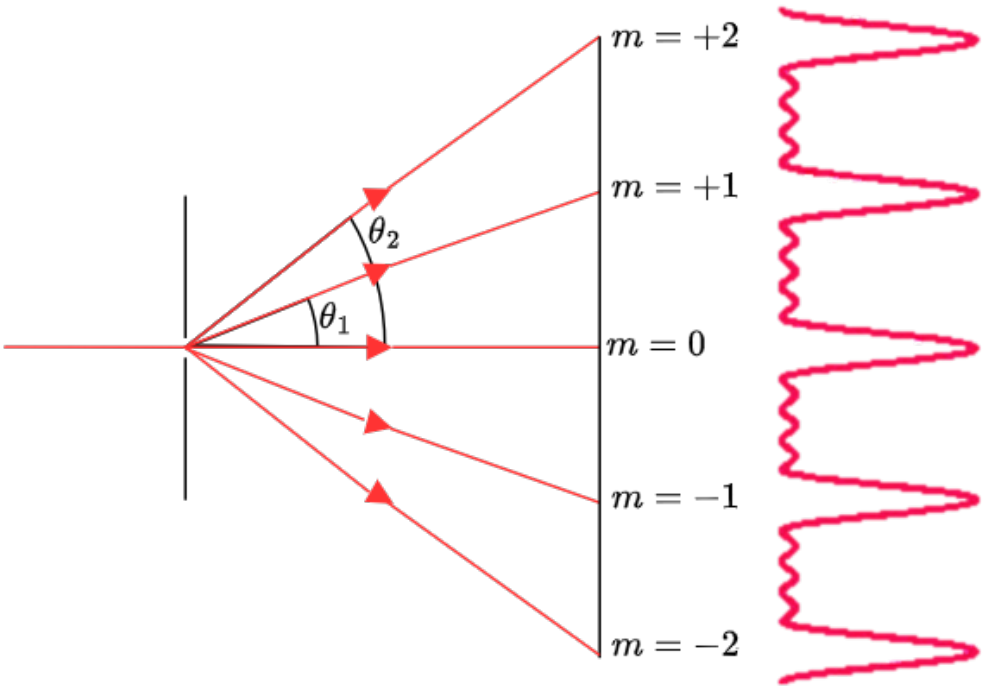


**Figure 1.2:** Diagram illustrating the diffraction of light through a grating, showing multiple diffraction orders. The central beam represents the zeroth-order ($m = 0$), where no diffraction occurs. The lower orders ($m = +1$, $m = -1$) and higher orders ($m = +2$, $m = -2$) are spread out at different angles ($\theta_1$, $\theta_2$), with each order corresponding to a specific wavelength of light. This separation of light into different orders and angles is a fundamental property of diffraction gratings, allowing the separation of light into its spectral components.

areas. This interference creates a spectrum, with different colours (wavelengths) being diffracted at different angles.

### The grating equation

The fundamental equation that governs the behaviour of diffraction gratings is the grating equation. It relates the angles of incidence and diffraction to the wavelength of the light and the spacing of the grating grooves. For the simple case where a plane light wave is at normal incidence to a grating with groove spacing $d$, the grating equation is given by

$$d \sin \theta_m = m\lambda, \tag{1.1}$$

where $\theta_m$ is the diffraction angle for the maximum of order $m$ and $\lambda$ is the wavelength.

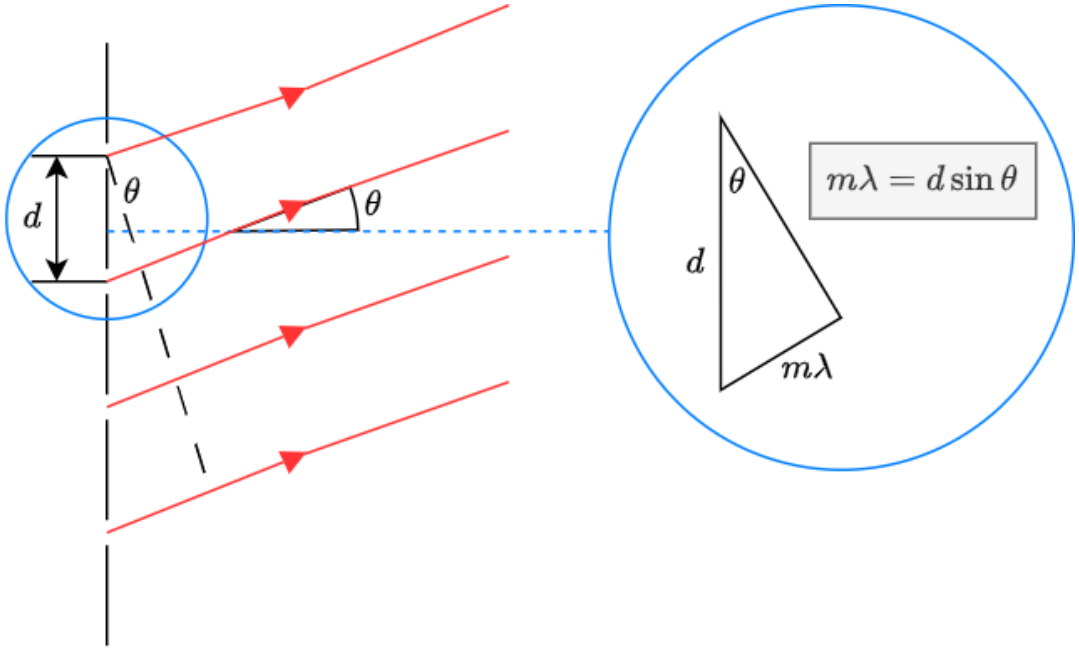


**Figure 1.3:** Diagram showing the geometry by which the grating equation is derived.

A diffraction order of $m = 0$ represents light which has been either directly transmitted through a transmission grating or specularly reflected off a reflective grating. The first orders on either side of that are $m = -1$ or 1, then comes $m = -2$ and 2, and so on, as shown in Figure 1.2. This equation is derived from the condition for constructive interference, where the path difference between adjacent slits must be an integer multiple of the wavelength the case of $m = 1$ is shown in Figure 1.3.

If the incident wave is not normal to the grating surface but at an angle $\theta$ in the orthogonal plane to the grooves, this equation becomes

$$d(\sin\theta \pm \sin\theta_m) = m\lambda, \tag{1.2}$$

where $\theta$ is the angle of incidence and $\theta_m$ is the angle of diffraction.

### Angular dispersion

Angular dispersion describes the rate of change of the diffraction angle with respect to the wavelength. It is given by

$$\frac{d\theta}{d\lambda} = \frac{m}{d\cos\theta_m}, \tag{1.3}$$

which is derived from Equation 1.1 via the chain rule. This relation indicates that the angular separation between different wavelengths increases with the diffraction order $m$ and decreases with the cosine of the diffraction angle. High angular dispersion is essential for achieving high spectral resolution in spectroscopic instruments.

**Resolving power**

For a diffraction-limited spectrograph where the resolving power is primarily determined by the diffraction grating and the optical system, rather than by the physical width of the entrance slit, the resolving power $R$ is given by

$$R = \frac{\lambda}{\Delta\lambda} = mN, \tag{1.4}$$

where $\Delta\lambda$ is the smallest difference in wavelength that can be resolved and $N$ is the number of grooves in the grating.

This type of spectrograph is optimised for high-resolution spectroscopy, making it ideal for applications requiring detailed spectral information, such as identifying chemical compositions and detecting fine spectral lines. Resolving power can be increased by increasing the total number of grooves in the grating, or by using higher orders. However, HARMONI and indeed most astronomical integral field spectrographs are not, in fact, diffraction limited. Their resolving power is limited by the slit width, or the pixel size on the detector.

A slit-width-limited spectrograph is one where the resolving power is primarily limited by the physical width of the entrance slit rather than by the diffraction grating.

The upper part of Figure 1.4 shows an imaging system with two lenses (a collimating lens and camera/imaging lens) with focal length $f_1$ and $f_2$ respectively, which produces an image of a slit, of width $\Delta x_s$, with a width of

$$\Delta x_i = \left(\frac{f_2}{f_1}\right) \Delta x_s. \tag{1.5}$$

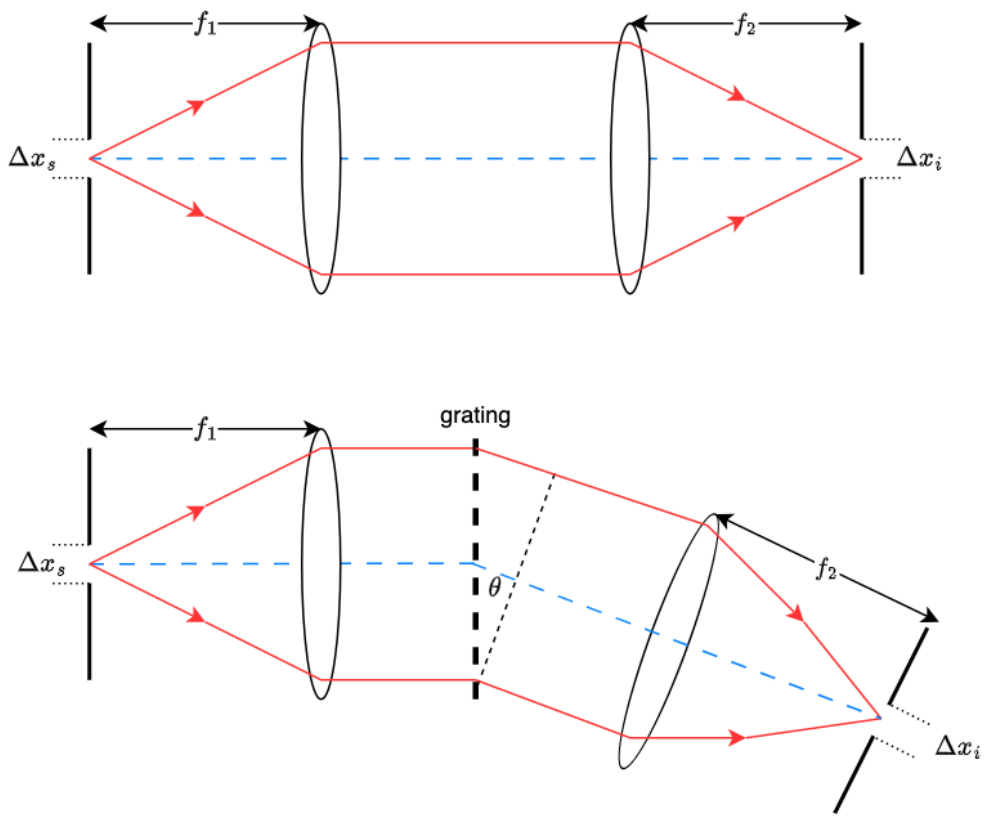


**Figure 1.4:** Basic imaging system to image a slit of width $\Delta x_s$ (top) and with the addition of a grating becomes the layout of a basic spectrograph (bottom) where the slit is imaged at angle $\theta$.

Adding a diffraction grating to this setup, shown in the bottom part of the Figure 1.4 gives a basic spectrograph, whereby a spectrally dispersed image of the slit at angle $\theta$ is foreshortened by $\cos\theta$. Equation 1.5 becomes

$$\Delta x_i = \left(\frac{f_2}{f_1 \cos\theta}\right) \Delta x_s. \tag{1.6}$$

The resolving power $R$ in this case can be approximated as

$$R = \frac{\lambda}{\Delta\lambda_{\text{slit}}}, \tag{1.7}$$

where $\Delta\lambda_{\text{slit}}$ is the broadening of the spectral lines due to the finite slit width.

The instrumental line width $\Delta\lambda_{\text{inst}}$ due to the slit can be expressed as

$$\Delta\lambda_{\text{inst}} = \frac{\Delta x_s}{m \cdot f} \cdot \lambda, \tag{1.8}$$

where $\Delta x_s$ is the slit width and $f$ is the focal length of the spectrograph.

In this case, the resolution is lower compared to a diffraction-limited spectrograph because the finite slit width causes broadening of the spectral lines. Narrowing the slit can improve resolution but reduces the amount of light entering the spectrograph for each slitlet, affecting sensitivity and signal-to-noise ratio (SNR). Also key is that reducing the 'slit' width for an IFU but maintaining the same field of view, means more slits. This increases the complexity and cost of the IFU due to the worsened manufacturability. This type of spectrograph is often used when light throughput is more critical than resolution, such as when observing faint objects.

To maintain the same field of view with narrower slices, you need more slices. This increases the complexity and cost of the IFU. If you keep the number of slices the same and make them narrower, you effectively decrease the field of view. As already mentioned, manufacturability is a significant factor. Creating very narrow and precisely aligned slices is technically challenging and expensive. The tolerances for slice width, surface quality, and alignment become increasingly stringent as the slices get narrower. Any imperfections can lead to scattered light, reduced throughput, and distortions in the spectra.

Optimising a diffraction-limited system can be done by increasing the number of slits and using higher diffraction orders. Careful alignment and high-quality optics are essential. Whereas a slit-width limited system can be optimised by balancing slit width with the required spectral resolution. Adaptive optics can be used to compensate for lower spatial/angular resolution.

**Efficiency**

The efficiency of a diffraction grating is a measure of how effectively it diffracts incident light into a specific order. Grating efficiency can be categorised as relative or absolute. Relative efficiency is measured as a percentage of the power diffracted compared to that transmitted by glass of the same material, geometry, and coating (or reflected by a mirror with the same coating in the case of reflection gratings),

while absolute efficiency is the percentage of the incident power that is diffracted into a particular order.

All optical components have efficiencies of $< 1$, however, despite improving technology and manufacturing techniques, diffraction gratings often have the lowest efficiency of any single component in a typical astronomical spectrograph's optical chain.

#### Bragg condition

Volume phase holographic gratings (VPHGs), introduced in Section 1.2.3, utilise the principles of Bragg diffraction to selectively diffract specific wavelengths of light. The Bragg condition [18] is a fundamental principle that describes how constructive interference occurs when light interacts with a periodic structure, such as the modulation of the refractive index in a VPHG.

The Bragg condition for VPHGs can be expressed as

$$m\lambda = 2dn_{\text{eff}} \sin\theta, \tag{1.9}$$

where $d$ is the grating period, the distance between adjacent planes of varying refractive index within the grating, $n_{\text{eff}}$ is the effective refractive index within the grating material, influenced by the modulation of the refractive index, and $\theta$ here is the Bragg angle, the angle at which the incident light meets the grating planes and undergoes constructive interference. The principle is shown in Figure 1.5 where three incident parallel rays labelled A, B, and C constructively interfere after interacting with a periodic structure.

In VPHGs, these parameters are carefully controlled to achieve high diffraction efficiency and wavelength selectivity, making them ideal for applications such as spectroscopy, telecommunications, and laser tuning.

### 1.2.3 Volume phase holographic gratings

VPHGs, a modern development, use a photosensitive material to record interference patterns which create the grating grooves, offering high efficiency and versatility in

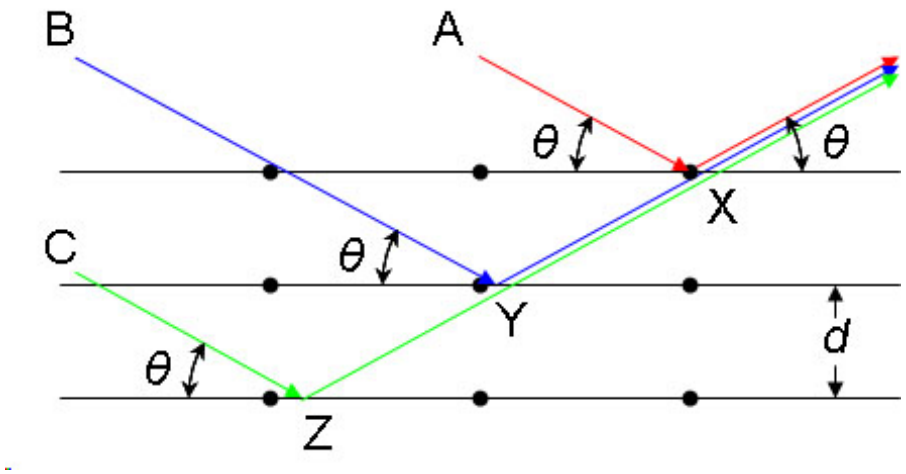


**Figure 1.5:** The Bragg condition for VPH gratings (source: ChemWiki (creative commons)).

spectral dispersion. The transition from ruled to holographic to VPHGs represents a continual quest for higher spectral resolution, efficiency, and versatility.

Unlike conventional surface relief gratings, VPHGs utilise volume holography, where light is recorded within the bulk of a photosensitive material (such as dichromated gelatin or DCG) in a periodic pattern. This creates a refractive index modulation along the thickness of the material, forming a grating structure. When incident light interacts with a VPHG, it undergoes diffraction, splitting the light into various diffracted orders based on the grating period and the angle of incidence like any other transmission grating. The refractive index modulation plays a pivotal role in dictating the efficiency and performance of VPHGs.

### Fabrication Methods

The fabrication of VPHGs involves a multi-step process that begins with the creation of a holographic pattern in a photosensitive medium. Typically, this medium consists of a polymer or a gelatin material doped with photosensitive molecules. The holographic pattern is recorded by splitting a coherent laser beam and interfering a reference beam with a signal beam, creating a complex interference pattern, as shown in Figure 1.6. This interference pattern causes the photosensitive material's refractive index to change, resulting in the desired grating structure.

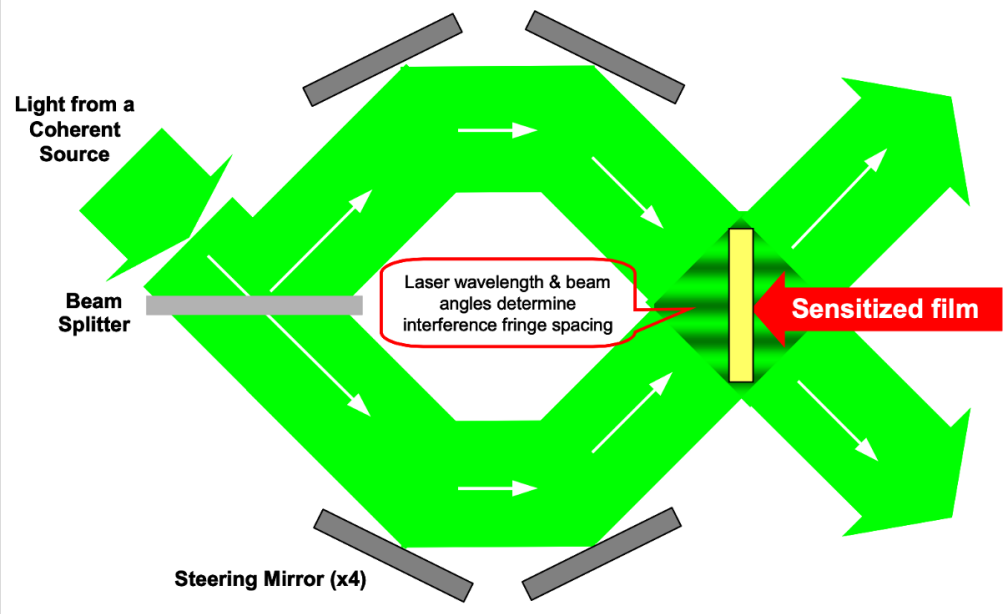


**Figure 1.6:** VPH grating manufacturing technique of interfering beams from a coherent laser (credit: Kaiser Optical Systems).

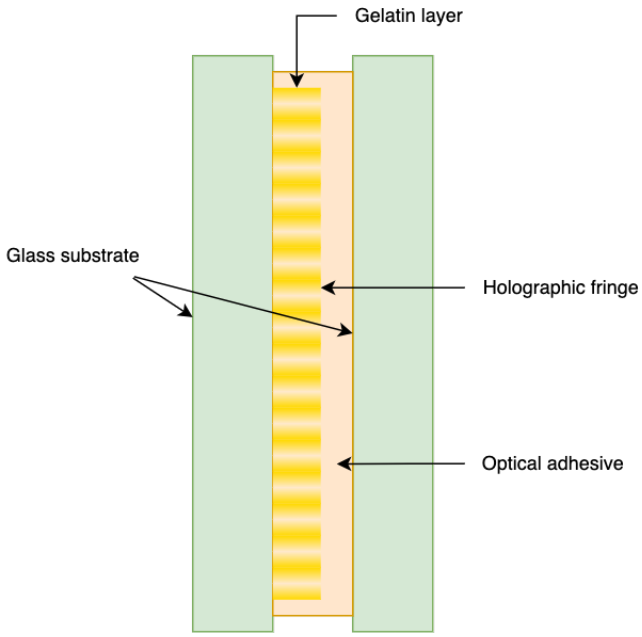


**Figure 1.7:** Schematic representation of a VPHG. The grating consists of a gelatin layer that contains the holographic fringes, which are periodic variations in the refractive index. These fringes cause diffraction of incident light according to the Bragg condition. The gelatin layer is sandwiched between two glass substrates, which provide structural support, and is bonded with optical adhesive.

After the recording step, the material is developed to stabilise the holographic pattern and fix the refractive index modulation. The development process is crucial in determining the final efficiency and spectral performance of the VPHG. The grating layer is then sandwiched with another substrate and all held together with an adhesive. Figure 1.7 shows a schematic representation of a VPH grating.

VPHGs are the chosen grating technology for HARMONI. Currently the only global supplier of astronomical VPHGs of sufficient sizes and specifications for HARMONI is Wasatch Photonics in the US. Previously, Kaiser Optical Systems Inc. (KOSI), who supplied the VPHGs for WEAVE [13] and MUSE [81], would have been an alternative supplier however they refocused their business partly due to the COVID-19 pandemic and then as part of a merger with SpectraSensors and subsequent acquisition by Endress+Hauser Optical Analysis, Inc.

A University of North Carolina (UNC) spin-out, Syzygy Optics, claims to be able to make novel curved VPHGs. A patent [76] details out the use of curved glass with optical power and tilted fringes. Applications for ELTs have been suggested, although no evidence for their use could be found in published literature or conference proceedings articles.

In Europe, the Italian National Institute for Astrophysics (INAF) has some history of manufacturing VPHGs which is emerging again with a new capability, as shown in Figure 1.8, to manufacture large gratings for astronomical applications which may help to add product and market diversity for future instruments.

The currently limited supplier pool means that all of the gratings with the specifications required by HARMONI are not simply available off-the-shelf, as described in Section 2.2.1. With only one likely supplier and specific requirements, the instrument development required an iterative research and development process in collaboration with the supplier (Wasatch Photonics, Inc.).

#### Advantages and Applications

VPHGs present several unique advantages over traditional surface relief gratings, making them a preferred choice for various advanced optical systems:

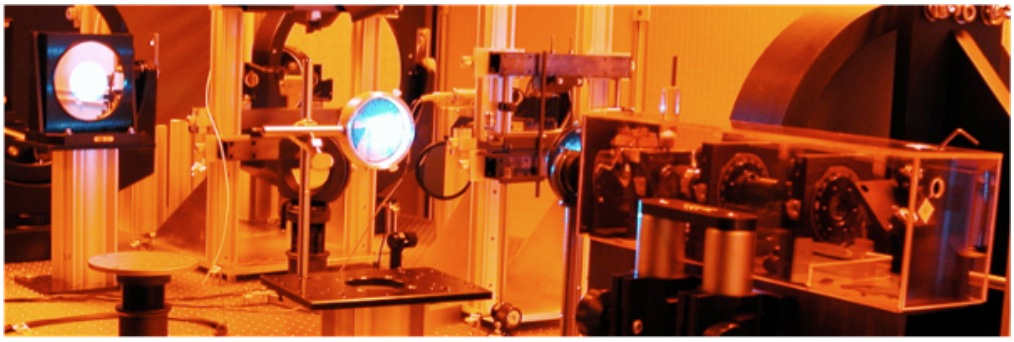

**Figure 1.8:** VPHG prototype manufacture (credit: Andrea Bianco, INAF).

- High Efficiency: VPHGs exhibit exceptionally high diffraction efficiencies, often greater than 90%, and can reach up to 99% for specific wavelengths (typically for laser pulse compression applications). This high efficiency translates into increased signal-to-noise ratios, enhancing the overall performance in spectroscopic applications, a key advantage particularly in light-limited environments such as astronomy [104]. The high efficiency, relative to ruled gratings, is largely down to the Bragg condition that VPHGs are operated in. Other factors play a part including: more uniform and precise grating structure due to holographic recording, reduced scattering and stray light, minimised polarization effects, and the ability to optimise efficiency for specific bands.

- Broadband Performance: VPHGs are adept at handling a broad range of wavelengths simultaneously without significant dispersion losses, which is critical for applications requiring multi-wavelength capabilities. This attribute makes them extremely versatile in a variety of spectroscopic techniques, where different substrates may be limiting for wide band applications, due to their bulk absorption properties [104].

- Compact Design: The inherent design of VPHGs allows for a more compact and lightweight optical setup. Since they operate in transmission rather than reflection, VPHGs eliminate the need for long optical paths and can be incorporated into space-constrained environments such as portable optical devices and space telescopes

- Low Polarisation Sensitivity: VPHGs show minimal sensitivity to the polarisation state of the incident light, which significantly reduces alignment issues and simplifies the optical design.

- Easy Handling and Durability: Encapsulated between two glass plates, VPHGs are more robust and easier to handle compared to traditional gratings. The sealed design helps protect the delicate diffractive structures from dust and moisture, thereby enhancing their durability and ease of maintenance.

The versatility and superior characteristics of VPHGs have led to their widespread adoption across multiple fields beyond traditional astronomical applications [8]:

- Heads-up displays (HUDs): In automotive and aviation applications, VPHGs are used to project navigation data, speed, and other essential information directly into the driver's or pilot's field of view. The use of VPHGs allows for the creation of compact and efficient HUD systems.

- Telecommunications: In the rapidly evolving field of telecommunications, VPHGs are employed in wavelength division multiplexing (WDM) systems. Their ability to efficiently demultiplex optical signals enhances the capacity and speed of fibre-optic communication systems.

- Ultrafast Lasers: VPHGs play a crucial role in the management of ultrafast laser pulses. They are used in laser pulse compression and shaping, vital for applications in materials processing, medical imaging, and fundamental research in physics.

- Hyperspectral Imaging: Beyond astronomy, VPHGs find extensive use in hyperspectral imaging systems for environmental monitoring, agriculture, and remote sensing. Their high efficiency and broadband performance enable these systems to capture detailed spectral data across a wide range of wavelengths, facilitating better material identification and classification.

As the demand for more sophisticated optical systems continues to grow, the role of VPHGs is expected to expand further. Ongoing research and development in holographic materials and fabrication technologies promise to enhance the capabilities of VPHGs.

## 1.3 E-ELT and HARMONI

Over time, the collecting areas, aperture sizes, or diameters - all equivalent parameters - of telescopes have steadily been increasing. Larger telescopes allow us to see fainter objects and in more detail, hence the desire to continually grow. The famous Rayleigh criterion, Equation 1.10, describes the smallest resolvable angle ($\theta$) two objects can be at, the best spatial (or angular) resolution, as a function of observed wavelength and telescope diameter. The equation,

$$\theta = \frac{1.22\lambda}{D}, \tag{1.10}$$

shows that by increasing the diameter D of a telescope we can improve the angular resolution for a given wavelength $\lambda$.

In the optical domain, the initial limitations in manufacturing large lenses, combined with the emergence of new techniques to shape and polish mirrors and the relative ease of physically supporting large mirrors compared to lenses, led to refractive telescopes being replaced by their reflective counterparts, which now dominate.

In the last thirty years, the attention of the international scientific community has been split between gradually growing ground-based telescopes and an increasing suite of space-based telescopes. Engineering advancements have enabled larger mirror production, improved adaptive optics, and greater launch capacity.

Arguably, most of the 'low hanging fruit' in astronomy has been picked, and now, as in other areas of scientific research such as particle physics, large international consortia are required to pool funds and expertise to break new ground. In Europe and the US, separate efforts are now underway to develop a new generation of the

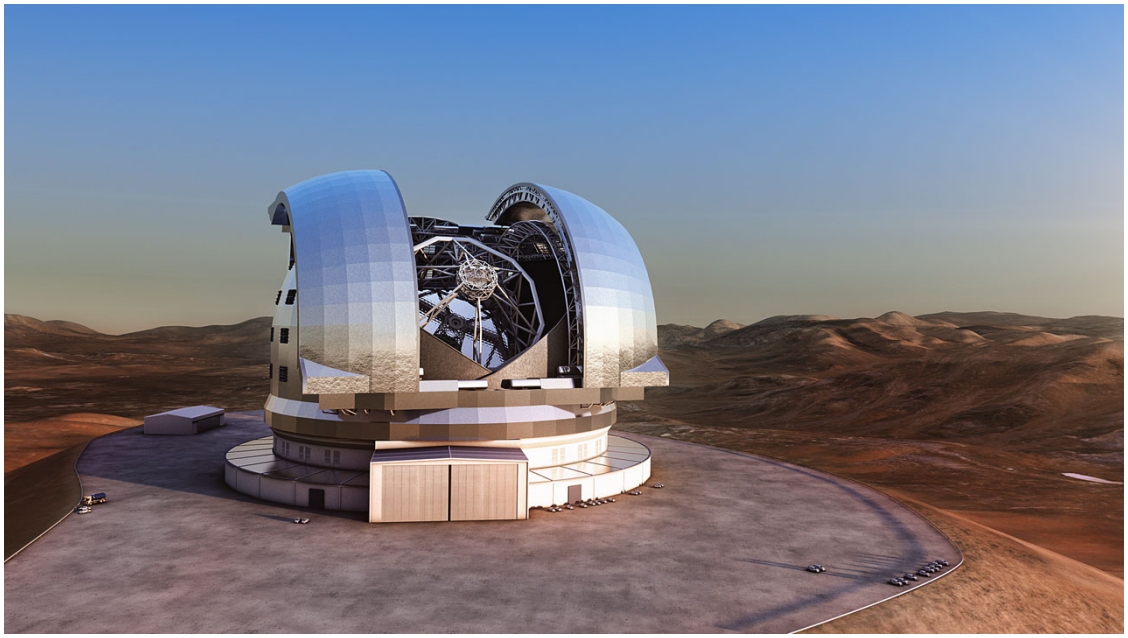

**Figure 1.9:** A render of the European Extremely Large Telescope (E-ELT) currently under construction (credit: ESO).

largest optical telescopes ever conceived: the extremely large telescopes (ELTs). This new era will define astronomy for the coming decades.

The European Extremely Large Telescope (E-ELT) is leading the way (Figure 1.9), under the auspices of the European Southern Observatory (ESO). Currently under construction in Chile, with the colossal dome structure taking shape, it is scheduled to see first light in 2028.

In parallel, the United States is pursuing two competing projects. The Giant Magellan Telescope (GMT), based at Las Campanas Observatory in Chile, will feature seven 8.4-metre mirrors working together to form an effective 24.5-metre aperture. Its early instrumentation will include GMTIFS (Giant Magellan Telescope Integral Field Spectrograph) [90], a diffraction-limited near-infrared IFS operating behind an adaptive optics system, and GMACS, a wide-field multi-object spectrograph optimised for survey work.

Meanwhile, the Thirty Meter Telescope (TMT), proposed for Mauna Kea in Hawaii (amid considerable protest and legal challenges) and as a backup option for La Palma, Spain, will host NFIRAOS (Narrow Field Infrared Adaptive Optics System) [32] as its adaptive optics system and several first-light instruments, including

IRIS (Infrared Imaging Spectrograph) [108], a near-infrared imager and integral field spectrograph. IRIS is designed to deliver diffraction-limited imaging and spectroscopy from 0.84–2.4 µm at unprecedented spatial resolutions.

Both GMT and TMT are currently facing funding and political uncertainties, which may delay their completion into the mid-2030s, whereas the E-ELT remains the most advanced in terms of construction progress.

The E-ELT is scheduled to be operational in 2028 and its first instruments will be MICADO, METIS, and HARMONI.

MICADO [36], the Multi-AO Imaging Camera for Deep Observations, will focus on providing high-resolution imaging stabilized by advanced adaptive optics systems. This instrument will be particularly effective in the study of individual stars within crowded stellar fields and the fine structures within distant galaxies.

METIS [19], the Mid-infrared ELT Imager and Spectrograph, will extend the E-ELT's observational reach into the mid-infrared spectrum, facilitating cutting-edge research into cooler and obscured objects in the universe, such as planet-forming discs around young stars and the densest regions of active galactic nuclei.

HARMONI [99](High Angular Resolution Monolithic Optical and Near-infrared Integral field spectrograph), is poised to be a cornerstone of the E-ELT's observational capabilities. Designed to provide integral field spectroscopy across visible to near-infrared wavelengths, HARMONI will enable detailed spectroscopic studies across a wide range of astronomical objects. Its high spatial resolution and large field of view are crucial for dissecting the fine-scale structure of complex astronomical phenomena, such as the dynamics of early galaxies, the formation processes of stars, and the environments of black holes. By allowing astronomers to gather both spatial and spectral information simultaneously, HARMONI will offer unprecedented insights into the physics and chemistry of celestial objects, from the formation of cosmic structures to the atmospheres of exoplanets.

ELT instruments are appropriately large constructions. HARMONI, as shown in Figure 1.10, is the size of a two-storey house and will sit on the Nasmyth platform of the E-ELT. It receives light from the E-ELT where it divides the sky into 8 sub-fields,

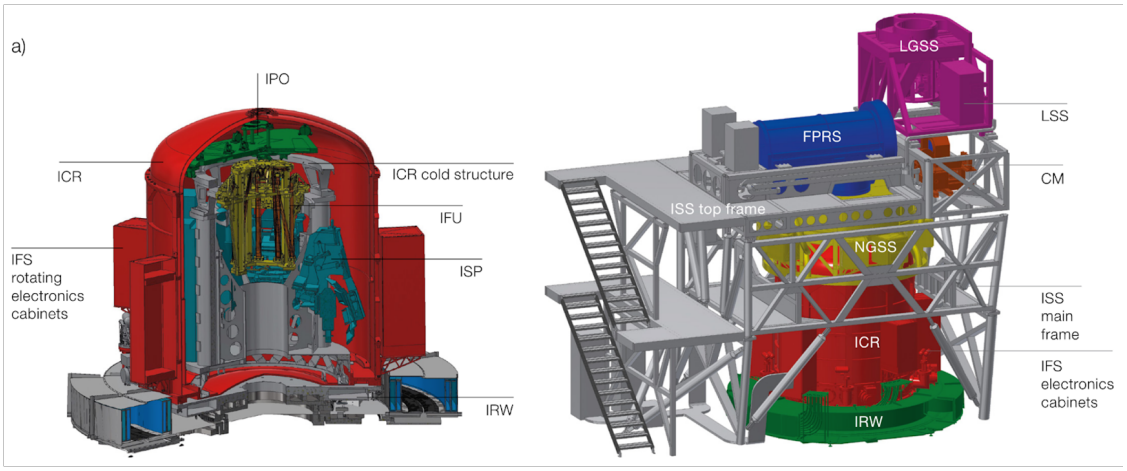


**Figure 1.10:** The full HARMONI instrument with subsystems (right), and inside the cryostat (left).

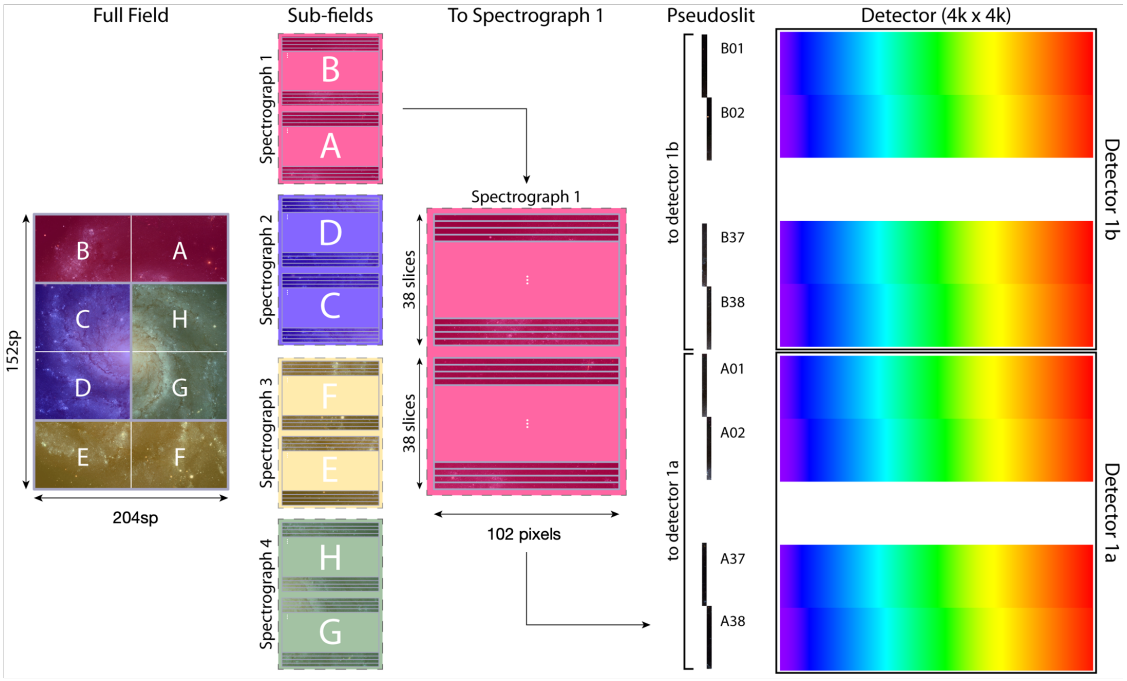


**Figure 1.11:** The layout of the IFU sub-fields.

as shown in Figure 1.11, fed into 4 spectrographs, each of which is spectrally dispersed by a VPHG onto a pair of 4k x 4k HgCdTe (MCT) CMOS detectors (H4RG)[6].

This thesis describes research conducted as part of the HARMONI engineering and science teams at the University of Oxford.

[6]H4RG is an acronym within an acronym and refers to the HAWAII-4RG which is part of the HgCdTe astronomical wide area infrared imager (HAWAII) detector series. The 4RG refers to the 4k x 4k pixels, the reference pixels and guide mode.

## 1.4 Intermediate mass black holes

In addition to the VPHG characterisation research, I have investigated a promising science case for HARMONI as described in Chapter 4.5.5 which is the detection and observation of intermediate mass black holes.

### 1.4.1 What are IMBHs?

Intermediate Mass Black Holes (IMBHs), with masses ranging from $10^2$ to $10^5 M_\odot$, are a missing link between stellar mass black holes and supermassive black holes. Their existence helps to bridge the gap in our understanding of the black hole mass spectrum. IMBHs are predicted to exist in environments like star clusters[40], where their gravitational influence could have profound implications for the clusters' stellar dynamics.

Using high angular resolution integral field spectroscopy to probe the line-of-sight velocity distributions of stars near the centres of star clusters is considered a promising technique for confirming the presence of IMBHs. As introduced in Chapter 4.5.5, the HARMONI instrument is ideally suited for this task, given its combination of high resolution and sensitivity.

### 1.4.2 Why are IMBHs interesting?

IMBHs are a pivotal element in our understanding of the formation and evolution of black holes across the Universe. Their detection could provide critical insights into multiple astrophysical phenomena:

1. Black Hole Growth Pathways [7][45]: IMBHs are hypothesised to be the seeds from which supermassive black holes grow. Their discovery and mass characterisation would therefore inform models of SMBH evolution.

2. Stellar Dynamics [31]: The presence of an IMBH affects the dynamics of its host cluster, leading to observable kinematic signatures, such as increased stellar velocity dispersion near the centre. This can also have consequences for the cluster's structural evolution.

3. Gravitational Wave Astronomy [39]: IMBHs could be sources of gravitational waves, particularly during mergers. Their detection in dense environments could aid in refining models of gravitational wave production and potentially be directly observable by missions such as the European Space Agency's Laser Interferometer Space Antenna (LISA) [1].

### 1.4.3 Formation pathways

It is thought that IMBHs can form through several different mechanisms, of which there are a few leading candidates:

- **Population III Remnants [92][80]:** The earliest stars, known as Population III, were likely formed from the primordial, metal-free gas in the early Universe. These massive stars could rapidly evolve and collapse into black holes with masses around $100M_{\odot}$. These large stellar mass black holes could then merge to form IMBHs [100].

- **Direct Collapse [10]:** In environments where gas cannot efficiently fragment into stars, it might directly collapse into a black hole. This process can produce seed black holes with masses ranging from $10^4$ to $10^6 M_{\odot}$. The occurrence of such direct collapse depends critically on specific environmental conditions, such as a strong ultraviolet radiation field that inhibits hydrogen cooling, preventing star formation and promoting the collapse of gas directly into a black hole.

- **Gravitational Runaway in Dense Clusters [80]:** Within regions of extremely high stellar densities, such as the cores of dense star clusters, collisions and mergers of stars might lead to runaway gravitational collapse, resulting in the formation of IMBHs. This mechanism could occur over relatively short astronomical timescales, with the resultant IMBHs potentially growing further by accreting more gas and stars from their surroundings.

Each formation pathway suggests different environments and mechanisms through which IMBHs could arise, influencing their mass distribution, spatial distribution, and the likely locations where they can be found. These characteristics are crucial for developing targeted observational strategies aimed at detecting IMBHs through various means such as dynamical influences on surrounding stars, accretion signatures, or gravitational waves produced during formation or merger events.

### 1.4.4 Detection methods and candidates

There are many studies in the literature that attempted to confirm the detection of IMBHs. Some prominent examples are described as follows.

Gerssen et al. (2002) [42] attempted to use data from the Space Telescope Imaging Spectrograph (STIS) on the Hubble Space Telescope (HST) to detect an IMBH in the globular cluster M15 using 64 stars. They too use the line-of-sight velocity technique to probe the velocity dispersion profile of the cluster and combine the space-based observations with pre-existing ground-based data. The study concluded that it was indeed likely that a central IMBH was present, however, they expressed caution for a few reasons. Firstly, their dynamical models are idealised (e.g. in hydrostatic equilibrium), and secondly, their observed kinematics from a small sample are assumed to be characteristic of the broader population, and not contaminated by orbital motions of binary systems.

Subsequent work by van der Marel et al. (2002) [69] examined G1, a massive globular cluster in M31, using similar line-of-sight velocity dispersion measurements and found evidence consistent with a $\sim 2 \times 10^4 M_\odot$ IMBH. However, as with M15, model degeneracies between an IMBH and alternative mass distributions (e.g., centrally concentrated populations of stellar remnants) made definitive conclusions difficult.

Further attempts to constrain IMBH masses have employed high-resolution proper motion measurements. Baumgardt et al. (2005) [9] used N-body simulations to argue that observed core properties of several globular clusters could be explained without invoking an IMBH, attributing the kinematic signatures instead to mass segregation and a population of dark remnants.

In more recent years, Lützgendorf et al. (2013) [66] carried out an extensive survey of Galactic globular clusters using integral field unit (IFU) spectroscopy with instruments such as VLT/FLAMES and found tentative kinematic evidence for central black holes in several clusters. However, their results similarly suffered from the limitations of spatial resolution, anisotropic velocity dispersions, and potential contamination from bright binaries.

Beyond stellar dynamics, some studies have used gas kinematics. For instance, Nguyen et al. (2019) [75] examined gas motions in low-mass galaxies in search of IMBHs, although distinguishing between gravitational and non-gravitational motions (e.g., due to feedback processes) remains a significant challenge in these environments.

Bellovary et al. (2019) [11] argued that IMBHs are particularly challenging to detect, yet they are of significant interest due to their potential role as seeds for the formation of SMBHs. The authors propose that IMBHs are likely to reside in dwarf galaxies or wander within the halos of more massive galaxies, environments where traditional detection methods—such as accretion events or dynamical signatures—are less effective. However, they suggest that upcoming missions like LISA will be instrumental in detecting IMBH mergers, potentially observing these events at high redshifts and providing accurate measurements of their masses.

Kızıltan et al. (2017) [59] examine the significant influence of an IMBH on the spatial distribution of stars in a star cluster. They explain that, during relaxation, massive stars migrate towards the cluster's centre more efficiently as they seek energy equipartition. As these stars approach the IMBH, they are scattered, leading to a heating effect in the cluster's core, which in turn disrupts the process of mass segregation. Over time, this disruption, combined with dynamical effects such as two-body relaxation, results in the outward propagation of the IMBH's influence beyond its immediate sphere of gravitational control, creating a detectable dynamical signature that extends across the cluster.

### Stellar kinematics and velocity dispersion

HARMONI on the E-ELT will be uniquely suited to determine the line-of-sight velocities of stars near the centres of star clusters (both open and globular - as introduced in Section 4.1.2). This is critical to characterise the velocity dispersion profiles of the clusters.

Velocity dispersion refers to the spread in velocities of stars moving within a collection of stars, such as galaxies or globular clusters. It is a statistical measure that describes how fast stars are moving relative to each other on average. The velocity dispersion profile shows how this dispersion varies with distance from the centre of the object.

In a star cluster without a central massive object, the velocity dispersion is primarily governed by the overall mass distribution of the cluster's stars. Typically, the velocity dispersion is slightly higher in the core due to the higher stellar density and decreases outward as the gravitational potential weakens.

When an IMBH resides at the centre of a cluster, it significantly alters the gravitational potential in its vicinity. The IMBH exerts a strong gravitational force on nearby stars, causing them to move at higher velocities to remain in orbit around the cluster's centre. As a result, the velocity dispersion increases sharply as one approaches the centre of the cluster, creating a noticeable rise in the velocity dispersion profile near the core known as a 'cusp'.

Another effect, known as energy equipartition, plays a part. In dense stellar systems, there is a tendency towards energy equipartition, where more massive objects (like an IMBH) interact with less massive ones (stars), imparting higher velocities to the stars near them. This phenomenon is described in more detail with the introduction of mass segregation below.

### Sphere of influence

The sphere of influence, typically indicated by its radius, is defined as the volume in which the gravitational potential of a central massive object, in this case, an IMBH, equals that of the smaller objects (stars) in that volume. It is expected that

these stars are gravitationally bound to the IMBH and their motion is influenced by the mass of the black hole more than by the other stars.

The sphere's radius is determined by:

$$r_{\rm inf} = \frac{Gm_{\rm IMBH}}{\sigma_{\rm cl}^2}, \tag{1.11}$$

where $m_{IMBH}$ is the IMBH mass and $\sigma_{cl}$ is the velocity dispersion of the star cluster in the central region. This equation is motivated by the virial theorem and is derived by equating the black hole's gravitational potential energy to the stars' typical kinetic energy. This relationship will help us understand the limits of our ability to detect IMBHs as the angle subtended in the sky of the influence radius will vary with object distance and black hole mass.

The sphere of influence of an IMBH essentially demarcates a boundary within which the black hole's gravitational pull is the dominant force shaping the orbits of stars. This region is pivotal for observational strategies aimed at detecting IMBHs, as the dynamics of stars within this sphere can provide indirect evidence of the black hole's presence. The subtended angle of this sphere on the sky, influenced by the black hole's mass and the observer's distance from the cluster, serves as a critical parameter in designing observational campaigns and interpreting astrometric data.

**Mass segregation**

Mass segregation is the observed phenomenon whereby more massive stars tend to concentrate towards the centre of a star cluster, and less massive stars drift outwards. This is caused by the equipartition of kinetic energy; this describes the exchange of energy and momentum by two bodies passing each other, and that statistically the kinetic energy will equalise during their encounter. Being proportional to mass and the velocity squared ($K_E = 1/2mv^2$), this means that larger bodies lose velocity and smaller bodies will speed up. Hence the decelerating bodies will drift towards the shared centre of mass - towards lower/smaller orbits, and vice versa.

This process happens over a long time scale, known as the relaxation time, which is approximated by

$$t_{\text{relax}} = \frac{N}{8 \ln N} \times t_{\text{cross}}, \tag{1.12}$$

where $N$ is the number of stars in the cluster and $t_{\text{cross}}$ is the time it would take a star to cross the cluster - resulting in a time period typically of 100 million years. This means that for the simulated star cluster this study uses in Chapter 4.5.5 which has evolved over 3 MYr, there would not be sufficient time for mass segregation to occur, and one could expect a more random distribution of masses throughout the cluster.

This natural sorting mechanism, driven by gravitational interactions, not only influences the spatial distribution of stars within a cluster but also affects the cluster's luminosity profile and core collapse timescale. In the context of detecting IMBHs, understanding the extent and impact of mass segregation is essential, as it can alter the dynamical signatures that astronomers rely on to infer the presence of these black holes.

### 1.4.5 Line-of-sight velocity-based IMBH detection with HARMONI

This study, the subject of Chapter 4.5.5, investigates the possibility of detecting an IMBH, using integral field spectroscopy with HARMONI. As the instrument is still in development, simulated data need to be produced, then analysis can be conducted on those data.

This project utilises simulated data by the MICADO team applicable to the IMBH candidate in the central region of the NGC 2070 star cluster, "R136", in the Large Magellanic Cloud. The MICADO[7] instrument team at INAF in Italy have simulated two N-body dynamical cluster models with and without an IMBH, with equivalent observing conditions of R136 [38]. They provided model data from their simulations in the form of two data sets. Each covers a patch of sky (10"×10") with 33,801 stellar objects in it. Each object (star) has a mass, XY location (arcsec at 50 kpc) in the plane of the sky, magnitudes in four bands (I, J, H, and K) and a line-of-sight velocity.

[7]Another E-ELT first light instrument.


**Figure 1.12:** The planned data analysis process for the IMBH work.

Figure 1.12 shows the planned data analysis process for simulating an observed datacube and extracting kinematic information from these data. This plan forms the basis for the contents of Chapter 4.5.5.

Figure 1.13 shows a real observation of R136 as seen by the HST and by MUSE in narrow-field mode (NFM), alongside a simulated HARMONI observation from this study. This figure provides context for the size of our simulated observations and showcases the increased spatial resolution and our improved ability to probe deeper into the core of star clusters. The HST and MUSE observations are of the same object, but as the HARMONI observation is simulated the comparative location of the images is indicative and not an exact comparison. However, it is clear that HARMONI on the E-ELT will have a greater ability to probe deeper into dense clusters than MUSE on the VLT.

## 1.5 Thesis aims and scope

The research aims of this thesis, which are addressed in one chapter each, are:

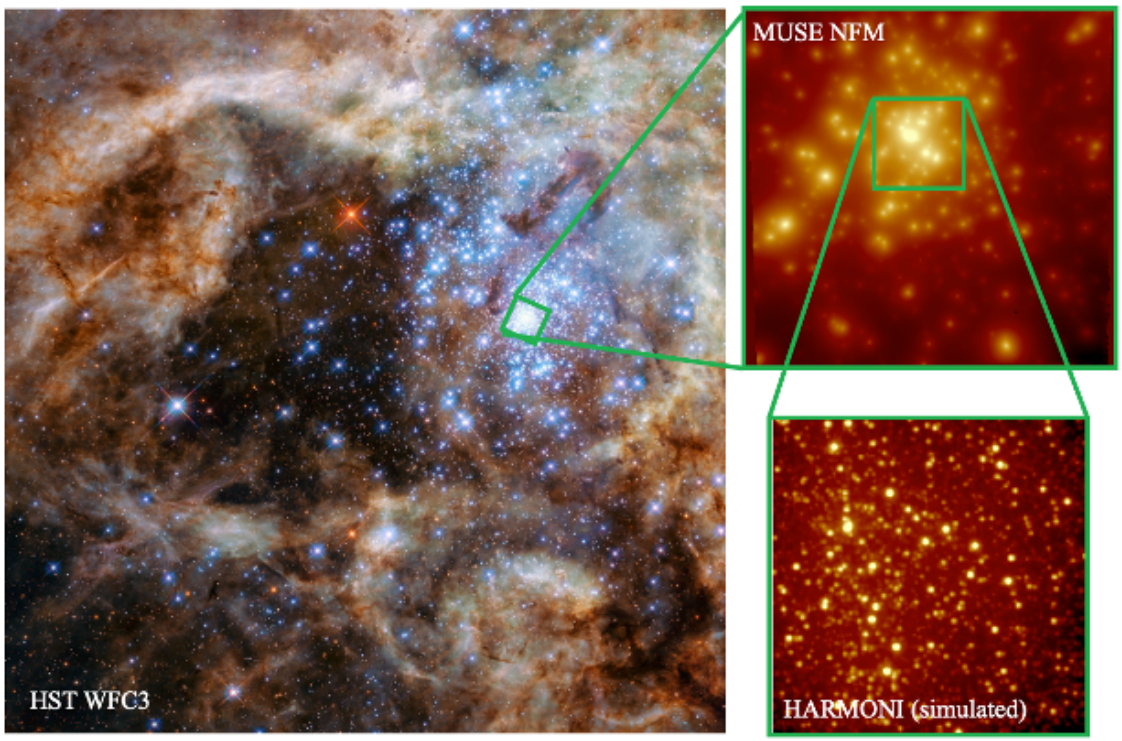


**Figure 1.13:** Comparison of an HST WFC3/STIS [34] observation with a MUSE (NFM) [26] observation of R136, and a simulated HARMONI observation from Chapter 4.5.5. The HST image is $2.65' \times 2.63'$ ($\approx 160'' \times 160''$), the MUSE image is $8 \times 8''$, and the HARMONI simulation is $2 \times 2''$ in the H-band with 10 mas spaxel scale.

1. Develop a test method to characterise the transmitted diffraction efficiencies of HARMONI VPH gratings.

2. Measure the efficiencies of prototype HARMONI VPH gratings and validate their performance so that real gratings can be manufactured for the instrument.

3. Determine the feasibility of HARMONI to detect an IMBH in a star cluster such as R136.

## 1.6 Thesis organisation

There are 4 chapters in this thesis, the primary subject is astronomical instrumentation of which the focus is the diffraction gratings for the HARMONI instrument. Secondary to this is the application of HARMONI to a science objective, namely the detection of IMBHs, of which the effectiveness is simulated and investigated.

Chapter 1.6 is the introduction to the thesis, providing the necessary background for the rest of the work. Chapter 2.4.3 addresses the first research aim and describes the development and operation of the test bench. Chapter 3.5.3 presents the results of the grating characterisation measurements related to the second aim. Chapter 4.5.5 addresses the third objective and the science aspect of the thesis.

Some of the work in Chapters 2.4.3 and 3.5.3 has been published by myself in conference proceedings [43].

# 2

# VPHG transmission efficiency test bench

## Contents



## 2.1 Introduction

The E-ELT will be the biggest optical light collector ever built. An intricate series of mirrors and lenses will usher the collected photons through the telescope and instruments before being converted into electrons by the detector, the output of which is ultimately stored as data for astronomers. It is highly desirable to retain as many photons and hence as much of this information about the observed celestial

objects as possible - this is the mission of the instrumentalist.

Despite being designed for maximum transmission efficiency, within HARMONI, the diffraction gratings will be the single biggest contributor to throughput loss in the telescope and spectrograph optical path. VPHGs, such as those used by HARMONI, can suffer from manufacturing inconsistencies, such as varying gelatine layer thicknesses, which can negatively impact their performance. It is important to ascertain if a manufactured grating meets the required specifications via characterisation upon receipt, and it is desirable to understand how the gratings perform in reality compared to simulations.

The HARMONI instrument is required to satisfy a number of technical requirements [88]. Following standard systems engineering practice, these top level requirements are flowed down to the IFS level, then to the spectrograph level, and finally to the individual modules of the spectrograph, including the gratings. Most relevant to the instrument's performance are the specifications for grating transmission, *"the spectrograph (excluding the detector) shall provide a transmission of* $\geq 60\%$ *(assuming unpolarised light) for* $95\%$ *spaxels in all configurations, averaged over the central* $80\%$ *of the instantaneous wavelength range of each configuration"*. This produces a derived requirement of 70% transmission efficiency, discussed further in Section 3.1.1. Prospective grating manufacturers have been sent a set of requirements that the gratings must satisfy, including tolerances [77]. These include achieving a certain line density, fringe tilt, physical size specifications, substrate quality and material, etc. Typically, manufacturers are only able to test the transmission with a pencil beam at 3 or 4 wavelengths. However, the uniformity of the transmission, and knowledge of the grating transmission across the entire bandpass are crucial to assessing the instrument's performance prior to acceptance. Thus, we decided to put considerable effort into characterising the grating efficiency as a function of position and wavelength. As there are over 40 gratings in the instrument, this needs to be done in an automated way.

HARMONI provides several different operating modes for astronomers including ten different near-infrared bands and four different spaxel scales (or fields of view)

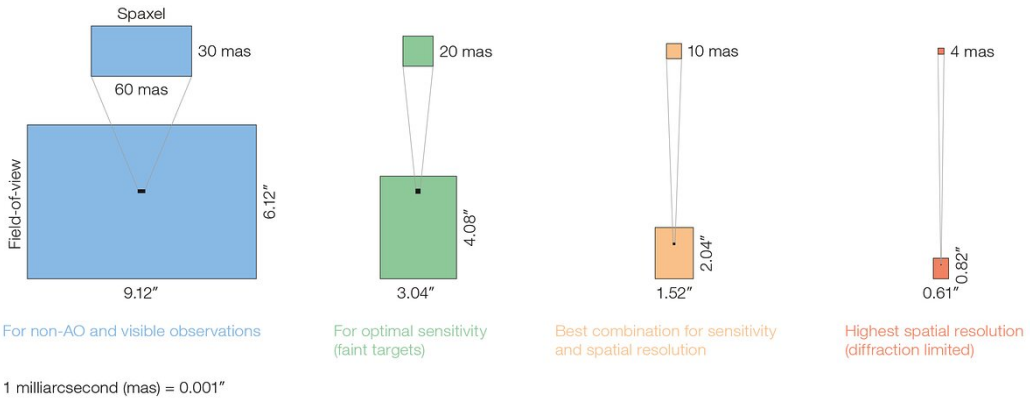


**Figure 2.1:** HARMONI field of view and spaxel scales. Credit: ESO/HARMONI Consortium.

as shown in Figure 2.1. VPHG diffracted transmission efficiency will vary between bands, across the wavelength range of a given band, and even between theoretically identical gratings. Also, spatial non-uniformity of transmission efficiency will result in varying efficiencies between spaxel scale operating modes. These spaxel scale modes are enabled by the pre-optics and result in four different beam footprints on the gratings, as shown in Figure 2.5. These beam footprints can also wander slightly over the surface of the gratings because of IFU and spectrograph collimator field-dependent aberrations. It is therefore desirable to measure the transmission efficiency at different points on the grating surfaces and understand spatial variations, as well as across their operating wavelength bands. This is the goal of the work described in this chapter.

HARMONI will have four spectrograph modules, each with ten infrared bands, resulting in a total of forty individual infrared gratings[1]. Characterising all of these across their full wavebands and their spatial variations would take a long time with a manual method, estimated at in excess of a year working full-time on a painstaking process. This time would cost the project money, be a limiting factor in the schedule of the instrument assembly integration and testing (AIT) phase,

[1]At the time of writing an eleventh band, the visible band, is pending technical, budgetary, and programmatic approval and is not relevant to this work.

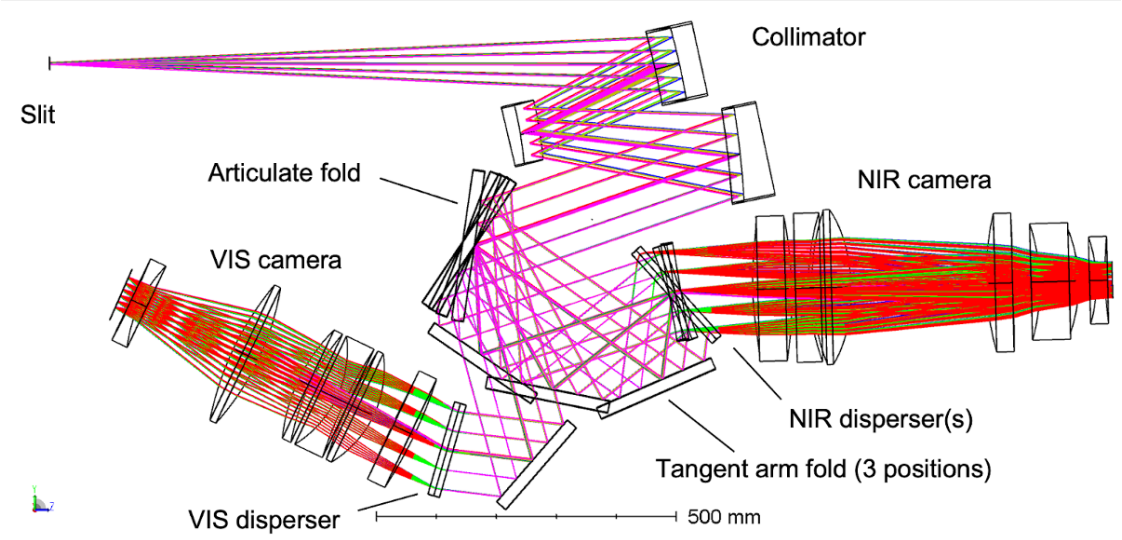


**Figure 2.2:** The HARMONI spectrograph optical design.

and potentially result in inaccurate measurements. Therefore a key part of this work is the automation of the test procedure developed here.

### 2.1.1 The HARMONI gratings

The HARMONI gratings sit in the spectrograph (ISP) subsystem within the integral field spectrograph (IFS) which is the core of the instrument. Each of the four identical spectrographs receives light via a slit from the integral field unit (IFU) which is then collimated and directed to the chosen grating. Figure 2.2 shows the optical design of the ISP, with the light from the IFU entering from the top left. This figure labels the VPHGs as 'dispersers' and also overlays several grating bands.

The ten NIR gratings, most relevant to this study, all sit within a grating wheel which enables operators to select the desired grating and maintain the required incident angle. This is known as the Infrared Grating Module (IGM), described below, and it is mounted mechanically on the main structure of the spectrograph. As with the rest of the spectrograph, it is operated under vacuum and at the cryogenic temperature of 130 K. The articulated fold mirrors provide the necessary incident angle for the selected grating. The diffracted first order is then imaged by the camera module onto the detectors.

The visible grating is designed as a single fixed VPHG, mounted just in front of the visible camera.

### Grating mechanical design

The gratings consist of a thin layer of DCG, sandwiched between two flat glass substrates, an adhesive layer to hold it together, and an anti-reflectance (AR) coating, a schematic of which is shown in Figure 1.7. Additionally, a metal foil is sometimes used to seal the outer edge to help prevent moisture or dirt from contaminating the DCG layer. Due to the bonding and mounting requirements, and operation at cryogenic temperatures, this foil is not used in the HARMONI gratings, instead cleanliness in handling and a hermetic seal by the adhesive layer is relied upon.

The substrates are 10 mm thick fused silica[2] (Corning 7980), chosen in part for its low coefficient of thermal expansion. The gratings vary from 160 to 200 mm in width (and 164 to 166 mm in height), so the entire IGM required to hold all of the gratings is a large mechanism.

The main feature of the IGM is the IR grating wheel (IGW), Figure 2.3, which holds all ten gratings and is mechanically rotated with high repeatability using stepper motors. Each individual grating is bonded into a 'picture frame' mount via four flexures, Figure 2.4. These have been specifically designed and manufactured to thermomechanically decouple the grating from the frame mount and wheel. They absorb any stresses which may otherwise deform the gratings when cooling down to, and operating, at cryogenic temperatures.

The orientation of the grating's lines or grooves around its Z-axis (the chief ray optical axis) is specified by the manufacturer with an accuracy of 1° relative to the grating's edge. The placement of the gratings is determined by the trajectory and angle of the light beam as it travels through the grating and towards the infrared camera. The alignment process will be conducted at room temperature within an optics laboratory, making the consistent mounting of the gratings crucial.

[2]There are two different substrate materials used, one for the short wavelengths, where water absorption is not an issue, and another set that uses OH-free fused silica (Infrasil) for the longer wavelengths.

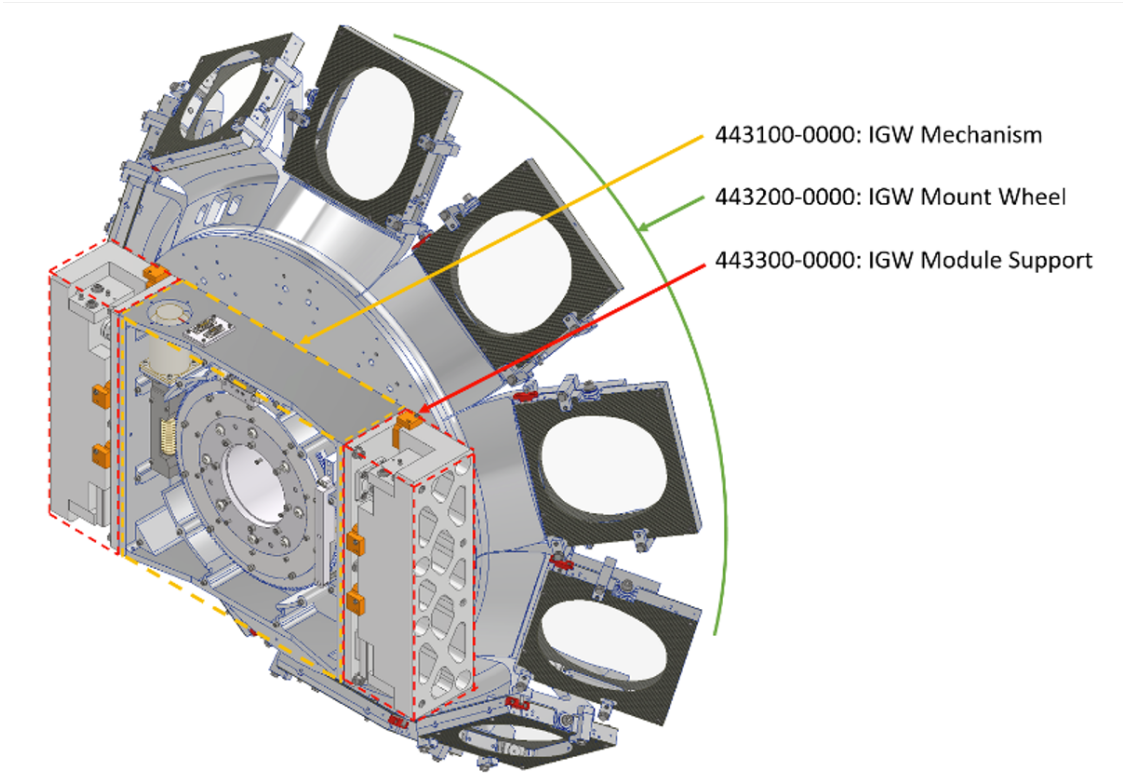


**Figure 2.3:** The IGM assembly.

Additionally, there must be allowances for positional adjustments to account for thermal expansion. It is essential that the alignment is performed with the grating installed in its operational position to accurately account for the effects of gravity and self-weight.

The picture frames used to mount the gratings on the instrument are also used in the transmission efficiency test bench to hold the gratings in place. On the instrument, additional baffles in the form of carbon fibre masks, shown in Figure 2.3, will be mounted to minimise straylight. Carbon fibre was chosen to minimise mass whilst also having a very low coefficient of thermal expansion (CTE).

### Grating optical design

Amongst the range of advantages that VPHGs provide over other types of gratings, detailed out in Section 1.2.3, the choice to use them in HARMONI was motivated by these key factors: (1) high grating efficiency, (2) broad customisability of line

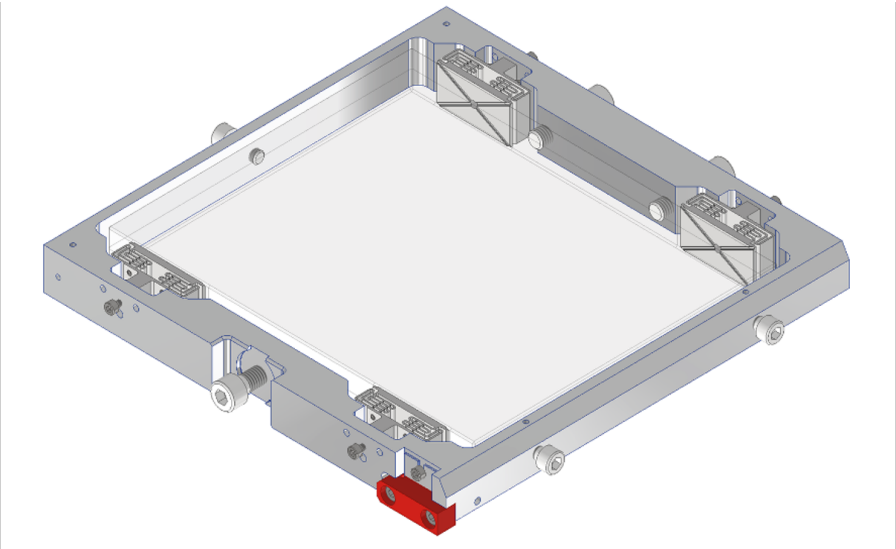

**Figure 2.4:** VPHG picture frame mount and flexures.

densities in the manufacturing process, and (3) being transmission gratings leading to a more compact optical design.

The HARMONI grating parameters: wavelength band, resolution, line density, and incident angle are shown in Table 2.1. The bands have unique identifying names for the HARMONI instrument which correspond to the resolution family low (LR), medium (MR), and high resolution (HR).

To achieve the best grating efficiencies, the HARMONI VPH gratings are mounted to satisfy the Bragg condition (see Section 1.2.2), where the incident and diffraction angles are identical at the central wavelength with respect to the fringes of the grating. All gratings with the same resolving power - low, medium, and high resolution (respectively $R \approx 3000$, 7000 and 18000) - are mounted with the same angle of incidence onto the near-infrared camera.

The fringes of VPH gratings may be tilted relative to the substrate to mitigate recombinant ("Littrow") ghosts and to make sure the $0^{th}$ order does not lie on the detector. The HARMONI gratings are placed at the pupil and have fringes tilted by $+3°$ clockwise (as seen from above).

Being at the pupil, when different spaxel scales (and corresponding fields of view, Figure 2.1) are selected there is a variation of the beam footprint on the selected diffraction grating, as shown in Figure 2.5. This effect drives the need to measure

**Table 2.1:** HARMONI grating bands and resolutions.

| Name | Band | $\lambda_{min}$ ($\mu$m) | $\lambda_{cen}$ ($\mu$m) | $\lambda_{max}$ ($\mu$m) | $R_{cen}=\lambda/d\lambda$ | Lines/mm | Incident angle (°) |
|---|---|---|---|---|---|---|---|
| LR1 | I+z+J | 0.811 | 1.090 | 1.369 | 3304 | 284.220 | 6.036 |
| LR2 | H+K | 1.450 | 1.950 | 2.450 | 3304 | 158.871 | 6.036 |
| MR1 | I+z | 0.830 | 0.940 | 1.050 | 7555 | 663.601 | 15.407 |
| MR2 | J | 1.046 | 1.185 | 1.324 | 7555 | 526.401 | 15.407 |
| MR3 | H | 1.435 | 1.625 | 1.815 | 7555 | 383.868 | 15.407 |
| MR4 | K | 1.951 | 2.210 | 2.469 | 7555 | 282.256 | 15.407 |
| HR1 | z-high | 0.827 | 0.865 | 0.903 | 17656 | 1413.951 | 35.217 |
| HR2 | H-high | 1.538 | 1.608 | 1.678 | 17656 | 760.568 | 35.217 |
| HR3 | K-short | 2.017 | 2.109 | 2.201 | 17656 | 579.844 | 35.217 |
| HR4 | K-long | 2.199 | 2.299 | 2.399 | 17656 | 531.946 | 35.217 |

the transmission at different spatial positions. The beam footprint figure shows the gratings are massively oversized for the smaller spaxel scales. The beam shapes in Figure 2.5 are approximate, they have been taken from an optical model of the IFS alone, not the rest of the instrument, therefore they are geometrical only and so do not take into account the effect of slit diffraction at the slicer.

The three-mirror anastigmat (TMA) collimators in the IFS introduce pupil wander and anamorphic increases in pupil size, both varying with slit position. The maximum pupil size is a key dimension in the optical system. At the nominal grating position, the pupil size is set at 150 mm (square aperture), constrained by the grating size available from the supplier. Considering all contributions including collimator thermal distortion, IFU-IFS alignment, and grating alignment the total wander is expected to be less than 5 mm.

## 2.2 Test motivations

This chapter describes the diffracted transmission efficiency test bench. These grating tests serve three main purposes:

1. Prototyping: Aid prototyping activities for grating manufacture to ensure consortium and supplier confidence in production feasibility.

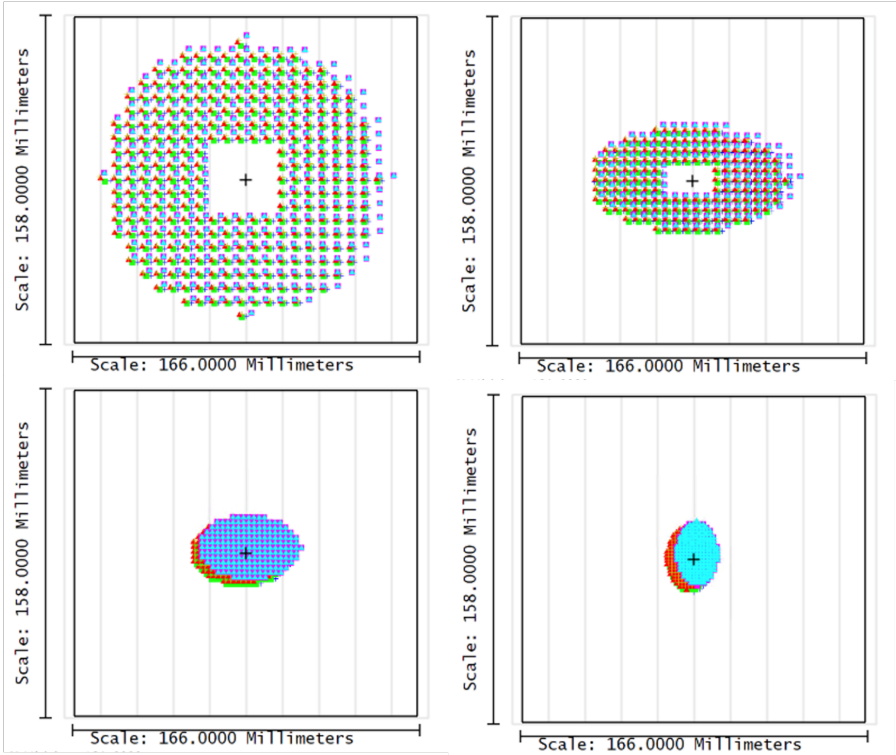


**Figure 2.5:** Beam footprints on example LR2 (H+K) grating for different spaxel scales: 60 mas x 30 mas (top left), 20 mas x 20 mas (top right), 10 mas x 10 mas (bottom left), and 4 mas x 4 mas (bottom right). The grating grooves run vertically in this image. The footprints shown are simplifications and do not account for diffraction effects at the IFU slicer.

2. Acceptance: To act as a screening of delivered gratings from the supplier to determine if they meet specification requirements.

3. Characterisation: To characterise the performance of the gratings to input into the instrument model for three main reasons:

   - Improve the accuracy of the model of the instrument to ensure instrument-level requirements are met.
   - Improve the accuracy of the instrument simulator to aid astronomers in observation preparation.
   - Improve the accuracy of the data reduction pipeline.

### 2.2.1 Prototyping activities

To expand upon the first of the three test motivations introduced above, we discuss the prototyping of two key grating types: LR2 and MR3.

#### LR2 (H+K band) grating prototyping

During the spectrograph preliminary design review (PDR), several items were selected for initial prototyping. These decisions, focusing on technology development and risk mitigation, were made while considering the risk register and technology readiness levels (TRL). As shown in Table 2.1, the LR2 grating spans the H and the K band and has the lowest line density of all the gratings; this is due to the long wavelengths resulting in a higher groove separation (as per Equation 1.1), and the wide band (high $d\lambda$) with an angular dispersion ($d\theta$), as per Equation 1.3, fixed by the camera resulting in a low incidence angle and hence a lower resolution and lower line density. The required low line density LR2 (H+K) grating was categorised at TRL-6, indicating that a prototype exists, but further testing is necessary.

One of the primary considerations was the selection of a VPH grating with a thick DCG layer. The thickness of the DCG layer is critical for several reasons:

1. Bragg Condition and Angular Selectivity: A low line density in the grating requires a thicker gelatine layer to achieve efficient Bragg diffraction (see Section 1.2.2), which is the condition under which light is diffracted most effectively. Low line density implies that the grating lines are spaced further apart, reducing angular selectivity. A thicker DCG layer compensates for this by extending the interaction between the incident light and the modulated refractive index structure, thereby broadening the range of angles over which efficient diffraction can occur.

2. Kogelnik's Coupled Wave Theory: According to Kogelnik's theory [60], the diffraction efficiency of a VPHG is dependent on both the thickness of the grating and the modulation depth of the refractive index. For low line density gratings, achieving high diffraction efficiency requires a thicker grating to

ensure that the light interacts sufficiently with the modulated refractive index. This interaction is essential for maintaining high efficiency, especially when the refractive index change is limited by the properties of the DCG material.

3. Physical and Structural Stability: A thicker DCG layer also contributes to the mechanical stability of the grating, which is particularly important for low line density configurations that might otherwise be prone to deformation. Additionally, the thicker layer helps to maintain the integrity and uniformity of the diffraction pattern over a range of operational conditions.

The areas of concern to address during the prototyping were: the availability of suppliers, the manufacturability of a VPHG with the specifications of the HARMONI 'H+K' grating (surface-ruled gratings are an alternative but present added challenges), the schedule, and the cost.

The decided approach was to have regular dialogue with suppliers and to measure sample devices from any willing suppliers. The most experienced VPHG producer for astronomical telescopes, Kaiser Optical Systems Inc. (KOSI), announced that they exited the custom grating business in January 2021 and this development made concerns about availability of suppliers even stronger. Wasatch Photonics is another experienced grating manufacturer for astronomical instrumentation and since the gratings, which must be supplied for HARMONI, cannot be produced with existing production technology, Wasatch has been willing to undertake a development process in phases[3]:

1. Development of processes to create a thick gelatine film >25 microns.

2. Delivery of a small sample grating for analysis.

3. Full-size LR2 manufacture: Requires iterating the manufacturing process to ensure uniformity of DCG coating and grating quality across the large grating area with high efficiency and reproducibility of the manufacturing process. [4]

[3]Described in internal project document HRM-00962.
[4]Detail is left out here to protect supplier intellectual property.

#### MR3 (H band) grating prototyping

After the Request For Information (RFI) documents had been sent out to prospective suppliers and responses had been received, it was clear that none of the companies would be compliant with the strict wavefront error (WFE) requirement using their standard processes. Wasatch suggested they could meet the requirement with an additional manufacturing step, but this would require using magneto-rheological finishing (MRF) which is a fine polishing technique. The WFE would be measured and then corrected by polishing the outer surfaces of the glass substrates.

To enable prototyping of this WFE refinement process, two fullsize prototype MR3 gratings were also manufactured. These early prototype gratings enabled further development of the transmission test bench, and allowed us to confirm the transmission efficiency performance of this subset of gratings.

These prototypes also allowed us to test the mounting procedure, perform vibration testing for transport, and look for deformation arising from cooling the grating and the mount to 130 K.

## 2.3 Transmission testing

The core of the work presented in this thesis is to measure how much of the light incident on each grating is diffracted and transmitted into the first order and hence is delivered to the camera of the spectrograph.

### 2.3.1 Test concept

Originally described, in the context of HARMONI, in Capone et al. (2018)[22], the concept of the test method is that of a *spectrophotometer*. A spectrophotometer is a device which measures the intensity of light at discrete wavelengths and is typically used to measure the optical transmission of material samples.

While commercially available spectrophotometers can provide precise measurements of the fraction of light transmitted through a medium, they are not well-suited for measuring the transmission properties of diffraction gratings like those used in

HARMONI. The small measurement chambers and complex diffracted light paths required for characterising VPH gratings require a bespoke setup.

To address these challenges and the needs expressed earlier, such as spatially resolved measurements and automation, a custom spectrophotometer setup has been developed for the HARMONI VPH grating characterisation. This setup uses a design similar to that used in commercial spectrophotometers but has been specifically tailored to meet the unique requirements of the HARMONI instrument.

To get an absolute transmission measurement, rather than just a relative result, a reference measurement is critical. The transmission efficiency at a given wavelength is therefore:

$$\mathrm{T}_\lambda = \frac{\mathrm{Signal}_\lambda}{\mathrm{Reference}_\lambda}, \tag{2.1}$$

where $\mathrm{Signal}_\lambda$ is the measured light intensity at a given wavelength through the grating, and $\mathrm{Reference}_\lambda$ is the same for the full optical path of the test bench minus the grating under test. This is repeated at different spatial locations on the grating.

### Methods in literature

Similar test set-ups have been demonstrated and used for VPHG characterisation for other astronomical instruments.

Tamura et al. (2005)[96] measured transmission of VPHGs for the FMOS (Fiber Multi Object Spectrograph) instrument of the Subaru telescope. They did this at three different spatial positions and three different incidence angles across wavelengths 0.9 to 1.8 $\mu m$. Using a Tungsten-halogen lamp light source and Oriel Cornerstone 130 monochromator arrangement [5] (nearly identical to the first iteration of our test bench), their method differed by the use of an area array detector that was mechanically swung about a co-rotating grating to capture different diffracted wavelengths. They reported a 10% variation peak-to-valley in efficiency between positions and explained these by a combination of small variations over grating

[5]This common approach uses a stable broadband light source coupled with a monochromator which enables wavelength selection and power stability over time.

aperture in: gelatine depth, refractive index modulation amplitude, energy loss by internal absorption, and surface reflection. These measurements used a 20mm beam at only three locations, and the authors noted, at the time, that optical uniformity of gratings is rarely investigated.

Subsequently, Renault et al. (2010)[81] measured the transmission efficiency of a prototype VPH grating for the VLT/MUSE instrument, and found it to fall short of the requirements. The supplier then modified their manufacturing process, and the first 'serial' manufactured grating was within specification. This work is a good example of an iterative prototyping development to meet strict requirements as is underway in this HARMONI work. The MUSE team measured efficiency at 12 different locations, in a 4×3 grid for a single wavelength (700 nm). They also measured across the whole MUSE band, 465 to 930 nm, for a single location in the centre of the grating. Their methodology once again used a similar light source however they made use of a dual path method for a simultaneous reference with two photodiode detectors and two lock-in amplifiers. Once again a rotation stage was used for the grating, and two linear stages to enable the spatial variation measurements.

Chonis et al. (2014)[28] describes the compact test bench designed for the many VPHGs of the Visible Integral-field Replicable Unit Spectrograph (VIRUS) instrument on the Hobby-Eberly Telescope (HET). Originally baselined for 150 identical copies, the VIRUS instrument now consists of 78 spectrographs [49]. The instrument works from 350 to 550 nm, and with 170 gratings manufactured and to be measured, including witness samples and spares, the team developed a robust method to quickly characterise the gratings. Three discrete wavelength photodiodes of 353.9, 452.3, and 549.5 nm were used, and measured in 9 individual subapertures. Results and statistics for all 170 gratings are shown in the paper[28] making it the highest statistical sample available. The results showed peak-to-valley spatial variations of 10.76, 19.10, and 18.74% for 353.9, 452.3, and 549.5 nm respectively.

Ishikawa et al. (2018)[52] measured 36 gratings in the visible to near-infrared from 360 to 980 nm as part of the Dark Energy Spectroscopic Instrument (DESI)

project. Spatially, the DESI team performed vertical, horizontal, and diagonal scans (shown in Figure 3 of [52]) to quickly calculate the average area-weighted efficiency of each grating for the entire active area.

The work in this thesis will provide the most detailed measurements of spatial variations in VPHG transmission efficiency available in the literature.

**Development process**

The concept of the measurement device was first demonstrated with available components in order to quickly and cheaply verify the approach.

The first iteration used a Quartz-Tungsten Halogen (QTH) lamp projected into a monochromator, the output of which is then approximately collimated with a doublet lens and divided into two beams, each of which is chopped at a different frequency. The two chopping patterns are mutually orthogonal, so as to allow synchronous "lock-in" measurements of the two paths with a single detector. One of these beams is the optical signal path directed to the grating, and the other acts as a simultaneous reference, or 'normalisation', path as shown in Figure 2.6. In this configuration, the transmission is calculated as:

$$T_\lambda = \frac{Signal_\lambda}{N_\lambda^{\mathrm{S}}} . \frac{N_\lambda^{\mathrm{R}}}{Reference_\lambda}, \tag{2.2}$$

where $N_\lambda^{\mathrm{S}}$ is the measurement of the normalisation path simultaneous with the signal measurement, and $N_\lambda^{\mathrm{R}}$ is during the reference measurement. The reference measurement is taken by removing the grating and directing the beam straight into the integrating sphere with all other optics in the path the same as the 'signal' measurement with the grating in place. The benefit of this method is to remove temporal variations in the light source intensity.

The QTH lamp was chosen due to its broadband emission close to a blackbody and temporal power stability. This white light is passed through a slit using a filter wheel to prevent lower or higher orders from passing through the monochromator. Without these cut-off filters, selecting a wavelength of 1200 nm, for example, would also allow light of wavelength 600 nm to pass through. This is because the

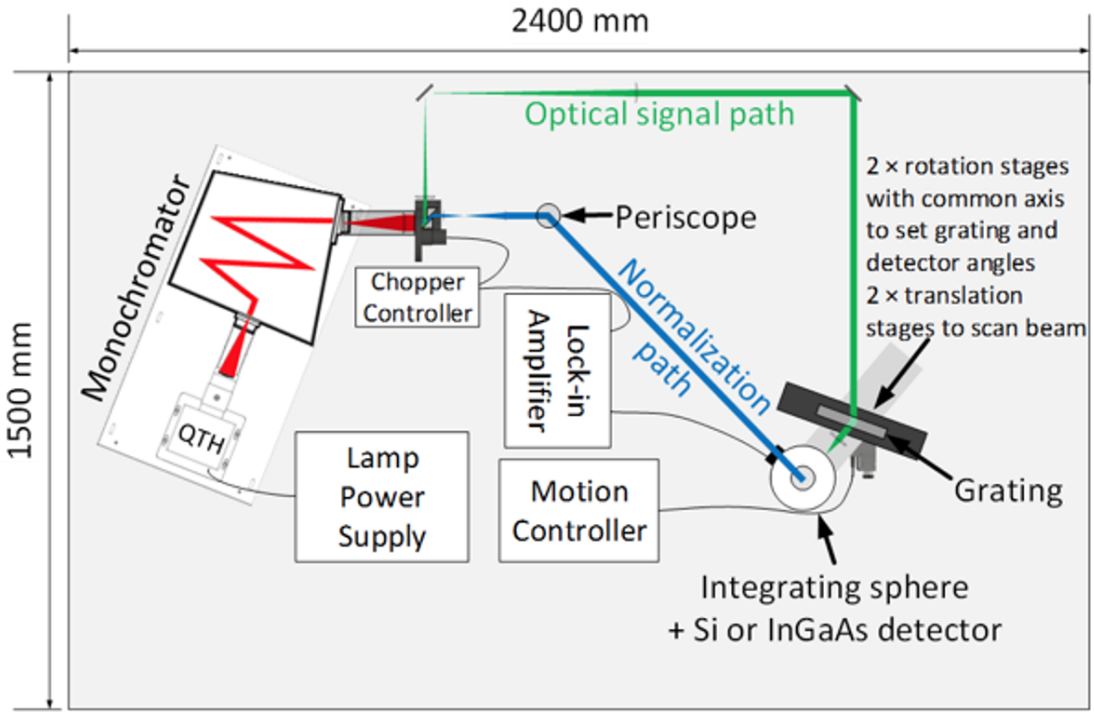


**Figure 2.6:** Original transmission test concept with two paths [22].

monochromator contains diffraction gratings (reflective ruled gratings) which diffract all incident light. These gratings can be selected and rotated using control software to choose a specific wavelength. The first order of the selected wavelength is directed to the output slit, and therefore second order light at half the wavelength will also be allowed. With this specific monochromator set-up, it was important to ensure that the correct filter was in place when taking measurements. Using this second-order shorter wavelength light to our advantage, the filter can be removed to allow visible light pass to through to make it much easier to align the optics on the bench.

Figure 2.7 shows the optical configuration of this monochromator whereby white light is projected through an entrance slit onto a collimating mirror and then onto a reflection diffraction grating and finally diverted to the exit slit. One of three gratings is selectable with a motor which also controls the incidence angle and hence the output wavelength. This is a typical configuration of a monochromator, and to a certain extent mirrors the principle of a spectrograph.

A photograph of the inner workings of the monochromator is shown in Figure 2.8 where one can clearly see the white light incident on the grating, and the

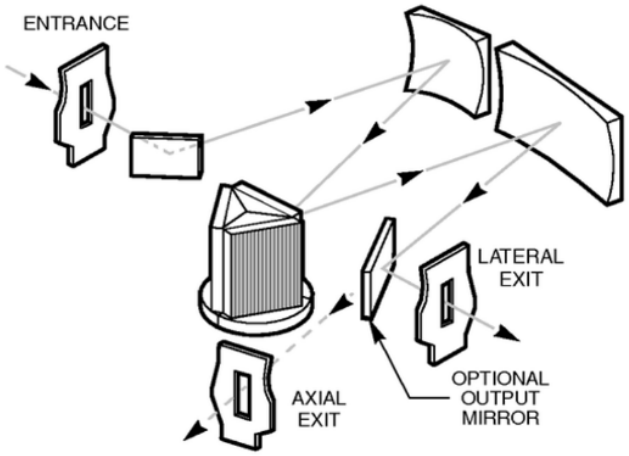


**Figure 2.7:** Optical configuration of the Oriel/Newport Cornerstone 260 Monochromator (credit: Newport).

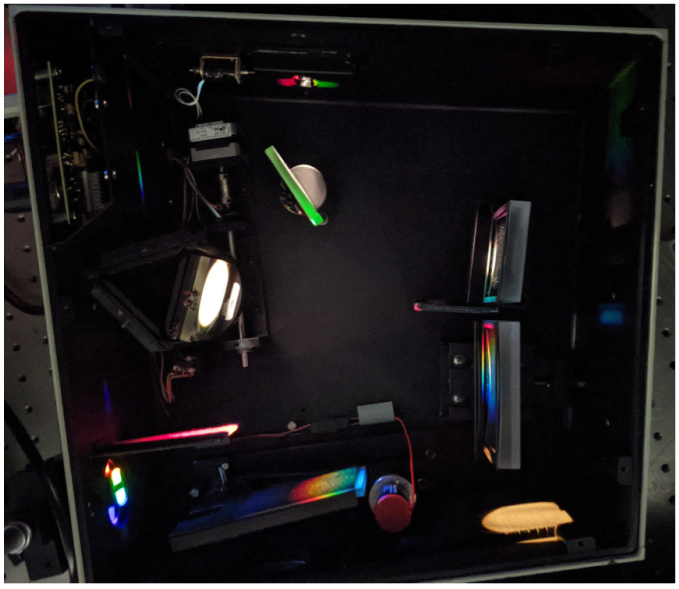

**Figure 2.8:** The inside of the monochromator, showing the white light split into a spectrum.

spectrum at the exit slit.

The output slit beam is collimated by an achromatic doublet lens, and a circular aperture pupil stop is placed in front of a chopper. The chopper is a rotating blade, as shown in Figure 2.10, with five openings that modulate the beam at the 5th harmonic of its rotation frequency, the first iteration of the test bench used a second circular pupil stop which is chopped by a different part of the rotating blade at 7th harmonic. The frequency is set by a lock-in amplifier to the chopper controller.

After the chopper, the beam is diverted to the grating via two-fold-mirrors, the second of which is on a motorised rotation stage. The diffracted path is then passed into the aperture of an integrating sphere with a Thorlabs InGaAs photodiode detector attached.

### Lock-in amplifier

A lock-in amplifier is a highly sensitive instrument used to detect and measure very small alternating current (AC) signals, all while rejecting noise that is not at the same frequency as the signal of interest.

The lock-in amplifier sets the chopping frequency of the optical chopper and hence the variability of the optical signal. The choice of frequency is crucial because it must be stable and distinct from frequencies of other potential noise sources, such as 50 Hz mains electricity, to enable effective signal isolation.

The lock-in amplifier then recovers the signal corresponding to the light pulses. It does this by synchronising its reference frequency (the frequency at which it expects the signal) with the chopping frequency. This synchronisation allows the lock-in amplifier to effectively "lock in" on the signal. It uses phase-sensitive detection to correlate the incoming signal with a reference signal at the same frequency. This method allows the amplifier to detect both the amplitude and the phase of the incoming signal relative to the reference, further improving measurement accuracy. Any noise not at the reference frequency or phase is effectively rejected, thus enhancing the signal-to-noise ratio of the measurement.

The device used in this work is the ‘Signal Recovery Model 7230 DSP Lock-in Amplifier’. Figure 2.9 shows a basic optical detection setup using this sort of lock-in amplifier with a mechanical chopper. This configuration is the basis of our experiment where the sample is the VPH grating.

### Chopper

The lock-in amplifier sets a reference frequency for the chopper controller, it then rotates the chopper at this frequency. The chopper used is the Thorlabs MC2F57B,

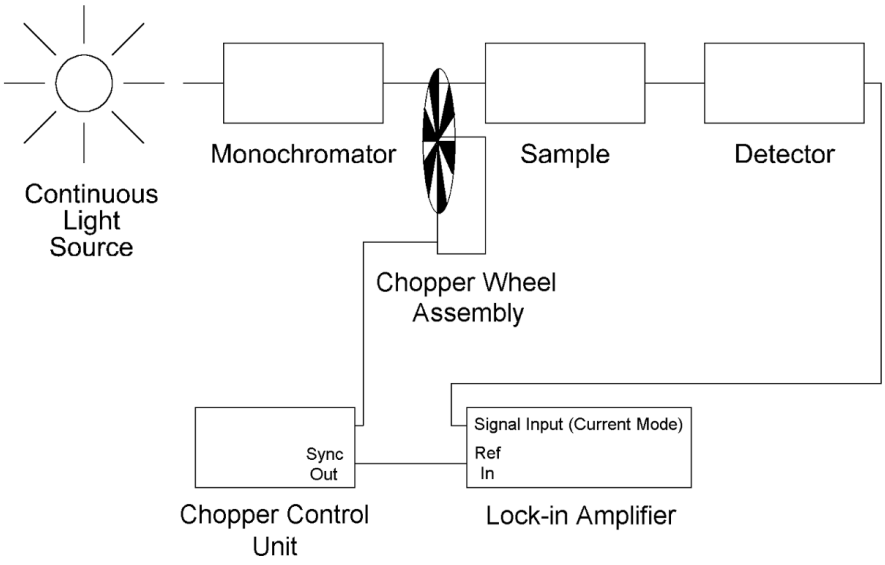


**Figure 2.9:** AC measurement system using a lock-in amplifier and mechanical chopper (credit: AMETEK).

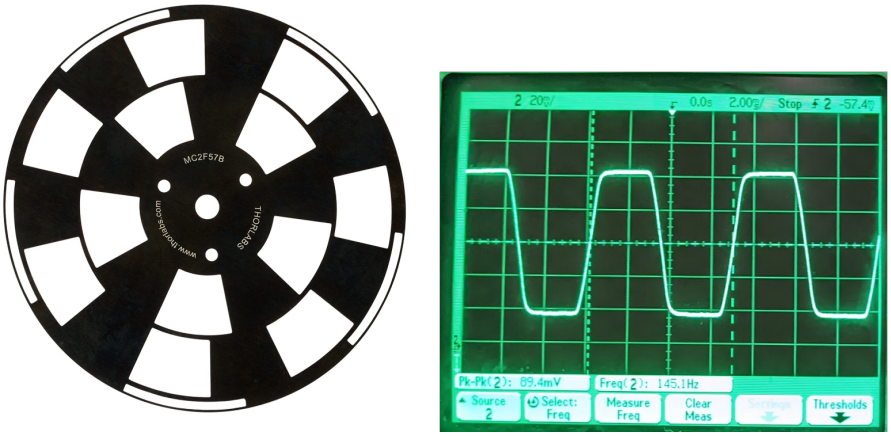


**Figure 2.10:** Optical chopper blade (left) with 5th and 7th harmonics (credit: Thorlabs). The output of an oscilloscope showing the chopped beam via a detector and power meter (right).

shown in Figure 2.10, which is a harmonic frequency optical chopper with inner and outer slots for use in either or both 5th and 7th harmonic.

To avoid the mains power frequency of 50 Hz and its harmonics, a frequency of 29 Hz was set for the chopper. This results in either a 145 Hz or 203 Hz signal if using the 5th or 7th harmonic respectively. Experiments were made to verify these frequencies were sufficiently separated from problematic frequencies by comparing noise levels for a range of different frequencies.

To verify that the chopper, integrating sphere, and detector combination are providing the lock-in amplifier with the expected signal and with sufficient SNR a test was conducted with an oscilloscope. Figure 2.10 also shows the output of the oscilloscope using the Thorlabs InGaAs detector with a frequency of 145 Hz, as expected for the 5th harmonic part of the chopper blade. If the beam diameter is small compared to the chopper aperture the wave will tend towards a square wave, and if the beam is large the wave will tend towards a sine wave. Figure 2.10 shows that the experiment configuration produces a rounded square wave as it is somewhere in between.

**Commissioning and test results**

Due to the technology development activities on the LR2 (H+K band) grating (described in 2.2.1), the first grating received from the supplier was a small 2 inch diameter circular sample LR2 grating. This provided a good opportunity to test out the grating test bench across a wide band all the way up to 2.5 $\mu$m, the longest HARMONI wavelength. It was also the first time the transmission efficiency of a grating of this specification was characterised.

The test bench configuration used at this stage is shown in Figure 2.11.

Measuring discrete wavelengths across the H+K band means gradually stepping from 1.4 to 2.5 microns. As the wavelength increases, so does the diffraction angle, as per Equation 1.3. To compensate for varying wavelengths so that the first diffracted order enters the integrating sphere, the grating in this setup must rotate, which also slightly changes the incident angle. To keep this angle constant, the fold-mirror before the grating is also slowly rotated. This simultaneous scanning enables us to scan the diffracted order across the integrating sphere's aperture, ensuring alignment and maximising the received signal. This technique is particularly useful for non-visible wavelengths where alignment is difficult.

This method is imperfect as it introduces a systematic error in the results which is the spatial variation in the transmission efficiency, this is acceptable for this early iteration.

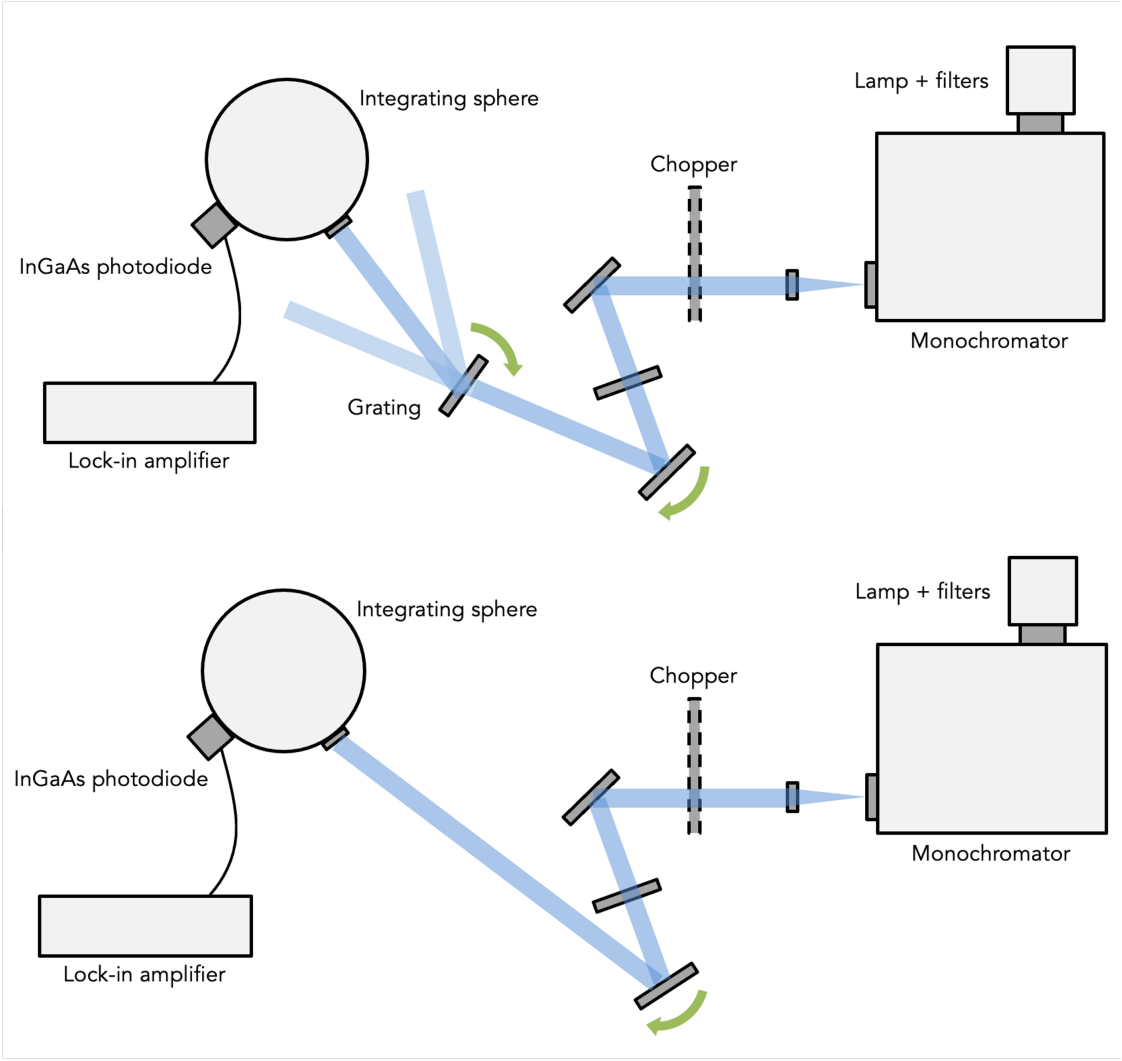


**Figure 2.11:** Test bench schematics for the sample LR2 test. The grating measurement configuration (top), and the reference (bottom).

The test method, which is only partially automated at this stage, is as follows:

1. The first measurement wavelength (1400 nm) is set with the monochromator input filter wheel set to 'open' to enable visible light through.

2. Align 2nd order of 1/2 measurement wavelength, or 3rd order of 1/3 measurement wavelength, whichever is visible by eye, in this case both (see Figure 2.12). Align beam to be at the edge of the integrating sphere aperture.

3. Set the monochromator input filter wheel to the required blocking filter to remove other orders.

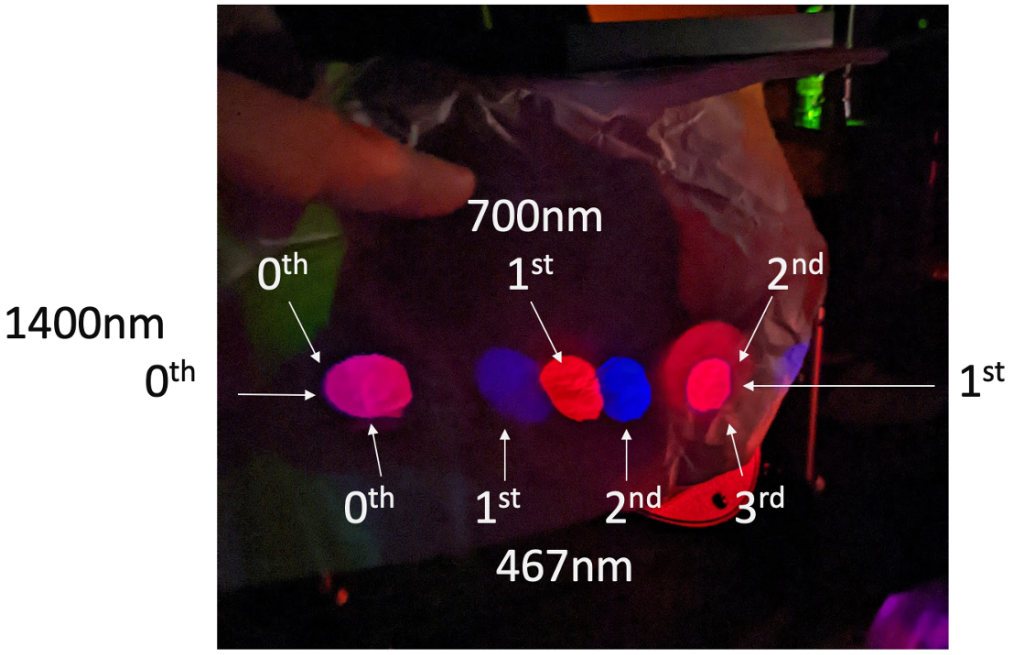


**Figure 2.12:** Aligning 1400 nm.

4. Scan the beam across the integrating sphere aperture taking 50 data points from the lock-in amplifier at each step, simultaneously adjusting the angle of the grating to maintain incident angle. This ensures maximum throughput for required angle of incidence.

5. Continue until after the order peak.

6. Repeat for the next wavelength.

To obtain reference measurements, we remove the grating and direct the beam into the integrating sphere, leaving all other components of the optical chain unchanged, as shown in the bottom half of Figure 2.11.

The alignment described in step 2, is shown in Figure 2.12, where one can see the 0th, 1st, 2nd, and even 3rd order for shorter wavelengths. Here the monochromator is set to output 1400 nm light, however the use of an open port on the filter wheel is letting lower orders pass through. By eye one can see the red (700 nm) and blue (467 nm) light. The larger circle that appears to be over the 1st order

for 1400 nm is the aperture of the integrating sphere, showing that this order is aligned and ready to be measured.

The results for this first test are shown in Section 3.4.6 on Figure 3.14, alongside simulated performance, and a few measurements at discrete wavelengths by the grating supplier. The key result with respect to the development of the test bench from these measurements is that the error bars beyond 2000 nm are far too large to produce meaningful results. These large error bars (explained further in Section 3.4.1) are caused by the low SNR of the test bench.

### SNR budget of the test bench

To understand the causes of the low SNR of the test bench a numerical model of the total transmission of the bench was built from 500 nm to 2500 nm. This model was built to identify key sources of transmission loss and to understand the impact of upgrading certain components. The model takes into account the lamp spectrum, filter band-pass transmission, monochromator grating efficiencies, lens glass transmission, lens AR coating transmission, integrating sphere reflectivity, and detector sensitivity.

The 250W QTH lamp is essentially a blackbody with its peak at 800 nm, which results in a signal 7 to 8× lower at 2500 nm. The filters are not a concern in terms of transmission loss as they can be selected for specific wavelengths; the chosen 1650 nm longpass filter for the K-band measurements has a transmission at 2500 nm of 95% for example.

The monochromator has three gratings inside, each with a different peak efficiency wavelength which is chosen automatically by the control software to optimise the output. For the relevant wavelengths, this efficiency is always above 90% and so is not a major concern.

The transmission of the lenses used for collimating the beam and for slit-reimaging is a key issue. As the beam is small and mainly passes through the centre of bi-convex lenses, keeping the number and thicknesses of lenses down to a minimum is desirable. The N-BK7 lenses used in the original setup have lower transmission

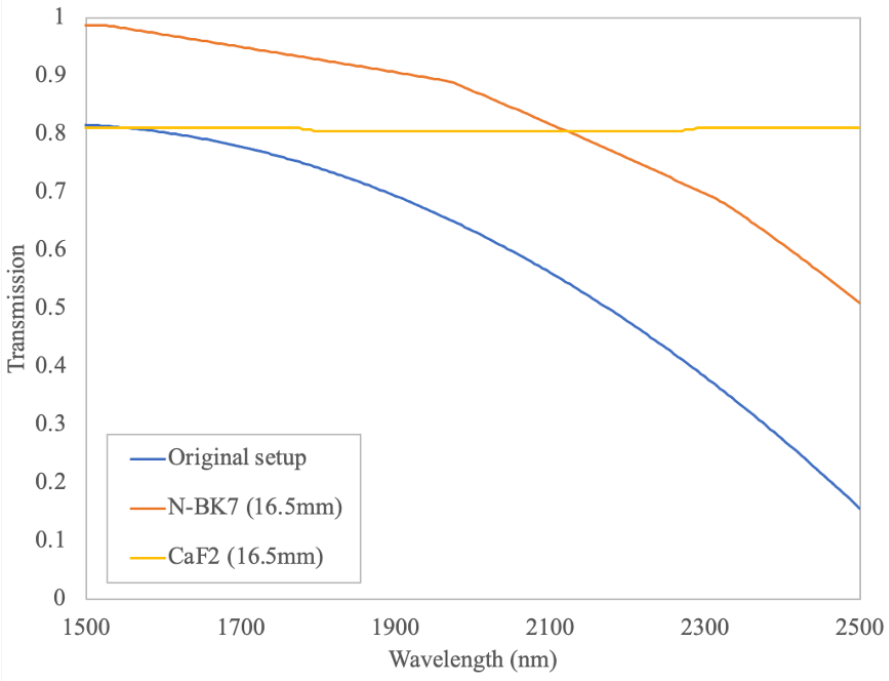


**Figure 2.13:** The bulk transmission of lenses in the optical path.

into the infrared, a proposed solution is to use Calcium Fluoride lenses which have a more consistent transmission profile, although they are fragile and require careful handling. Figure 2.13 shows the bulk transmission of the lenses in the optical path. It shows the original set-up as described above, a modified version with thinner lenses with N-BK7 glass and the same for CaF2 glass. Clearly significant improvement in the transmission beyond 2 microns can be made with the proposed modification.

The integrating sphere, an important component to ensure consistent illumination of the detector, must also be chosen carefully. Suppliers typically provide a range of internal coating options with different characteristics. The light input into the sphere will reflect several times before finding its way onto the detector's sensitive area a conservative estimate of 10 reflections is used in the model based on the data from the chosen supplier in Figure 2.14. The original sphere already available in the lab and hence used in the first iteration of the experiment has a 'Spectrareflect' coating. Clearly, the figure shows that selecting 'Spectralon' would be beneficial for the NIR applications. This material is a fluoropolymer that has the "highest diffuse reflectance of any known material or coating over

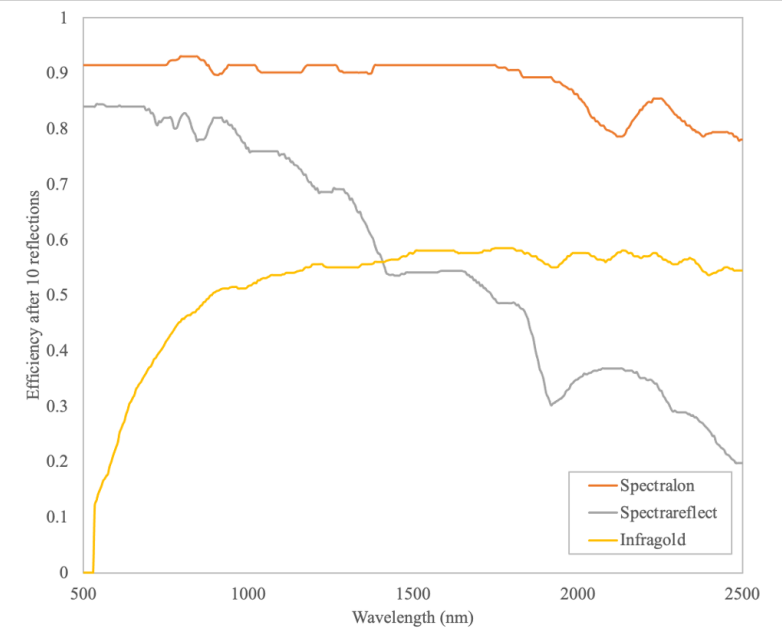


**Figure 2.14:** Integrating sphere coating efficiencies. Efficiency after 10 reflections is shown for relative comparison of different coatings. Credit: LabSphere.

the ultraviolet, visible, and near-infrared" according to the manufacturer's data sheet. The only disadvantage of this coating compared to its alternatives is the handling requirements as it is powdery to touch. For some use cases, this might be a concern, however, this is taken into account in our lab practices including careful handling and therefore not an issue for us.

The numerical model was used to understand the impact of incremental improvements: variations in lenses, filters, integrating sphere coatings, and detectors were experimented with.

Figure 2.15 shows the simulated transmission of the test bench in the K-band, from just after the lamp to just before the detector. The line marked 'original' is the state of the test bench when conducting measurements for the LR2 sample in Figure 3.14. The figure shows improvements can be made simply by changing the integrating sphere, and further improvements using CaF2 lenses in the proposed 'new' bench.

After experimentation both with the simulation and with real components, a large number of improvements were implemented to maximise the signal across the band and also to improve the automation. Funding was also found to improve

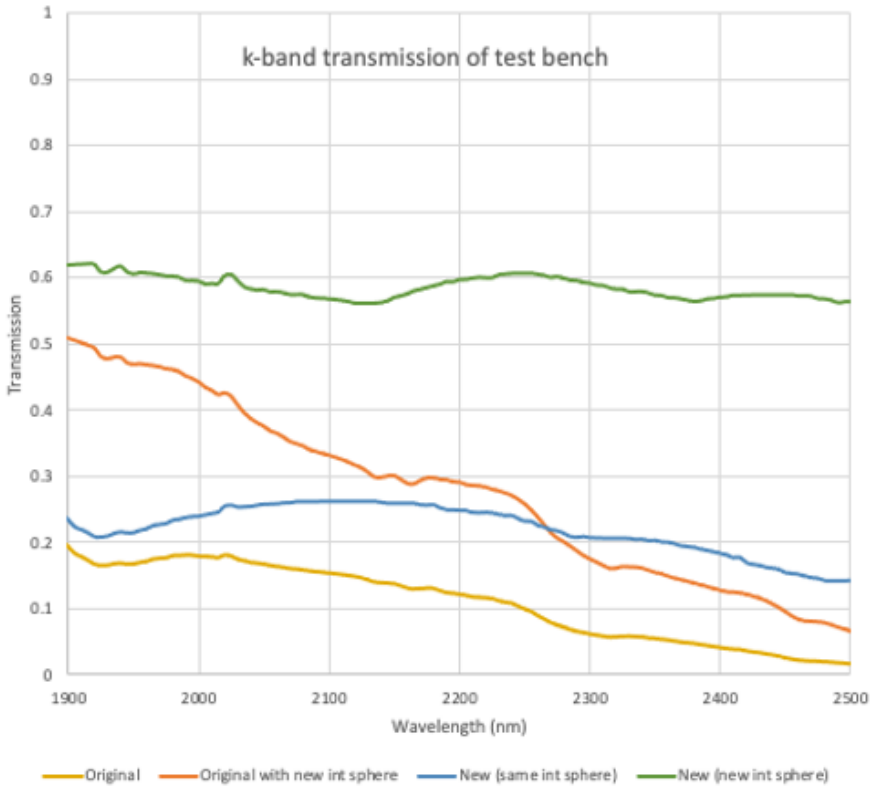


**Figure 2.15:** Simulated optical transmission of the test bench. The yellow line marked 'Original' is the test bench shown in Figure 2.11, the orange line is the same bench if only the integrating sphere is upgraded. The blue line is if the proposed lens modifications are made with unchanged integrating sphere, and the green line is if all changes are made, showing a marked improvement across the important K-band.

the light source and monochromator[6].

### 2.3.2 Improvements

#### Light source design

The test bench requires a bright monochromatic stable collimated pencil beam that is wavelength selectable across a broad range.

To achieve this, a near-infrared (NIR) supercontinuum laser was identified from a supplier which would provide a bright and stable light source across the whole required spectral range. The chosen laser is the LEUKOS Electro IR, a pulsed supercontinuum laser with emission from 700 to 2800 nm. The laser has a total average power of $> 1300$ mW, a repetition rate of 250 kHz, and a pulse width of

[6]UKRI (STFC) grants ST/S001409/1, ST/X002322/1, and ST/X004775/1.

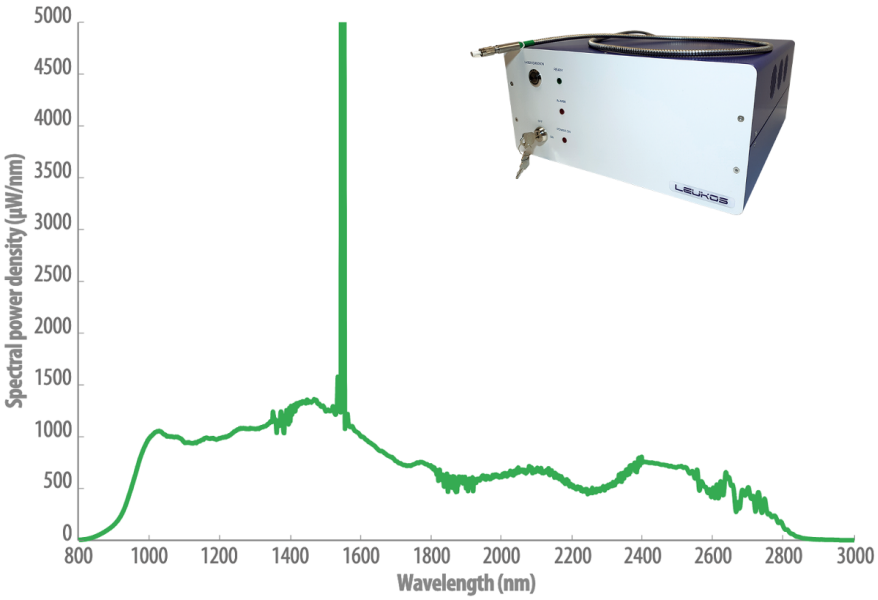


**Figure 2.16:** The emission profile of the LEUKOS Electro IR supercontinuum laser, and a photo of the laser itself (credit: LEUKOS).

$<$ 1 ns. The pump wavelength of the laser is around 1530 nm which means there is a significant spike in power at this wavelength, as shown in Figure 2.16.

Next, a new monochromator was required that could handle the high power broadband input, precisely pick off a chosen wavelength, and be controllable with automation software. A custom solution from Bentham (FTMC50-SCL) was chosen with the addition of a collimator optic attachment (a set of two mirrors which provide the required output beam). The monochromator is based on the same principle as the previous Newport model, with the addition of an input port compatible with the laser fibre output, durable optics, high efficiency in the NIR, and easy control via a Python SDK (Software Development Kit) called *bendev*. Another benefit of the new monochromator is that it automatically selects an appropriate filter to block lower order light from leaking from the monochromator. It does this by utilising a number of pre-installed long pass filters which it then selects ensuring that the cut-on wavelength is greater than half of the selected wavelength. At 1500 nm, for example, the active filter will be blocking everything up to roughly 1000 nm, therefore 750 nm light will be blocked, with $<$0.0001% transmission. Similarly for the full spectral range of the monochromator.

### Optical design

A ray tracing model of the test bench was built using Zemax OpticStudio, as shown in Figure 2.17. A single lens is used in place of the monochromator collimator module for simplicity, and the pencil beam of 7 mm diameter[7] is directed to the grating. The two fold-mirrors used in the earlier iteration of the design to direct the beam onto the grating as desired are removed as the new configuration will benefit from a set of linear stages to move the grating across a static beam of light.

The optical model contains all the HARMONI gratings which are defined by their line density, incidence angle, and substrate material and thickness. The ray tracing simulation calculates diffraction angles for chosen wavelengths.

A multi-configuration approach is used to enable the switching, or simultaneous viewing, of gratings. Each grating family has a different fixed required incident angle, and so there are three key configurations.

Figure 2.17 shows a multi-configuration view of the optical design whereby all three families of gratings are visible. The diffracted first orders from each are captured by a lens and integrating sphere combination which moves and is realigned for each family. The rays are coloured by wavelength in each configuration, corresponding to the start (blue), middle (green), and end (red) of each relevant bandpass. The re-imaging lens was chosen as an off-the-shelf 2-inch diameter lens made from Calcium Fluoride (CaF2). This material was chosen for its high transmission in the near-infrared, better than the commonly used BK7. The usual downside of CaF2 as a lens material is its fragility, however this is not a concern with careful handling and use in a static test bench in a laboratory environment.

To capture all of the 1st order diffracted light across the whole waveband, and to prevent leakage of 0th and 2nd order light, the re-imaging lens is also used as an order sorting lens in combination with a focal plane mask, shown in Figure 2.18. The mask is a simple rectangular aperture in a metal disc with dimensions designed to precisely allow the orders required to pass and to block the undesired light. The

[7]This is the diameter of the beam out of the laser fibre as defined by the supplier test report at 2000 nm, and is not magnified by the monochromator.

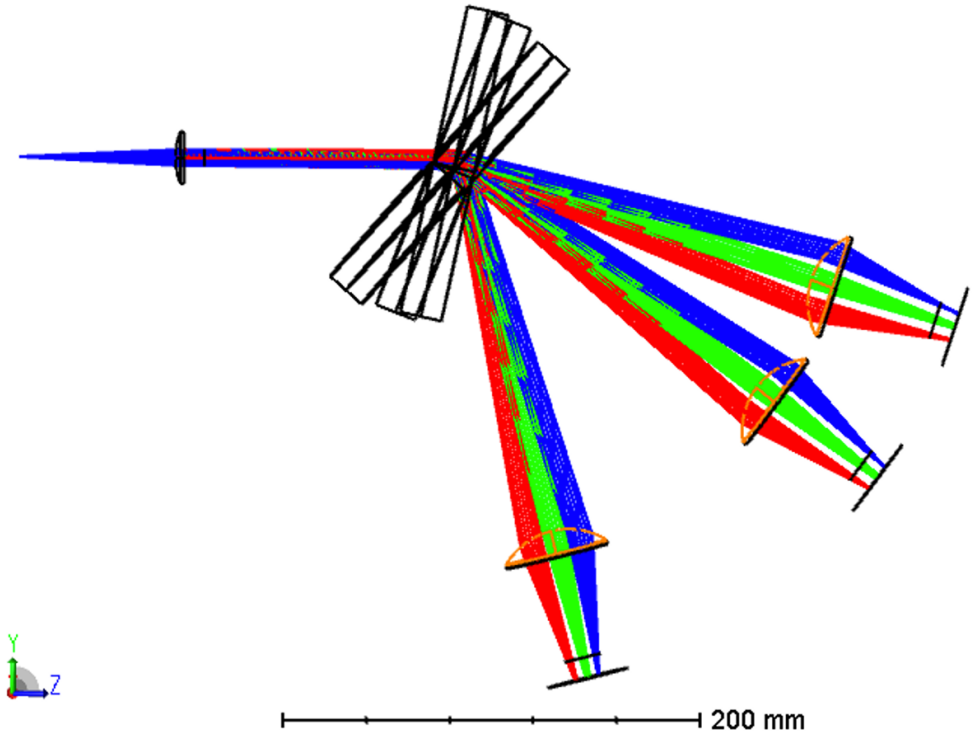


**Figure 2.17:** Multi-configuration view of the optical design of the updated test bench. The three configurations are one for each grating family: low, medium, and high resolution. Each shows how the lens, mask, and detector sub-assembly are realigned to capture the required wavelengths.

lens and mask are specified to be aligned to the central wavelength of the grating waveband and capture the start and end of the waveband. This light is focused through the rectangular mask and into the integrating sphere. The bottom part of Figure 2.18 shows the beam footprints of the three wavelengths (start, middle, and end of the grating band) at the mask for the 0th, 1st, and 2nd order light from left to right respectively. The figure shows that, if aligned correctly, no light gets through the mask in the 0th order, the 1st order passes through uninterrupted, and the 2nd order of the lower wavelength (in blue) is blocked. The alignment is most sensitive in the low resolution gratings (the case shown in the figure) as the deviation angles are smallest and so the orders are more bunched together. There is very little risk of order leakage in the medium and high resolution gratings.

The alignment of the order sorting sub-assembly is achieved with a number of steps. Firstly, the sub-aperture mask is aligned relative to the lens by making use

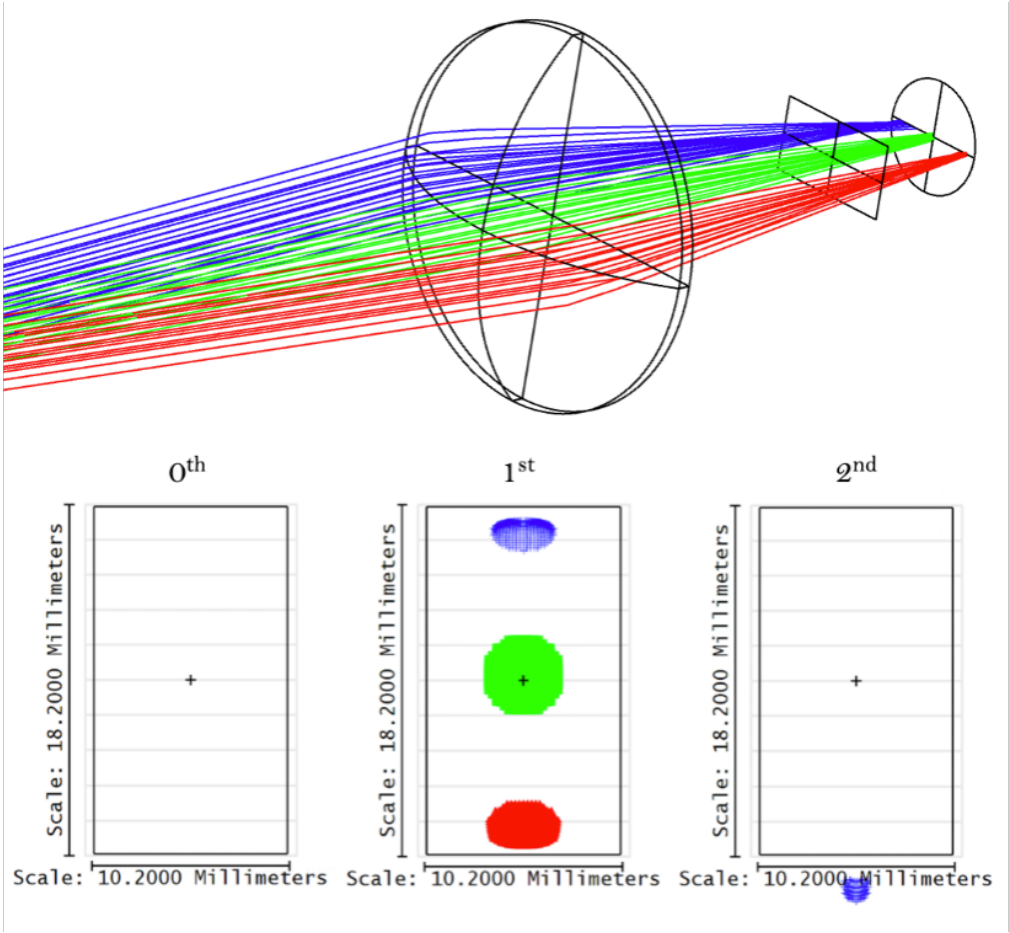


**Figure 2.18:** The design of the order sorting lens and rectangular mask (top), and the beam footprint for the expected wavelengths (green - middle of the band, blue and red - either extreme of the band) at the mask (bottom) for 0th, 1st, and 2nd order in the low-resolution family case (worst case). The beam in the 0th order is far from the rectangular aperture and so does not even appear in this figure.

of a Thorlabs 2-inch diameter lens tube system. The mask is cut from a 2-inch metal disc and the lens tube ensures it is concentric with the lens itself, the rotation about the optical axis is set manually to an accuracy of 1 degree. The distance of the mask to the lens is set with spacers and measured with a digital Vernier caliper[8]; the same method is used to set the distance from the back of the mask to the entrance of the integrating sphere.

Once the subassembly is built, it is attached to a small breadboard which also holds the integrating sphere and detector. The lens tube is butted against the

[8]A precise measuring device which can be used to make internal and external depth measurements.

integrating sphere aperture to set its distance which also sets the height above the optical bench so that the only remaining degrees of freedom for alignment are the distance of the lens from the grating and rotation of the small breadboard which sets the angle of the lens with respect to the beam from the grating. The distance from the grating in the optical axis is initially set to within a couple of millimetres with a ruler. Finer alignment of the grating-lens separation and lens tilt is done optically. This coarse mechanical alignment is sufficient to get a signal on the detector, from there, the alignment is achieved iteratively by monitoring the signal at the detector and changing the wavelength from the start to the end of the band. By changing from the start to the end wavelength of the band, and getting the first order to pass at the edges of the aperture as shown in Figure 2.18 the lens can be aligned to the expected position. A live plotting feature in the automation software can be used to see the effect of moving the lens on the signal, maximising the signal received across the wavelengths whilst preventing other orders leaking into the integrating sphere results in optimal alignment. A useful general technique employed is the use of a small piece of card to block the beam in various places and by gradually moving the card whilst watching the detected signal one can find invisible beams of infrared light.

### Mechanical design

The laser and monochromator sit on an optical bench and are encased in a black-out laser safety box to prevent any leakage of potentially hazardous laser light. There is a small cut-out for the eye-safe monochromatic output beam.

The beam is chopped immediately and then enters a simple two-mirror periscope which brings the beam up to the height required by the mounted grating. An X+Y linear translation stage holds the grating so that it can be scanned around the static incident beam, both movements are in the plane of the grating. This translation stage set-up consists of two identical linear stages mounted together perpendicularly. The Newmark NLS4 series stages are used which have a bidirectional repeatability

of 15 $\mu$m and a step resolution of 0.13 $\mu$m. The good repeatability is important to ensure consistent spatial variation measurements.

The re-imaging lens, order sorting sub-aperture, integrating sphere, and detector are all mounted on a small optical breadboard plate to maintain co-alignment so that they can be re-positioned all together. Posts are used to hold the components of this subassembly up at the required height to match the diffracted beam.

The subassembly slides on the bench into four repeatable positions: 1) the reference position, 2) for low resolution gratings, 3) for medium resolution gratings, and 4) for high resolution gratings. These positions are made repeatable by using a three-point mount made from optomechanical table clamps, as visible in Figure 2.21.

The full size VPH gratings are mounted in picture frames, as shown in Figure 2.4, however, for the prototype testing they have been mounted temporarily and not permanently bonded into their frames. This temporary mounting of the grating was done so that wavefront error measurements could be made before and after bonding and cooling so a comparison could be made. The transmission was measured before this process. The temporary mounting uses three nylon screws to hold the grating in place, one locked in from the top and two more through a metal interface plate at the bottom. The weight of the grating is held on the lower two screws and pinned in place by the upper screw. They are fastened to be flush against the grating edge to pin it in place. Also, small kapton tape covered metal plates attached to the corners of the picture frame are used to prevent the grating from falling out of the frame in the event that it slips from the nylon screws, as shown in Figure 2.19.

### Electrical design

The interface between the optical and the electrical domain is the detector. This test bench makes use of a photodiode detector which is known to be highly linear, fast, and have high quantum efficiency (QE)[9].

Like other detectors (CCD, CMOS, SPAD, etc.), photodiodes can be made from different materials which provide different optoelectrical properties, summarised

[9]The fraction of incident photons converted to electrons by the device.

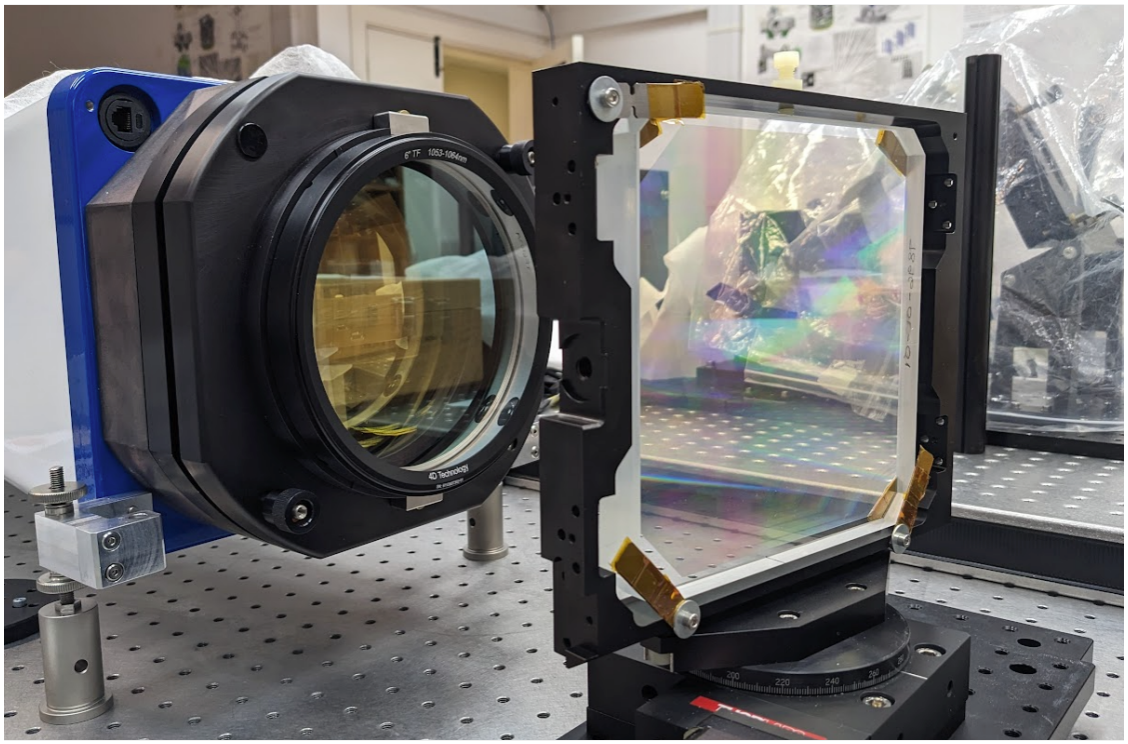

**Figure 2.19:** An MR3 prototype grating in its temporary mounting configuration on the WFE test bench.

in Table 2.2. Considering these properties an InGaAs detector was selected from Thorlabs for the first iteration of the test bench. This was the Thorlabs PDA10DT, which is an amplified photodetector with a built-in thermoelectric cooler designed to improve sensitivity (cools down to -10°$C$). To improve upon this, the detector was upgraded to the more sensitive Hamamatsu C12486-210 infrared detector module with a preamplifier, which can cool the detector element down to -20°C. The photosensitive area, like the Thorlabs detector, is only 1 mm in diameter however the improved cooling results in higher sensitivity.

This detector requires a direct current (DC) power supply an 'Aim-TTi EL302RT DC Linear Power Supply' was chosen and connected to the detector as per the pin drawing in Figure A.1 in the appendix. The figure also shows a block diagram of the detector showing the InGaAs diode, the cooler and temperature controller, and the power inputs.

The detector output is a coaxial cable with BNC[10] connectors which passes the

[10]BNC (Bayonet Neill–Concelman) is a type of quick-connect/disconnect radio-frequency

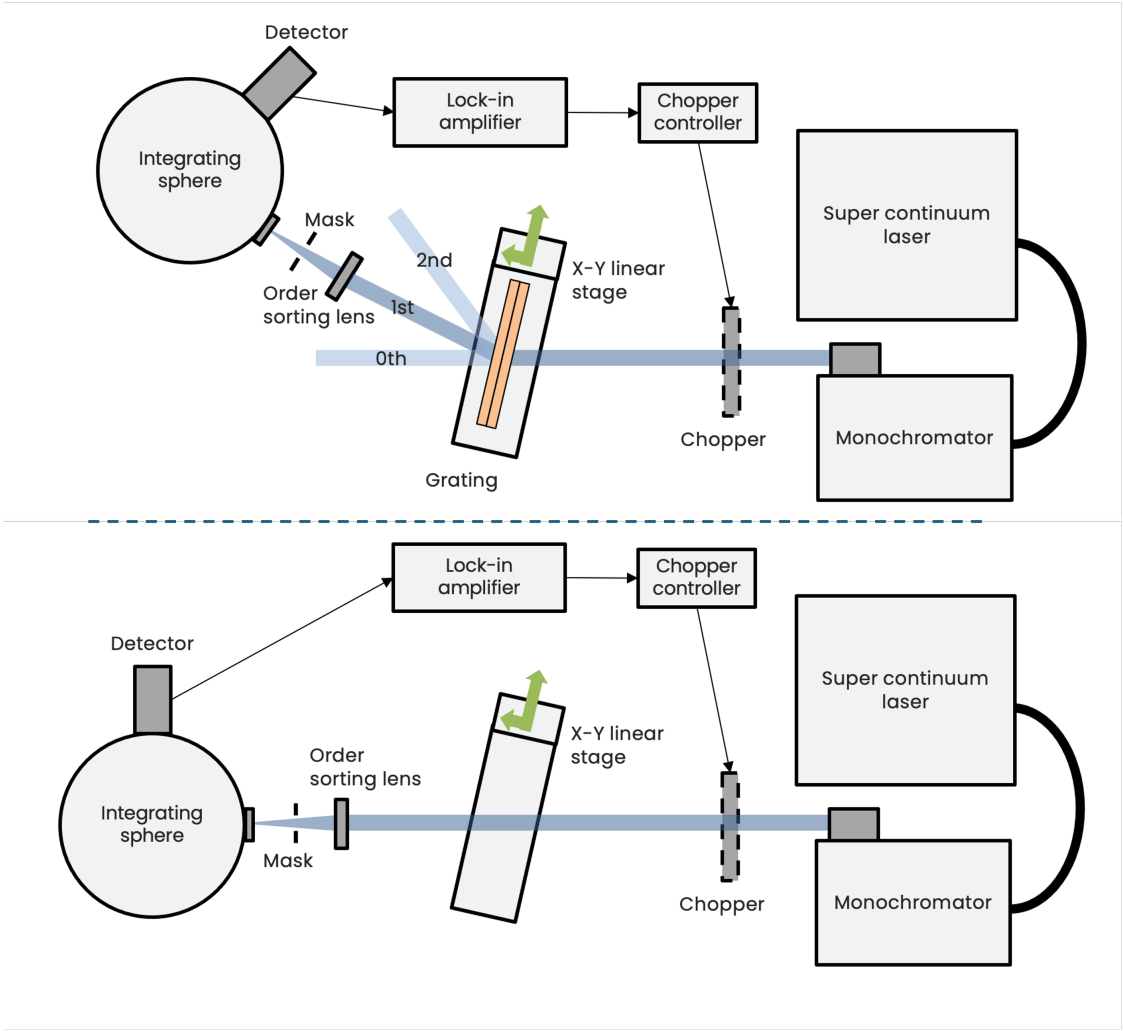


**Figure 2.20:** The final test bench configuration. Testing a grating (top), and a reference measurement (bottom).

output radio frequency from the detector to the lock-in amplifier. No change was made to the lock-in amplifier or its settings, only that a single channel was used instead of two. In the first iteration of the experiment, the beam was split into two paths using subapertures and a pick-off mirror so that a simultaneous reference measurement could be taken. The new light source is stable enough to not require this feature, and by not splitting the path up into two using subaperture masks in a large beam footprint, a significant gain in SNR is achieved.

connector used primarily with coaxial cables.

**Table 2.2:** Comparison of materials based on dark current, readout speed, spectral range, and cost (credit: Thorlabs).

| Material | Dark Current | Speed | Spectral Range | Cost |
|---|---|---|---|---|
| Silicon (Si) | Low | High | Visible to NIR | Low |
| Germanium (Ge) | High | Low | NIR | Low |
| Gallium Phosphide (GaP) | Low | High | UV to Visible | Moderate |
| Indium Gallium Arsenide (InGaAs) | Low | High | NIR | Moderate |
| Indium Arsenide Antimonide (InAsSb) | High | Low | NIR to MIR | High |
| Mercury Cadmium Telluride (HgCdTe) | High | Low | NIR to MIR | High |

#### Summary of improvements

A summary of all the key improvements to the test bench is shown in Table 2.3. Also schematics are shown in Figure 2.20 of both the measurement and reference configuration. Changes have been made across the board with a focus on improving the SNR, enabling automation, and ease of alignment.

### 2.3.3 Automation

A software tool has been developed in Python to automate the test bench, called 'HARMONI Grating Tester' and is available on GitHub[11].

Each piece of hardware that is controlled by the software is connected to the control PC via USB and communicated with using either supplier-provided Python SDKs or third-party libraries. These connections and communication protocols have all been tested and verified individually to ensure actions are performed as expected.

The control functions and automation algorithms are accessible to the human user via a Graphical User Interface (GUI), as shown in Figure 2.22.

The GUI is divided into four sections, the first provides the ability to connect to and verify the connection status of all the hardware. This is useful when starting up the software and ensuring that it can successfully communicate with the connected

[11]Automation code found at: `https://github.com/DavidJonGooding/harmoni-grating-tester`

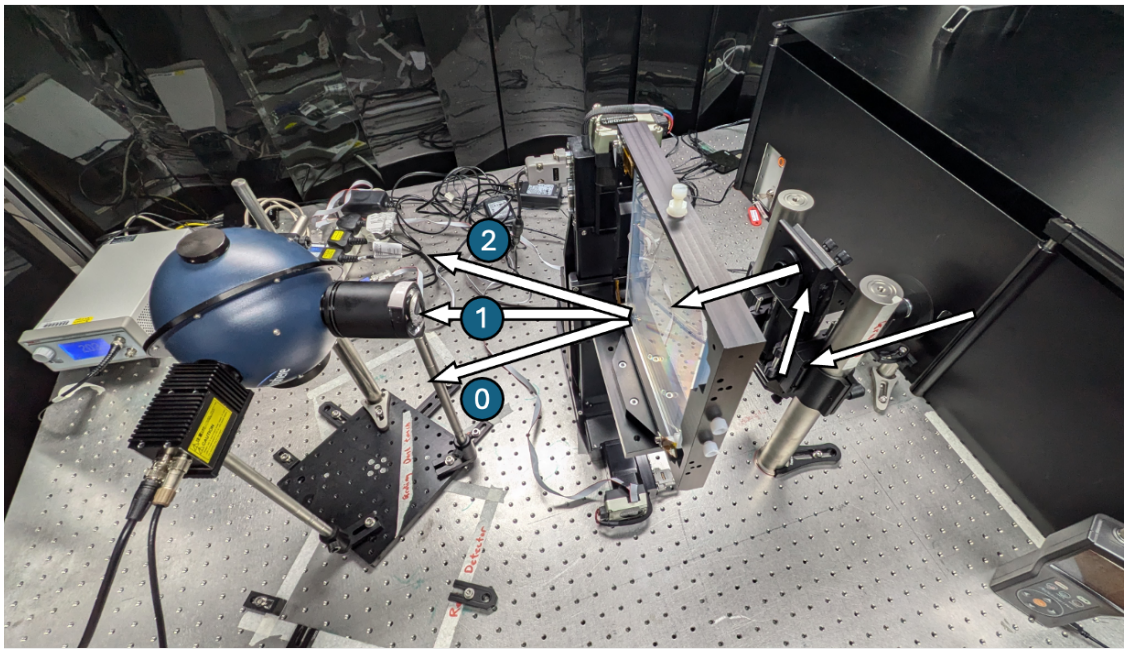


**Figure 2.21:** A photograph of the final test bench. The white arrows show the light path leaving the monochromator and then split into 0th, 1st, and 2nd orders. The black box on the right contains the laser and the monochromator. After being chopped, the beam is raised by a periscope and directed to the grating. After the grating, the order sorting lens is mounted to a tube containing the sub-aperture before the light reaches the integrating sphere. The detector can be seen, the black box, mounted to the side of the integrating sphere.

hardware. The second, enables control of the hardware at an individual level, for example moving translation stages or setting monochromator output wavelength. This is used when setting up, commissioning, aligning, and experimenting with the test bench. The third section provides the operator with fields to input the desired measurement characteristics, and the automated experiment can then be run and data saved to a chosen folder. Finally, at the bottom, an output text field provides the user with a log of all completed actions to help monitor the status and progress of experiments.

Critical to the measurements are the translation stages, the lock-in amplifier, and the monochromator. Ancillary meta-data is taken in the form of temperature and humidity, which can be logged at the start and end of any measurement run for traceability in case of unexpected discrepancies in results. A lightweight grating calculator function is provided with the GUI so that the operator can quickly check

| Hardware | Original | Improved |
|---|---|---|
| Light source | QTH lamp | Super continuum NIR laser fibre-coupled to monochromator |
| Filters | Selectable; Open, closed, 850 nm cut-on, 1000 nm cut-on | Automatic filtering of lower orders in monochromator |
| Monochromator | Newport/Oriel monochromator; 3 gratings inside optimised between 270 and 2200 nm | Bentham monochromator, Python controllable |
| Collimator lens | NIR-II anti-reflectance coating | Built in reflective collimator optics module to monochromator output, 10 mm pencil beam. |
| Chopper | 29 Hz; 5th and 7th harmonics | Same chopper, only using one beam in 7th harmonic |
| Fold mirror | Standard mirror, steerable with rotation stage | Removed |
| Translation stages | Not implemented | Newmark linear translation stages (X/Y) |
| Rotation stages | Thorlabs | Removed |
| Lenses | 3× BK7 lenses, NIR-II anti-reflectance coating | 1× CaF2, NIR-II anti-reflectance coating |
| Integrating sphere | 6-inch Lab Sphere; 4 ports; Spectrareflect coating | 6-inch Lab Sphere; 4 ports; Spectralon coating |
| Detector | Thorlabs InGaAs for NIR; Thorlabs Si for vis | Hamamatsu actively cooled InGaAs photodiode |
| Lock-in amplifier | Signal Recovery; two measurements simultaneously low-noise | Same hardware, only using one channel |

**Table 2.3:** Summary of all improvements to the test bench.

expected angles with input line densities and wavelength. Also, a remotely accessible webcam is installed, so that an operator can remotely verify the status of the test bench and whether the laser is powered on. This is accessed separately from the GUI.

The laser itself is required to be operated from a separate manufacturer-supplied GUI to ensure safe operation with robust commercially provided software.

A summary of the individual modules in the main python file `gratinggui.py` is shown in Table 2.4.

During the development of the automation, a recurring issue was that the y-axis

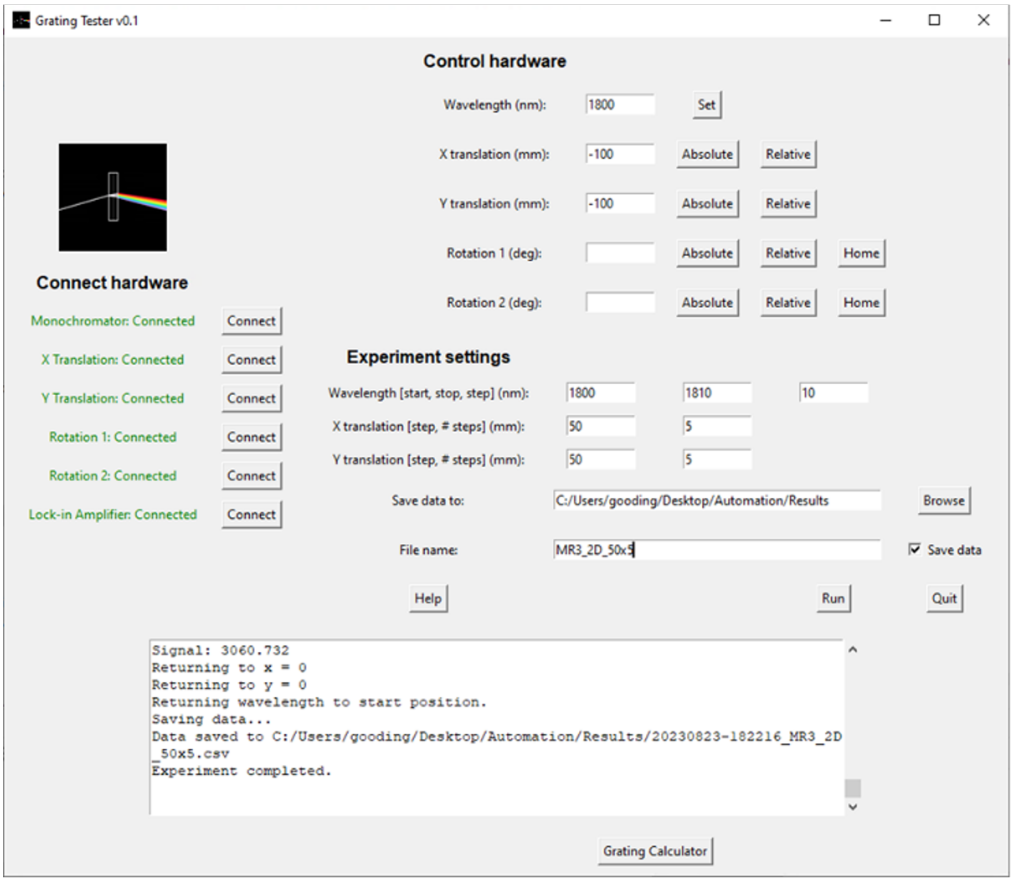


**Figure 2.22:** A screenshot of the automation software GUI.

(vertical) linear translation stage struggled to repeatably return to its top position after scanning downwards, often skipping and ruining the automated test. The effect wasn't completely consistent so it was hard to debug. Initially, the problem was thought to be software-based but after a lot of investigation, it was discovered that the mass mounted on the stage was prohibiting its motion. The grating was mounted in a picture frame which itself was mounted on a motorised rotation stage all together on the linear stage, as shown in Figure 2.23. The rotation stage was redundant and so after some minor modifications to the interface plates, it could be removed and drastically reduce the mass. This solved the issue, and was demonstrated by replacing the hardware on the stage with a pen and tracing the scanned line on a piece of paper as shown in Figure 2.24. The photo shows clearly where the translations form a 10mm grid despite the pen fading away due to its orientation.

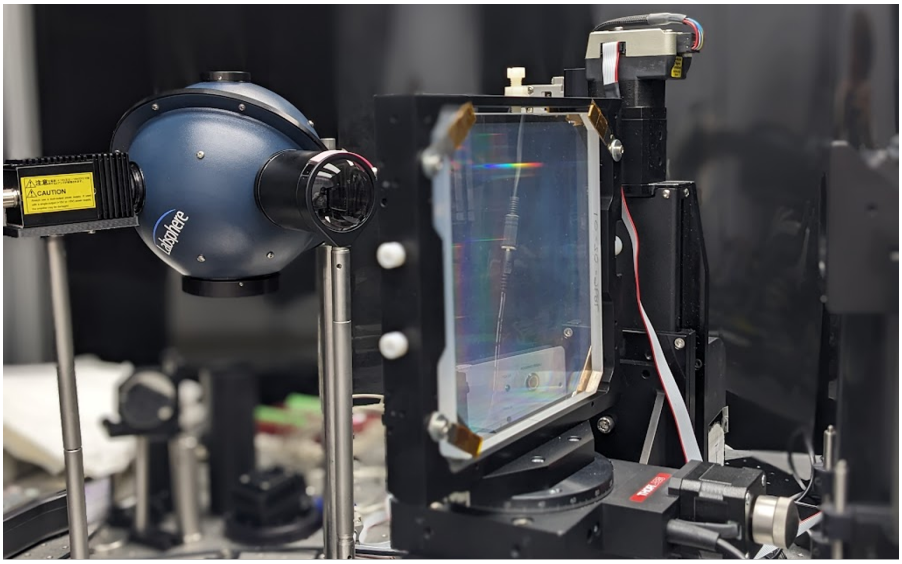


**Figure 2.23:** Another view of the test bench showing the grating temporarily mounted in its picture frame with the rotation stage in place. The reimaging and order sorting lens set-up is visible on the left with the integrating sphere and detector.

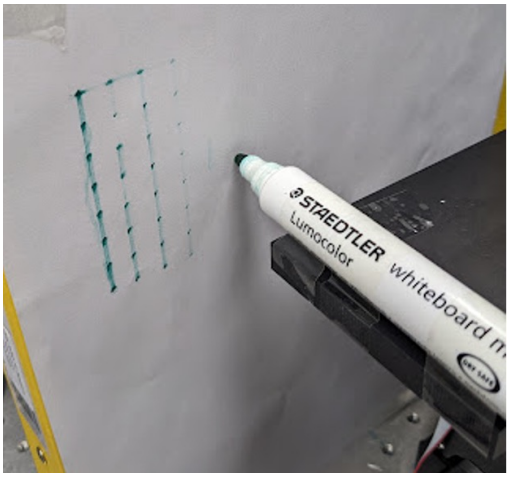


**Figure 2.24:** The 2D scanning of the linear stage was verified using this simple method of a pen being traced along a piece of paper.

### 2.3.4 Procedure

The full test procedure flowchart from handling of the grating on arrival, alignment, and automated test is shown in Figure 2.25. The repetitive and time-consuming part is fully automated and data becomes available to analyse in a CSV file.

There are two key automated measurements. The first is a '1D' scan across wavelength at a single physical location, and the second is a '2D' translation scan at a single wavelength. Depending on the fidelity of the measurements these would

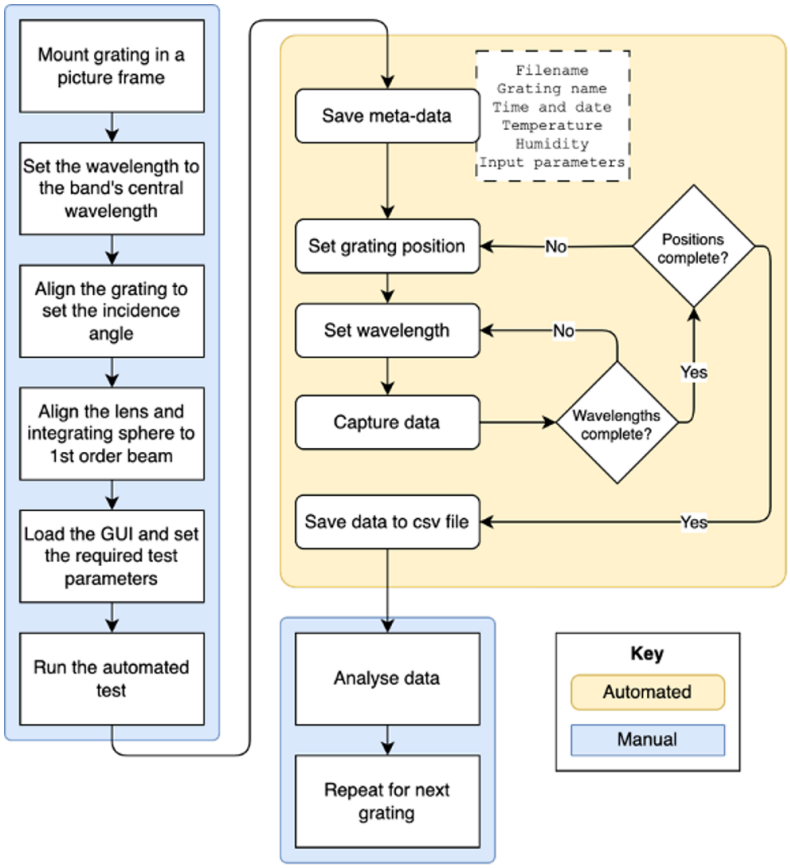


**Figure 2.25:** The test procedure for automated experiment.

both take somewhere between 30 minutes to 2 hours. Whilst it is entirely possible to measure both simultaneously and create a full '3D' datacube of transmission efficiency in a single measurement, this takes a long time and it is prudent to check the status of the test bench every few hours in case of error. To minimise the use of the motors in the monochromator which select the wavelength by rotating its internal grating (which would be much harder to replace upon failure), the decision was made to construct the software to build up the 3D datacubes by completing a full 2D scan of a single wavelength before moving to the next.

Chapter 3.5.3 shows the results, but for a 1D measurement, 10 nm is typically used as a step size to provide sufficient detail in the data. For 2D measurements, grids of 10 mm steps across the whole grating surface were made[12].

[12]A time lapse video of the 2D scanning is available at the following unlisted YouTube video: `https://youtu.be/N9yxJzktU5M`

## 2.4 Discussion and conclusion

In this last section, the chapter is summarised, lessons learnt are identified, and implications of the research are discussed.

### 2.4.1 Chapter summary

This chapter detailed the development and implementation of a dedicated test bench for characterising the diffracted transmission efficiency of VPHGs used in the HARMONI instrument. Key topics included the motivations for the work, the challenges faced during prototyping, and the iterative improvements made to enhance performance and efficiency.

The test bench underwent significant upgrades, including the adoption of a supercontinuum laser light source, a high-performance monochromator, a more sensitive detector, and other optical and mechanical components. These enhancements addressed limitations in SNR and alignment precision, enabling robust and automated testing of the gratings across their operational wavelength ranges and spatial dimensions.

This chapter also highlighted the automation of the testing process through the development of Python-based software, facilitating precise, repeatable, and efficient measurements. This automation reduced the time and effort required for characterisation, addressing both technical and project management constraints.

This work lays the foundation for comprehensive grating characterisation and ensures that the HARMONI instrument meets its performance goals, ultimately contributing to the success of the E-ELT in delivering groundbreaking astronomical data.

### 2.4.2 Lessons learnt

A number of lessons were learnt during this work. Here I summarise some of those.

- One of the key lessons learnt from this work was the value of defining requirements for an optical system before prototyping, especially when components are expensive or have long lead times. Whilst in some instances there is value

in fast prototyping to verify an approach, if a better analysis of the required performance of the test bench had been made at the start, then the solution may have been reached quicker and more efficiently. Clearly defined goals followed by an analytical assessment of the feasibility of the approach are required.

- Remote control and automation of electronic equipment via third-party software is rarely straightforward. Significant time was spent learning how to interact with the various components, in particular the linear stages and lock-in amplifier. My preferred language Python, with the advantages of ease of development, large online support, and free use, etc., has drawbacks including interfacing with older hardware where native support is not provided by the supplier. Ideally, all the hardware would have been purchased with automation in mind, and it did indeed help when procuring the upgraded monochromator which has a supplier-provided Python SDK. It is important to carefully consider automation and software requirements when selecting electronic equipment. A lot of time and effort can be saved if this stage is done well.

- Optical alignment in the infrared is difficult. The advantage of the ability to see the light you are aligning should not be underestimated. There are potential workarounds such as laser alignment cards which are visibly fluorescent when illuminated with a bright IR source, and as described previously, using the monochromator to produce a visible beam in the same path. The alignment strategy should be an important consideration during the design process.

- Another lesson learnt is how variable the optical transmission of different glass components is in the infrared. It is easy to take for granted the high transmission of glass lenses in the visible. This can significantly change when when operating at infrared wavelengths, and care should be taken to assess the transmissive properties of each optical component when working in this wavelength regime.

### 2.4.3 Implications

With the development of this automated test bench it is now possible to perform spectro-spatial efficiency characterisation of VPHGs quickly and robotically. The test bench can be used for any VPH grating operating between 800 and 2500 nm, less than 250 mm in width or height (without changing the translation stages), and is agnostic to line density.

This test bench will enable the HARMONI team to characterise the instrument's diffraction gratings in a short space of time, which will facilitate the on-time delivery of the critical AIT phase of the instrument.

**Table 2.4:** Summary of modules in `gratinggui.py`.

| Module Name | One-Line Description | Lines |
|---|---|---|
| ___init___ | Initialises the main GUI, frames, widgets, and event bindings | 130 |
| connect_monochromator() | Connects to the Bentham monochromator | 20 |
| connect_x_translation() | Connects to the X translation stage | 12 |
| connect_y_translation() | Connects to the Y translation stage | 12 |
| connect_rotation1() | Connects to the first rotation stage | 14 |
| connect_rotation2() | Connects to the second rotation stage | 14 |
| connect_lockin_amplifier() | Connects to the SR7230 lock-in amplifier | 10 |
| update_indicator_lights() | Updates the status text for each piece of equipment | 19 |
| output_message() | Inserts messages into the Tkinter text box | 7 |
| set_wavelength() | Sets the monochromator to a given wavelength | 17 |
| auto_wavelength() | Automates setting the monochromator's wavelength | 4 |
| convert_steps() | Converts translation steps into millimetres | 9 |
| convert_signal() | Converts raw lock-in data into a voltage reading | 5 |
| move_x_abs() | Moves the X stage to an absolute position | 17 |
| move_y_abs() | Moves the Y stage to an absolute position | 17 |
| move_x_rel() | Moves the X stage by a relative distance | 14 |
| move_y_rel() | Moves the Y stage by a relative distance | 14 |
| zero_x() | Resets the X stage's position to zero | 6 |
| zero_y() | Resets the Y stage's position to zero | 6 |
| reset_buffers() | Clears the input buffers for the X and Y stages | 6 |
| move_rotation1_abs() | Moves rotation stage 1 to an absolute angle | 13 |
| move_rotation2_abs() | Moves rotation stage 2 to an absolute angle | 13 |
| move_rotation1_rel() | Moves rotation stage 1 by a relative angle | 13 |
| move_rotation2_rel() | Moves rotation stage 2 by a relative angle | 13 |
| move_rotation1_home() | Homes rotation stage 1 | 7 |
| move_rotation2_home() | Homes rotation stage 2 | 7 |
| threading() | Launches the experiment in a separate thread | 5 |
| run_experiment() | Main experiment loop for scanning and data acquisition | 200 |
| acquisition() | Gathers data from the lock-in amplifier | 20 |
| browse_root_folder() | Allows selection of a folder for saving data | 6 |
| open_help() | Opens the PDF help document | 5 |
| save_data_csv() | Saves the experimental results to a CSV file | 12 |
| open_grating_calculator() | Opens a Python script for grating calculations | 4 |

# 3

# VPHG transmission efficiency results

## Contents

# 3.1 Introduction

This chapter presents the diffracted transmission efficiency measurement results of a range of prototype gratings and discusses their implications. The specifications and characteristics of the devices under test are provided in Section 3.2, and a comprehensive discussion on sources of error is made in Section 3.3.

The full results of each grating are presented in Section 3.4 along with a description of the error bars.

## 3.1.1 Transmission efficiency requirement

The formal HARMONI spectrograph requirement regarding transmission is *"the spectrograph (excluding the detector) shall provide a transmission of* $\geq 60\%$ *(assuming unpolarised light) for* 95% *spaxels in all configurations, averaged over the central* 80% *of the instantaneous wavelength range of each configuration"*. This is from HARMONI technical document HRM-00180 [88].

This requirement is for the full optical path of the spectrograph from the slit up until, but excluding, the detector. To meet this formal requirement, it is anticipated that the gratings will have to provide a transmission of $\geq 70\%$ across the same central 80% of the wavelength range. This has been determined by considering the expected impact of the other optical components and thus deriving the requirement for the gratings, referred to as the 'derived requirement' from this point.

This requirement is applicable to the final gratings with anti-reflection coatings in their operating environment in the specified order.

There is no specific requirement on the spatial variability of efficiency; it just needs to be understood, and the average value across the grating beam footprint needs to meet the derived requirement.

# 3.2 Devices under test

Due to the various prototyping activities, described in Section 2.2.1, a range of different gratings have been available for testing ahead of the delivery of the final

instrument gratings. The key characteristics of these prototypes are shown in Table 3.1 of 'devices under test' (DUTs).

The blank grating is a mechanical prototype, identical to a real grating without the gelatin layer. It was designed to be used for early mechanical and bonding tests to ensure the grating performs and survives as expected during assembly, transport, cooling, and operation. As there is no actual grating, it does not diffract light and so is also useful to compare the transmission test bench with a commercial spectrophotometer.

A commercial-off-the-shelf (COTS) grating was bought with similar characteristics to the MR2 (J-band) grating as a low-cost way of verifying the grating bench.

Two full size MR3 prototypes, described in Section 3.4.5, were made and provided the first opportunity to measure efficiency variation over the grating surface.

The crucial development of the low line density LR2 grating resulted in a small 2-inch sample grating, followed by a full-size grating, described in Section 3.4.6 and 3.4.7 respectively.

**Table 3.1:** The prototype gratings' characteristics.

| Grating Name | Line Density (lines/mm) | Bandpass ($\mu$m) | Physical Size (mm) | Aperture (mm) | Bragg Angle (deg) |
|---|---|---|---|---|---|
| Blank | n/a | n/a | 164 × 164 × 20 | 154 × 154 | n/a |
| COTS (MR2) | 550 | 1.050–1.500 | 50.8 dia. × 6 | 42 dia. | 21.4 |
| MR3 | 383.868 | 1.435–1.815 | 164 × 164 × 20 | 154 × 154 | 15.41 |
| LR2 sample | 159 | 1.450–2.450 | 50.8 dia. × 6 | 42 dia. | 6 |
| LR2 | 158.871 | 1.450–2.450 | 160 × 164 × 10 | 150 × 154 | 6.04 |

## 3.3 Sources of error

Before presenting the results, we discuss the sources of error in the measurements and how they are accounted for. These include systematic, statistical, operational, and environmental factors.

### 3.3.1 Systematic errors

Systematic errors are consistent inaccuracies that occur in measurements and can be difficult to detect without calibration or by comparing with a known standard. Due to the length of time (many months at a minimum) that this test bench will be used for, repeatability is something to be considered. A measurement taken one day should be the same as one taken a few months later.

#### Alignment errors

Misalignment of the optical components (laser, grating, detector) can lead to significant errors in measuring the intensity of transmitted light.

The laser interfaces to the monochromator via an optical fibre which simply slides into place. The tolerances are tight so the repeatability is high, however, in theory there is still room for potential error if the equipment is moved or adjusted. Care has been taken to ensure the fibre does not move and is easy to return to its original position in the case it is moved. Variations in power caused by internal misalignment of the monochromator optics are taken care of by the reference measurement; the important aspect to consider is the output beam direction as this has the potential to wander, although in practice this was not appreciable and therefore very difficult to measure and quantify.

Next, the collimated beam leaving the monochromator is chopped and it is important that the beam is not clipped or vignetted by the inner or outer radius of the chopper wheel. The monochromator and chopper assembly are secured to the optical bench to ensure they don't move, once aligned this is fixed and so does vary and cause any issues.

The method of taking reference measurements close to the time of the test measurement mitigates the previously described alignment errors, and so the most important alignments are of the grating itself and the order sorting sub-assembly (the most sensitive component) which are different between reference and test.

The grating is aligned to within an accuracy of 1 degree which can account for a maximum loss of up to 1% in transmission. This is small because grating

efficiency curves vs angle are quite flat at the peak and a small change in angle means a small or even negligible change in efficiency. The initial coarse alignment of the grating is done mechanically to set the incidence angle relative to the optical bench. Finer alignment is achieved optically in an iterative fashion by making small adjustments and hunting for a maximum signal at the detector.

The key issue with aligning the order sorting sub-assembly is the potential to clip the beam at the edge of the band. It has been designed to allow some room for error so any loss in signal at the edges of the band is prevented with care, as shown in Figure 2.18 in Chapter 2.4.3.

**Calibration of instruments**

Any lack of calibration or improper calibration of the monochromator, detector, or lock-in amplifier can introduce measurement errors. This includes wavelength calibration of the monochromator and sensitivity calibration of the detector. The wavelength is selected via software using the monochromator supplier (Bentham) provided Python package "bendev". The device is calibrated by the supplier and is stated to be accurate to within 1.2 nm. Calibration also ensures that the bandwidth (FWHM - Full Width at Half Maximum) settings are consistent and accurate, impacting the light intensity and spectral resolution.

**Optical aberrations and imperfections**

Imperfections in the monochromator gratings, the optical chopper, and any optical lenses or mirrors used can introduce aberrations that affect the beam quality and intensity measurement. This effect is expected to be negligible as they are either calibrated out in the reference measurement or the environment is stable enough to render them unimportant.

**Chopper frequency stability**

If the optical chopper does not have a stable frequency, the synchronisation with the lock-in amplifier can be off, leading to incorrect signal modulation detection.

The chopper is rated to have a frequency drift of <20 ppm/°C, which over an expected maximum drift of 5°C in the lab will amount to less than 100 ppm which equates to a change of 0.02 Hz. The lock-in amplifier is capable of handling such a variation.

**Lock-in amplifier settings**

Incorrect phase or time constant settings on the lock-in amplifier can lead to errors in detecting the signal amplitude accurately. A potential human error here is forgetting to auto-phase the lock-in amplifier when the light source, chopper, and detector are switched on. This is written very clearly in the instructions to prevent this error.

### 3.3.2 Statistical errors

Statistical errors are random variations that occur in measurements due to various uncontrollable factors.

**Photon shot noise**

Photon shot noise is the random fluctuation in the number of photons detected, inherent to the quantum nature of light, and is more significant at lower light levels. To determine if the system is shot noise limited, we must perform some calculations.

Firstly we must determine how many photons are output by the laser and monochromator setup. The laser output as defined by the data sheet [64] is approximately 1 mW/nm at a worst case, and the monochromator has a bandwidth of 10 nm (FWHM) with a throughput of approximately 50% [12]. This results in a 5 mW output beam from the monochromator, which is then further chopped to 2.5 mW.

Using the Planck relation

$$E = hf = \frac{hc}{\lambda}, \tag{3.1}$$

where $h$ is Planck's constant and $c$ is the speed of light, the number of photons $N$ per second is calculated as

$$N = \frac{P\lambda}{hc} = \frac{2.5 \times 10^{-3} \cdot 1 \times 10^{-6}}{hc} = 1.26 \times 10^{16} \text{ photons per second.} \quad (3.2)$$

Then the losses in the optical path are accounted for including 20% loss from glassware (lenses + grating) and a conservative estimate of 99.999% loss from the integrating sphere.

From this estimated flux (photons per second) at the detector and the photon energy, which at 1 µm is $\approx 2 \times 10^{-19}$ joules, the power $P$ is calculated to be $\approx$ 20 nW, given by

$$P = \text{Photon Flux} \times \text{Energy per Photon.} \quad (3.3)$$

Next, we compare this with the noise equivalent power (NEP) of the detector. The detector data sheet [47] specifies the NEP as typically $5.2 \times 10^{-14}\,\text{W/Hz}^{1/2}$ for the C12483-250 Hamamatsu detector. This value represents the minimum detectable power per square root bandwidth due to the detector's noise alone. Converting this to a value we can compare to the power requires the frequency of the chopper $f_c$ =145 Hz, which allows SNR to be determined as follows

$$\text{SNR} = \frac{P}{\text{NEP}\sqrt{f_c}}. \quad (3.4)$$

The SNR is calculated to be $\approx$ 30,000, which is very high. Even if the conservative estimates above are wrong by an order of magnitude then the SNR is still high enough to show that shot noise is not a significant problem as the detector is very sensitive and the signal is high.

**Thermal noise and dark current in detector**

These are inherent to the electronics of the detector and can contribute to noise, especially significant in low-signal scenarios. In our case, these sources are not significant as proved above.

**Fluctuations in laser output**

Even with a supercontinuum laser, there may be slight fluctuations in output power, which can vary the input intensity across measurements. The laser specifications state the power stability to be within 1%, and the test report for the specific unit used states ±0.2% once the laser has been allowed to warm up for a minimum of 30 minutes. This step is also included in the instructions.

**Ambient light and electromagnetic interference (EMI)**

Any ambient light leaking into the system or EMI can add noise to the detector, affecting the accuracy of transmission measurements. The use of the chopper and lock-in amplifier minimises the impact of ambient light, and the choice of chopped frequency minimises the EMI issue. During commissioning measurements were taken with the room lights on and off, and no detectable difference was found.

### 3.3.3 Other errors

Operational errors can also arise from the method or procedure used in conducting the experiments, such as:

- **Reproducibility of setup** - Each time the setup is assembled or adjusted, slight variations can occur, for example, in alignment as previously discussed.
- **Data acquisition errors** - In theory, errors in the timing or method of data acquisition by the data logging system can introduce errors. For instance, miss-timed readings due to delay in the electronics can result in data not representing the intended measurement conditions.

Environmental factors can significantly affect precision in optical measurements, these include:

- **Temperature and humidity variations** - These can affect the physical properties of the optical components, especially the grating, altering its refractive index and thus affecting transmission. Because of these sensitivities,

the VPH gratings are hermetically sealed during manufacture. A stable lab environment is also used to mitigate this potential risk. The HARMONI gratings will be operated at the cryogenic temperature of 130 K in the instrument, our measurements will take place in laboratory conditions (room temperature and pressure), Tamura et al. (2006) [97] shows no clear evidence that this temperature change impacts transmission efficiency.

- **Vibrations and acoustic noise** - Mechanical vibrations and acoustic noise can disturb the optical alignment and affect the stability of the optical components. An optical bench with vibration isolation legs is used, which prevents most vibrations, and the lab environment is stable. Also, a separate electronics rack is used to host most of the electronic components to prevent the effect of micro-vibration and unwanted air currents from the cooling fans.

## 3.4 Results

### 3.4.1 Error bars

Each measurement retrieved by the automation software consists of a mean of 50 individual measurements from the lock-in amplifier, $I$, and a standard deviation of those 50, $\sigma_I$. This number of measurements was chosen after some experimentation as a trade-off between statistics and time taken. The dominant source of error in $\sigma_I$ appears to be photon noise, amongst other sources discussed in Section 3.3. To best represent the error in the transmission measurements, considering we have the mean values and standard deviations for both the diffracted beam and the reference beam for each wavelength, we use error propagation techniques to quantify and display the uncertainty in the transmission calculations. The transmission, $T$, is calculated by dividing the intensity of the light that passes through the glass, $I$, by the intensity of the reference light, $I_0$, i.e.,

$$T = \frac{I}{I_0}. \tag{3.5}$$

Since we have the standard deviations for both $I$ and $I_0$ it is possible to calculate the standard deviation of the transmission ($\sigma_T$) using the error propagation formula for division:

$$\sigma_T = T\sqrt{\left(\frac{\sigma_I}{I}\right)^2 + \left(\frac{\sigma_{I_0}}{I_0}\right)^2}. \tag{3.6}$$

This formula accounts for the relative errors of both measurements and how they contribute to the overall uncertainty of the transmission measurement. $\sigma_T$ is then displayed as error bars on the transmission curves.

### 3.4.2 Fresnel losses

Fresnel losses, named after the French engineer Augustin-Jean Fresnel, describe the reflection losses that occur when light passes through the interface between two different optical media. These losses are crucial to consider in optical system design, as they impact the overall transmission efficiency of the system.

When light encounters a boundary between two materials with different refractive indices (e.g., air and glass), a portion of the light is reflected back into the first medium, and the remainder is transmitted into the second medium. The reflection coefficients for s-polarized (perpendicular) and p-polarized (parallel) light are given by the Fresnel equations:

$$R_{\mathrm{s}} = \left|\frac{n_1\cos\theta_i - n_2\cos\theta_t}{n_1\cos\theta_i + n_2\cos\theta_t}\right|^2 = \left|\frac{n_1\cos\theta_i - n_2\sqrt{1-\left(\frac{n_1}{n_2}\sin\theta_i\right)^2}}{n_1\cos\theta_i + n_2\sqrt{1-\left(\frac{n_1}{n_2}\sin\theta_i\right)^2}}\right|^2, \tag{3.7}$$

$$R_{\mathrm{p}} = \left|\frac{n_1\cos\theta_t - n_2\cos\theta_i}{n_1\cos\theta_t + n_2\cos\theta_i}\right|^2 = \left|\frac{n_1\sqrt{1-\left(\frac{n_1}{n_2}\sin\theta_i\right)^2} - n_2\cos\theta_i}{n_1\sqrt{1-\left(\frac{n_1}{n_2}\sin\theta_i\right)^2} + n_2\cos\theta_i}\right|^2. \tag{3.8}$$

Here, $R_{\mathrm{s}}$ and $R_{\mathrm{p}}$ are the reflection coefficients for s- and p-polarized light, respectively, $n_1$ and $n_2$ are the refractive indices of the two media, $\theta_i$ is the angle of incidence, and $\theta_t$ is the angle of transmission, which can be calculated using Snell's law.

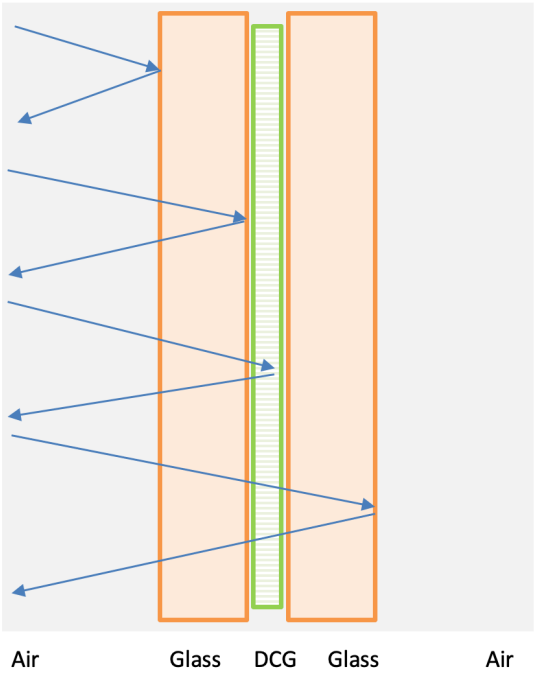


**Figure 3.1:** The surfaces considered when estimating Fresnel losses in transmission.

To quantify the total Fresnel loss for unpolarized light, the mean reflectance is calculated by averaging $R_s$ and $R_p$:

$$R_{\text{mean}} = \frac{R_s + R_p}{2}. \tag{3.9}$$

In VPH gratings there are four surface interactions to consider, as shown in Figure 3.1, between air and glass, glass and gelatin, and vice versa. The instrument will operate in a vacuum, for which the refractive index is 1. However, our experiment is conducted in laboratory conditions and hence air is used, with a refractive index of 1.000293 at 589 nm. Although the refractive index does change with wavelength, the change is very small for air in the wavelength regime of interest (less than 0.001%), and so will be treated as constant. The refractive index also varies with temperature, although once again the variations of expected lab air temperatures are very small in our wavelength regime.

There is a larger variation in refractive index over wavelength for the Fused Silica (approximately 2% over the whole HARMONI range), and so a mean value is taken.

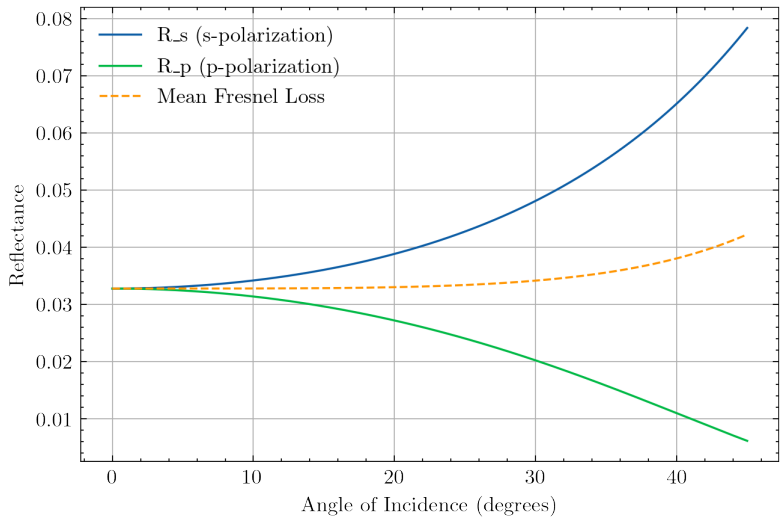


**Figure 3.2:** Fresnel reflection losses for the air to fused silica surface.

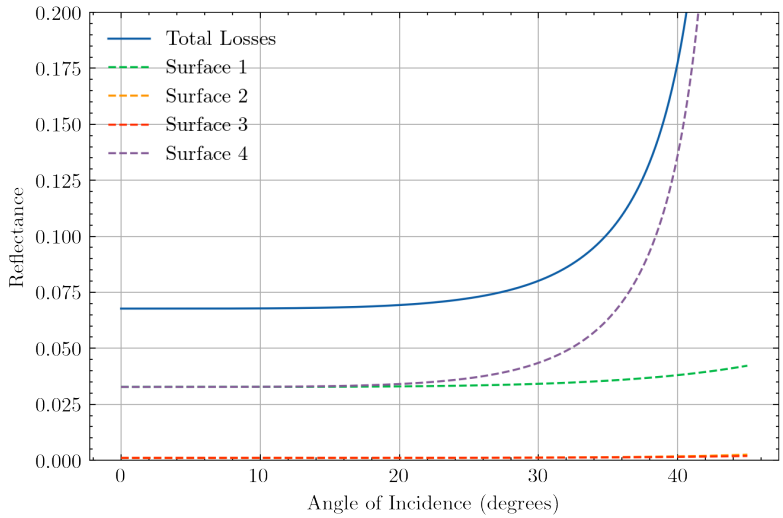


**Figure 3.3:** Total Fresnel losses vs angle of incidence.

When estimating the expected Fresnel loss the angle of incidence for the grating is used for the first two surfaces (an approximation ignoring refraction), and the angle of diffraction is used for the last two surfaces.

The final HARMONI gratings will have high performance anti-reflectance (AR) coatings on their outer surfaces which will all but prevent Fresnel loss. The prototype gratings do not have this AR coating so these calculations will be used to estimate the performance difference between the "as measured" prototypes and the final operational gratings. Table 3.2 shows the expected Fresnel loss from each family of prototype grating, roughly 7% for the low and medium resolution

gratings as measured in this work.

**Table 3.2:** Estimated Fresnel losses for the three grating families for four surfaces and the total loss for the specified angle of incidence (AoI) on the glass.

| Family | AoI (deg) | Surface 1 | Surface 2 | Surface 3 | Surface 4 | Total Loss |
|---|---|---|---|---|---|---|
| LR | 6.036 | 0.0328 | 0.0011 | 0.0011 | 0.0329 | 0.0678 |
| MR | 15.407 | 0.0328 | 0.0011 | 0.0011 | 0.0341 | 0.0692 |
| HR | 35.217 | 0.0356 | 0.0014 | 0.0015 | 0.1391 | 0.1777 |

### 3.4.3 Blank grating

A 'blank' grating was procured for mechanical testing which has no gelatin layer and hence no grating inside. As shown in Figure 3.4, the 'blank' is otherwise mechanically identical to a real grating, with two substrates (Corning 7980) bonded together with an adhesive. Typically the grating manufacturer uses a foil strip to seal the gap between the substrates as the gelatin layer is very sensitive to moisture, however, there were concerns about the addition of this foil with regards to the bond pads used to mount the grating in its frame. This prototype therefore was designed to have foil on two sides and no foil on the other two sides so that a bonding test and comparison could be performed.

This grating arrived in 2022 during the testing of the first iteration of the transmission efficiency test bench and so was measured in the bench and with a COTS spectrophotometer for comparison. The spectrophotometer used was the LAMBDA 750 spectrophotometer from PerkinElmer, and works simply by inserting the sample and choosing the wavelength ranges and steps to be measured. These devices can be used for measuring the transmission or the reflectance of different samples [1], but do not have the capability to characterise diffractive devices like gratings because of the geometry required from deviated light paths.

The Corning 7980 glass substrate is expected to have some absorption features which will limit the grating's transmission at certain wavelengths (1400 nm, 2200 nm, and beyond 2400 nm).

[1] Spectrophotometers are regularly used in chemistry, biology and materials science.

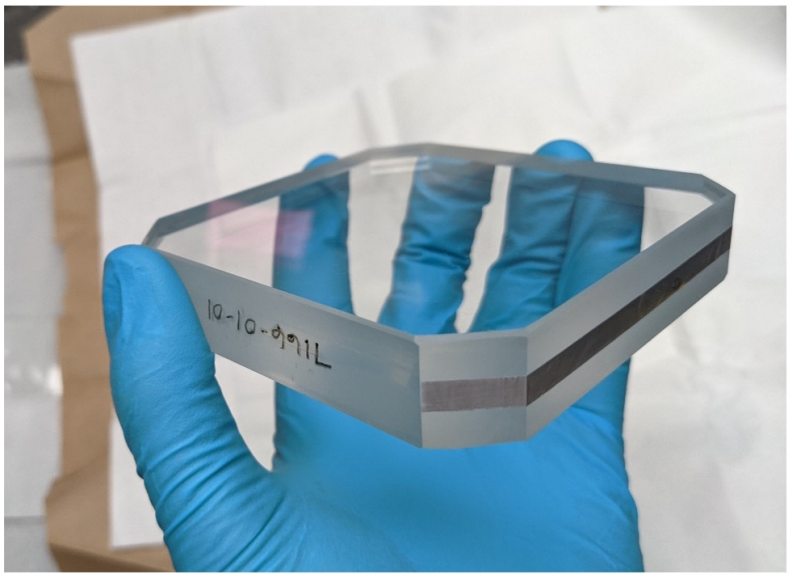

**Figure 3.4:** Full size grating blank for mechanical testing and spectrophotometer verification.

With no diffractive element inside, the alignment of this measurement was simple. A reference measurement was taken for each wavelength step and then the blank was dropped into the path with the beam perpendicular to the surface.

Figure 3.5 shows the measured signal transmitted through the 20 mm thick blank grating and a reference measurement without the blank. It's clear here that the test bench has very low signal beyond 2000 nm. The other large shifts are due to either changing gratings or filters internally within the monochromator. The noise is roughly constant and so the signal-to-noise ratio (SNR) degrades with signal.

Figure 3.6 shows the transmission measured on the bench in blue with error bars calculated as per equation 3.6, and the spectrophotometer measurements with 1 nm steps are shown in orange. The grey line shows the absolute residuals of the two measurements, and the yellow line shows the error in our measurements on the same secondary axis.

The spectrophotometer measurements have an accuracy of around 0.12% [12] or better, and so we shall treat these as our ground truth. These results show that the test bench is accurate to better than 1% below 2000 nm which is suitable for our needs, but worse at higher wavelengths.

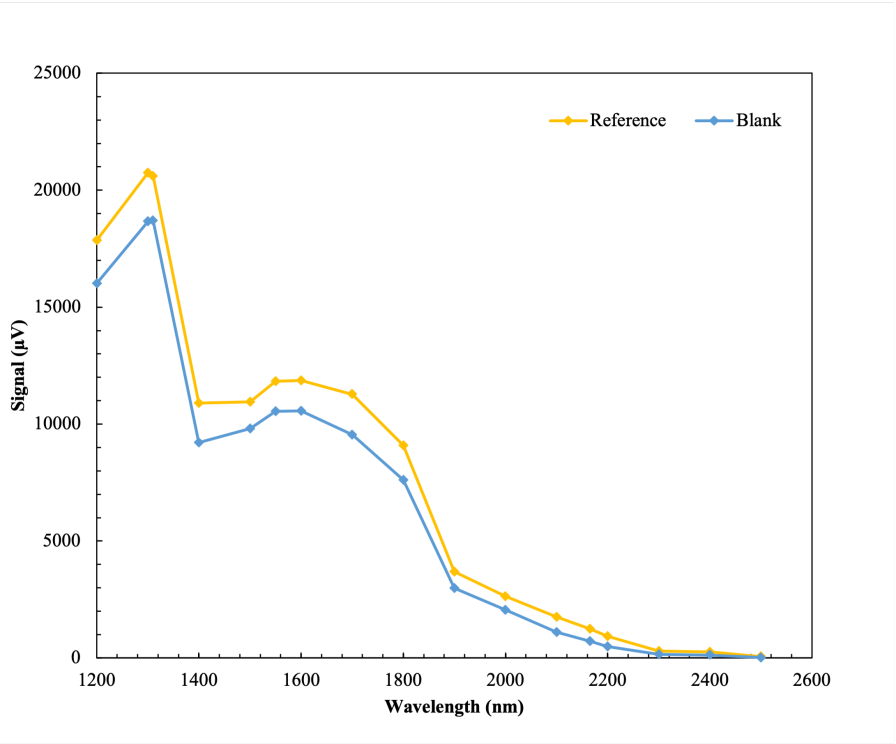


**Figure 3.5:** Grating blank and reference measurements over wavelength.

### 3.4.4 COTS grating

A low cost commercial-off-the-shelf (COTS) grating was available with a short lead time from the same supplier and so was bought to enable early testing of the experiment. The COTS grating has a line density of 500 l/mm, compared to 526 l/mm for the MR2 grating design. The central wavelengths are 1273.5 nm and 1185 nm respectively.

Other than a similar line density, the COTS grating is quite different, being 42 mm diameter circle and only 6 mm thick. The tests here are partly to validate the method over the MR2 band, and partly to understand typical grating performance at these line densities.

The results in Figure 3.7 show a typical grating performance curve centred around the designed wavelength. This test was done using the method shown in Figure 2.11 with the first iteration of the test bench. The error bars are small and show that this earlier version of the test bench is good enough for the measurement of bands below 2000 nm, although with limited automation the procedure is much slower.

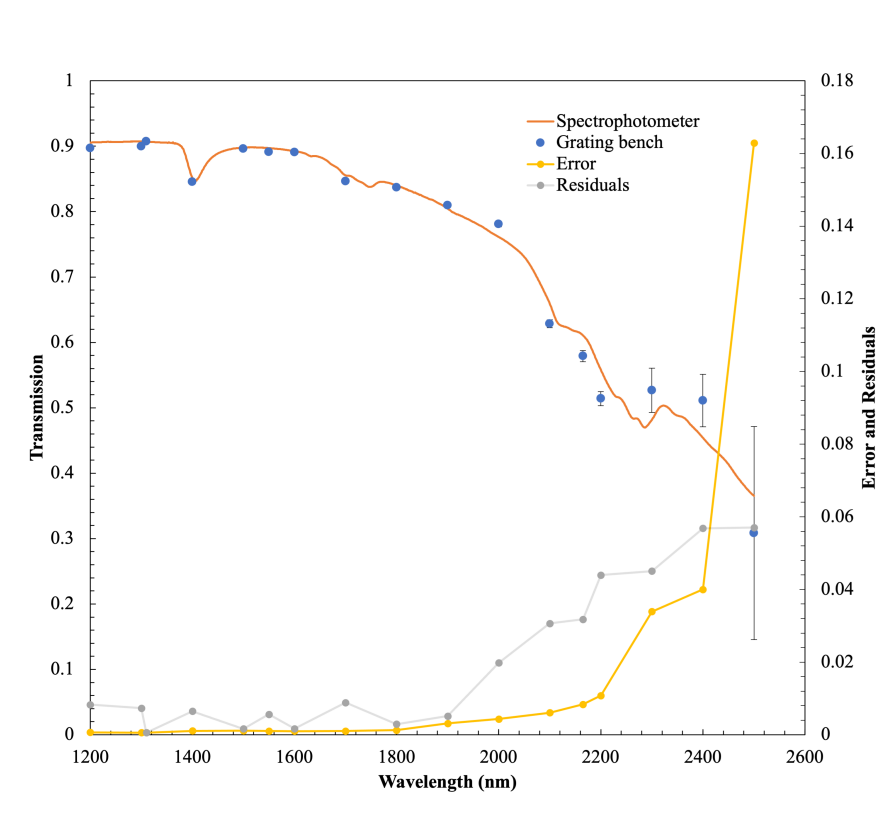


**Figure 3.6:** Grating blank transmission and spectrophotometer measurements for comparison.

This grating is AR coated therefore Fresnel losses are not considered. The results show that a grating of these specifications would meet the derived requirement for transmission efficiency.

### 3.4.5 MR3 prototypes

In 2023, the first full size HARMONI VPH grating prototypes were developed. The chosen grating for prototyping of wavefront error, adhesives, bonding, cryogenic testing, etc., was the MR3 grating, a photograph of which is shown in Figure 3.8. As the first full-size grating received, it was ideal for verifying the full automation of the test bench.

Two prototype MR3 gratings were prepared by Wasatch Photonics following the design drawing in Appendix A.2.1 and are mounted temporarily within a picture frame mount, part of the IR grating module package.

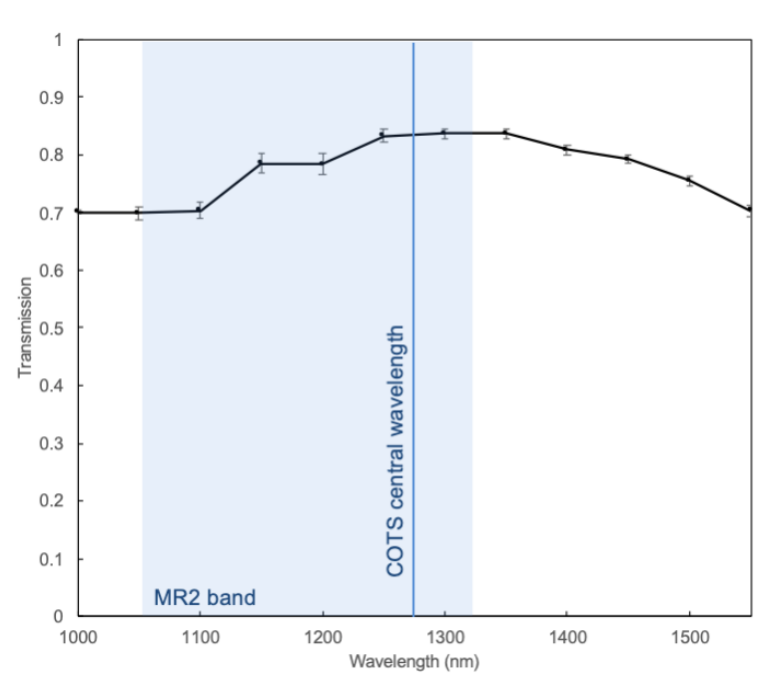


**Figure 3.7:** Transmission efficiency of the COTS grating, showing the as designed central wavelength, and the MR2 band for comparison.

The temporary mounting uses nylon screws to hold the grating in place and small kapton tape-covered metal plates to prevent the grating from falling out of the frame in the event that it slips from the nylon screws, as shown in Figure 2.19.

Physically the gratings are made of a holographic DCG layer sandwiched between two 164 mm × 164 mm × 20 mm UV Fused Silica Corning 7980 substrates. The optically active area has a central 154 mm square aperture with bevelled corners, a line density of 383.868 l/mm, a central wavelength of 1625 nm, and a nominal incident angle of 15.407°. The only difference between the two prototype gratings is the internal adhesive used' with UV-650 and NOA63 for MR3 grating serial numbers 7896-1 and 7896-2, respectively. NOA63 was the original adhesive planned for use in the MR3 gratings, however, UV-650 was introduced by Wasatch Photonics to solve issues related to the grating robustness and so both have been supplied with these prototypes. All of the transmission results shown here are from the 7896-1 grating with the UV-650 adhesive, the other grating was used by colleagues for other experiments on mechanical properties and bonding trials.

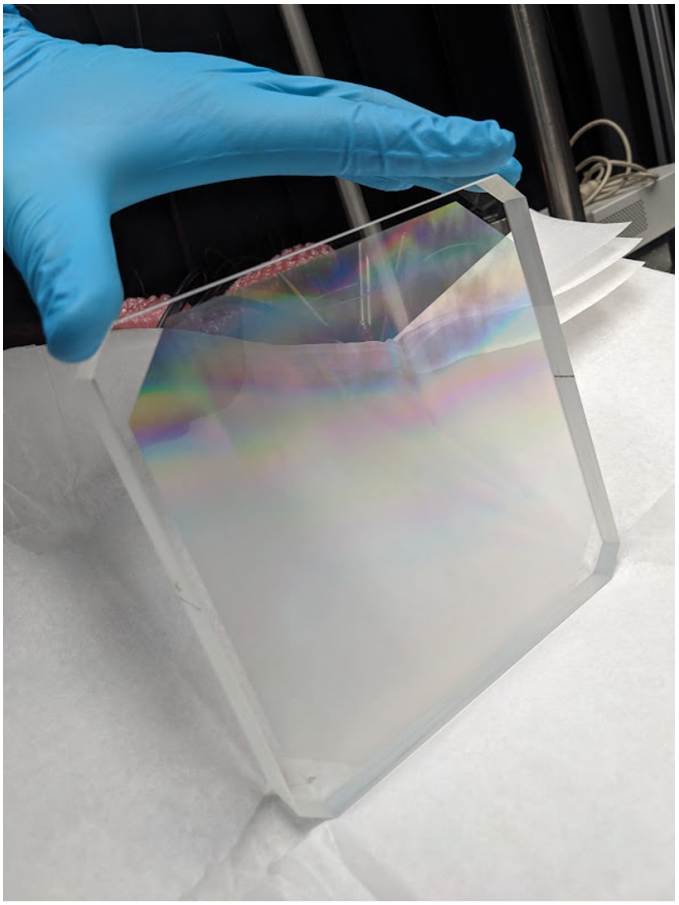

**Figure 3.8:** The first MR3 (H band) grating prototype delivered to Oxford; serial number 7896-1.

First, the 'one-dimensional' transmission efficiency was characterised at the centre of the grating across the waveband. Figure 3.9 shows the results including the anticipated requirement, and factoring in Fresnel losses. The error bars vary due to the varying SNR caused by the output laser power from the monochromator, detailed in Equation 3.6.

We also carried out measurements of spatial variations in efficiency. Here a single wavelength was set at a time, and the grating was scanned about the stationary input beam. The beam was aligned to the bottom corner of the grating, and it was automated to scan upwards in one column, return to the bottom, move one step to the side and repeat until the whole surface was covered. 10 mm step size was chosen as a trade-off between time and accuracy, the beam diameter is 7 mm so there is potential scope to increase the resolution of the scanning in future.

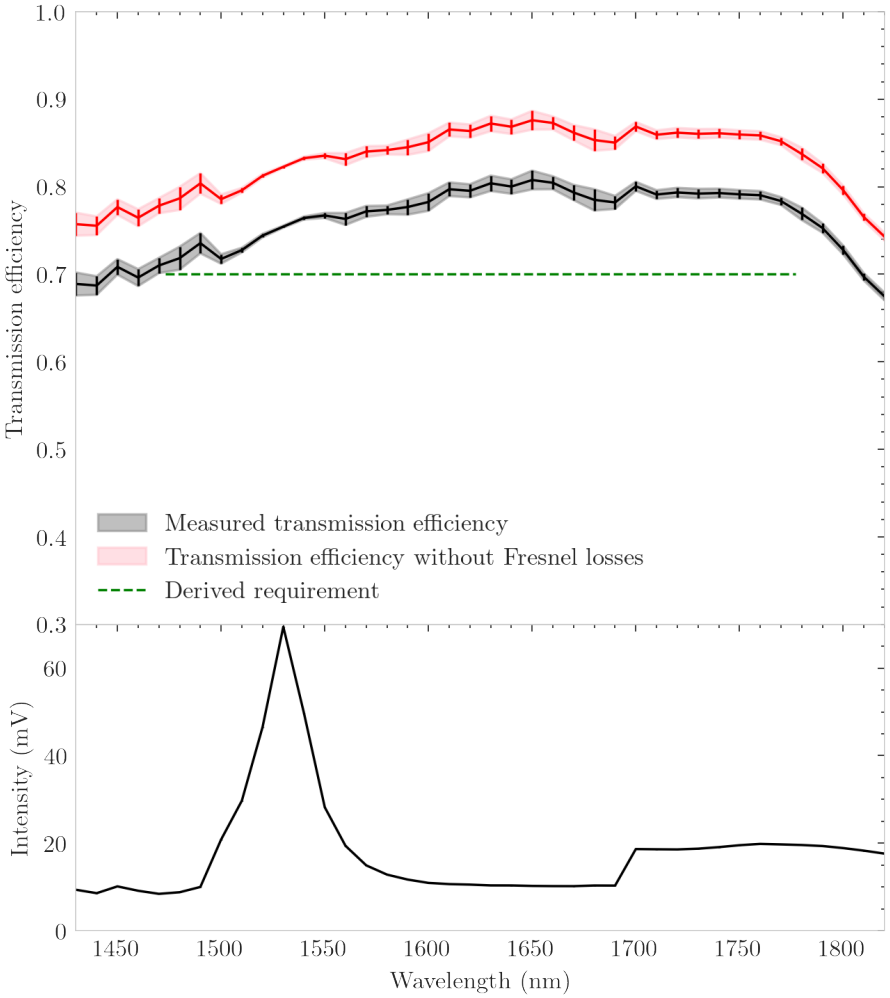


**Figure 3.9:** Transmission of the MR3 (H-band) 7896-1 grating: measured (black), estimated removing Fresnel loss (red), and derived requirement (green). The lower subplot shows the light intensity detected in the reference measurements, which directly correlates to the transmission measurement error bars. The laser pump wavelength is visible as a spike, and a monochromator grating change is visible in the transition at 1700 nm.

The maps in Figure 3.10 show the first-order transmission efficiency of the grating for a specific wavelength across the whole grating surface. We measure at 1450, 1540, 1625, 1710, and 1800 nm; the start, middle, and end of the MR3 band with two intermediate points. Fresnel loss has not been accounted for here, and hence the values are the as-measured transmission efficiencies of the whole prototype grating. The maps have the same colour scale, and the figure shows the efficiency peaking at the central wavelength and reducing at the edge of the band as expected. The maps have been masked in software to remove data at the

edge of the grating where the pencil beam was partly overlapping the grating and partly passing directly through the glass missing the grating. This explains why the measured size of the grating is slightly smaller than what might be expected. A single reference value for each wavelength is used to calculate the transmission.

Of particular interest is the variation in efficiency across the grating surface most pronounced at lower wavelengths, shown on the figure as varying colours. The maps also show contour lines in case the colour is not clear to the reader. The spatial features are consistent in form across the shorter wavelengths, but become less prominent at 1800 nm.

The same data are plotted in Figure 3.11 which makes clear the increase of the variability at lower wavelengths by showing a single line for each 'pixel' of the spatial maps.

Statistics are shown in Table 3.3 including the mean, standard deviation, and peak-to-valley of the transmission efficiency for each wavelength and for different spaxel scales. The values for different spaxel scales are extracted by employing a software mask, shown in Figure A.3 in Appendix A.2.2, that matches an approximation of the expected beam size at each scale, not accounting for slitlet diffraction.

Fresnel loss has not been accounted for here, if it were, all of the values would be meet and exceed the requirement. The interesting parameter peak-to-valley, which shows the maximum minus the minimum value in the masked area, shows a worst case of 15% for the larger beam footprint for 1450 nm and as good as 3% at higher wavelengths. It is important to note that these results show that the mean transmission efficiency of the grating can vary by 2% between different spaxel scales for the same wavelength. However, in theory, if the same peak-to-valley effect of up to 15% were to be spatially distributed differently then the impact on the mean variation between spaxel scales could be much worse than 2%.

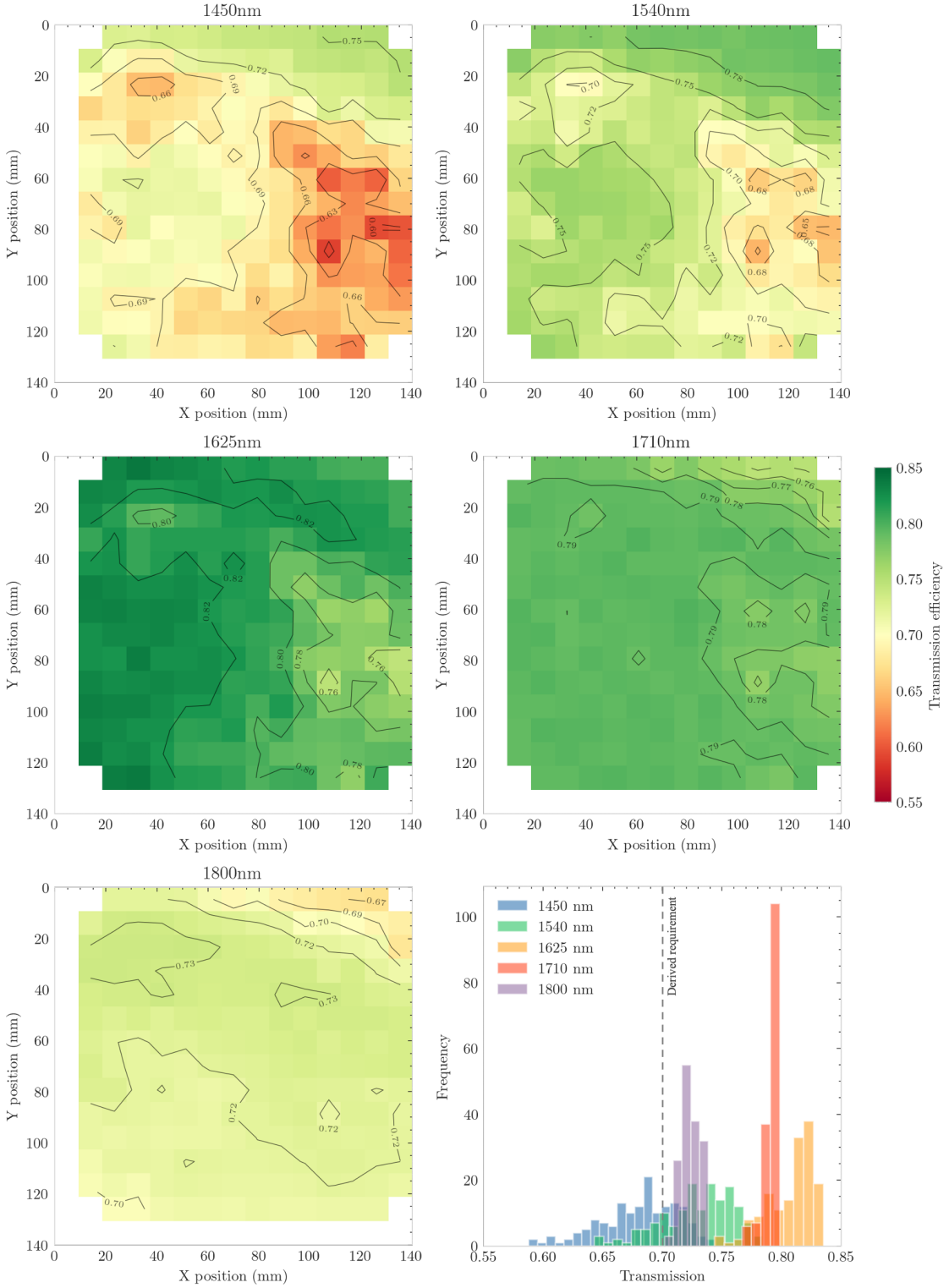


**Figure 3.10:** Maps of transmission efficiency across the MR3 grating 7896-1 for five wavelengths, and a histogram of the data. Fresnel loss has not been accounted for.

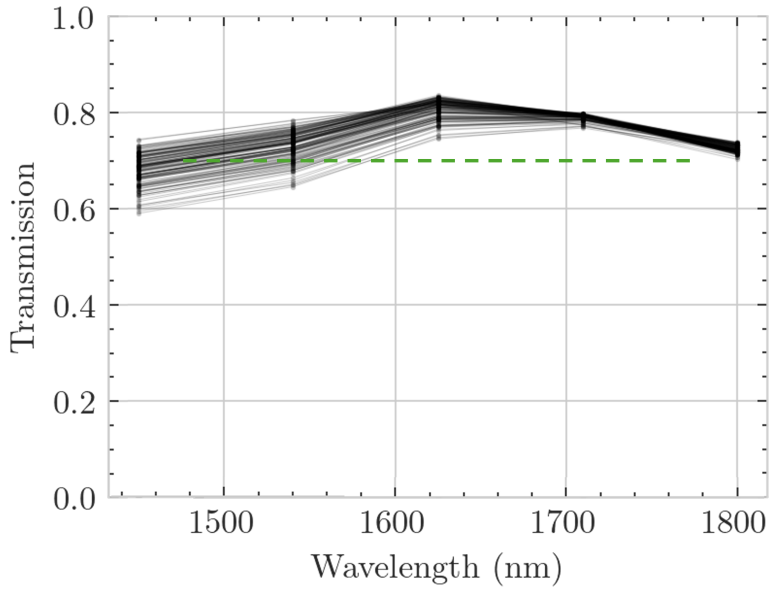


**Figure 3.11:** Spatial spread of transmission for MR3 grating 7896-1. The derived requirement is included at 70% for reference but the Fresnel loss has not been accounted for.

### 3.4.6 LR2 sample

The first grating prototype from the supplier was the small LR2 sample grating, developed early due to the need to prototype the manufacturing process for these low line density gratings, as described in Section 2.2.1.

Figures 3.12 and 3.13 are photographs taken from the inspection upon receipt of the grating. I have formalised an 'incoming inspection' process, described in Appendix A.2.3, for the team to use for all newly arrived optics to ensure delivered optics meet basic specifications and enable traceability.

Physically the grating is made of a holographic DCG layer sandwiched between two 50.8-mm (2-inch) diameter and 3-mm thick UV Fused Silica Corning 7980 substrates. The gelatin layer has a line density of 159 l/mm and a central wavelength of 1950 nm. This grating does not have anti-reflection (AR) coating.

The efficiency of this grating was measured on the first iteration of the test bench, and it allowed us to understand the limitations of that configuration. The results shown in Figure 3.14 are compared with measurements from Wasatch Photonics at three discreet wavelengths, and with two different simulations of performance.

**Table 3.3:** MR3 transmission efficiency statistics for different wavelengths and spaxel scales.

| Wavelength & Scale | Mean | Std Dev | P-V |
|---|---|---|---|
| 1450_60mas | 0.68 | 0.03 | 0.15 |
| 1450_20mas | 0.68 | 0.03 | 0.13 |
| 1450_10mas | 0.70 | 0.01 | 0.04 |
| 1450_04mas | 0.70 | 0.01 | 0.03 |
| 1540_60mas | 0.73 | 0.03 | 0.14 |
| 1540_20mas | 0.73 | 0.03 | 0.12 |
| 1540_10mas | 0.75 | 0.01 | 0.04 |
| 1540_04mas | 0.75 | 0.01 | 0.02 |
| 1625_60mas | 0.81 | 0.02 | 0.09 |
| 1625_20mas | 0.81 | 0.02 | 0.09 |
| 1625_10mas | 0.817 | 0.007 | 0.029 |
| 1625_04mas | 0.817 | 0.005 | 0.017 |
| 1710_60mas | 0.790 | 0.006 | 0.031 |
| 1710_20mas | 0.791 | 0.005 | 0.031 |
| 1710_10mas | 0.793 | 0.002 | 0.009 |
| 1710_04mas | 0.794 | 0.002 | 0.009 |
| 1800_60mas | 0.724 | 0.008 | 0.036 |
| 1800_20mas | 0.725 | 0.007 | 0.024 |
| 1800_10mas | 0.723 | 0.005 | 0.017 |
| 1800_04mas | 0.722 | 0.005 | 0.014 |

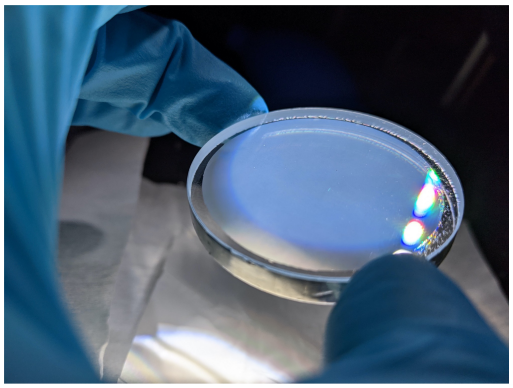

**Figure 3.12:** The small LR2 (H+K band) sample grating.

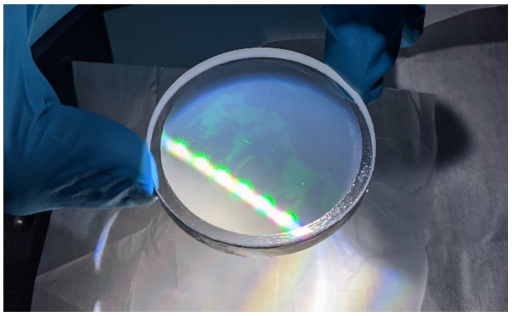

**Figure 3.13:** The small LR2 (H+K band) sample grating, showing some stain features in the gelatin found during inspection.

There is some but limited agreement between these values, and the limiting factor for our measurements is SNR beyond 2000 nm, as seen by the very large error bars. This was a key motivation for the development of the improved test bench as discussed in Section 2.3.2.

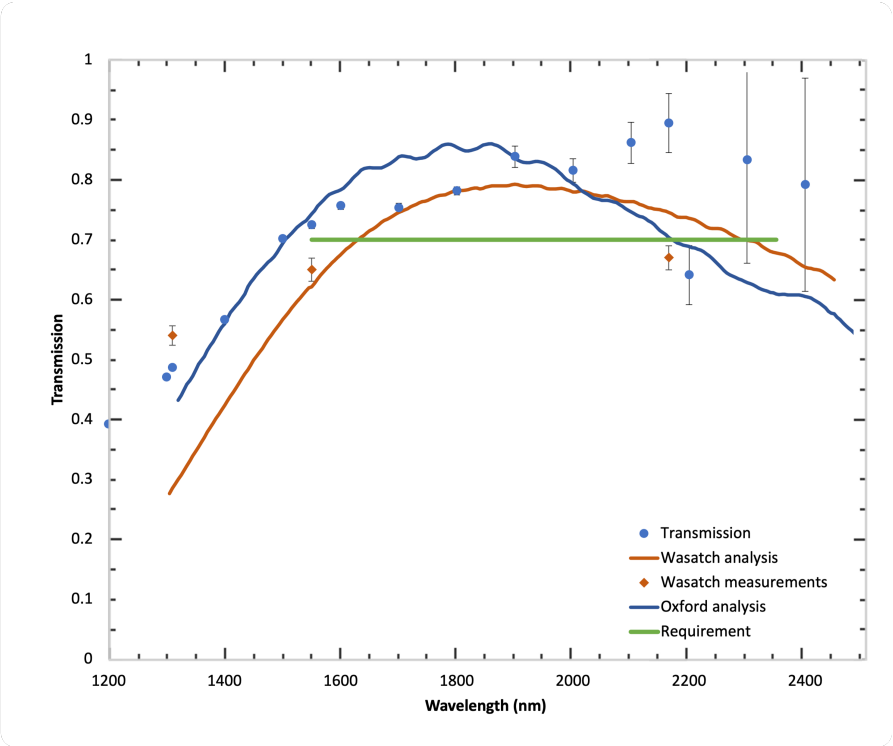


**Figure 3.14:** Sample LR2 grating transmission. Fresnel loss is not accounted for here.

### 3.4.7 LR2 prototype

A first full size prototype of the LR2 (H+K band) grating was delivered in May 2024. Its full specifications are shown in Table 3.4, and it differs from the final HARMONI grating in two ways. The substrate of the final gratings will be Suprasil rather than Corning 7980, and they will be twice as thick. These modifications were chosen for cost and schedule reasons to enable prototyping of the grating manufacturing process to verify that the line density could be achieved with the required efficiency. Due to the material change, we expect the transmission of this prototype to be worse beyond 2000 nm than that of the final grating. The transmission of a 5 mm sample of each of the two different glasses is shown in Figure A.5 in the Appendix for reference. The absorption features seen in the Corning 7980 data are consistent with our results below.

The transmission results are shown in Figure 3.16, once again showing the expected improvement without Fresnel loss, as the final gratings will have AR coatings. The lower-cost substrate used in this prototype causes most of the

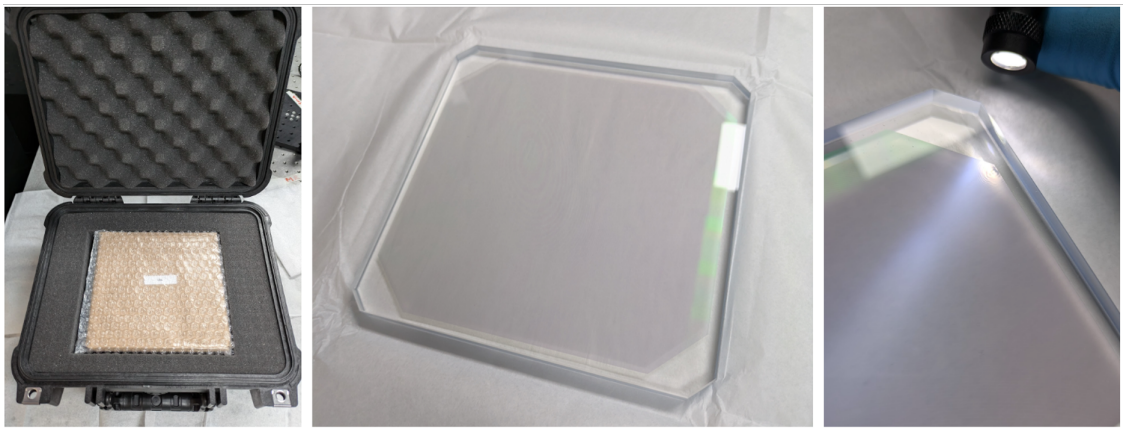

**Figure 3.15:** The full-size LR2 (H+K band) prototype grating, upon delivery (left), during inspection (centre), and a small defect in the grating layer (right).

**Table 3.4:** LR2 prototype VPH grating specifications.

| **Deliverables** | **Specifications** |
|---|---|
| 1st-order efficiency uniformity @ 1950 nm | +/- 7% |
| Spatial frequency | 158.9 +/- 0.5 lppm |
| Wavelength range | 1450-2450 nm |
| Centre wavelength | 1950 nm |
| Size | 160.0 +/- 0.3 × 164.0 +/- 0.2 mm |
| AoI | 6 deg |
| Thickness | 10.0 +/- 0.25 mm |
| Substrate material | UV Fused Silica (Corning 7980) |
| Clear aperture | >150 mm × 154 mm |
| Scratch/dig | 120/80 |
| AR coating | None |
| Grating lines | Perpendicular to long edge |
| Wavefront (in waves @ 633nm) | >3 PV; >1.5 RMS |
| Adhesive | Sylgard 184 |

significant transmission dip at 2100 to 2300 nm, as shown in Figure A.5. It is clear this grating has a lower performance than the MR3 and is much closer to the derived requirement. The laser + monochromator combination results in a low SNR beyond 2200 nm and so the error bars grow substantially.

The spatial variation measurements were repeated with the same method as the MR3 grating, with the results presented here in a similar fashion. Figure 3.17 shows clearly that there is a different spatial pattern than the MR3 grating. It appears to show a vertical gradient, however, as shown in Figure 3.18 which is

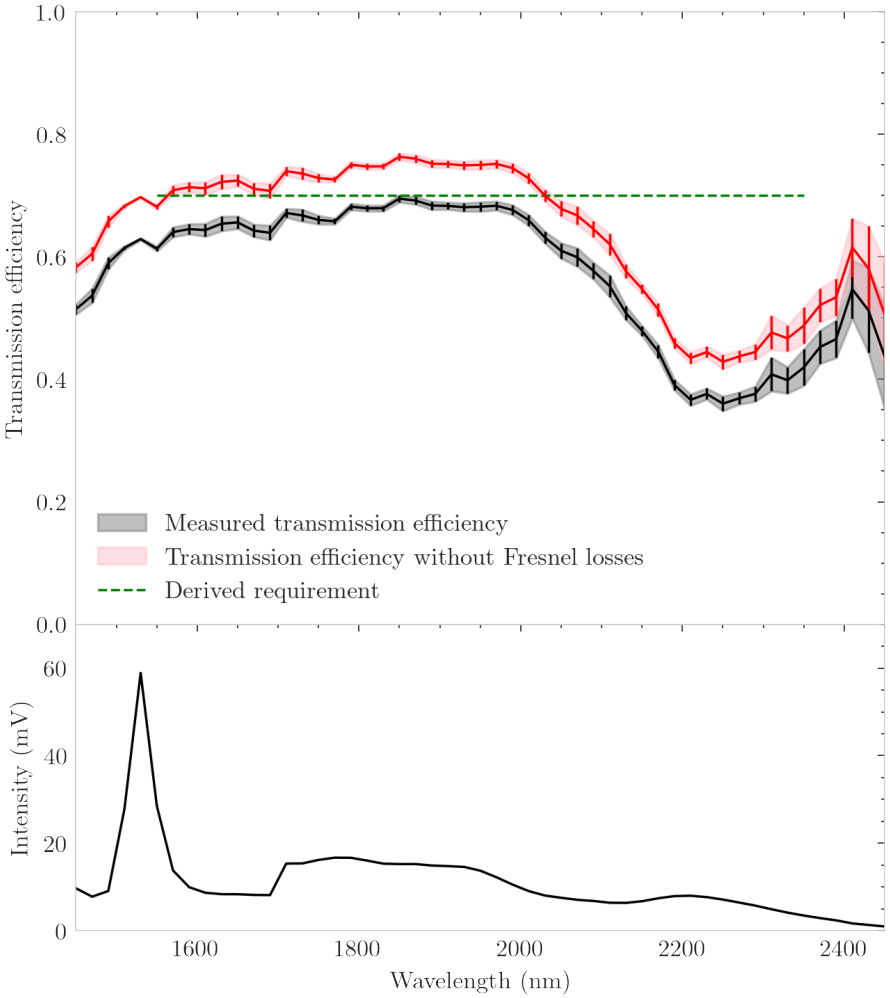


**Figure 3.16:** Transmission of the LR2 (H+K band) prototype grating. The lower subplot, as per Figure 3.9, shows here the low signal intensity beyond 2200 nm resulting in high measurement uncertainty.

coloured by row (blue to green from top to bottom of the 2D scan), this gradient flips direction between 1450 and 1700 nm. The uniformity tightens up at 1950 and 2200 nm as one might expect, however, the low SNR at 2450 nm prevents us from a clear understanding of the spatial variations here.

The statistics in Table 3.5 show the results for the LR2 prototype and that it exhibits a mean efficiency variation between spaxel scales of around 1%, slightly better than the MR3. Also the peak-to-valley is improved, except for the 2450nm possibly due to the SNR being low because of the bulk transmission of the alternative substrate.

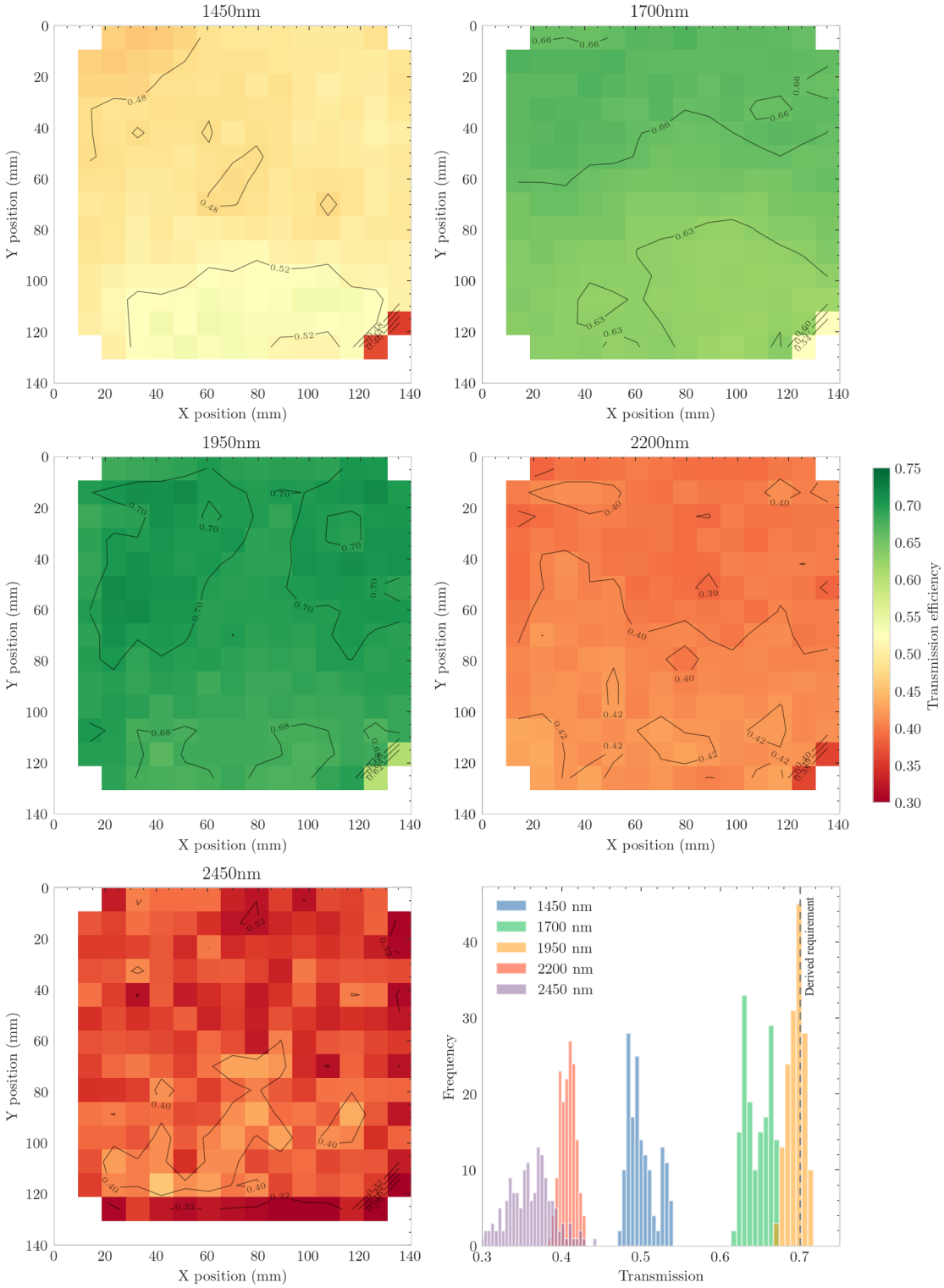


**Figure 3.17:** Maps of transmission efficiency across the LR2 grating. The derived requirement at 70% is shown in the histogram for reference, but Fresnel loss has not been accounted for.

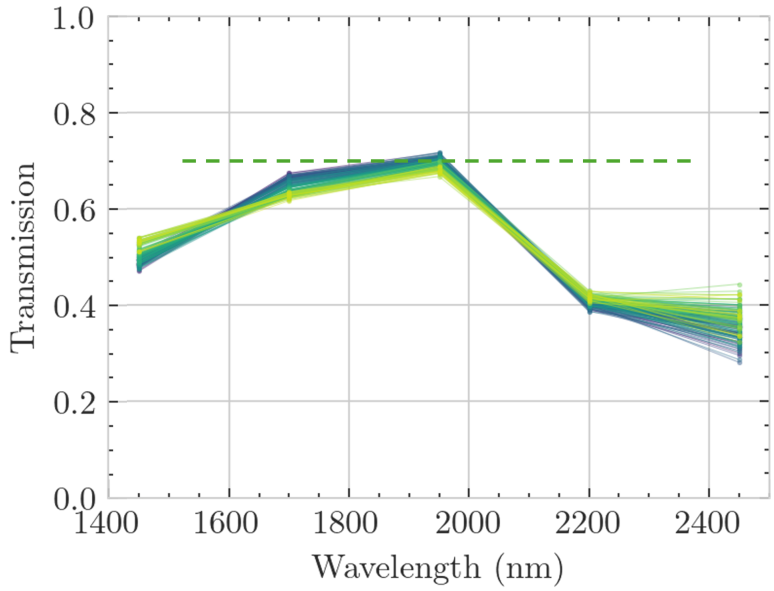


**Figure 3.18:** Spatial spread of transmission for LR2 grating, coloured by row (blue to green from top to bottom of the 2D scan). The derived requirement at 70% is shown for reference, but Fresnel loss has not been accounted for.

**Table 3.5:** LR2 transmission efficiency statistics for different wavelengths and spaxel scales.

| Wavelength & Scale | Mean | Std Dev | P-V |
|---|---|---|---|
| 1450_60mas | 0.50 | 0.02 | 0.07 |
| 1450_20mas | 0.50 | 0.02 | 0.06 |
| 1450_10mas | 0.49 | 0.01 | 0.04 |
| 1450_04mas | 0.486 | 0.009 | 0.027 |
| 1700_60mas | 0.65 | 0.02 | 0.06 |
| 1700_20mas | 0.64 | 0.01 | 0.05 |
| 1700_10mas | 0.64 | 0.01 | 0.03 |
| 1700_04mas | 0.639 | 0.007 | 0.019 |
| 1950_60mas | 0.69 | 0.01 | 0.05 |
| 1950_20mas | 0.69 | 0.009 | 0.04 |
| 1950_10mas | 0.695 | 0.005 | 0.024 |
| 1950_04mas | 0.695 | 0.003 | 0.011 |
| 2200_60mas | 0.407 | 0.009 | 0.044 |
| 2200_20mas | 0.407 | 0.009 | 0.040 |
| 2200_10mas | 0.405 | 0.007 | 0.026 |
| 2200_04mas | 0.404 | 0.005 | 0.013 |
| 2450_60mas | 0.36 | 0.03 | 0.16 |
| 2450_20mas | 0.36 | 0.03 | 0.15 |
| 2450_10mas | 0.36 | 0.02 | 0.08 |
| 2450_04mas | 0.36 | 0.01 | 0.05 |

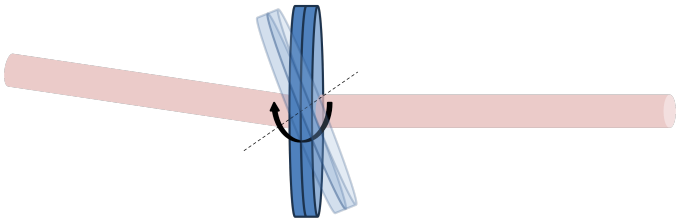

**Figure 3.19:** The LR2 sample grating is rotated up to 12 degrees about the x-axis (parallel to the diffraction plane, and hence orthogonal to grating lines). The beam is entering from the right, and the first order diffracted path is shown to the left.

### 3.4.8 Off-axis transmission

The grating equation, shown on Equation 1.2, describes a diffraction grating with a plane wave incident at an angle $\theta_i$ in the orthogonal plane to the grating grooves. In a more general case whereby light can be incident off this plane, the diffraction effect is described by:

$$d(\sin\theta_i + \sin\theta_m) = \frac{m\lambda}{\sin\gamma}, \tag{3.10}$$

where $\gamma$ is the angle between the grating normal and the incident light plane: this is known as conical diffraction.

An experiment was devised to understand if the transmission from an off-axis incident beam is degraded. The small circular LR2 sample grating was mounted to a mechanical rotation stage which enabled rotation of the grating about the x-axis, parallel with the diffraction plane. Figure 3.19 shows how the grating is rotated with respect to the incoming beam. Angular rotation steps were made and transmission across the wavelength band was measured.

The results in Figure 3.20 show the transmission across the LR2 (H+K) band for a grating titled backwards about the x-axis. The experiment was quickly aligned so the absolute values may be a little lower than expected, however, the important parameter to note is the relative difference between the measurements. Fresnel loss is not accounted for here. The plot, alongside Figure 3.21 of the residuals, shows no discernable relationship between angle and efficiency. A dip is shown at around 2200 nm which corresponds with an absorption line in the material, and

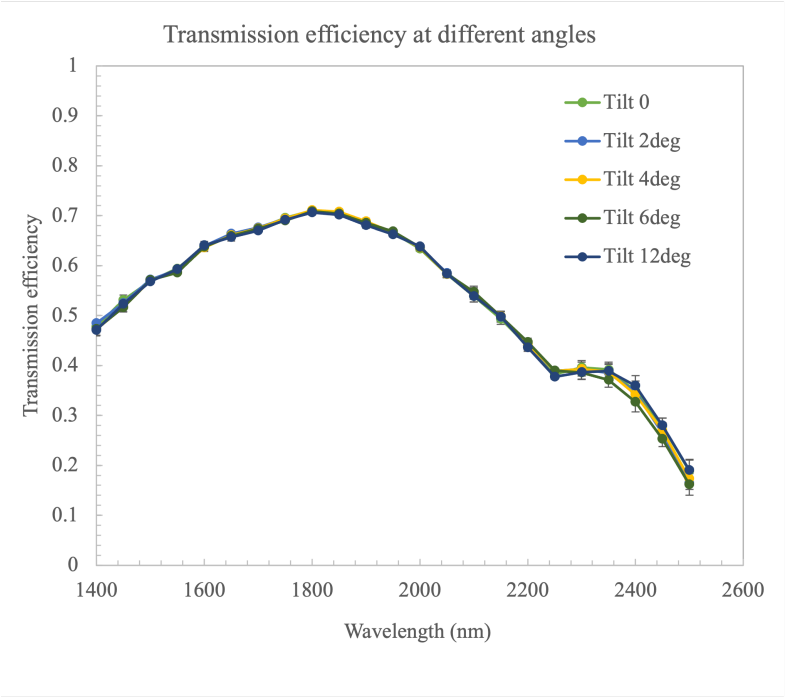


**Figure 3.20:** Off-axis transmission measurements of the LR2 sample grating.

some variations in the results appear beyond this point which can be put down to low SNR. The test was repeated by tilting the grating forward, with similar results.

From this, we can conclude that there is no measurable impact on transmission efficiency at different conical angles.

### 3.4.9 Spatial variations in efficiency

Spatial variations in the transmission efficiency of VPH gratings can be attributed to a range of factors. Non-uniformity in the refractive index modulation ($\Delta n$) across a grating surface may result from inconsistencies in the holographic recording process. These inconsistencies can include uneven exposure to the recording light or variations in the chemical composition of the photosensitive material. Similarly, variations in the thickness of the grating layer can alter the interaction strength between the incident light and the grating, leading to spatial differences in efficiency.

Another significant factor is the periodicity of the grating. If the grating period, $\Lambda$, varies across the surface, the local Bragg condition is altered, causing shifts in efficiency at specific wavelengths or angles of incidence. The substrate and surface

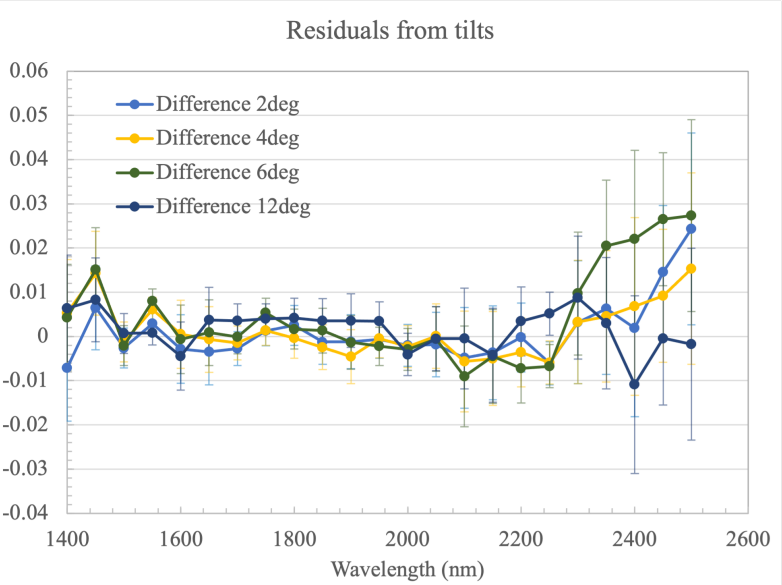


**Figure 3.21:** The residuals of subtracting the nominal on-axis transmission from each off-axis transmission measurement.

quality can also contribute to efficiency variations. Unevenness in the substrate or the grating surface can distort the wavefront of the incident light, reducing the diffraction efficiency in affected areas. Additionally, localised defects like those found during inspection (see Figure 3.15), such as air bubbles, dust particles, or scratches, may scatter or absorb light, resulting in localised efficiency losses.

The fabrication process itself can introduce spatial variations in efficiency. Misalignment of the recording beams during the holographic recording process or warping of the grating can lead to angular misalignments that vary the Bragg condition across the surface. Post-fabrication factors, such as contamination or uneven coatings, may also contribute to spatial inconsistencies.

### 3.4.10 Comparison with wavefront error

The full-size prototypes were also used to measure the as-built WFE performance[2] (in the test bench shown in Figure 2.19) and to understand the impact on WFE of bonding and cooling to 130 K [3]. One of the MR3 prototype gratings was

[2]These measurements were carried out by HARMONI team member Elliot Meyer[72].

[3]These WFE measurements were taken at room temperature before and after cooling the grating, and at time of writing a new test bench is being developed to measure the WFE whilst the grating is held at 130 K.

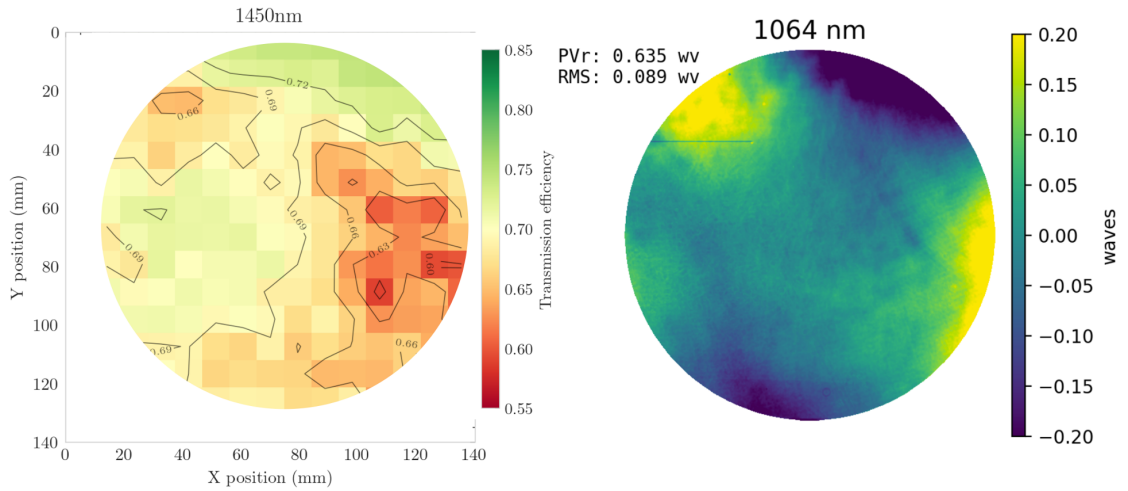


**Figure 3.22:** Comparison of WFE (right) with spatial variations of transmission efficiency (left) for MR3.

also measured for WFE before and after the use of a fine polishing technique called magneto-rheological finishing (MRF). This technique uses a magnetically sensitive fluid that can quickly change viscosity when exposed to a magnetic field and so can be used to make very fine adjustments to a surface quality based on interferometer measurements.

Meyer et al. (2024)[72] present WFE measurements of the same MR3 grating as this study. Whilst WFE and efficiency have been measured for different reasons, the uniquely detailed spatial efficiency maps allow us to compare the two. WFE is ususally dominated by the form of the glass which does not have an appreciable impact on the efficiency so there was not expected to be a correlation. Figure 3.22 shows the transmission variations at 1450 nm and the WFE at 1064 nm side by side. The different wavelengths are due to the available laser wavelength in the interferometer (an AccuFiz Infrared Wavelength Fizeau Interferometer) and the nearest wavelength in the grating band. Both measurements were taken after MRF polishing of the outer surface. The WFE is measured as peak-to-valley (PV) and root-mean-square (RMS) in wavelength units, in our case 1064 nm.

WFE of this grating was measured and then improved significantly by the MRF polishing. The source of the remaining WFE is not explicitly known as it is likely a combination of small contributing factors. However, being able to compare it

with spatial variations in diffraction efficiency for the first time may shed some light on this. Diffraction efficiency variations are not considered to originate from very minor geometric deformations in the glass substrate, unlike WFE. However, they could originate from sources which cause non-trivial variations in refractive index or transmission efficiency, such as gelatin thickness, line spacing non-uniformity, and index modulation. There appears to be a strong correlation in the patterns produced which leads us to believe that they have major contributors in common, perhaps dominated by the non-uniformity of gelatin thickness. It is therefore possible that improving this will improve both parameters. Now that the manufacturers have this data, it may be possible to further improve the performance of the gratings with both a lower WFE and a more uniform efficiency.

The WFE was also measured for the LR2 prototype grating with the same test bench. In Figure 3.23 we compare the results with the efficiency map at 1450 nm once again. The WFE plot shows clearly that the amount of surface error is significantly higher for this grating than for the MR3, this is because it has not been polished, unlike the MR3. The peak-to-valley WFE of 8.9 waves at 1064 nm will therefore be largely dominated by the substrate surface error that has not been removed through polishing; as a result, it is difficult to conclude anything with regards to the gelatine layer-induced WFE and compare with spatial variations in efficiency despite there being an apparent vertical gradient in both.

## 3.5 Discussion and conclusions

This section summarises the chapter, explores some lessons learnt during the research, and discusses its implications.

### 3.5.1 Chapter summary

This chapter has showcased the diffracted transmission efficiency measurements from a newly developed test bench, covering both small and full-size VPH gratings designed for HARMONI. Early validation measurements of the COTS grating

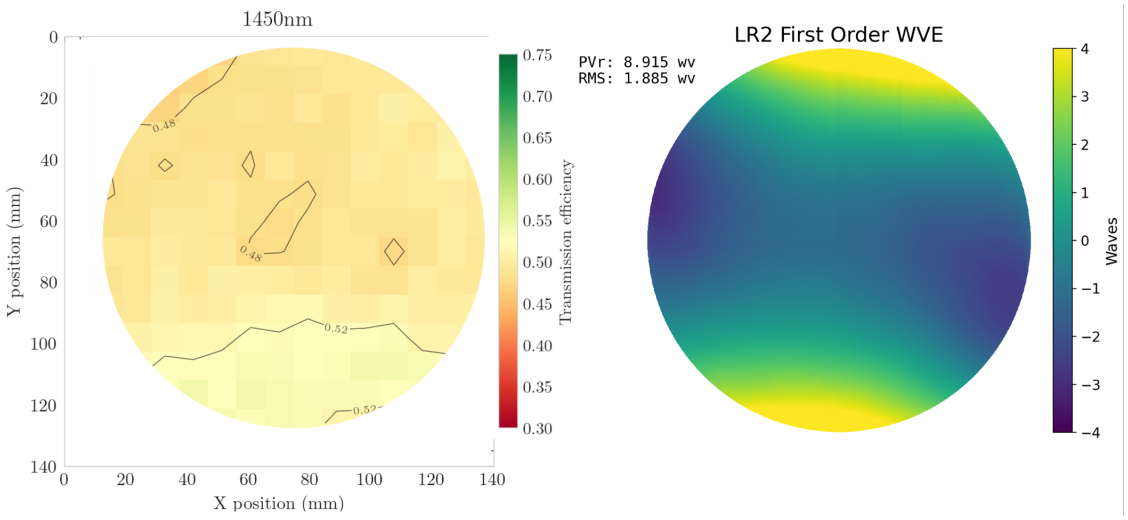


**Figure 3.23:** Comparison of WFE with spatial variations on transmission efficiency for LR2. The WFE was once again measured at 1064nm. The colour bar on the right panel shows that the WFE is an order of magnitude worse than for the fine polished MR3 grating.

established that the system could capture transmission efficiency curves within the MR2 band.

Full-size prototypes (MR3 and LR2) then underwent thorough testing, which included one-dimensional scans of diffracted transmission across each grating's wavelength range, highlighting peak transmission at or near the design wavelength, and two-dimensional spatial mapping, revealing where localised non-uniformities in refractive index, layer thickness, and/or defects could affect diffraction efficiency.

An off-axis study on the small LR2 grating was performed indicating negligible change in transmission for conical angles up to 12 degrees.

Sources of systematic and statistical errors were discussed in detail, confirming that the setup is primarily shot-noise limited in typical operating conditions. Additional investigations compared measured wavefront errors in the prototype gratings to their spatial efficiency maps, suggesting that common fabrication factors can influence both the uniformity of the refractive index modulation and the surface figure.

These results demonstrate that the test bench can provide the repeatable measurements needed to qualify each HARMONI VPH grating and identify any

variations in performance well before final instrument integration.

### 3.5.2 Lessons learnt

Several key insights have emerged from the grating prototyping and testing campaign:

- **Measurement accuracy and repeatability:** The blank grating data showed that the test bench can reliably measure transmission to within 1%. Close monitoring of alignment, reference signals, and calibration is essential to maintain accuracy.

- **Spatial mapping value:** Two-dimensional scans of large-format gratings highlight the importance of monitoring efficiency across the entire active area. Local variations in the grating layer, substrate, and/or even assembly methods can all affect the performance in different regions of the optics.

- **Fabrication and finishing impacts:** Comparisons between wavefront error maps and efficiency distributions suggest shared root causes—such as non-uniform layer thickness or refractive index modulation—affecting both optical quality and diffraction efficiency. Additional fine polishing can mitigate surface-related errors, although deeper material inhomogeneities remain.

- **Adapting for different designs:** The procedure worked equally well for low and medium resolution gratings, underlining the test bench's flexibility. Minor adjustments in alignment and test protocol suffice to handle a range of line densities and substrate thicknesses.

- **Future scalability:** High-automation methods proved vital for consistent data collection and will facilitate upcoming measurements on all HARMONI gratings. The ability to characterise multiple prototypes efficiently is crucial for iterative design feedback and final acceptance testing.

These lessons will guide further refinements of the test bench and the ongoing fabrication of VPH gratings for HARMONI, helping to ensure that transmission requirements and uniformity targets are met across the instrument's operating band.

### 3.5.3 Implications

We have presented a new VPH grating transmission efficiency test bench for the HARMONI spectrograph. Absolute diffracted transmission efficiency results and spatial variations have been shown for two full-size prototype gratings: a medium resolution H-band grating, and a low resolution H+K-band grating.

The test bench in its final form is suitable to determine if the manufactured VPH gratings meet the transmission efficiency requirement as part of the acceptance testing and provide robust characterisation appropriate for further analysis and use in the instrument data processing pipeline, and also for highlighting manufacturing defects. The prototype MR3 (H-band) grating has been shown to meet and exceed the requirement for all spaxel scales. The LR2 prototype results suggest the final grating can meet the requirement once AR coatings are applied and the final substrate is used; including lessons learnt in the manufacturing process from the non-compliant sample grating. As identified at the instrument PDR, the LR2 grating was the most at-risk in terms of meeting the requirement, so the progress here gives confidence that all gratings will be compliant.

It has been shown that there is some correlation between the diffracted transmission efficiency and the diffracted wavefront error. Meyer et al. (2024)[72] concludes that the remaining WFE after fine polishing *"is the result of a phase effect arising from the construction of the DCG layer, aberrations in the hologram itself, or a combination of these factors"*. This study goes a step further and is able to link this with the spatial variations of the efficiency, strengthening the argument that the origin of these effects is in the DCG layer. It shows, for the first time, the uniformity limitations of the current manufacturing processes and will help the supplier (Wasatch Photonics) to further improve the performance for increasingly demanding future applications.

Transmission efficiency variations with wavelength and spatial variations will be characterised with this method for all HARMONI VPH gratings over the coming 12-24 months as the project enters its manufacturing phase. Assuming one per day, taking into account alignment and data analysis, these measurements are expected to take a minimum of two calendar months (many months faster than without automation), although likely spread out considering delivery schedules.

The test bench is theoretically grating agnostic, and so could be used for characterising transmission gratings of any size and shape from 0.7 to 2.5 $\mu$m for future projects. The automation makes measurements fast and reliable.

# 4

# On the detection of IMBHs in star clusters with E-ELT/HARMONI

## Contents

## 4.1 Introduction

This chapter presents the HARMONI observation simulation work to study the instrument's potential effectiveness in detecting an IMBH in the centre of a star cluster and explore optimal instrument settings and needs for bespoke analysis tools specific to this science case.

This section (4.1) explains the motivations for performing these simulations for the HARMONI instrument, introduces star clusters (open and globular) as potential hosts for IMBHs, and reintroduces IMBHs. Further explanation of the origins and evolution of such black holes is found in Chapter 1.6.

Section 4.2 explains how an observation of a star cluster can be simulated for an instrument that is yet to be built and details the methodology adopted in this study. Section 4.3 describes the data analysis process to determine the line-of-sight velocities of observable stars from the simulated as-observed datacube, the critical step to begin to understand the kinematics of the system.

Section 4.4 assesses the kinematics derived from the extracted velocities and what can be learnt from them. Finally, Section 4.5 concludes by discussing the work and its implications.

### 4.1.1 Motivations for simulations of HARMONI observations

The booming global astronomy and astrophysics community compete for observing time on the world's largest telescopes, and so strong science cases are required to justify their selection. Computer simulations of astronomical telescopes and instrumentation have become useful tools to assess the capability, in theory, of the technology to perform certain scientific observations. It is now common practice

to assess the feasibility of a successful observing campaign by running numerical models of increasing complexity to build the case.

Instrument simulators range in complexity from simple exposure time calculators and point spread function (PSF) estimations to sophisticated software pipelines factoring in detailed instrumental nuances.

In addition to helping secure observing time, simulations provide a risk mitigation tool for expensive and resource-intensive observing campaigns. By evaluating the feasibility and potential limitations of proposed observations, scientists can anticipate challenges such as poor signal-to-noise ratios, crowding within stellar fields, or atmospheric conditions that may hinder successful data acquisition. Simulations allow for optimising observing strategies, such as selecting appropriate filters or bands, setting exposure times, or fine-tuning the telescope pointing, thereby increasing the likelihood of achieving the desired scientific outcomes. They can also help understand the constraints imposed by observing conditions such as atmospheric turbulence, elevation angle, and moonlight contamination.

The E-ELT and its instruments take many years to design, build, and get on sky; during this time many simulations are being conducted in preparation to understand the capabilities and assess the feasibility of specific science cases[1].

In our case, these simulations help determine the scientific reach of HARMONI for probing the dynamics of complex stellar systems. The presence of an IMBH in a dense cluster will exert gravitational forces that influence the stellar velocities, creating distinctive kinematic signatures. With HARMONI's ability to provide high angular resolution integral field spectroscopy, we have the opportunity to detect these signatures by mapping the velocity dispersion as a function of radial distance from the cluster's centre. Simulating such observations allows us to understand how accurately HARMONI will be able to detect these subtle signatures amidst the noise and complexities inherent in crowded fields.

This work also serves to establish the potential of using HARMONI to bridge the observational gap between stellar-mass black holes and SMBHs by seeking

[1]This is a continually evolving body of work, the foundations of which can be found on the ESO website `https://www.eso.org/sci/facilities/eelt/science/doc/`.

evidence of IMBHs. As IMBHs are hypothesized to play a critical role in the growth of SMBHs, confirming their presence in nearby star clusters would be a significant milestone in understanding black hole formation and the evolution of galaxies. These simulations lay the groundwork for creating an effective observational approach, contributing directly to the construction of a strong scientific argument for dedicated observing time on the E-ELT.

### 4.1.2 Star clusters

Star clusters are gravitationally bound collections of stars that form and evolve together. They are broadly divided into two main categories: open clusters and globular clusters. Despite their differences in structure, density, and age, both types of clusters are potential hosts for IMBHs, making them intriguing targets in the search for such objects.

Open clusters and globular clusters represent two distinct evolutionary paths for star groups, with open clusters typically young and sparse, while globular clusters are generally old and densely packed.

#### Open clusters

Open clusters are relatively young ($10^6$ to $10^8$ years), loosely bound groups of stars that form within the disk of galaxies. These clusters contain anywhere from a few dozen to several thousand stars and hence typically have total masses between $10^2$ and $10^4 M_\odot$. Open clusters are formed from giant molecular clouds and often disperse over hundreds of millions of years as their stars drift away due to gravitational interactions with nearby objects and internal stellar motions, with tidal forces being important for the disruption of such clusters.

Open clusters are most commonly found in the spiral arms of galaxies, including the Milky Way, where active star formation is ongoing. Famous examples include the Pleiades and the Hyades in our own galaxy, which are visible to the naked eye. These clusters tend to have relatively low stellar densities compared to globular

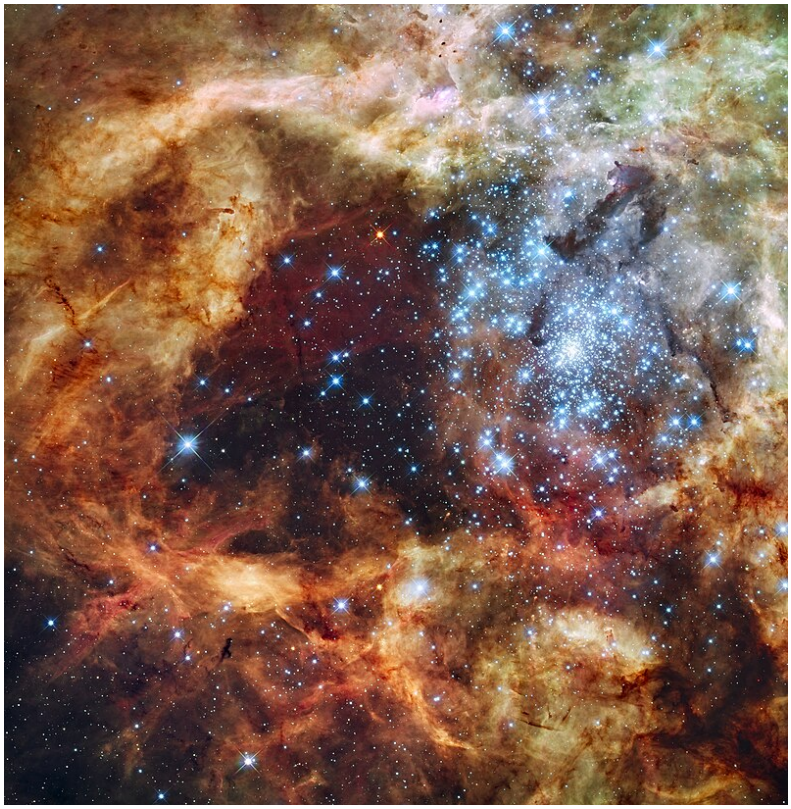

**Figure 4.1:** A famous HST image of an open cluster, R136, illuminating the Tarantula Nebula (credit: NASA).

clusters, which allows for individual stars to be more easily resolved and studied. Figure 4.1 shows an example of an open cluster.

Due to their young age and the proximity of many open clusters, they serve as ideal laboratories for studying the early stages of stellar evolution and the initial mass function (IMF)[2]. The comparatively low-density environment of open clusters also presents a unique opportunity to study the influence of IMBHs in a dynamical regime different from that found in globular clusters. Open clusters offer a complementary perspective in the search for IMBHs, potentially shedding light on the formation pathways and dynamical evolution of these elusive objects.

In the southern sky lies the Large Magellanic Cloud (LMC) inside of which is the Tarantula Nebula (also known as 30 Doradus). This nebula contains the star cluster NGC 2070, the centre of which is R136. Shown in Figure 4.1, this object is a potential

[2]The IMF is a statistical function that describes the distribution of stellar masses in a star-forming region.

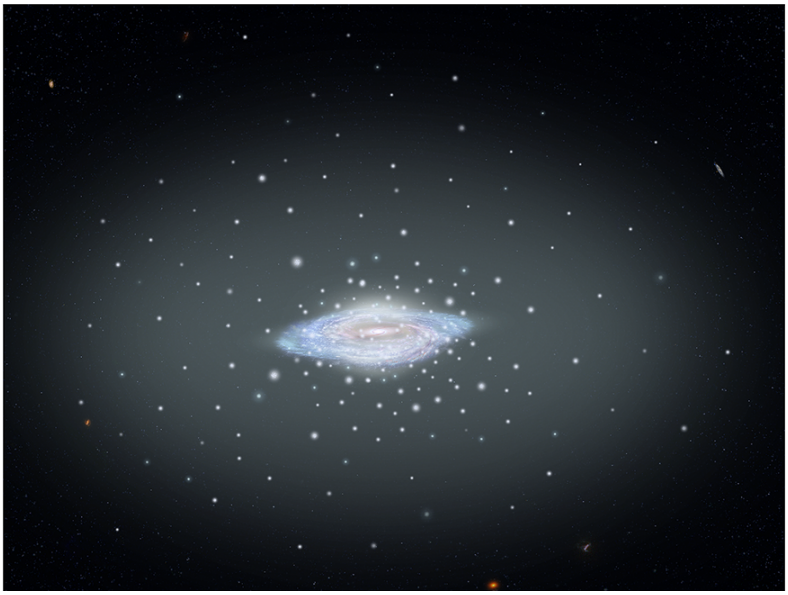

**Figure 4.2:** An artist's impression of globular clusters around the Milky Way galaxy (credit: NASA).

IMBH host and the subject of many studies [56][83]. It is also the inspiration for the N-body simulation used in this study, as introduced in Section 4.2.1.

### Globular clusters

Globular clusters are densely packed, spheroidal groups of stars that are gravitationally bound and generally much older than open clusters ($10 - 12 \times 10^{10}$ years old). They range in mass from $10^3$ to more than $10^6 M_\odot$ and are typically found orbiting in the halos of spiral galaxies, including our own Milky Way [70]. There are more than 150 known globular clusters within the halo of the Milky Way, an artist's impression of which is shown in Figure 4.2. Other galaxies, such as Andromeda, host even larger populations of globular clusters, with over 300 identified. Elliptical galaxies, too, can harbour significant numbers, as demonstrated by M87, which has a remarkable population of around 15,000 globular clusters.

As some of the oldest structures in the Universe, globular clusters provide a unique window into the conditions of the early Universe and the processes that governed galaxy formation. Their ancient stellar populations, with ages often exceeding 10 billion years, make them invaluable for studying stellar evolution, chemical enrichment, and the dynamics of tightly bound star systems. The dense

cores of globular clusters are of particular interest, as their high stellar densities increase the likelihood of interactions between stars, which could foster the formation and retention of IMBHs.

Globular clusters, therefore, serve as important astrophysical laboratories, not only for understanding stellar and galactic evolution but also as prime candidates in the search for IMBHs [67]. The presence of IMBHs in these clusters, if confirmed, would have significant implications for our understanding of black hole formation and the dynamical evolution of dense stellar environments.

### 4.1.3 IMBHs

IMBHs are theorised to exist with masses ranging from 100 to 100,000 times that of the Sun, filling the gap between stellar-mass black holes and the SMBHs that lurk at the centres of galaxies. Despite their pivotal role in the hierarchical growth models of SMBHs and their importance in understanding the continuum of black hole masses [103][44], IMBHs remain elusive, with few candidates identified to date.

The search for IMBHs in open and globular clusters not only advances our understanding of black hole demographics across the mass spectrum but also sheds light on the processes governing star cluster dynamics, the fate of massive stars, and the intricate dance of gravitational interactions that shape the Universe [30, 68].

ELTs, as introduced in Section 1.3, will be able to provide unprecedented deep observations of individual stars in open and globular clusters. In particular, IFSs, such as HARMONI, performing resolved spectroscopy will be able to probe the stellar dynamics towards the cores of these objects for the first time. Whilst an imager on an ELT, such as MICADO, will be able to assess the proper motions[3] of these stars with multiple measurements over several years, an IFS will be able to determine the line-of-sight velocities[4] with a single observation. Thus, it is a powerful tool to detect the kinematic signatures of resident IMBHs.

[3]Proper motions of stars refer to their apparent angular movement across the sky relative to distant background objects, as seen from Earth, typically measured in arcseconds per year.

[4]Line-of-sight velocities refer to the component of an object's motion along the line of sight relative to an observer, such as on Earth. It measures how fast an object is moving toward or away from the observer and is typically expressed in kilometres per second (km/s).

### 4.1.4 Stellar kinematics

Stellar kinematics involves studying the movement of stars within a system, such as a star cluster, to derive key insights about its internal structure and gravitational influences. One of the key parameters used in stellar kinematics is velocity dispersion, which represents the spread in velocities of stars in a given region of the cluster. Higher velocity dispersion indicates a wider range of star speeds, which can point to complex gravitational interactions.

In the context of detecting IMBHs, stellar kinematics plays a pivotal role. By measuring the velocities of stars and identifying patterns or deviations, we can infer the presence of a central massive object exerting gravitational influence [41]. For instance, a rapid increase in velocity dispersion towards a cluster's core can be a signature of a central black hole [67].

Using HARMONI, we can extract the line-of-sight velocities of a large number of individual stars in the same field, and from these derive the velocity dispersion of that population of stars. These kinematic measurements, when mapped spatially, reveal the dynamical state of the cluster, including rotation, dispersion, and deviations due to gravitational influences like an IMBH. By combining these observations with advanced modelling, we can discriminate between different mass distributions and assess the presence of an IMBH at the cluster's core.

#### E-ELT and HARMONI

Introduced in Section 1.3, HARMONI is an IFS currently being built for the E-ELT and will be on sky in the coming years.

HARMONI is a highly capable AO-assisted instrument with a range of different operating modes. Four different spaxel scales are available with corresponding changes in field of view, and 10 different NIR bands with varying spectral resolution.

Important to this science case is the combination of AO-enabled high angular resolution integral field spectroscopy and the large telescope collecting area providing extreme sensitivity. This telescope and instrument combination will provide the best view we have ever had of the internal kinematics of star clusters and similar

objects. The majority of the kinematic signature (shown later in Section 4.4.2) of the IMBH in our simulations is within 1 arcsec of the cluster centre which will be uniquely achievable with this instrument. Figure 5 of Watkins et al. (2015) [105] shows results for HST data of 47 Tucanae which is limited to 8 arcsec from the centre and Kamann et al. (2018) [55] shows results for MUSE data which probes slightly deeper to 4-5 arcsec. Both of these struggle to measure the kinematics within that vital central arcsec radius which leaves room for improvement by a larger more capable instrument. Figure 2 of Kızıltan et al. (2017) [59] presents results the 47 Tuc data alongside some simulations of velocity dispersion of different mass ratios of a central IMBH and shows that, like our simulations, that the central arcsec is important for detecting IMBH kinematic signatures. This angle is of course dependent on the distance of the object from earth and the mass of the black hole (sphere of influence), but these cases provide us with a useful scale for reference.

With the E-ELT and HARMONI, we anticipate the discovery and characterisation of IMBHs residing in star clusters, the effectiveness of such observations is the subject of study in this chapter.

## 4.2 Observation simulation

To simulate an observation of a theoretical star cluster with and without a central black hole by an instrument on a telescope which has not yet been built, we need a number of different inputs.

Firstly, a dynamically representative model of the cluster is required. We make use of an N-body simulation [38] produced by the MICADO instrument science team which was created with the aim of conducting a similar study using proper motions measured with separate observations over a 5-year time period. We instead will investigate using instantaneous line-of-sight velocities in a single observation. This study and the resulting N-body simulation are described in detail in Section 4.2.1.

Secondly, we need representative stellar spectra (simulated or otherwise) which can be appropriately prepared and assigned to each star in the cluster. A number of

libraries are available, and this selection and preparation process is described in Section 4.2.2.

Thirdly, and finally, we need a numerical model known as an instrument simulator to prepare the final 'as-observed' datacube. The HARMONI instrument simulator, HSIM [110], is described in Section 4.2.4.

Combining these different elements requires careful handling of the data, ensuring flux/magnitude scaling, correct spatial and spectral sampling, coordinate consistency, and preservation of dynamical parameters such as redshift. Another important element to consider is the observing strategy that would be adopted in reality. The telescope and instrument combination imposes limitations on individual observations such as field of view, band pass, and angular resolution which can be traded off against each other.

To create the raw datacube for the instrument simulator, detect sources, extract the spectra, determine the line-of-sight velocities, and perform the kinematic analysis a lot of Python software has been written[5]. A summary of the key programmes and their lengths is provided in Table 4.1. A description of each module/function for the first programme `'create_marcs_datacube.py'`, as an example, is given in the Appendix in Table A.1.

### 4.2.1 N-body simulation

This study focuses on the young star cluster R136, which is part of the 30-Doradus region (Tarantula nebula) within the LMC which is 50 kpc away from Earth. This type of object is interesting for scientific cases of ELTs because their high resolutions allow us to probe deep inside the cluster and constrain kinematics in unprecedented detail to characterise the dynamics.

Our research uses the foundation established by prior direct N-body simulations modelling a star cluster *analogous* to R136, as described in Section 2 of Fiorentino et al. (2020) [38]. A sample of the data is shown in Table 4.2, and the full dataset (for one case) is represented in histogram form in Figure 4.3. The velocities are given

[5]The repository for the code can be found at `https://github.com/DavidJonGooding/harmoni-imbh/`.

**Table 4.1:** The Python scripts and their purposes.

| Filename | Purpose | Lines |
|---|---|---|
| `create_marcs_datacube.py` | Builds raw datacube with MARCS spectra using MICADO N-Body simulation data. | 720 |
| `harmoni_source_extractor.py` | Finds source locations using DAOPHOT routine in as-observed datacubes. Also, conditions datacube ready for Pampelmuse if required. | 551 |
| `catextract.py` | Alternative to above, extracts the spectra based on the catalogue positions. Skips DAOPHOT. | 331 |
| `harmoni_losv.py` | Get LOSVs for each sources, this uses pPXF routines. | 517 |
| `vdispersion.py` | Calculates $\sigma$ and plots dispersion profiles. | 448 |
| `imbh_master.py` | Can be used to run all other routines automatically, requires configuration file 'imbh-config.json' | 52 |

relative to the cluster with zero systematic velocity, however the X/Y positions are given relative to an approximate cluster centre which needs to be determined more precisely. There is no appreciable bulk rotation or anisotropic velocity dispersion and so the impact of projection effects and viewing angle is therefore limited especially since the analysis focuses on the inner region of the cluster. The analysis in this paper focuses on two distinct models of the R136-like cluster; one featuring a central IMBH with a mass of $10^4$ $M_\odot$ and another without it. Both configurations simulate 100,000 stars, adhering to a Kroupa mass function [61] spanning masses from 0.1 to 150 $M_\odot$, resulting in an initial cluster mass of approximately 60,000 $M_\odot$.

The resulting IMBH-to-cluster mass ratio of 1:6 is large compared to typical expectations, where ratios are usually in the range of 0.1–1% for dynamically plausible IMBH formation scenarios. However, Fiorentino et al. (2020) explicitly adopt this high mass ratio as a deliberate upper-limit case to evaluate the astrometric capabilities of ELT-class instruments under favourable conditions. Their aim was not to reproduce a physically typical cluster, but rather to assess whether a strong

**Table 4.2:** A small sample of the input data provided by the N-body model. Each star in the simulation has an assigned mass (in solar masses), age (in Myr), and four near-infrared magnitudes (I, J, H, K), given in the 2MASS Vega-based system. From the N-body kinematic simulation, we obtain each star's projected (x, y) position (in arcseconds) and line-of-sight velocity (in $\mathrm{km\,s^{-1}}$).

| mass ($M_\odot$) | X1 (arcsec) | Y1 (arcsec) | I1 (mag) | J1 (mag) | H1 (mag) | K1 (mag) | vr ($\mathrm{km\,s^{-1}}$) |
|---|---|---|---|---|---|---|---|
| 5.1011 | 0.201123 | -0.172421 | 18.263 | 18.519 | 18.597 | 18.659 | 2.068092 |
| 0.1099 | 0.734276 | -1.811833 | 26.555 | 24.642 | 24.089 | 23.714 | 4.622326 |
| 0.2157 | -2.777314 | 4.866406 | 25.704 | 24.072 | 23.483 | 23.168 | -3.901217 |
| 0.3283 | -0.194277 | -1.729290 | 25.098 | 23.646 | 23.013 | 22.739 | 10.154643 |
| 0.1877 | 0.486192 | -0.003597 | 25.900 | 24.203 | 23.625 | 23.295 | 2.976947 |

dynamical signature from a massive central object could be recovered in crowded-field proper motion measurements. As they note, a $10^4$ $M_\odot$ IMBH in a cluster of this size lies at the upper theoretical bounds of formation via runaway stellar collisions or successive black hole mergers, and serves as a benchmark to test detectability thresholds for future observations.

The cluster model is started from virial equilibrium[6] is evolved over 3 million years (each star is assigned age 3 Myr in the N-body data). While the MICADO science team recognised the significant role of stellar evolution and binary systems in cluster dynamics, these factors were not included in these simulations.

Although the simulation timescale of 3 Myr is short compared to the cluster's two-body relaxation time, some early dynamical processes can still take place, particularly in the dense central regions. The simulations allow for the formation of binaries dynamically (despite excluding primordial binaries), and adopt a small softening length ($\approx$4 $\mathrm{R_\odot}$) to permit close gravitational encounters. As noted by Fiorentino et al. (2020), this setup enables modest central dynamical evolution, such as the onset of mass segregation and gravitational interactions that may concentrate massive stars and black holes toward the core. These effects, while limited in scope over such a brief timescale, contribute to shaping the kinematic signature

[6]Virial equilibrium is the state of a system of gravitationally interacting particles where the system is stable and does not expand or collapse.

of the IMBH and ensure that the resulting models are dynamically plausible for testing ELT-era astrometric capabilities.

Figure 4.4 shows the running average of the LOSV[7] of each of the two cases with increasing radial distance from the centre of the cluster.

It is important to note that this N-body simulation is not meant to be a direct representation of the R136 system, but an analogous system of a similar scale at the same distance. Whilst R136 is considered an open cluster, our simulation shares characteristics of both open (age and distance) and globular (mass and spheroidal form) clusters.

The spatial and velocity distributions of the stars at the outset are determined by a King [57] distribution, featuring a central dimensionless potential of $W_0 = 9.0$ and a core radius of 0.10 pc, yielding an initial half-mass radius of 2.9 pc.

The central dimensionless potential, $W_0$, is a measure of the depth of the potential well at the centre of the cluster normalised by the velocity dispersion squared. It is a key parameter that describes the concentration of the cluster. A higher value of $W_0$ indicates a deeper potential well, which corresponds to a more concentrated cluster.

**Implication of $W_0$=9.0** A value of $W_0$=9.0 suggests a significantly concentrated cluster with a dense core. This means that the gravitational potential at the centre is deep, leading to a high central density of stars. Clusters with high $W_0$ values are more centrally condensed, and the transition from the core to the halo (less dense area) is sharper compared to clusters with lower $W_0$ values.

The core radius, $r_c$, is the scale length that characterises the size of the central, nearly uniform-density region of the cluster. Technically, it is defined as the radius at which the surface brightness falls to half its central value in the case of a projected density profile.

[7]The LOSV is also sometimes referred to as radial velocity as in this plot, but not generally used in this thesis to avoid confusion between this and the velocity of stars radially from the cluster centre

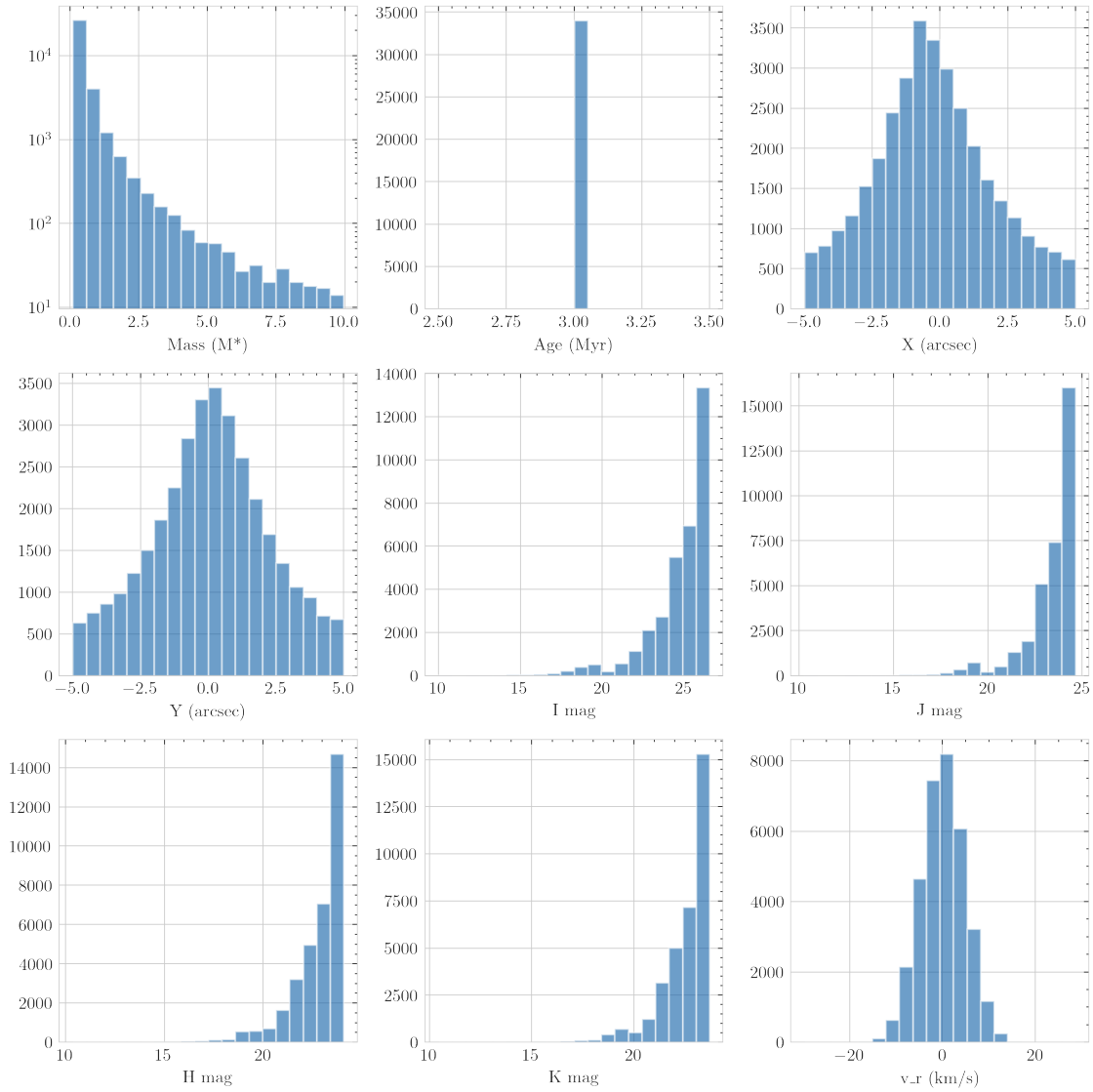


**Figure 4.3:** Histograms of the input data as provided as model data from the N-body simulation.

**Implication of $r_c$=0.10 pc** A core radius of 0.10 pc indicates a relatively small core region, suggesting that the cluster's central density remains high over a compact area. In practical terms, this small core radius, combined with a high $W_0$, points to a cluster that is both highly concentrated and has a sharply defined central region compared to its outer regions.

Stellar evolution, not expected to affect velocity profiles, is not accounted for in this model. The goal of the N-body simulations is to assess the feasibility of the E-ELT detecting an IMBH in a massive young star cluster, not to produce

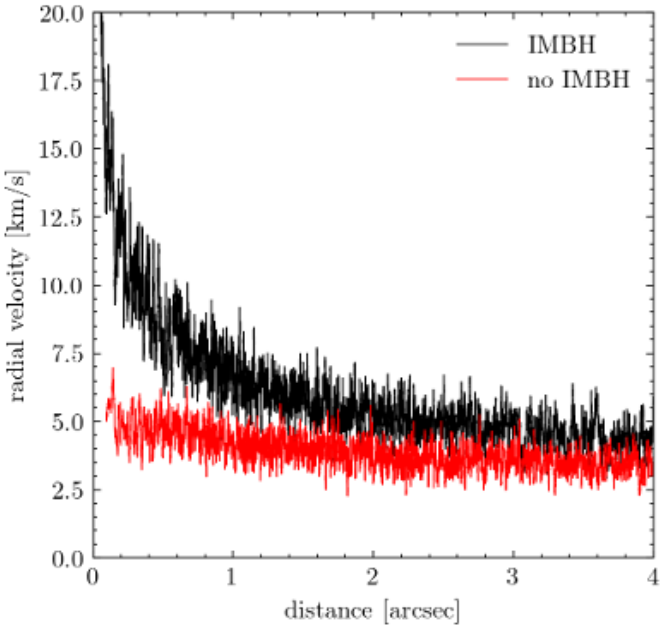


**Figure 4.4:** The running mean of the N-body cluster line-of-sight velocity in the presence (black) or not (red) of an IMBH in the cluster centre. The running mean is calculated in bins of 40 stars moving outwards from the cluster centre.

a perfect simulation of the object itself.

Our target object, R136 in the LMC, is at a distance of $d = 50\,\mathrm{kpc}$, where a physical distance of 1 pc is equivalent to 4.125 arcsec on the sky. Therefore, the data shown in Figure 4.4 encompass the central 1 pc in radius of the cluster.

A central black hole of mass $10^4\ M_\odot$ would, using Equation 1.11 in Chapter 1.6, have a sphere of influence of about 1 parsec, corresponding to 4 arcsec at the distance of the target.

### Raw data

The data provided by the MICADO team from this N-body simulation is a $5 \times 5$ arcsec snapshot for two scenarios: with and without the central IMBH present. 33,037 stars (33,989 for the without-IMBH case), out of the 100,000 from the model, are found within this field of view. This is within a physical volume of about 2.5 parsecs across: for scale that would mean thousands of stars within the volume of our solar system's Oort cloud (0.6 parsecs), highlighting the high number density of this stellar cluster.

A sample of the data can be seen in Table 4.2, and histograms of the parameters are in Figure 4.3. These figures show the case where the IMBH is present.

Figure 4.4, which can be directly compared to Figure 1 of Fiorentino et al. (2020)[38] using proper motions, shows how the line-of-sight velocity changes in the two scenarios. The key identifying kinematic signature of the central IMBH is clear to see as the velocities increase towards the cluster centre.

### 4.2.2 Synthetic spectra

A stellar spectrum is required to be associated with each N-body source in order to correctly represent the spectral dimension of the observed IFS data cube. The spectrum needs to be high resolution, across a broad band, and have relevant stellar characteristics for our model. Libraries of measured and synthetic spectra exist for this purpose. Table 4.3 lists a number of these libraries with their key parameters compared to our requirements, these were investigated to find an appropriate match for this work and to future proof the simulation software development to be expanded to include many spectra from the same library. The requirement of $R = 7500$[8] is a minimum as that is the spectral resolution of the medium resolution bands (including the chosen H-band) of HARMONI. In this context, $\sigma$ is the line broadening in the spectral library: a smaller value, and hence less broadening, is better for our use case. $\sigma$ and $R$ are directly related, whereby $\Delta\lambda \approx= \text{FWHM} = 2.35 \times \sigma$. Oversampling is required, as explained in Section 4.2.3 where the raw spectrum given to the instrument simulator[9] has a higher fidelity that than of the selected grating, so ideally the input spectrum would have a high resolution.

For HARMONI, the full NIR wavelength range spans from around 9000 to 24500 Å, so this limits the number of applicable libraries, in this study we focus on the H-band and so our current requirements are for coverage from 14000 to 18500 Å.

[8]Resolving power $R \equiv \lambda/\Delta\lambda$ is a dimensionless quantity indicating how well a spectrograph can distinguish between two closely spaced wavelengths. A higher $R$ means the instrument can resolve finer details in the spectrum.

[9]The HSIM instructions state that: "*it is recommended to oversample the spectral dimension of the input cube by a factor of 4 with respect to the nominal resolving power (R) of the selected grating*"[110]

**Table 4.3:** A list of spectral libraries (measured and synthetic) compared to the spectral requirements.

| **Parameter** | **No. of objects** | **R** | **$\lambda$ range (Å)** | **$\sigma$ (km/s)** |
|---|---|---|---|---|
| *Requirements* | *>10* | *>7500* | *14000-18500* | |
| Indo-U.S. Coude Feed Spectral Library [101] | 1273 | 4200 | 3460-9464 | 30 |
| MILES Library [27] | 985 | 2000 | 3525-7500 | 64 |
| MILES Ca II triplet library [85] | 706 | 5700 | 8348-9020 | 22 |
| ELODIE [79] | 1388 | 10000 | 4000-6800 | 13 |
| MaNGA Stellar Library (MaStar) [109] | 10000 | 1800 | 3622-10354 | 70 |
| X-Shooter Spectral Library [102] | 683 | 10000 | 3000-24500 | 13 |
| GNIRS library of late spectral templates [107] | 40 | 6600 | 21800-24300 | 19 |
| MARCS synthetic library [46] | 52000 | 20000 | 1300-200000 | 6.4 |
| SYNTHE synthetic library [74] | 20000 | 20000 | 2500-10500 | 6.4 |

The MARCS library [46] contains many different spectra for a range of conditions, such as metallicity and temperature, over a large band and with high resolution. This library is chosen over the X-Shooter library due to its larger dataset as future proofing for follow on work requiring many different spectra. The data are available to users via an online portal where one can choose a range of parameters such as effective temperature, metallicity ([Fe/H][10]), and specific model type.

The mean mass of the N-body model stars is 0.67 $M_{\odot}$, which on the main sequence is a G-type star, so for a single representative spectrum, 5000 K was chosen. This decision is based on catalogue mass vs temperature data [25] as shown in Figure 4.5. A more robust approach would involve assigning a different representative spectrum to each star, however, for simplicity in this case we have chosen a single spectrum to be used throughout the datacube as this was not deemed to be a critical factor in the study at the time[11].

[10]Metallicity, when expressed as [Fe/H], is a logarithmic measure of the abundance of iron (Fe) relative to hydrogen (H) in a star compared to the Sun. It provides an estimate of how "metal-rich" or "metal-poor" a star is, where "metals" in astronomical terms refer to all elements heavier than helium.

[11]The focus of the study was to assess the capability of spatially resolved spectroscopy in the

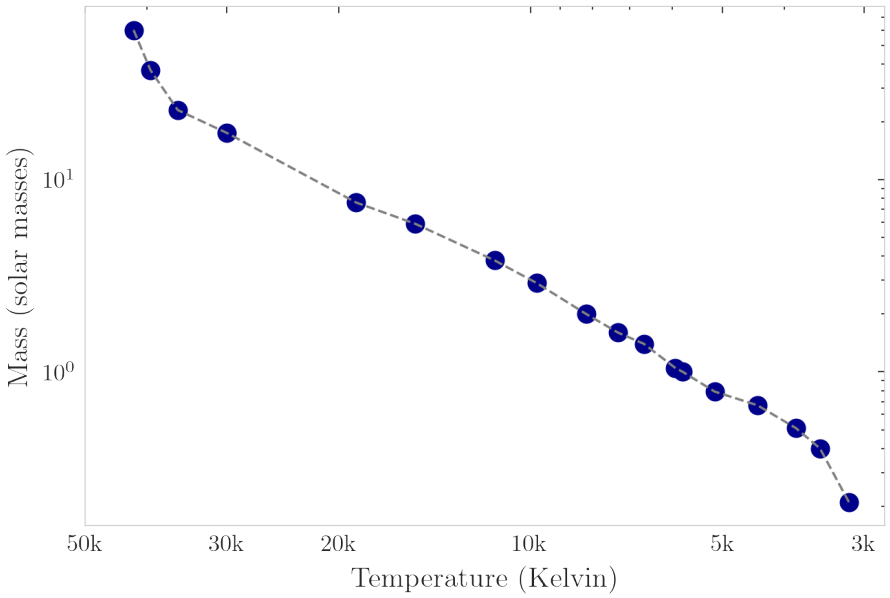


**Figure 4.5:** Mass vs temperature of main sequence stars [25].

From MARCS we take a spectrum with representative characteristics, the H-band of which is shown in Figure 4.6. The two key characteristics chosen are:

- **Temperature = 5000 K** as explained above.
- **Metallicity = -0.25** [Fe/H] as the nearest option to the −0.35 as defined by the N-body model paper [38].

The library provides spectra across a very broad band of 130-20,000 nm, whereas HARMONI covers approximately 800-2500 nm. The H-band, chosen in this study, covers 1400-1850 nm, just a small subset of the available data.

### 4.2.3 Datacube construction

The datacube is fundamentally composed of a 3D array of numbers representing pixel values, along with associated metadata in the form of header information, which provides essential context for interpreting the data.

The 3D array is initially created as a large array of zeroes. Spectra are then added to this array, where the $x$ and $y$ axes correspond to the angular field of view

star cluster rather than a robust attempt to understand the limitations imposed by different star types.

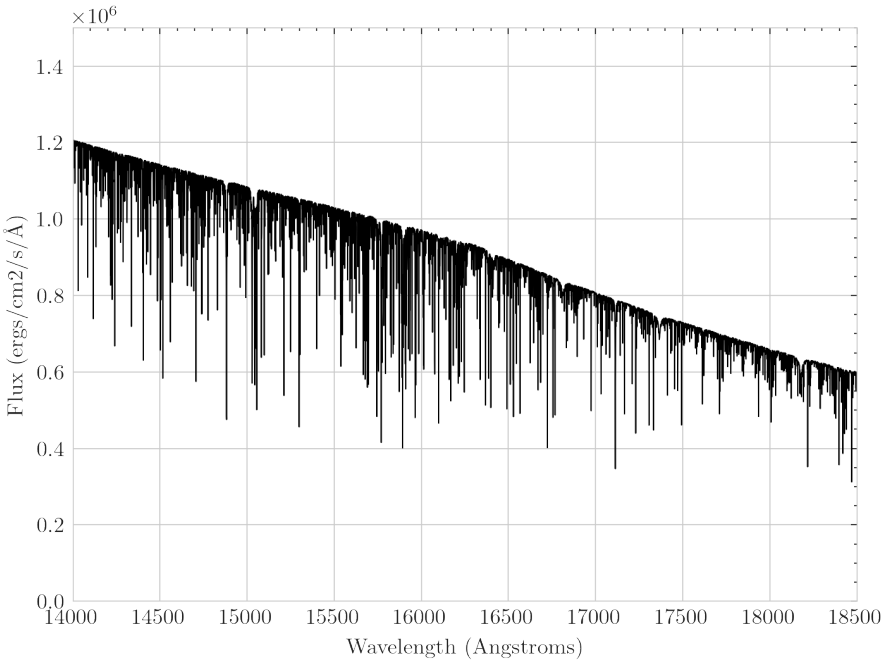


**Figure 4.6:** The H-band of the chosen synthetic spectrum from the MARCS library.

of the observation, and the $z$-axis represents the spectral dimension. To ensure the accuracy of the simulation, the input 'raw' datacube is constructed with a higher sampling than the expected output cube, a process known as oversampling.

Oversampling the input datacube is essential for accurately modelling the effects of the telescope, optics, and atmosphere on the observed data. Spatially, oversampling prevents the positions of features in the field of view from being rounded to the size of a spaxel, thereby preserving precise positional information. Spectrally, oversampling ensures that, during convolution with the instrument's line spread function (LSF)[12], the spectrum is adequately sampled to avoid introducing artefacts or misrepresenting velocity features.

HSIM deals with the spectral axis in the following way. If we take for example an infinitesimally sharp emission or absorption line (delta function), the instrument's observed data cube will have a spectral width for that line that is exactly the LSF width of the instrument, by definition[13]. Therefore when we specify the SPECRES parameter to HSIM (as defined in Table 4.4), it assumes that this delta

[12]The LSF of a spectrograph is the spectral response of the instrument to a delta function, in this case, a theoretical infinitely narrow spectral line.

[13]In our case the HARMONI LSF is Gaussian with a FWHM of 2.138 Å.

function was observed with some other instrument to create the input cube, and that instrument had an LSF width given by SPECRES. To account for this, it subtracts, in quadrature, the SPECRES width from HARMONI's LSF width, and applies that function as the spectral convolution function. This is so that the delta function line from the sky source will come out with width = LSF width, as expected.

The sampling therefore needs to be at least Nyquist for the input spectrum, and as the input spectrum is higher resolution (smaller width) than the HARMONI LSF, this automatically provides sufficient sampling for the input cube spectrally.

By resolving both spatial and spectral details effectively, oversampling helps to ensure the fidelity of the simulated data.

Furthermore, oversampling supports a more accurate application of the PSF (spatial axes) and atmospheric effects (spectral axis) including both absorption and emission. By maintaining high sampling throughout the input datacube, the simulator can better replicate real observational conditions and ensure robust results.

**Header information**

The FITS header plays a critical role in providing metadata that describes the structure and content of the data contained in a FITS file. It acts as a blueprint that defines how the data should be interpreted, including information about the dimensions of the data cube, the physical units, and any calibration details. By including the header, users and software tools can accurately understand and process the data without requiring additional information. The header is composed of key-value pairs that are both human-readable and machine-readable, ensuring that the data are self-describing and easily transportable across different systems.

Table 4.4 provides an overview of the FITS header keywords used in the creation of the data cube. Each keyword is described with its corresponding unit and a brief explanation of its purpose.

An example of the header information from one of the output HSIM datacubes is shown in the appendix in Figure A.7.

**Table 4.4:** Explanation of FITS header keywords.

| **Header Name** | **Unit** | **Description** |
|---|---|---|
| SIMPLE | – | Indicates whether the file conforms to the FITS standard (True or False). |
| BITPIX | – | The number of bits per data value; -32 indicates 32-bit floating-point. |
| NAXIS | – | The number of data axes in the data cube (in this case, 3 axes). |
| NAXIS1 | pixels | The size of the first axis (spatial x-dimension). |
| NAXIS2 | pixels | The size of the second axis (spatial y-dimension). |
| NAXIS3 | pixels | The size of the third axis (spectral or wavelength dimension). |
| CRPIX1 | pixels | Reference pixel along the x-axis. |
| CRPIX2 | pixels | Reference pixel along the y-axis. |
| CRPIX3 | pixels | Reference pixel along the wavelength axis (usually set to 1). |
| CRVAL1 | milliarcsecond (mas) | World coordinate (e.g. RA or x-position) at the reference pixel along the x-axis. |
| CRVAL2 | milliarcsecond (mas) | World coordinate (e.g. Dec or y-position) at the reference pixel along the y-axis. |
| CRVAL3 | angstrom | Wavelength value at the reference pixel. |
| CDELT1 | milliarcsecond (mas) | Pixel size in arcseconds for the x-dimension. |
| CDELT2 | milliarcsecond (mas) | Pixel size in arcseconds for the y-dimension. |
| CDELT3 | angstrom | Wavelength increment per pixel along the spectral axis. |
| CUNIT1 | – | The unit of the first spatial axis, determines the units of CRVAL1 and CDELT1. |
| CUNIT2 | – | The unit of the second spatial axis, determines the units of CRVAL2 and CDELT2. |
| CUNIT3 | – | The unit of the spectral axis (e.g. microns), determines the units of CRVAL3 and CDELT3. |
| CTYPE1 | – | The label for the first axis (spatial x-dimension). |
| CTYPE2 | – | The label for the second axis (spatial y-dimension). |
| CTYPE3 | – | The label for the third axis (wavelength). |
| BUNIT | erg/s/cm$^2$/Å/arcsec$^2$ | The physical unit of the data values (flux per wavelength per area). |
| SPECRES | – | The spectral resolution, defined as the central wavelength divided by the resolving power. |

### Spatial dimensions

The 10 mas spaxel scale of HARMONI is chosen to balance spatial sampling and sensitivity, a single observation of which will cover approximately 1.5"×2", so a 2"×2" window is chosen in these simulations for simplicity. Oversampling by a minimum factor of 2 results in a cube with 400×400 spatial pixels.

The spatial resolution of an observation is the smallest angular separation between two objects that can be distinguished as separate, determined by the PSF of the telescope + instrument system. Spatial sampling however describes how finely the detector samples the image — i.e., the angular size per detector pixel or spaxel (spatial pixel). To avoid information loss, the spatial sampling should typically be at least twice as fine as the spatial resolution; known as the Nyquist criterion. The HSIM output states the instrument PSF as 4.71 mas for the parameters selected in this study, and so 10 mas is appropriate.

The pixel locations of the stars are given by the N-body data in units of arcsec from -5 to +5. This full population of stars is then windowed by the required field of view, $-2 < x < +2$. To convert these into useful units for addressing pixel locations in the input datacube, the origin is moved to the bottom left and they are rescaled.

### Spectral dimensions

The MARCS library provides spectra logarithmically sampled in wavelength, as is common with similar libraries. This log-wavelength sampling corresponds to constant velocity intervals, and is therefore equivalent to maintaining a constant spectral resolving power, R.

The wavelength axis needs to be 4× oversampled to ensure spectral information is retained when convolving with the instrument LSF [110]. HARMONI samples the wavelength in the medium resolution H-band is ≈1.04 Å, so a suitable step size for the raw cube is $\approx 1.04/4 = 0.26$ Å.

The H-band is from 14350 to 18150 Å, resulting in 14618 pixels in the z-axis.

### Magnitude scaling

Each source is assigned an apparent magnitude in the broad band filters of I, J, H, and K. These magnitudes are not reddened, meaning that the extinction caused by interstellar dust has not been accounted for. This is because it is not deemed to be a crucial factor impacting this study and its omission aids simplicity. The effect of including an extinction coefficient would be to slightly reduce the magnitude of the stars, and as dust scatters blue light more strongly than red, the wavelength dependency of extinction would also redden these magnitudes.

An absolute magnitude, $M$, translates to an apparent magnitude, $m$, at the distance to the LMC in parsecs, $d$, by the relationship

$$m - M = 5\log_{10}(d) - 5. \tag{4.1}$$

The formula to calculate the difference in apparent magnitude between two stars with intensities $I_1$ and $I_2$ is given by:

$$m_1 - m_2 = -2.5\log_{10}\left(\frac{I_1}{I_2}\right). \tag{4.2}$$

To scale each source by its magnitude we first calculate the flux of the template spectrum within a defined band. We choose the H-band and for this context, we make use of the 2MASS H-band filter [29] as shown in Figure 4.7. We then calculate the magnitude of this spectrum using Equation 4.2 and the flux of Vega. A magnitude difference between this initial spectrum magnitude and the required magnitude is calculated. Then this is used to enable scaling of the input spectrum to match the target magnitude.

### Redshift

A critically important step is to redshift each individual spectrum by the required amount due to the line-of-sight velocity of the star.

There are two components to consider here; the group velocity of the cluster, and the star's individual velocity within that group as the provided velocities are centred about zero, and therefore in the reference frame of the cluster.

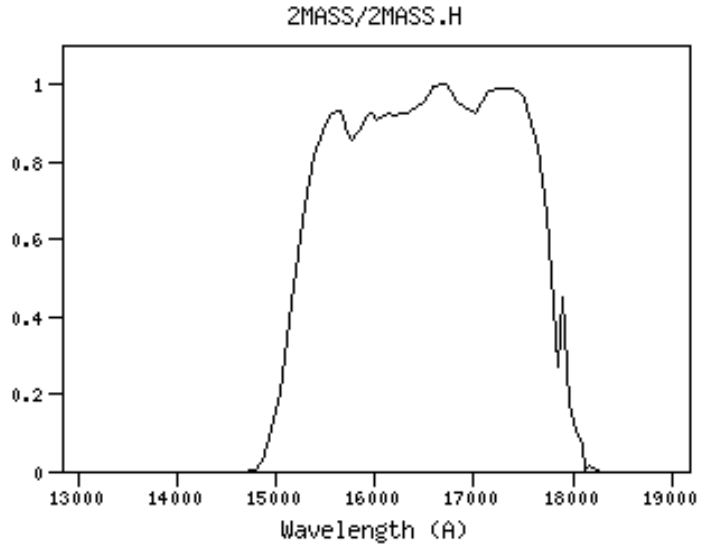


**Figure 4.7:** Filter response curve for the 2MASS H-band (credit: SVO).

The group redshift of the LMC which hosts R136 is $z = 0.00093$. Given the redshift of the LMC as $z_{\rm LMC}$ and the line-of-sight velocity of the star relative to the LMC as $v_{\rm star}$, the total redshift combining both contributions can be calculated using the formula:

$$z_{\rm total} = (1 + z_{\rm LMC}) \cdot \left(1 + \frac{v_{\rm star}}{c}\right) - 1. \tag{4.3}$$

The array of wavelength values is then multiplied by $(1 + z_{\rm total})$ to stretch it by the required amount.

### Spectrum rebinning, scaling, and placement

Before assigning the spectrum to the desired spaxel we rebin the spectrum to get the sampling expected by the simulator, HSIM. This is where the log spectrum is scaled to match the HSIM linear wavelength sampling.

The rebinning of the spectrum is achieved using linear interpolation. In this process, the original spectrum, which consists of flux values at specific wavelengths, is interpolated onto a new set of wavelengths with the desired sampling. This allows the spectrum to be represented with a constant spectral sampling across all wavelength points.

It is also at this stage where we convert the spectrum from units of ergs/cm$^2$/s/Å to erg/s/cm$^2$/Å/arcsec$^2$ by accounting for the angular resolution. This step is required because HSIM works with surface brightness, which is expressed as flux per unit area on the sky (arcsec$^2$).

For a point source, such as a star (effectively a delta function in spatial extent), the light is concentrated into a single point rather than spread over a spaxel. To interface correctly with HSIM, the light of the point source must first be distributed spatially over a spaxel, with the flux normalised to reflect the corresponding surface brightness. This involves spreading the flux over the spaxel area, effectively converting the total flux into a surface brightness that accounts for the angular sampling of the simulation.

Finally, the spectrum is inserted into the datacube at the spaxel containing the coordinates of the star. This results in a raw oversampled datacube with spectra of many stars assigned to individual spaxels ready to be run through the instrument simulator.

### 4.2.4 HSIM

HSIM [110] is a Python-based simulation pipeline designed for detailed performance modelling of the HARMONI IFS. The tool enables high-fidelity simulations by integrating a variety of astrophysical, atmospheric, and instrumental effects. By inputting high-resolution spectral and spatial data cubes, HSIM generates mock observed data cubes, simulating how HARMONI would observe these astrophysical sources.

This simulation process accounts for key factors such as the E-ELT's AO performance, telescope and instrument-induced aberrations, atmospheric dispersion, and detector characteristics. By including detailed models of the instrument and sky, HSIM provides an accurate representation of the final data quality achievable under various observing conditions. The tool is used extensively to assess the instrument's capabilities in support of key science cases, aiding in the design and development phases of HARMONI.

**Parameter/variable explanation**

The HSIM simulation is set up using a range of parameters that model both the observational and instrumental conditions for HARMONI.

A configuration file is used to set these parameters, including the required total integration time. To expedite the simulation process, the computational load is distributed across 10 CPUs, allowing for parallel processing.

The most critical parameters are integration time, spaxel scale, and grating band and resolving power.

Our integration time, which we vary from 2 to 8 hours to test the sensitivity in our science case, is composed of many short exposures. We choose exposures of 5 seconds, with 1440, 2880, 4320, and 5760 exposures for 2, 4, 6, and 8-hour integration times respectively. This technique of many short exposures is chosen to avoid saturation and persistence at the detector for the brightest stars.

Amongst the available gratings from HARMONI, as shown in Table 2.1 in Chapter 2.4.3, are a choice of spectral bands and resolving powers. The medium resolution (MR) family of gratings is chosen as a balance between resolving power and bandwidth. The velocity resolution of our simulation is reached with the MR gratings, and we are not limited by this resolution. A lower spectral resolution may not be enough, and a higher resolution would result in a shorter band pass and hence fewer spectral lines to fit. Amongst the MR gratings are I+z, J, H, and K bands. According to the sensitivity tables for HSIM [110] the H-band grating (MR3) has the highest sensitivity [14] of the MR gratings, and there are plenty of spectral features in our chosen spectrum in this waveband.

Other important factors are the adaptive optics and atmospheric conditions, described below.

The temperature of the Focal Plane Relay System (FPRS) is set to 2 degrees Celsius, influencing the thermal background from the instrument itself, and the telescope temperature to 280 K. These parameters are set to typical expected values

[14] H-band reaches a limiting AB mag of 24.81 for 10 mas spaxel scale with LTAO, 20×900s exposure, 2x2 spaxels, including sky subtraction noise.

as they are not the subject of this investigation. A more detailed study could look into the impact of varying observation conditions on the effectiveness of the observation in achieving the goals of the science case.

Table 4.5 shows the key observing parameters used in the mock observations in this study.

**Table 4.5:** The key observing parameters as HSIM inputs.

| Parameter | Value |
|---|---|
| Integration time | 2, 4, 6, 8 hours |
| Spaxel scale | 10 mas x10 mas |
| Grating | H-band ($R \approx 7500$) |
| Zenith seeing | 0.55 arcsec |
| AO mode | LTAO |
| LTAO star H mag | 15 |
| LTAO star distance | 30 arcsec |
| Air mass | 1.5 |
| Telescope temperature | 280 K |
| FPRS temperature | 2 °C |

### Adaptive optics and atmospheric turbulence

AO, the correction of atmospheric turbulence, is applied using laser tomography adaptive optics (LTAO)[15], which corrects atmospheric distortions over a narrow field of view. It is assumed that the AO correction is assisted by a reference star with an H-band magnitude of 15, located 30 arcseconds away from the target.

The observational conditions are further defined by a zenith seeing of 0.55 arcseconds (at 500 nm), which reflects the atmospheric turbulence at zenith. This is an optimistic value as the seeing at Paranal, for example, is 0.72" for the 50% percentile. A value of 0.55" is more consistent for the 25% percentile[16], which for a short observation such as ours is not unreasonable.

[15]In theory, single conjugate AO (SCAO) could be used in these observations instead of LTAO as there will be bright enough stars in the vicinity to act as a natural guide star, however, there will be many other stars nearby and so there will be contamination. This crowding means that despite there being a bright enough star for SCAO, LTAO is chosen and justified.

[16]The seeing statistics are from the ESO website: `https://www.eso.org/sci/facilities/paranal/astroclimate/site.html`.

Seeing is a measure of the blurring and distortion of astronomical images caused by atmospheric turbulence. It is quantified as the angular size of the PSF of a star observed through the Earth's atmosphere, and given by:

$$\text{Seeing} = \frac{\lambda}{r_0}, \tag{4.4}$$

where $\lambda$ is the observing wavelength and $r_0$ is the Fried parameter, which quantifies the coherence length of the atmosphere. The Fried parameter depends on the strength of atmospheric turbulence and represents the diameter over which the wavefront error remains approximately one radian.

This equation highlights the inverse relationship between seeing and $r_0$: as $r_0$ decreases due to stronger turbulence, the seeing value increases, indicating poorer spatial resolution. Similarly, at longer wavelengths, the seeing improves, as atmospheric turbulence has a reduced impact on longer-wavelength observations. This is because $r_0$ varies with $\lambda^{6/5}$, so the net effect of Equation 4.4 is that seeing varies as $\lambda^{-1/5}$. Seeing is typically defined at zenith in the visible ($\lambda = 500$ nm), and so we must also factor in the geometry of the observation.

The airmass of an observation, which quantifies the column of atmosphere through which the target's light travels, directly influences the observed seeing conditions. The minimum zenith distance, related to the airmass, is determined by the difference between the telescope's latitude and the target's declination. Our target, R136 / 30 Doradus, is located at a declination of $\delta \approx -69°$ and is observed from the E-ELT at a latitude of $\phi \approx -24.5°$. At its highest elevation (when the target is on the meridian), the zenith distance is calculated as:

$$ZD = |\phi - \delta| = |-24.5 - (-69)| = 44.5°.$$

Using the relationship between zenith distance and airmass, airmass $\approx \sec(z)$, this zenith distance corresponds to an airmass of approximately 1.4. This is the minimum and is not possible to maintain for a several-hour observation, so a value of 1.5 is chosen.

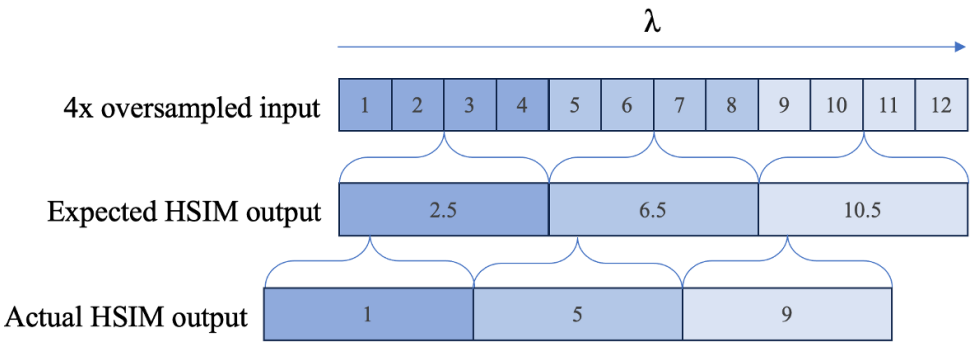


**Figure 4.8:** How HSIM handles oversampled wavelengths resulting in a minor error.

### Oversampled wavelength handling bug

During this study, a bug[17] was discovered in the HSIM code which resulted in a minor error in the way that the software handles oversampled spectral pixels.

Figure 4.8 shows how we might expect pixels with wavelength values of, for example, 1, 2, 3, 4 etc. to transform when resampled to a quarter of the sampling rate compared with what actually happens. The figure shows, in the case of a 4× oversampled spectrum, that whilst we would expect the output value to be in the middle of the input range, the reality was that it did not factor in the size of the input pixel. The input wavelengths were assumed to be the left edge of input pixel group.

When these values are replaced with real wavelengths, in Angstroms for example, it results in a shifted spectrum which appears as an artificial redshift in the data. In fact, a redshift results in a stretching of the spectrum (a wavelength dependency), whereas this effect is a linear shift.

When the stellar spectra are extracted and the line-of-sight velocity is determined, a systematic error is introduced by this bug.

Rearranging the redshift equation whereby $z \approx v/c$ for small $v$ yields

$$\frac{v}{c} \approx \frac{\Delta\lambda}{\lambda_{\text{emit}}}, \tag{4.5}$$

where $\lambda_{\text{emit}}$ is the emitted wavelength, and $\Delta\lambda$ is the value of the shift introduced by the bug, i.e. $\lambda_{\text{obs}} = \lambda_{\text{emit}} + \Delta\lambda$.

[17]This bug was fixed in an update on 10/10/2024.

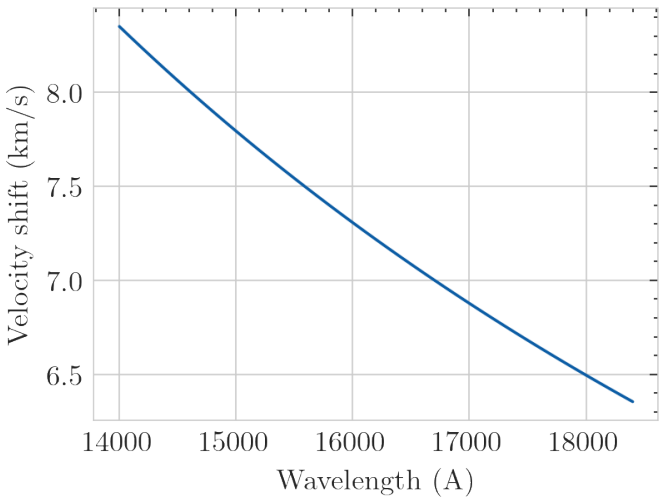


**Figure 4.9:** The impact on perceived LOSVs induced by the HSIM bug.

This results in an error of about 6.5 to 8 km/s across the H-band, as shown in Figure 4.9.

This expected shift will impact all sources equally and therefore can be partially circumvented by considering a median population velocity to zero-centre the velocities rather than the expected group velocity of the object. This works because we are interested in the line-of-sight velocity dispersion of the stars in the population rather than the absolute velocities.

However, the impact on the velocity determination may be more complicated than that. An unexpected linear shift in a spectrum compared to a template (used for fitting) rather than an expected logarithmic shift (or stretching), would limit the ability of the algorithm (in this case pPXF) to fit the template and hence limit the minimum (best possible) chi-squared value that is achievable. This may cause error or uncertainty in the velocity determination.

This bug was spotted late in the work and there was not enough time to re-run all of the simulations with the updated HSIM version.

### 4.2.5 Simulated observational data

The final output of our simulated observations are two datacubes in FITS file format: one with the IMBH present in the N-body, and one without. These are to

be treated as real observational data for an operational HARMONI on the E-ELT in the next part of the process described in Section 4.3. In fact we have 8 datacubes in total when including different exposure times.

Figure 4.10 shows a snapshot of a single frame from an example output datacube with a larger field of view: the 2 arcsec field used in the main study is overlaid. Many sources are visible with a range of magnitudes along with PSF artifacts and background noise. This figure clearly shows the disproportionate impact of a few very bright sources. The impact of the PSF spreading out and contaminating the spectra of other stars is discussed in Section 4.3. To minimise this effect, it was decided to remove the very brightest sources by artificially limiting the magnitudes to $H > 15$ when creating the input datacube for HSIM. This simplification removes 17 stars from the with-IMBH case and 21 from the without-IMBH case, and is justified as we use simple methods for spectra extraction: a more robust method would not suffer as much from the contamination as discussed in the next section and the lessons learnt in Section 4.5.4.

## 4.3 Kinematic extraction

In this section, the simulated as-observed datacubes, described in Section 4.2, are analysed to extract the kinematics of the stars. The primary objective is to determine the line-of-sight velocities of individual stars, which form the basis for investigating the kinematics of the observed system. This involves detecting sources within the datacube, extracting their spectra, and deriving their velocities.

### 4.3.1 Source detection with DAOStarFinder

The first step in this process is source detection. To identify stellar sources, we employ the DAOFIND algorithm [94], implemented in Python via the `DAOStarFinder` class from the `photutils` package [17]. The algorithm is tailored to enhance the visibility of point sources and distinguish them from background noise and artefacts. It works with 2D images, and so we take a mean 2D image of the 3D datacube.

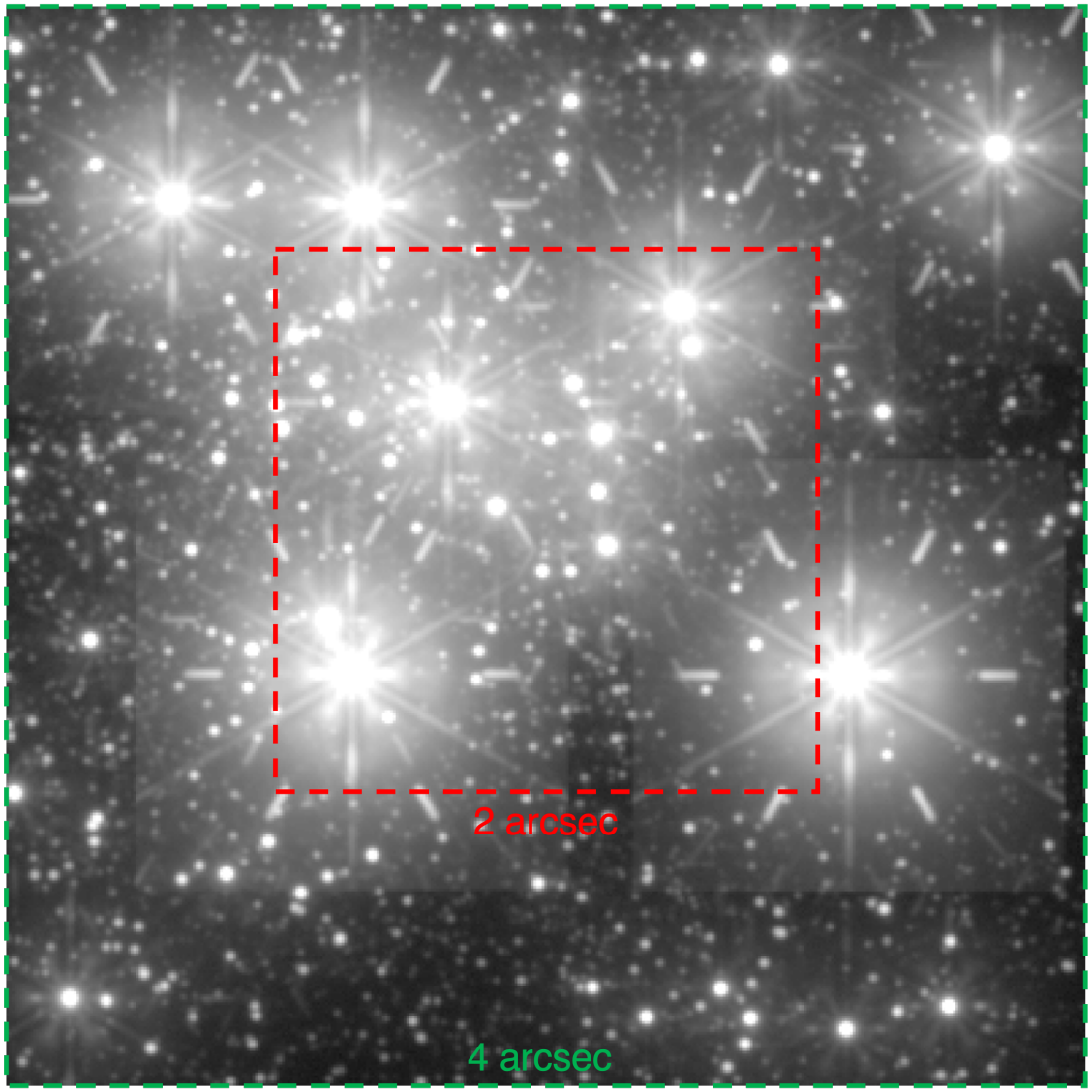


**Figure 4.10:** Snapshot of a simulated observation, logarithmically scaled with an 8-hour exposure time, of the central 4 arcsec of the N-body. The cube is averaged (mean) in the spectral direction to boost the SNR. This is with the IMBH present. A 2 arcsec window overlayed in red to show the field of view of the data used in the rest of this study of a single 10mas observation. The boosted contrast shows the square outer limits of the simulated PSF around the brightest stars.

`DAOStarFinder` begins by convolving the input image with a two-dimensional Gaussian kernel optimised to highlight sources with a full width at half maximum (FWHM) matching the expected size of stars (approximated as FWHM = 2 pixels[18]). This convolution enhances features with stellar morphology while suppressing high-frequency noise. Local maxima in the convolved image—rather than in the residual—are then identified as candidate sources, consistent with the original DAOFIND algorithm.

To minimise false detections from noise, a threshold is applied to the identified maxima. For this study, we set the threshold at three times the standard deviation of the background noise, ensuring that only the most significant peaks, likely corresponding to actual stars, are retained.

An additional filtering criterion based on roundness is used to refine the list of detected sources. The roundness filter rejects asymmetric features, such as residual PSF artefacts. For our analysis, we used $-0.75 < \text{roundness} < 0.75$.

The output of `DAOStarFinder` includes key parameters for each detected source, such as centroid coordinates, peak values, and shape characteristics. These parameters form the basis for subsequent photometric and kinematic analyses. Figure 4.11 shows two example observations with the detected sources overlaid in red circles. These two images are for the case with the IMBH present, and show a comparison with and without the brightest stars included, using the threshold of $H_{mag} > 15$ as proposed in the previous section.

To compare the algorithm's ability to detect sources in each of these scenarios, and for different exposure times, Table 4.6 lists the number of input and detected stars as well as the detection fraction, for different exposure times, and comparing the models with and without the presence of an IMBH. The data shows that source detection increases from 9-10% to 13-14% when the few bright stars are removed.

Figure 4.12 shows the population of detected stars in the case with an IMBH and for an 8-hour observation as an example. To make a direct comparison with the N-body input data, each detected star needs to be identified. An algorithm was

[18]As stated previously, the instrument PSF is 4.71 mas, combined with LTAO this comes to 5.61 mas. This drives the 2 pixel approximation for the FWHM.

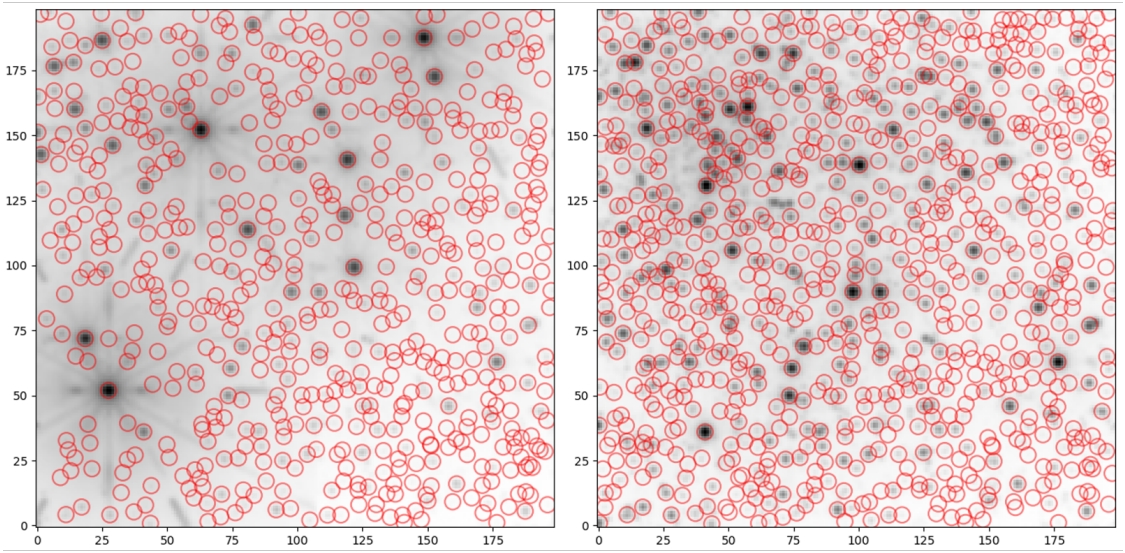

**Figure 4.11:** Comparison of the DAOFIND source detection results with all the stars (left) and, using the threshold of H> 15, without the brightest 17 stars (right). Red circles are where a source has been detected, and a mean greyscale image of the datacube is underneath. Note the elongated PSF features in the left panel which are wavelength-dependent discrete features spread by the averaging of every wavelength step. They are discounted as sources by their ellipticity, but these PSF features clearly limit the ability to detect faint stars in that region.

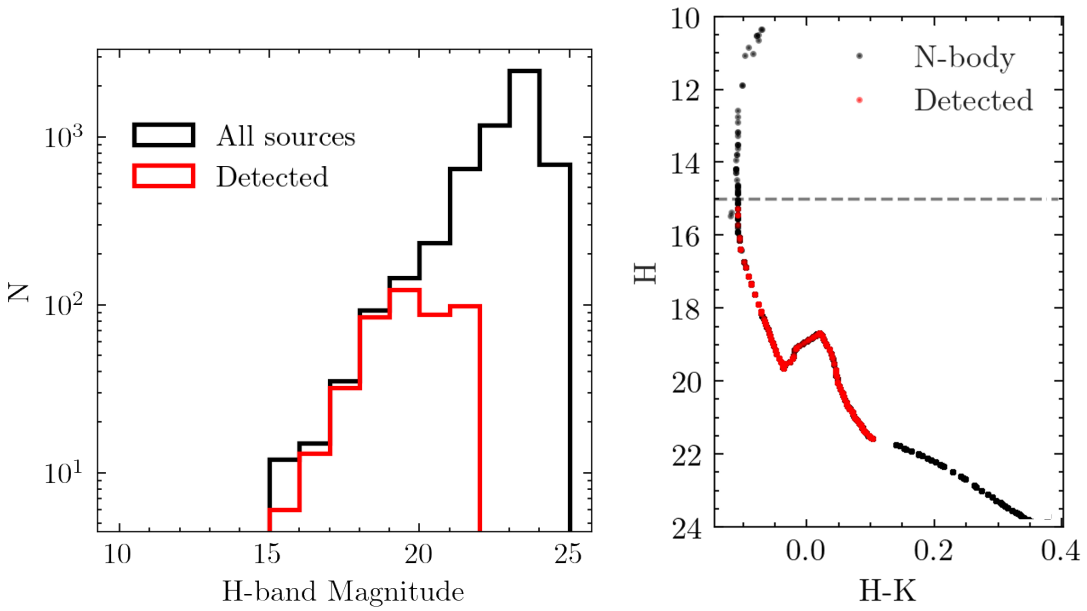


**Figure 4.12:** A histogram of the population of stars detected versus the full input population by magnitude (left), shows that most bright sources are detected as expected. Source identification/matching is required to make this comparison, a process introduced in Section 4.3.4. The colour magnitude diagram (CMD) of the input versus the detected sources (right) shows the depth of the observation with the threshold of 15 mag stars shown as a dashed line. The stars with $H_{mag} > 15$ are shown in the CMD for completeness.

**Table 4.6:** Number of input and detected stars, as well as detection fraction, for different exposure times, comparing the presence/absence of an IMBH and including/excluding stars brighter than 15 mag in the H band.

| | All Stars | | | Only H>15 | | |
|---|---|---|---|---|---|---|
| Exp Time (hr) | Input | Detected | Fraction | Input | Detected | Fraction |
| **Case with IMBH** | | | | | | |
| 2 | 6093 | 580 | 0.095 | 6076 | 784 | 0.129 |
| 4 | 6093 | 574 | 0.094 | 6076 | 795 | 0.131 |
| 6 | 6093 | 581 | 0.095 | 6076 | 798 | 0.131 |
| 8 | 6093 | 590 | 0.097 | 6076 | 797 | 0.131 |
| **Case without IMBH** | | | | | | |
| 2 | 5516 | 575 | 0.104 | 5495 | 774 | 0.141 |
| 4 | 5516 | 568 | 0.103 | 5495 | 764 | 0.139 |
| 6 | 5516 | 578 | 0.105 | 5495 | 785 | 0.143 |
| 8 | 5516 | 581 | 0.105 | 5495 | 767 | 0.139 |

written to do this, described in Section 4.3.4, however, it is imperfect and limited in its ability to accurately identify sources in the image with stars in the N-body 'catalogue'. The deviation of the histogram in Figure 4.12 between H=15 and 16 may be caused by a misidentification, as these stars are the brightest left in the image and would be expected to be easily detected.

### Source identification

To probe the depth of the observation and source detection, determine the accuracy of the velocity determinations, and to understand the limiting magnitude for which robust velocities can be determined, we need to identify which source is which and compare the results with the input N-body.

Due to the significant crowding of sources and the effect of the PSF this is not straightforward and it is easy to misidentify sources which leads to false results. Initially selecting simply the nearest source was attempted, but many fainter sources which have not been detected are then incorrectly identified as the detected source: this is an issue that would be expected in a crowded field.

Other techniques were trialled such as choosing the brightest source from the N-body catalogue within a defined radius from the expected location. This led to

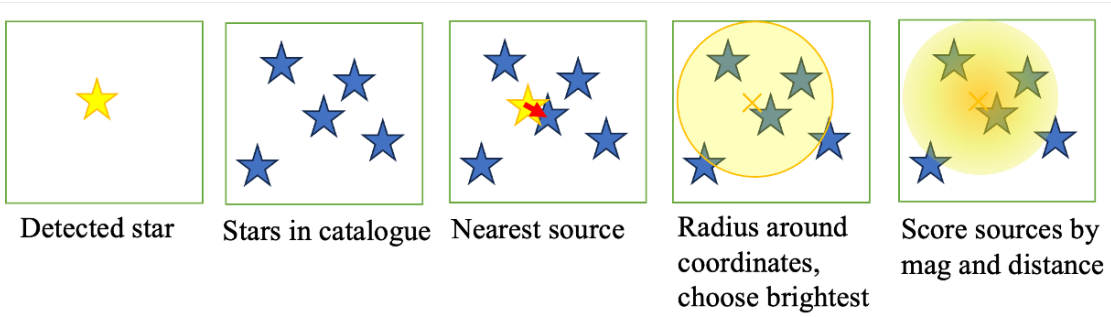


**Figure 4.13:** Methods of identifying detected sources with the N-body catalogue.

a bias for brighter sources being detected and many duplicates whereby brighter sources were being identified multiple times.

Finally, a weighted approach was implemented which considered brightness and distance by assigning a score to each source within a defined radius as per:

$$S = \frac{1}{m^2 \cdot d}, \tag{4.6}$$

where $S$ is the score assigned to each source, $m$ is the magnitude of the source, and $d$ is the distance of the source from coordinates in pixels. These techniques are shown in Figure 4.13, showing for a typical detected star there are several stars in the catalogue in the vicinity. A simplistic technique of choosing the nearest star is shown, then choosing the brightest star within a certain radius, and finally the weighted approach.

The results of this process are shown in Figure 4.12, and whilst it may appear to be quite accurate, there are several duplicates (sources identified twice), sources mid-identified, and other errors because of false sources found by DAOPHOT (such as PSF features described in Section 4.3.3).

### 4.3.2 Spectrum extraction

With the locations of the sources identified the spectral information can be extracted.

A simple way to extract a spectrum from a source location is to co-add the five spaxels in a '+' shape about the central spaxel. This method captures a significant portion of the star's flux.

Extracting the spectrum from a single central spaxel typically captures 10-18% of the flux depending on how centred the star is on that spaxel and the brightness of the star. When this is changed to the five spaxel '+' shape, the captured flux increases to between 50 and 60% of the total. This is a significant increase and whilst more flux can of course be captured with more spaxels, the SNR of the outer spaxels is worse and the risk of contamination from nearby sources increases, and so the five spaxel method was chosen for this study.

This imperfect method does not account for star locations being not exactly centred on a spaxel, and the impact of any residual differential atmospheric refraction[19], which would cause the stars' centroids to move with wavelength, is only mitigated by the use of source locations taken from a mean image and by the coordinates of the input star locations being defined for the centre of the band. It also does not factor in the different PSF sizes of the stars caused by variations in brightness, and the wavelength dependency of the PSF width.

A more sophisticated method might involve a growth curve approach which would account for low order variations in PSF size from source to source, or by fitting of the point spread function.

### 4.3.3 Point spread function

The PSF characterises the response of a telescope or any optical system to a point source of light, such as a distant star. Ideally, in a perfect diffraction-limited optical system, a point source would be imaged as an Airy pattern in the focal plane. In reality, several unavoidable factors lead to the spreading of light, resulting in a blurred representation of that point source. The PSF describes this spreading and provides a complete description of how light is distributed in the image plane from any given point source. In practical terms, the PSF encompasses all the imperfections of an optical system, both intrinsic and extrinsic, which influence the quality of the final image.

[19]This wavelength-dependent phenomenon is first simulated by HSIM and then corrected for in the same way it would be in the science pipeline.

Even in a perfectly built telescope, the wave nature of light introduces limitations due to diffraction. When light passes through the aperture of the telescope, the finite size of the aperture causes the light to diffract and spread out, forming an Airy disk pattern at the focal plane, consisting of a bright central spot surrounded by a series of concentric rings. The diameter of this central spot depends on the wavelength of light and the diameter of the telescope aperture, and it defines the fundamental diffraction limit of the telescope.

Other intrinsic contributors include the optical system's design and its aberrations. The telescope's design, the configuration of its mirrors, and the presence of support structures such as secondary mirror spider vanes all contribute to specific patterns within the PSF, such as diffraction spikes seen around bright stars. Imperfections in the telescope's optics, also contribute to the broadening of the PSF. Even with precise manufacturing, slight deviations in the shape or alignment of these components introduce aberrations like coma, astigmatism, and spherical aberration, all of which distort the image of a point source.

The other major contributors to PSFs for ground-based telescopes are atmospheric turbulence and the adaptive optics used to mitigate it. The turbulence results in a blurring effect known as 'seeing', which spreads the light and causes the stars to twinkle and appear as blurred blobs rather than precise points. Large ground-based telescopes rely on AO to largely overcome the effect of turbulence. However, AO introduces complexity to the PSF, often making it spatially and temporally variable [89]. This means that the PSF is not always uniform across the field of view or over time, complicating image analysis, particularly in dense fields.

In adaptive optics-assisted systems such as HARMONI on the E-ELT, the PSF can be quite complex, consisting of a sharp core surrounded by diffuse "wings" caused by residual uncorrected atmospheric aberrations. The sharpness of the PSF, often quantified by the FWHM, is a key metric used to assess the quality of an image.

The Strehl ratio is an alternative metric popular with AO scientists which is defined as the ratio of the peak intensity of the observed PSF to the peak intensity

of the ideal diffraction-limited PSF. A Strehl ratio close to 1 indicates a high-quality PSF that closely approaches the diffraction limit, while lower values suggest significant degradation due to aberrations or atmospheric effects.

The Strehl ratio is particularly useful in AO because it provides a straightforward way to assess the overall effectiveness of the correction, focusing on how well the system maintains a sharp central peak in the PSF.

For an integral field spectrograph, the FWHM is more relevant as it captures the PSF's overall spatial extent and its distribution across spaxels. A narrower FWHM indicates a better-resolved image, while a broader PSF suggests significant spreading of light due to aberrations or seeing effects.

The highly complex optical path of the combination of the E-ELT and HARMONI results in the PSF shown in Figure 4.14. This figure shows both linearly and logarithmically scaled views to highlight the range of features. This is the oversampled version used internally within HSIM.

The non-axisymmetric components are caused by segmented optics, the telescope's secondary mirror support structure, and the adaptive optics system including the laser guide stars. These include artefacts such as 'arms' spreading from the centre and discrete spots such as the two on either side of the central core and six spread out further.

A limitation of HSIM is that the field rotation that would occur in a real observation is not accounted for, so the simulated data of a multi-hour observation creates features which are not necessarily consistent with reality. HSIM has a fixed PSF orientation with respect to the sky, whereas in real observations, the PSF rotates with the pupil, not with the field, so there is a differential rotation of PSF with respect to the sky. Very relevant to this study are the six point source features in a hexagonal shape around the central core, and the two other point source features near the central core. For the brighter sources, these appear as faint sources, and can only be distinguished from real stars by their wavelength dependency in the field which results in them moving away radially from the central core with increasing wavelength.

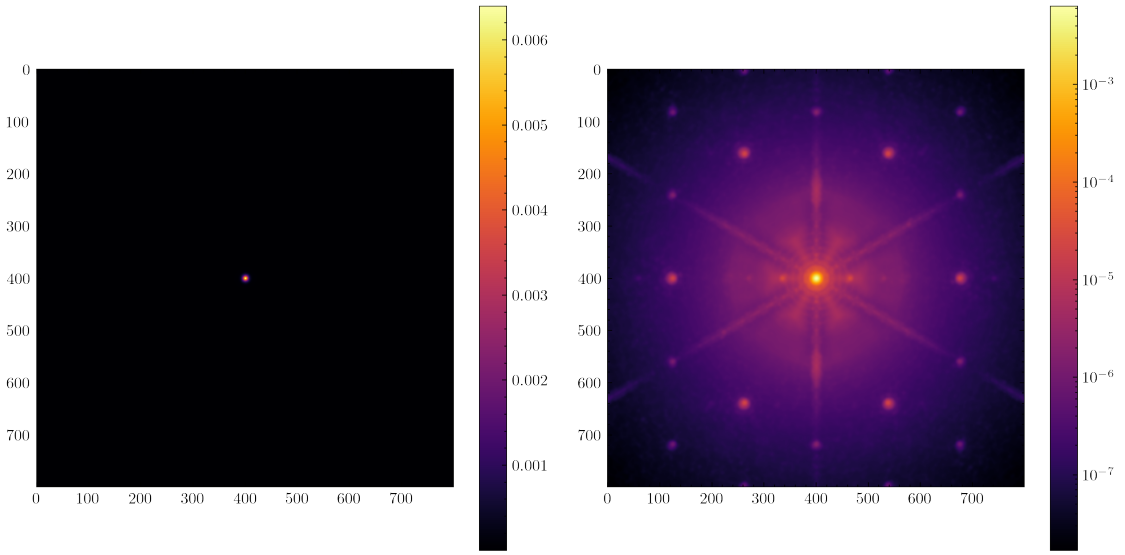


**Figure 4.14:** E-ELT-HARMONI 2D point spread function. This representation is the spatially oversampled version used internally within HSIM. The field of view of these images is 1.6" × 1.6", and the PSF is at 1625 nm. Linearly scaled (left) shows the small tight core of the PSF while logarithmically scaled (right) shows the extended features.

This is a concern for resolved crowded field integral field spectroscopy with non-axisymmetric PSFs.

### PSF contamination

When simulating a dense field of stars the PSFs of different stars can overlap each other, causing confusion when extracting spectra.

In our simulations, the point-like PSF artefacts appear as stars. The wavelength dependence of the PSF structure means that these spots move radially away from the central source with increasing wavelength. This can cause significant contamination with our 'real' sources, as shown in Figure 4.15 where a PSF spot artefact moves directly over a star causing a large bump in the spectrum in the datacube at that wavelength.

A technique was used to artificially identify each source by setting a range of spectral pixels to 0 value in the datacube input to HSIM. Approximately 150 input pixels were set to 0 starting at the shortest wavelengths for the brightest source and then moving along the bandpass for each subsequently fainter source, thus providing an identification embedded in the spectra of the 100 brightest stars in

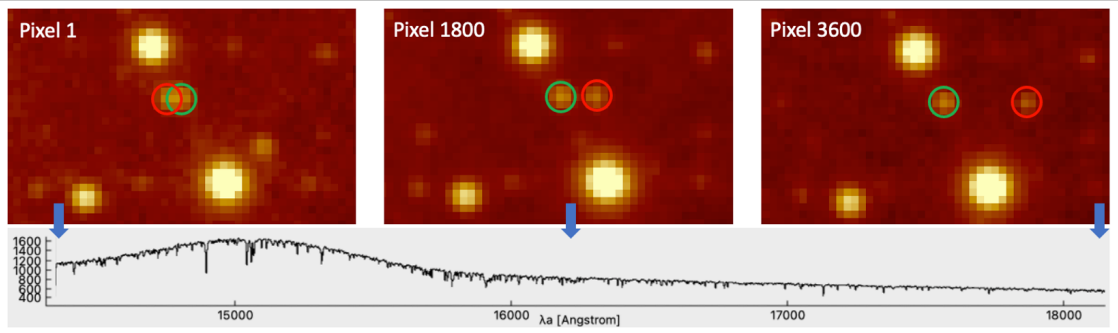


**Figure 4.15:** An example of a wavelength-dependent PSF artefact contaminating a source. The three panels show the same part of the field for the start, middle, and end of the H-band. The green-circled source is a real star while the red-circled source is a discrete PSF artefact from a nearby bright star moving with wavelength. The lower panel shows the spectrum of the pixel at the centre of the source in the green circle and hence how the red source influences it.

the field of view. The small 'notches' that appears in the resulting spectra are not sufficiently large to negatively impact the velocity estimates.

Figure 4.16 shows the spectra from four adjacent spaxels all showing varying levels of contamination. Inspecting the image by eye there appear to be two sources overlapping; a brighter source towards the bottom left as indicated by the spectral notch at 14,500 angstroms, and another towards the top right indicated by the notch at 14,600 angstroms. These two would be blended together with the simple spectral extraction technique. A third less obvious source with its notch at around 14,700 angstroms also appears particularly in spaxel 3 and 4. Together these three sources would result in a miscalculation of the line-of-sight velocity.

### 4.3.4 Line-of-sight velocity determination

The line-of-sight velocity, often abbreviated as LOSV, measures the relative motion of an object directly along the line connecting it to an observer. This velocity component can be determined by analysing the Doppler shift of light emitted by the object (such as a star) or reflected from it.

We use the widely adopted software package pPXF (Penalized Pixel-Fitting)[24], which is specifically designed to extract stellar kinematics and other essential information from galaxy or stellar spectra. pPXF is primarily applied to measure the

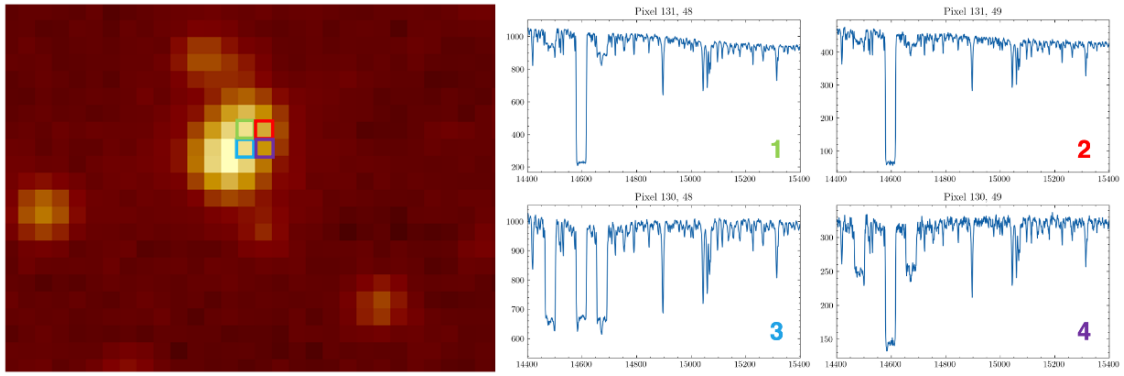


**Figure 4.16:** An example of multi-source PSF contamination. The four panels on the right show the spectra of each of the four pixel locations on the left image. The artificial notches in the spectra show three sources are overlaid and contaminating each other whilst not apparent in the image.

line-of-sight velocity distributions (LOSVDs) of stars in galaxies, star clusters, and other stellar populations. By employing advanced fitting techniques, pPXF compares observed spectra with template spectra, enabling the derivation of velocities, velocity dispersions, and other kinematic properties of stars within a system.

This study is not to determine the effectiveness of pPXF, but to use it as a tool to investigate the effectiveness of HARMONI observations to determine the LOSVs in a dense star cluster.

### Results

For each given spectrum pPXF provides an estimated LOSV. Figure 4.17 shows an example output plot from the program. The black line shows the input spectrum and the red line is the overlaid best fitting template which is shifted and stretched to fit the input. The residuals from this fit are displayed in green at the bottom of the plot. This example is a good fit with a high signal-to-noise ratio (SNR).

Figure 4.18 shows the running average (calculated by moving a bin containing 40 stars outwards from the centre of the cluster) of the observed absolute line-of-sight velocity for different integration times using the same method as in Figure 4.4 from the MICADO team [38].

The error in the velocity measurements can be calculated from the standard deviation of the residuals between the observed velocities and the expected velocities.

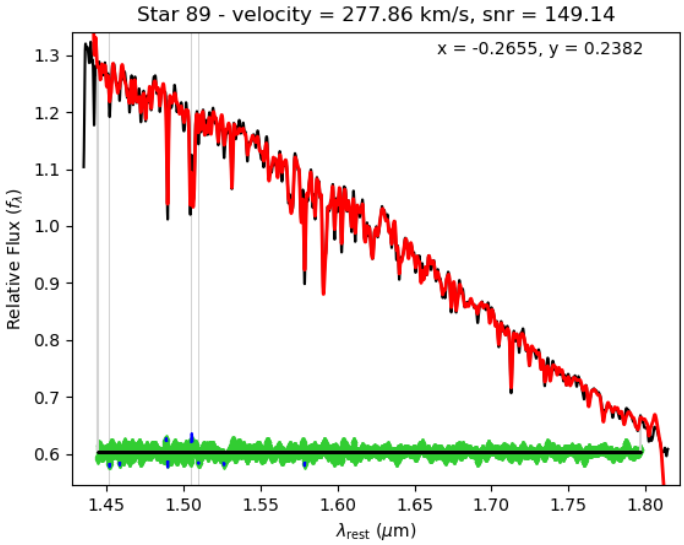


**Figure 4.17:** An example output plot of pPXF on one of the extracted spectra. The black curve is the 'observed' spectrum, the red is the best fitted template, and the green is the residuals between these. The Y axis is a normalised relative flux, and the X axis is the wavelength.

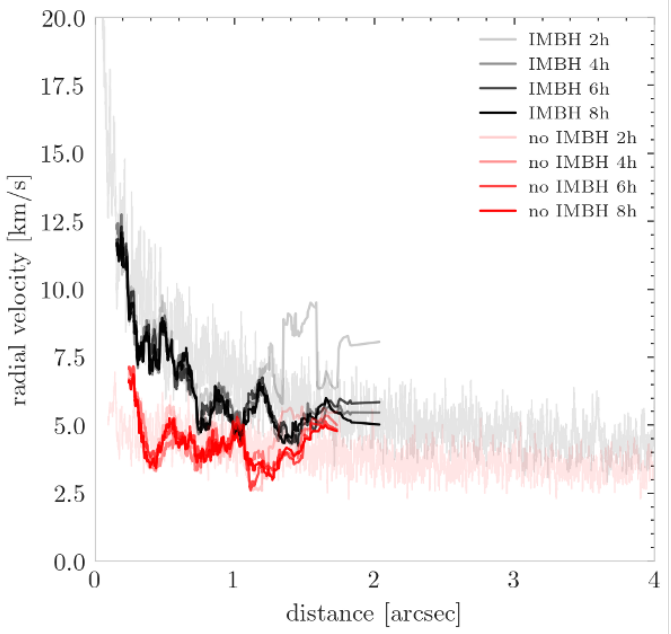


**Figure 4.18:** The running average of the observed line-of-sight velocity in the presence (black) or not (red) of an IMBH in the cluster centre for different integration times in the foreground and as per the N-body simulation in Figure 4.4 in the background.

This can be achieved because of the nature of this simulation, and of course, it would not be possible in a real observation where 'true' velocities are unknown. Whilst standard deviation is typically denoted by the symbol "$\sigma$", to avoid confusion with the velocity dispersion in Section 4.4, we make use of the symbol "$\psi$". The error in the velocity determination is then given by:

$$\psi_{\text{losv}} = \frac{\psi_{\text{residuals}}}{\sqrt{2}}, \tag{4.7}$$

where $\psi_{\text{residuals}}$ is the standard deviation of the residuals from the velocity fit. The factor $\frac{1}{\sqrt{2}}$ arises naturally from the mathematical derivation of velocity uncertainties when using template-fitting methods such as pPXF. The measured velocities are determined by finding the best-fit shift (velocity offset) between the observed spectrum (which contains inherent observational noise) and a model template spectrum (assumed to be essentially noiseless). The velocity uncertainty is estimated from the standard deviation of the residuals between observed and fitted spectra. Since the velocity determination through template fitting involves minimising symmetric Gaussian residuals around the best-fit velocity shift, the variance of these residuals effectively combines two symmetric Gaussian contributions. This approach aligns with standard practices in stellar kinematics (e.g. Cappellari 2017 [23]), ensuring a proper statistical interpretation of fitting residuals in velocity estimation.

**SNR**

The SNR is determined by dividing the median stellar flux ($F_{\text{median}}$) of a spectrum by the standard deviation of the residuals obtained after fitting the spectrum with a template. To minimise the impact of outliers on the standard deviation, a robust sigma (biweight scale) approach is taken.

The biweight scale [91], also known as the biweight sigma, is a robust statistic that measures the spread of the residuals. It is less sensitive to outliers compared to the standard deviation. The biweight scale $\sigma_{\text{biweight}}$ for $n$ data points is calculated using the following formula:

$$\sigma_{\text{biweight}} \equiv \sqrt{n} \sqrt{\frac{\sum_{|u_i|<1}(r_i - M)^2(1-u_i^2)^4}{\left|\sum_{|u_i|<1}(1-u_i^2)(1-5u_i^2)\right|}}, \tag{4.8}$$

where $r_i$ are the residuals, $M$ is the median of the residuals, and $u_i$ is given by:

$$u_i = \frac{r_i - M}{c \times \text{MAD}}, \tag{4.9}$$

where MAD is the median absolute deviation of the residuals, and $c$ is a tuning constant that determines the extent to which data points are down-weighted, often, and in our case, set to 9. Smaller values of $c$ increase the rejection of outliers, while larger values allow more data points to contribute.

Unlike the standard deviation, which is sensitive to outliers, the biweight scale provides a more reliable estimate of dispersion when outliers are present by down-weighting data points with large deviations. The MAD is used as a robust initial estimate of scale, ensuring the method starts with a stable measure of dispersion.

The SNR is then:

$$\text{SNR} = \frac{F_{\text{median}}}{\sigma_{\text{biweight}}}. \tag{4.10}$$

This method provides a robust way to calculate the SNR of an observed stellar spectrum by leveraging the median stellar flux and the biweight scale of the residuals, ensuring reduced sensitivity to outliers and non-Gaussian noise in the data.

**Direct comparison with catalogue**

To bypass potential issues with source matching and identification previously discussed, another test was conducted which simply extracted spectra for the given locations of the stars in the N-body simulation, ran those through pPXF, and then directly compared the resulting velocity estimations with the ‘real‘ velocities from the N-body. This method guarantees a like-for-like comparison.

Figures A.10 and A.11 in the appendix show this comparison of expected vs detected velocities for the brightest 500 sources as determined by the input magnitude. The left column is for the N-body case with the IMBH present, and

the right column is without an IMBH. From top to bottom, the total integration time of the simulated observation increases as 2, 4, 6, and 8 hours. A perfect set of velocities would result in a straight line, and deviations away from this are errors in the velocity estimations. There is a greater spread in velocities along the diagonal in the observations with the IMBH as would be expected. Interesting to note is the increasing error in the velocity estimation in the presence of the black hole too, perhaps due to a more severe impact of the PSF contamination when the population of stars have a wider range of velocities to begin with.

Subtracting the expected velocity from the estimated velocity and plotting against SNR of the pPXF fit gives the plots in Figure A.11, in the same layout as the previous figure. Here it is evident the SNR values increase with increasing integration time as expected, and generally the 'LOSV difference' worsens with lower SNR. The points are coloured by input magnitude showing a clear relationship between velocity estimation quality and star magnitude.

Figure 4.19 shows the number of sources which have a LOSV error of less than 5 km/s for each case, this value was chosen as it can be considered a reasonable accuracy for a velocity determination. The plot shows a modest increase of this number with integration time suggesting how integrating for longer, and hence increasing the SNR of spectra, can improve the LOSV estimation, although the effect is subtle here especially for the with-IMBH case. The improvement with integration time is more limited than we might expect. Also, the absolute number of sources within this error range is higher for the case without an IMBH as discussed previously.

The standard deviation of these velocity errors with decreasing maximum magnitude for each integration time is plotted in Figure 4.20, for the with-IMBH case. This plot shows that for the brightest sources, there's only a small difference in the error achievable by increasing the integration time but this gets better for fainter sources. The limited improvement with increasing integration time, compared with expectations, shown in Figure 4.19 and Figure 4.20 is discussed in Section 4.4.3.

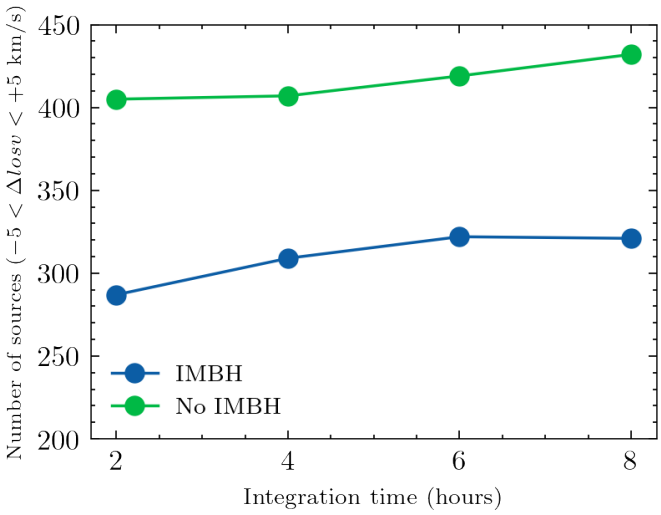


**Figure 4.19:** The number of sources out of the brightest 500 which have an error of less than 5 km/s for each observation of increasing integration time.

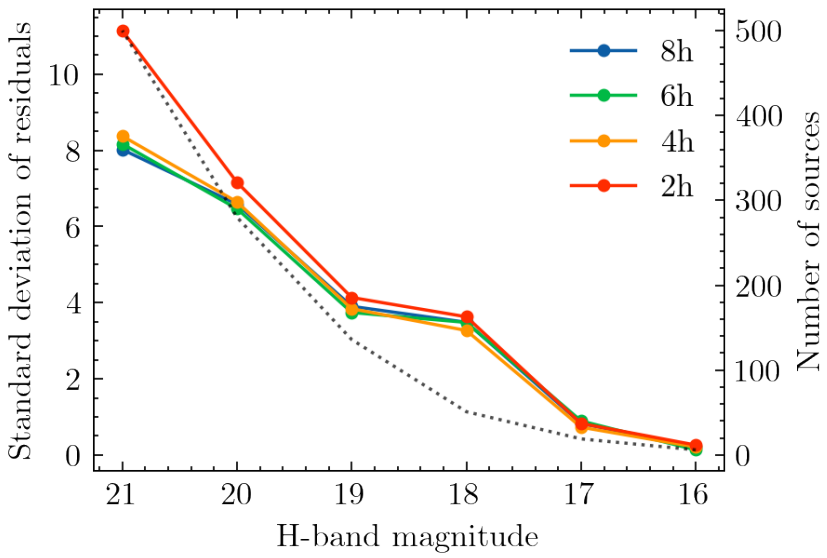


**Figure 4.20:** The standard deviation (in km/s) of the residuals of the velocity estimations by decreasing minimum input magnitude (increasing minimum brightness) for each exposure time. The black dotted line shows the number of sources brighter than that maximum magnitude. This figure shows that as one decreases the maximum magnitude (from 21 to 16) the uncertainty of the velocity determination goes down, however, there is not a big difference between the exposure times; improvements are only made at high magnitudes.

## 4.4 Kinematic assessment

The extracted velocities from the observed datacube form the basis for deriving the kinematic properties of the cluster. Using the line-of-sight velocities of individual stars, we can calculate the velocity dispersion as a function of radius from the cluster centre, described in Section 4.4.2. The velocity dispersion profile offers critical information about the gravitational potential, and, specifically, can reveal the presence of an IMBH.

By dividing the stars into concentric radial bins around the cluster centroid (determined in Section 4.4.1), we can compute the average velocity and the velocity dispersion in each bin. If an IMBH is present at the centre of the cluster, we expect to observe an increase of the velocity dispersion towards the centre due to the strong gravitational influence of the black hole. This profile can be compared against simulations without an IMBH to establish significant deviations that could indicate its presence.

There is no discernable net rotation of our simulated cluster although in reality rotation is often found in such objects. The real R136 has a measured rotation of $\approx 3\,\mathrm{km\,s^{-1}}$[48], and rotation has also been measured in 47 Tuc both with line-of-sight velocity[95] and in the plane of the sky[2].

Another important kinematic signature involves assessing any anisotropies in the velocity distribution, although this is not within the scope of this thesis. In the presence of a central IMBH, stars near the core might show increased line-of-sight velocities compared to tangential ones, due to the radial nature of the gravitational acceleration exerted by the black hole. The kinematic analysis, therefore, helps differentiate between various mass distributions and ascertain whether the observations align with a model involving an IMBH.

### 4.4.1 Centroiding

To accurately determine a cluster's velocity dispersion, the cluster's centre needs to be precisely known. In the case of a real observation of a real object, a luminosity-

weighted centroid can be determined by using an image from a separate observation, for example from HST or JWST.

In our case, the object is not real and so we rely on the input N-body simulation. The IMBH is centred with respect to the cluster, but is not precisely centred with respect to the simulation and hence the cluster centroid is slightly misplaced from [0,0]. Likewise, in the case without the IMBH, the cluster is not quite centred on the field of view of the simulation.

To determine the centroid we use an iterative approach to improve the centroiding position based on an initial estimate, using the full N-body dataset. First, we find an approximation with a density-weighted approach. Then the field is cropped about this point to minimise the bias introduced by only having a limited field offset from the centroid and then a mass-weighted centroid improves upon this.

**Density-weighted centroid**

For each star $i$ with coordinates $(x_i, y_i)$, we compute the local density $\rho_i$, which is the number of stars within a projected radius $r$ of star $i$. The projected distance between two stars $i$ and $j$ is given by

$$d_{ij} \equiv \sqrt{(x_i - x_j)^2 + (y_i - y_j)^2}.$$

The local density $\rho_i$ is then computed as:

$$\rho_i \equiv \sum_{j=1}^{N} \mathbb{I}(d_{ij} < r),$$

where $\mathbb{I}(d_{ij} < r)$ is an indicator function that equals 1 if the distance $d_{ij}$ is less than the radius $r$, and 0 otherwise.

Once the local densities $\rho_i$ are calculated, we compute the density-weighted centroid $(x_{\text{centroid}}, y_{\text{centroid}})$ using, in the example of $x$, the following equation:

$$x_{\text{centroid}} \equiv \frac{\sum_{i=1}^{N} \rho_i \cdot x_i}{\sum_{i=1}^{N} \rho_i}.$$

Here, the positions of the stars are weighted by their local density $\rho_i$, giving a centroid that reflects the denser regions of the cluster more heavily.

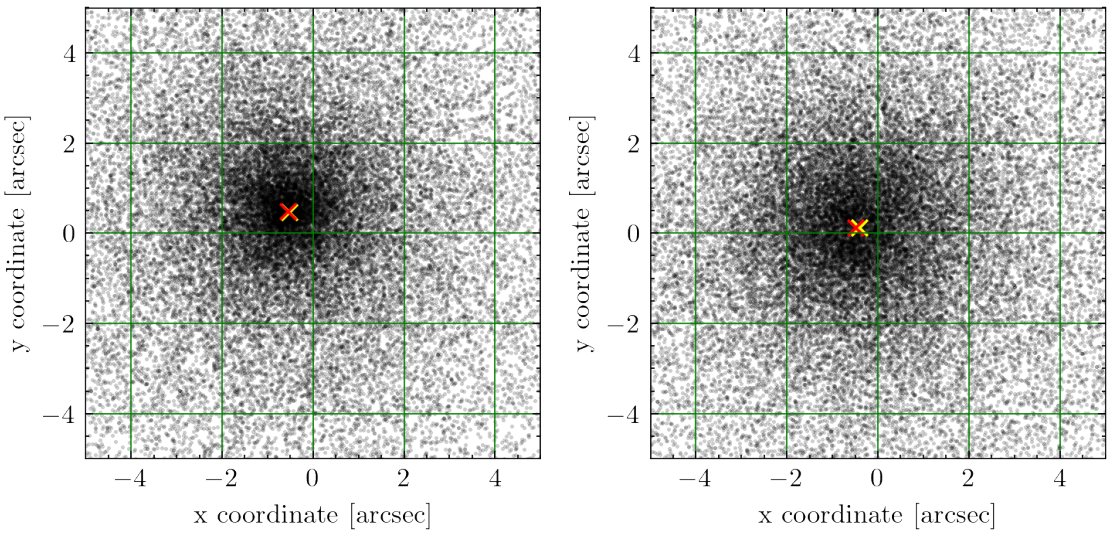


**Figure 4.21:** Centroiding the N-body data with (left) and without (right) an IMBH present. The initial density-weighted centroid estimate is shown in yellow, and the final mass-weighted centroid in red.

Once this initial estimate is calculated a circular region with an 8 arcsec diameter (using the full N-body dataset) is cropped around it to minimise the bias associated with a non-centred square cropped region (the original dataset). Then a mass-weighted centroid is taken to fine-tune the centroid position.

### Mass-weighted centroid

The N-body dataset provides a mass for each individual star and so given a set of stars with coordinates $(x_i, y_i)$ and masses $m_i$ for $i = 1, 2, \ldots, N$, the mass-weighted centroid is calculated as:

$$x_{\text{centroid}} \equiv \frac{\sum_{i=1}^{N} m_i \cdot x_i}{\sum_{i=1}^{N} m_i}$$

$$y_{\text{centroid}} \equiv \frac{\sum_{i=1}^{N} m_i \cdot y_i}{\sum_{i=1}^{N} m_i}$$

This method gives the centroid of the cluster by considering the mass of each star, ensuring that more massive stars contribute more heavily to the final position of the centroid. The sum of the masses $\sum_{i=1}^{N} m_i$ ensures that the centroid is normalized by the total mass of the system.

**Table 4.7:** Final centroid values in arcsec about the (0,0) point of the N-body simulation.

| Axis | With IMBH | Without IMBH |
|---|---|---|
| x | -0.561791 | -0.487467 |
| y | 0.488932 | 0.132982 |

Figure 4.21 shows for each case, with and without the IMBH, the initial estimate of the density-weighted centroid and the fine-tuned centroid location with a mass-weighted approach. Imperfections in the centroiding lead to errors in the inner velocity dispersion calculation which we attempt to avoid here.

The final iteratively-determined coordinates of the cluster centroid for both N-body simulations are shown in Table 4.7.

### 4.4.2 Line-of-sight velocity dispersion

The line-of-sight velocity dispersion, denoted as $\sigma$, is a crucial quantity in the study of stellar dynamics, particularly when investigating the presence of a central black hole in star clusters. In this context, $\sigma$ represents the spread in velocities of stars as observed along the line of sight. The gravitational influence of a massive object, such as a black hole, alters the velocity distribution of stars in its vicinity. Specifically, the presence of a central black hole causes stars to move more rapidly due to the strong gravitational potential, resulting in an increased velocity dispersion near the centre of the cluster [15].

By measuring $\sigma$ as a function of radius from the cluster centre, we can infer the dynamical mass distribution of the system. A significant rise in the velocity dispersion towards the cluster core is often indicative of the gravitational influence of a compact object, potentially a black hole. Thus, accurate measurements of $\sigma$ are essential for constraining the mass and the presence of such objects.

The velocity dispersion profile is calculated in radial bins around the centroid of the stellar system. For each star, the projected radial distance from the centroid, $r_i$, is calculated using:

$$r_i \equiv \sqrt{(x_i - x_{\text{centroid}})^2 + (y_i - y_{\text{centroid}})^2} \tag{4.11}$$

where $(x_i, y_i)$ are the coordinates of the $i$th star and $(x_{\rm centroid}, y_{\rm centroid})$ are the coordinates of the system's centroid.

The stars are then sorted into radial bins based on their distances from the centroid. For each bin, the velocity dispersion is calculated using the velocities of the stars in that bin. For this study we have used logarithmically spaced bins in an attempt to gain greater fidelity closer to the cluster centroid and therefore to probe deeper into the cluster. As the bins head out from the centre the statistics improve and hence the $\Delta\sigma$ decreases improving our certainty. An alternative would be to maintain constant error bars by setting the bins sizes to contain a constant number of sources. There is a trade off here between precision and depth probed into the cluster.

The line-of-sight velocity dispersion, or sigma ($\sigma$), of a population of stars within a bin is calculated using the following equation:

$$\sigma = \sqrt{\frac{\sum_{i=1}^{n}(v_i - v_{\rm sys})^2}{n}}, \tag{4.12}$$

where

- $v_i$ are the individual velocities within the bin,
- $v_{\rm sys}$ is the systemic velocity which is the median velocity of all stars in the whole observation and not just in the bin, hence the denominator is $n$ and not $n-1$,
- $n$ is the number of velocity points in the bin.

This formula computes the unbiased estimator for the standard deviation of the velocities by taking the square root of the sum of the squared deviations from the systemic velocity, divided by $n$, which accounts for the degrees of freedom in the sample.

To estimate the uncertainty of the velocity dispersion, $\Delta\sigma$, we use the following relation:

$$\Delta\sigma = \frac{\sigma}{\sqrt{2n}}. \tag{4.13}$$

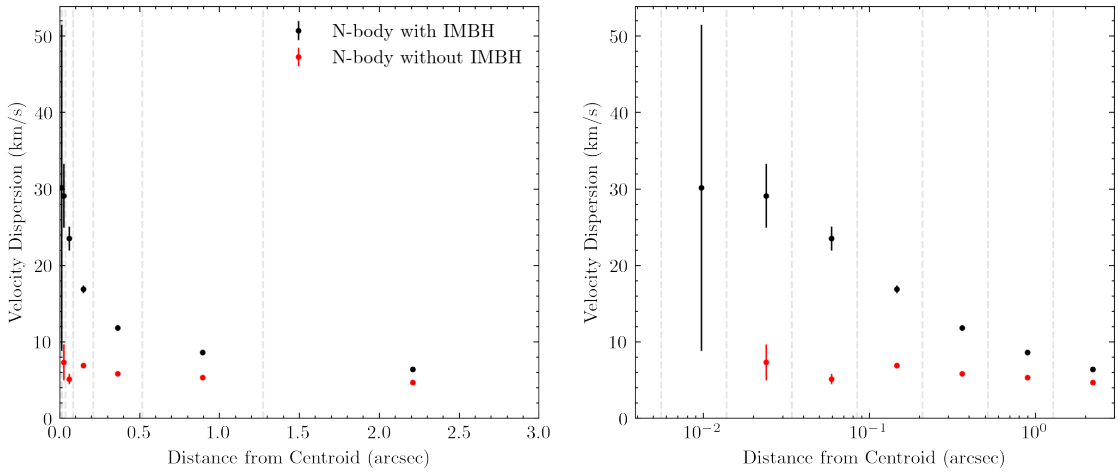


**Figure 4.22:** Velocity dispersion profiles of the cluster N-body datasets as a function of projected distance from the core. The black data points show the case with an IMBH, while the red datapoints show the case without an IMBH. The central presence of the black hole boosts the dispersion near the cluster centre but converges toward a lower value at large radii. The vertical dashed lines show the edges of the bins; and the data are plotted in the middle of the bin. The two plots are identical, except the right plot uses a logarithmic axis.

This formula is derived based on the assumption that the velocity distribution follows a normal distribution and that the uncertainty in the dispersion decreases as the sample size increases. The factor $\sqrt{2n}$ arises from the properties of the chi-squared distribution, which describes the variance of a sample with $n$ degrees of freedom. This method provides a reasonable approximation for the uncertainty in $\sigma$, especially for large sample sizes. However, for small $n$ or non-Gaussian distributions, more sophisticated methods such as bootstrapping may be required for a more accurate estimate.

### Line-of-sight velocity dispersion of N-body data

Figure 4.22 shows the line-of-sight velocity dispersion radial profile of the N-body models for both cases, with and without the central IMBH. This is calculated using Equation 4.12 and with the bins shown in Figure 4.23. The high number of sources, and use of 100% of included sources, compared to the simulation data means that this acts as our truth data for the kinematics of the system.

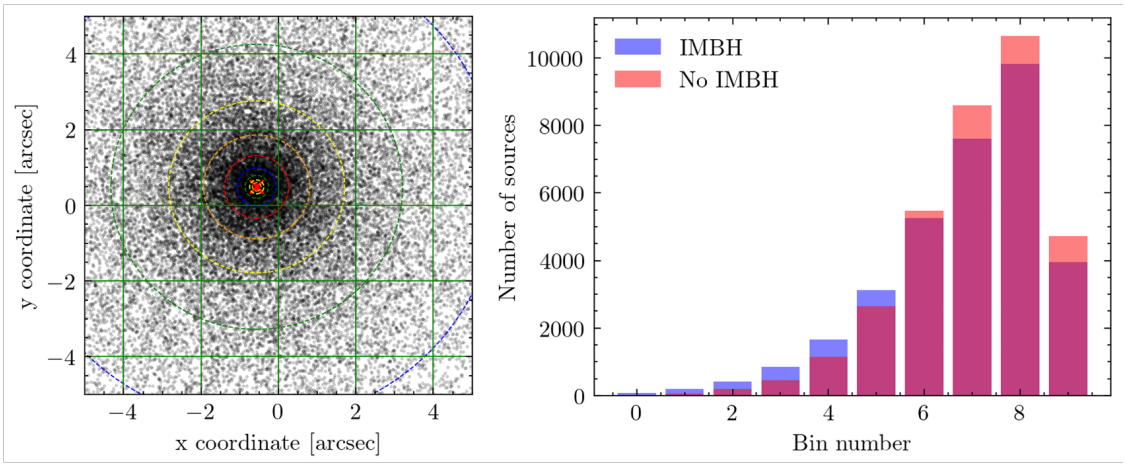


**Figure 4.23:** Binning scheme used for the velocity dispersion measurements. Left: An image of the cluster field (with-IMBH case) for the full N-body data set showing the concentric annuli (coloured dashed circles) used to define the radial bins. Right: The resulting number of sources in each bin for the IMBH (blue) and no-IMBH (red) models. Note the centroids are in different positions for each case although the bin radii are the same.

### Line-of-sight velocity dispersion of simulated observations

Figure 4.24 shows the positions of the extracted star positions in the without-IMBH simulated observation, and the bins used in the line-of-sight velocity dispersion radial profile calculation. These are the same bins as used in the N-body line-of-sight velocity dispersion calculation as shown in Figure 4.23, except that the narrower FOV does not extend out to the two outermost bins.

Figure 4.25 shows the velocity dispersion, $\sigma$, profile from the extracted individual stellar line-of-sight velocities from the simulated observation of the without-IMBH case. The data used are the simulation without the very brightest stars, an 8-hour total integration time, and a minimum SNR of each source used of 15, as lower SNR spectra produce greater errors in the velocity determinations. The dispersion profile is also shown for a statistically similar sample from the N-body, selected by taking the brightest stars in the bin, in this case $15 < H < 19$[20] to make a more realistic comparison with the observed data. These are not however all the same stars there is no one-to-one matching of individual stars in this case.

[20]The very brightest stars with $H < 15$ have been excluded from the simulation entirely.

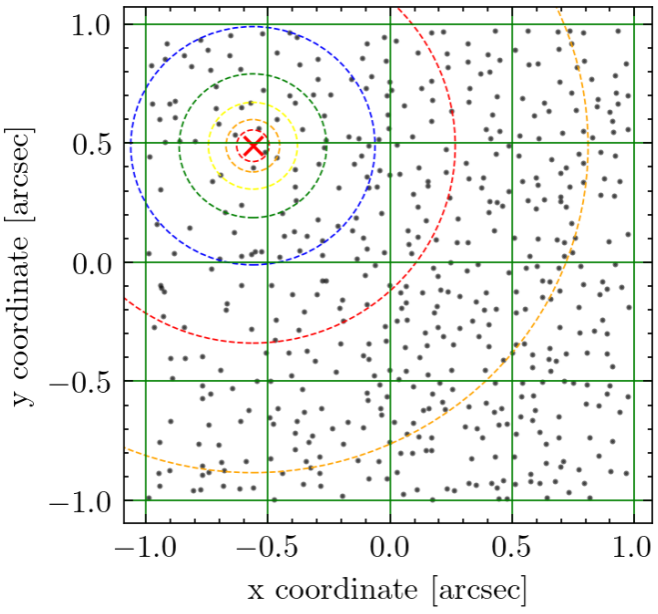


**Figure 4.24:** Binning scheme used for the velocity dispersion measurements of the simulated observation. The extracted star locations (without-IMBH case) and the concentric annuli (coloured dashed circles) used to define radial bins are overlaid.

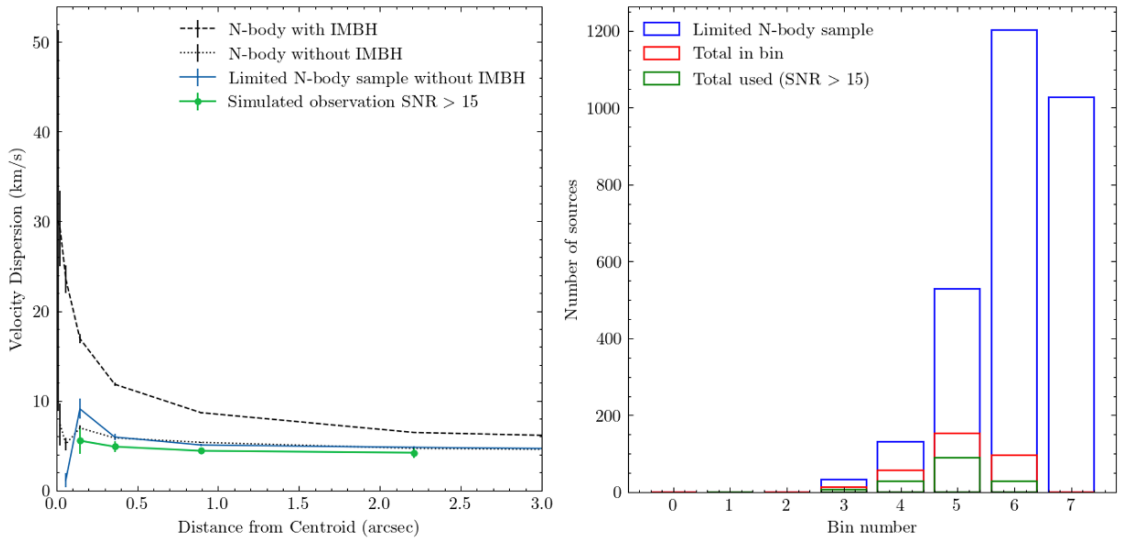


**Figure 4.25:** Velocity dispersion profile (left) of the simulated observation of the without-IMBH scenario (green line). The blue line shows the equivalent N-body data restricted to the brightest stars. On the right, the bar chart shows how many sources populate each radial bin in the simulated observation: green bars for the total, blue for those with SNR>15, and red for the bright N-body stars.

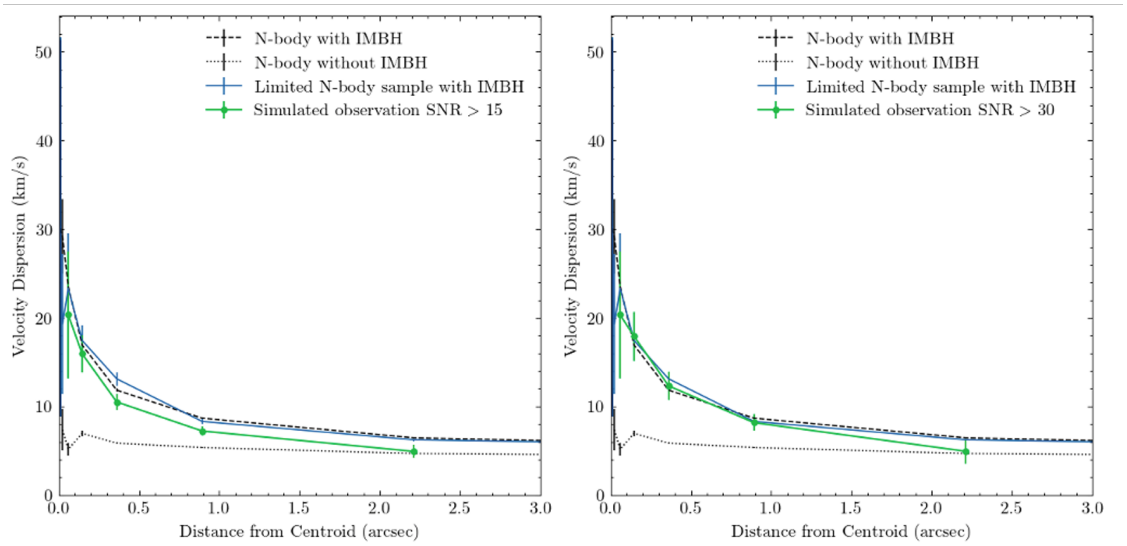


**Figure 4.26:** Velocity dispersion radial profiles from simulated observations of the with-IMBH scenario with two SNR thresholds. Left: only stars with SNR $> 15$ are used; Right: only stars with SNR $> 30$. The dashed and dotted lines show the N-body models with and without an IMBH, respectively, while the solid blue line is the IMBH model restricted to its brightest stars. The green lines show the simulated observations, demonstrating how higher SNR cuts affect the measured dispersion relative to the underlying models.

There is quite a good correlation between the two profiles, the error bars of which grow larger in the inner bins due to low statistics, as determined by Equation 4.13.

The SNR threshold of SNR $> 15$ appears to work well for the without-IMBH case, as exhibited by the broad agreement between the models. However, in Figure 4.26, we plot the with-IMBH case with a threshold of SNR $> 15$ and SNR $> 30$. The first shows a correlation in the form of the profile, but exhibits a shift to lower $\sigma$. When we increase the threshold this gap gradually closes until SNR $> 30$ as shown. Of course, the number of sources diminishes a little and so the error bars grow.

One might expect that with fewer sources used per bin, when increasing the SNR threshold, the variance and hence the dispersion would decrease rather than increase. This effect tells us something about our data. Upon investigation, several possible 'duplicates' were identified whereby very similar LOSVs were seen very near each other. If multiple sources in the bin have the same LOSV then the variance decreases, however, whilst possible, it is unlikely that they would be nearby. The cause of this phenomenon is believed to be the PSF contamination previously mentioned and is investigated in Section 4.4.4.

**Table 4.8:** Sigma results with IMBH for 8-hour simulation and a limited sample of the N-body data (15<H<21). N is the number of sources in each bin.

| | Simulation with IMBH | | | N-body - limited sample | |
|---|---|---|---|---|---|
| Bin centre | $\sigma \pm \Delta\sigma$ | N | $N_{SNR>15}$ | $\sigma \pm \Delta\sigma$ | N |
| (arcsec) | (km/s) | | | (km/s) | |
| 0.0239 | - | 1 | 1 | 19 ± 8 | 3 |
| 0.0591 | 20 ± 7 | 4 | 4 | 23 ± 6 | 7 |
| 0.1461 | 16 ± 2 | 28 | 28 | 17 ± 2 | 52 |
| 0.3614 | 10.5 ± 0.9 | 92 | 92 | 13.1 ± 0.8 | 151 |
| 0.8937 | 7.2 ± 0.5 | 187 | 90 | 8.2 ± 0.3 | 532 |
| 2.2100 | 4.9 ± 0.7 | 82 | 23 | 6.2 ± 0.1 | 1113 |
| 5.4649 | - | 0 | - | 5.3 ± 0.1 | 1021 |

**Table 4.9:** Sigma results without IMBH for 8 hour simulation and a limited sample of the N-body data (15<$H_{mag}$<21).

| | Simulation without IMBH | | N-body - limited sample | |
|---|---|---|---|---|
| Bin centre | $\sigma \pm \Delta\sigma$ | N | $\sigma \pm \Delta\sigma$ | N |
| (arcsec) | (km/s) | | (km/s) | |
| 0.0239 | - | 1 | - | 1 |
| 0.0591 | - | 0 | 1.1 ± 0.8 | 1 |
| 0.1461 | 6 ± 1 | 12 | 9 ± 1 | 33 |
| 0.3614 | 4.9 ± 0.6 | 56 | 5.9 ± 0.4 | 131 |
| 0.8937 | 4.4 ± 0.3 | 152 | 5.1 ± 0.2 | 528 |
| 2.2100 | 4.2 ± 0.6 | 96 | 4.8 ± 0.1 | 1202 |
| 5.4649 | - | 0 | 4.3 ± 0.1 | 1028 |

### 4.4.3 SNR with integration time

The plot in Figure 4.27 illustrates the relationship between SNR and increasing integration time for individual stars, with the dashed line representing the theoretical expectation for SNR growth under ideal conditions. In an ideal scenario, where photon noise is the dominant noise source, we expect the SNR to improve proportional to the square root of the integration time, as indicated by the Poisson limit (SNR$\propto \sqrt{\text{exposure time}}$). This means that as the exposure time increases, the SNR should increase consistently, leading to a higher quality spectrum with reduced noise (which increases as $\sqrt{t}$).

Most of the stars in this plot approximately follow this theoretical trend, especially the faint to moderately bright stars. As the integration time increases, the influence of detector read noise diminishes, and the dominant source of noise

becomes photon noise, which allows the SNR to grow effectively as expected. This is evident from the lines for individual stars having the same slope with increasing integration time as the dashed line (theoretical curve).

However, the behaviour of the brighter stars deviates from this ideal trend. Instead of experiencing the same SNR growth, their SNR improvement with increasing exposure time is more limited. This deviation is partly due to contamination from nearby star PSFs. For these bright stars, overlapping PSFs from adjacent sources introduce additional noise that is not mitigated by simply increasing the integration time. As the integration time increases, the contamination remains a significant factor, preventing the SNR from increasing as effectively as it does for fainter stars. Consequently, the SNR of these bright stars do not reach the ideal Poisson limit, resulting in much slower improvement rates compared to uncontaminated stars.

Another source of this unexpected relationship between SNR and integration time is the presence of an extra system effect which is the systematic template mismatching caused by the wavelength shift bug in the HSIM software described earlier. This issue will systematically restrict pPXF's ability to match the template to the spectra causing the increase in residuals.

In summary, while increasing integration time generally improves SNR by reducing the impact of read noise, the presence of overlapping PSFs complicates this improvement for bright stars. The additional systematic noise from PSF contamination and template mismatch becomes the limiting factor, leading to a less pronounced SNR gain with increasing exposure time compared to what is theoretically expected under photon noise limited conditions.

### 4.4.4 Effect of PSF contamination on velocity determination

To understand the impact of PSF contamination on the success of the LOSV determination process the simulated data can be compared with the input N-body 'truth' data.

Figure 4.28 shows two example extracted spectra in the left panel. They both feature the artificial notches described in Section 4.3.3. The black spectrum show

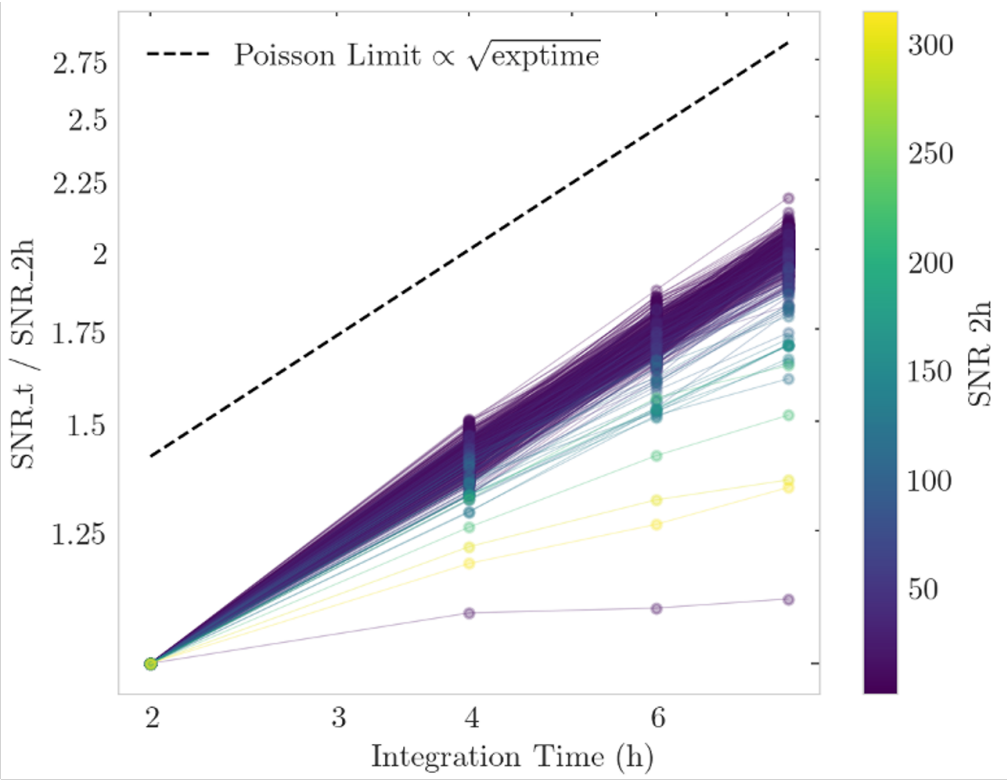


**Figure 4.27:** SNR improvement with integration time for individual stars. The plot shows the ratio of SNR for varying integration times ($SNR_t/SNR_{2h}$) against integration time, highlighting how the SNR increases with longer exposure. Each line represents an individual star, coloured by the initial SNR at 2 hours. The dashed line indicates the theoretical Poisson limit ($\propto \sqrt{\text{exposure time}}$), showing the expected scaling for an ideal noise-limited case. A single outlier to this is shown as the purple line at the bottom.

not clear sign of PSF contamination, whereas the red spectrum shows three clear notches between 14,500 and 15,000 Å. In the right panel, statistics are plotted for each of the two spectra. The solid lines show how the (unnormalised) chi-squared fit from the pPXF template spectrum fitting varies when forcing LOSV to be a specific value, the minima denote the estimated velocity as shown by the vertical dotted line compared to the input velocity from the N-body in the dot-dashed line. The dashed curve shows how the SNR, from Equation 4.10, varies from the same pPXF fits.

The plot clearly shows that the contaminated spectrum produces a larger error in the velocity estimated. The chi-squared curve is broadened and the SNR curve is misshapen due to the effect of contamination. Figure 4.28 is just one example, more are shown in the Appendix in Figure A.12.

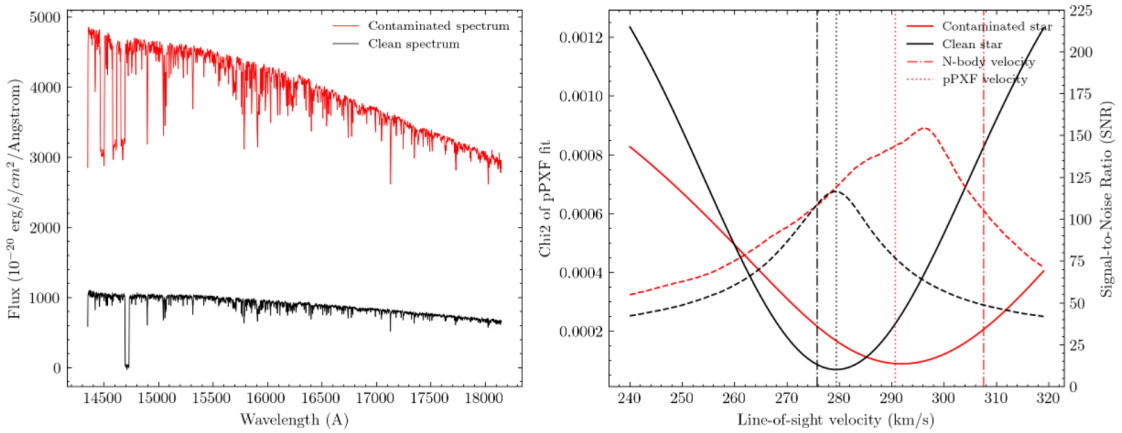


**Figure 4.28:** The extracted spectra of two example stars (left) one which has no obvious PSF contamination and another with significant contamination from at least two other nearby stars as shown by the three notches. The varying chi-squared fit of the spectra for fixed LOSVs are plotted with solid lines (right) and the SNR at the same velocities as dashed lines. The input LOSV from the N-body for each star is shown as a vertical dot-dashed line, and the resulting estimated velocity by pPXF as a dotted line.

## 4.5 Discussion and conclusion

This study demonstrates the potential of using HARMONI on the E-ELT to detect IMBHs within star clusters by employing sophisticated simulations and data reduction methods. The simulated observational data enabled an investigation into the kinematic profile of a star cluster representative of R136, and the results show that HARMONI's high angular resolution spatially resolved spectroscopic capabilities are well-suited for this science case.

The primary kinematic indicator for the presence of an IMBH is an elevated velocity dispersion towards the centre of the cluster, which can be captured through high-fidelity line-of-sight velocity measurements. The simulations conducted with and without an IMBH reveal notable differences, particularly in the central velocity dispersions, thereby supporting the potential of kinematic studies for IMBH detection.

Whilst these simulations indicate that the fundamental performance of HARMONI is capable of resolving stars and their spectra in crowded fields to provide strong evidence for the presence or absence of a central IMBH, extracting the

full potential of such an observation requires a more robust approach to spectra extraction accounting for the instrument PSF.

### 4.5.1 Improvements to spectrum extraction

Accurately extracting spatially resolved stellar spectra with high SNR from IFS datacubes of observations of crowded stellar fields requires sophisticated algorithms. They need to account for a spectrally varying PSF and make the effort over many stars computationally feasible.

This work could make use of a software tool called 'PampelMuse', the workings of which are originally described in [54]. This Python-based software package is designed to aid the analysis of IFS observations of crowded stellar fields. It requires, as a prerequisite, a high-fidelity catalogue of input source locations. For real observations, this would typically be provided by high-resolution HST data from publicly available catalogues. However, for N-body simulations, this catalogue could be generated using the source detection algorithm DAOFIND [94] as described in Section 4.3.1.

PampelMuse enables a range of different instrument PSFs to be used for the disentanglement of crowded fields such as Gaussian or Moffat approximations, however, they are typically rotationally symmetric (barring some slight ellipticity) which limits their effectiveness with HARMONI.

#### PSF fitting

A proper model of the PSF allows to accurately extract photometric and spectral information, especially from densely populated star clusters where sources are close together and overlapping.

The Moffat profile, introduced by Anthony Moffat [73], is frequently used to describe the PSFs of optical systems. It is characterised by its ability to handle the extended wings of the PSFs, particularly relevant to AO PSFs, better than a Gaussian. The Moffat profile is given by the equation

$$M(r, r_d, \beta, I) = \frac{I \cdot (\beta - 1)}{\pi r_d^2} \left(1 + \left(\frac{r}{r_d}\right)^2\right)^{-\beta}, \tag{4.14}$$

where

- $I$ is the intensity normalization factor, related to the peak intensity of the PSF.
- $\beta$ is the shape parameter, affecting the kurtosis or the decay of the profile's wings.
- $r_d$ is the effective radius, indicating the scale of the PSF spread.
- $r$ is the radial distance from the centre of the profile,

$$r = \sqrt{(x - x_0)^2 + (y - y_0)^2}. \tag{4.15}$$

- $x, y$ are the spatial coordinates in the 2D image.
- $x_0, y_0$ are the coordinates of the centre of the PSF.

The normalisation factor ensures that the total integral of the Moffat function over the plane equals the peak intensity $I$. The parameter $\beta$ significantly influences the profile's wings; higher values lead to a sharper peak and less pronounced wings, which is often a more accurate representation of star images in astronomical data.

The double Moffat profile is an extension that uses two Moffat functions to capture different components of the PSF:

$$M(x, y) = M_1(x, y) + M_2(x, y), \tag{4.16}$$

where $M_1$ and $M_2$ are individual Moffat profiles.

The double Moffat profile allows for better fitting of the central and peripheral light distribution of stars, enhancing the accuracy of flux measurements. It can also enable improved deblending of overlapping stars by accurately modelling the wings and preventing flux from one star from contaminating another.

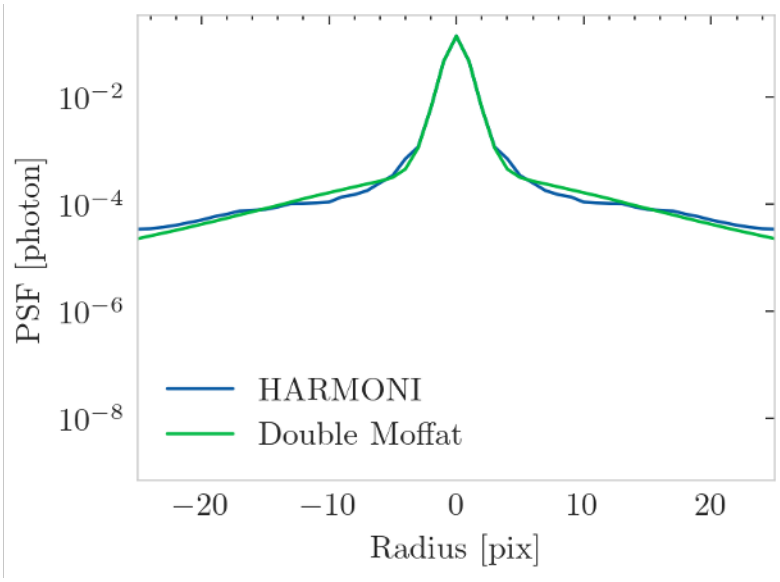


**Figure 4.29:** Double Moffat fit to the over-sampled HARMONI PSF.

A double Moffat fit of the HARMONI PSF provided by HSIM is shown in Figure 4.29; whilst using this to extract spectra might improve the contamination from the PSF wings, it is still axisymmetric and so the discrete PSF features would remain. A more sophisticated model of the PSF including these non-axisymmetric features is required to fully deal with the impact of PSF contamination in the extraction of spectra from crowded stellar fields.

### 4.5.2 Assumptions and simplifications

Throughout this chapter's work there were a number assumptions and simplifications made. In the absence of a full quantitative analysis of each of these and their impact on the results, the key aspects are qualitatively discussed below.

- **Spectral extraction using fixed '+' shaped apertures.** As described previously a large proportion (50 to 60%) of the expected total flux of a star. A more sophisticated approach could increase this value significantly. A perfectly isolated star with very high SNR, one might aim to extract close to 100% of its light using an appropriately sized aperture or a well-fitted PSF model. The accuracy might be limited by photon noise from the star itself, detector noise, and calibration uncertainties, potentially reaching accuracies

of a few percent or better. In moderately crowded fields, good PSF fitting techniques can still recover a large fraction of a star's flux, but with increased uncertainty due to the deblending process. In extremely crowded fields (like the core of a star cluster), it becomes very challenging. Significant blending means that the flux attributed to any given star is an estimate that depends heavily on the deblending algorithm's ability to apportion the light from overlapping profiles. For faint stars, the fraction of flux reliably extracted is limited by the SNR. Below a certain brightness, the star becomes undetectable against the noise. This all suggests that for the moderately or well isolated stars the SNR of the extracted spectra could be improved leading to more accurate LOSV determination, but the impact would be more limited in more crowded parts of the field.

- **Every star has the same spectrum.** Ideally a unique spectrum for each star would be used. In a real observation, one would rely on the availability of a library of templates suitable for the ages and metallicity of the R136 cluster that would match the observed stars, if these cannot be found then the analysis would suffer. If some stars are relatively featureless in the H-band, then you will have few absorption lines with which to determine the LOSV, so that may become less accurate. However, on the upside, not having the same spectra will mean that it is easier to detect contamination.

- **Removing the brightest stars from simulation to reduce contamination.** Also hard to quantify, the existence of brighter stars in the field would exacerbate the blending issue and increase reliance on robust spectra extraction. It is argued here that the combination of the removal of the bright stars and the lack of robust extraction for the remaining stars counteract each other in their impact.

### 4.5.3 Chapter summary

This chapter presented a detailed framework for simulating HARMONI observations of globular clusters to detect IMBHs. It included the preparation of observational simulations, data reduction procedures, and kinematic analyses. By utilising realistic N-body simulations and advanced data processing tools, we demonstrated that detecting IMBHs is feasible using line-of-sight velocities obtained from an IFS such as HARMONI.

We have highlighted the criticality of deblending PSFs in crowded fields, the need to account for field rotation in simulated observations with non-rotationally symmetric PSFs, and the necessity of accurate modelling of complex AO PSFs in spectrum extraction.

With these improved analysis techniques we deem the E-ELT with an IFS such as HARMONI capable of identifying a central IMBH of mass $10^4$ $M_\odot$ in a star cluster.

### 4.5.4 Lessons learnt

Here I summarise some key lessons learnt during this research.

- **Efficient and robust software design:** When embarking on simulation and data analysis-based research such as this, it is important to consider early on the approximate data sizes that will need to be handled so that the appropriate hardware and software considerations can be made. It is also good practice to write software in a robust yet flexible manner which can be used in a number of ways, for example not hard-coding specific values which may need to be modified or varied in future. I've learnt a lot a software development and improved significantly throughout this process.

- **PSF complexity matters:** The use of an AO-corrected PSF, replete with side lobes and spatial asymmetries, significantly complicates both source detection and spectrum extraction in crowded fields. Any future data analysis strategy must incorporate detailed PSF models or iterative methods that can handle non-axisymmetric and wavelength-dependent features.

- **False detections and contamination:** Even moderate levels of contamination in a compact star cluster lead to misidentified sources and false velocity measurements. Embedding artificial spectral "markers" helped track star-by-star contamination, this method is of course limited to simulated work, therefore more robust methods are needed to simultaneously fit overlapping PSFs and isolate valid LOSVs in real observations.

- **Multi-hour exposure advantages:** Longer total integration times improve results up to a point—particularly for moderately bright and faint stars—yet bright-star contamination remains an intrinsic limitation. This finding underlines the need for robust data reduction software capable of handling overlapping PSF wings rather than relying solely on increased exposure time.

- **Value of advanced software tools:** Techniques like PampelMuse, or other advanced crowded-field IFS data analysis tools, are indispensable for extracting high-fidelity spectra in highly dense clusters. Incorporating flexible PSF models, especially double Moffat or higher-order fits, can mitigate the challenges inherent to AO-fed instruments.

### 4.5.5 Evaluation and future work

There are a number of aspects which can be improved upon or developed further in this research. Here are some proposed future activities:

- **Incorporate more realistic stellar spectra:** Assigning each star a unique synthetic spectrum based on its mass, metallicity, and evolutionary stage would yield more accurate mock data. This step would allow for improved velocity measurements and more nuanced assessments of contamination.

- **Improve binning and visualisation:** A simplistic approach was taken to the binning which used a logarithmic spacing regardless of the number of sources in each bin. Ideally, we would have greater statistics towards the centre, but crowding is a limiting factor here. An improvement would be to

fix the number of sources per bin to guarantee maximum uncertainty. Then when plotted on the line-of-sight velocity dispersion profile the bin location was taken as the mid-point between the bin start and end, this is slightly misleading and could be improved by using a geometric mean, or perhaps better yet, taking the median sample radius from the sources used.

- **Develop a non-axisymmetric PSF-fitting tool:** Expanding upon existing algorithms, an instrument-specific pipeline would handle the distinctive shapes produced by segmented ELT mirrors and AO corrections. Such a code could enable star-by-star modelling of residuals to optimise LOSV recovery.

- **Simulate field rotation and time dependence:** Incorporating realistic field rotation during multi-hour observations, plus time-dependent changes in the AO system or atmospheric turbulence, would generate more faithful data sets. This is crucial for establishing the reliability of multi-night or long-exposure campaigns designed to detect IMBH-induced kinematic signatures.

- **Explore anisotropy and rotation in cluster dynamics:** Beyond a purely isotropic velocity dispersion profile, many real clusters show rotation or line-of-sight vs. tangential velocity anisotropies [15]. Investigating these complexities through extended simulations would provide an even stronger test of HARMONI's IMBH detection capabilities.

- **IMBH mass estimation:** Further dynamical modelling can be performed to estimate and constrain the mass of the detected IMBH [87][15], noting that care must be taken in distinguishing between mass and orbital anisotropy [14].

The era of extremely large telescopes is nearly upon us and many astronomical discoveries await. We hope this study can help play its part in laying the groundwork for confirmed detection of IMBHs.

# Appendices

# A

# Appendices

## Contents



## A.1 Chapter 2 Appendix

This appendix is used for additional supporting material relating to the diffraction grating test bench development work discussed in Chapter 2.4.3.

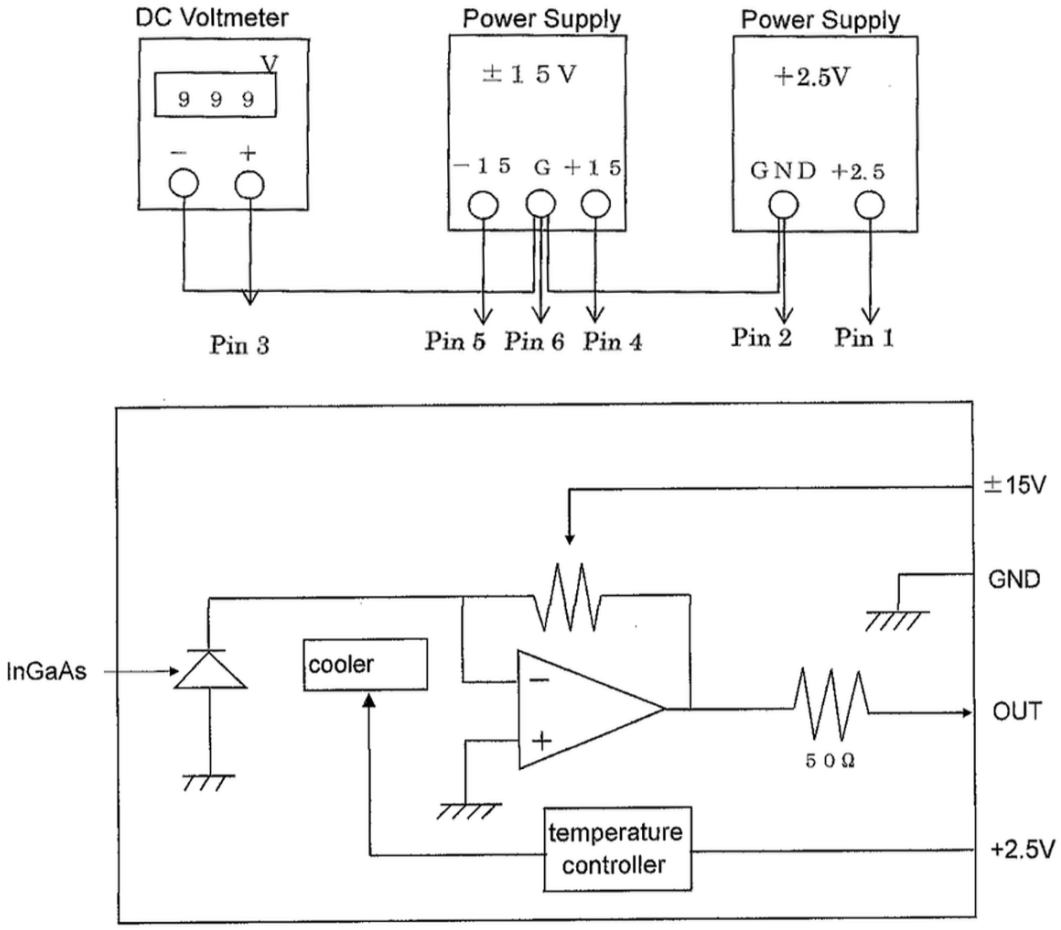


**Figure A.1:** Hamamatsu photodetector electrical power pin drawing (top) and block diagram (bottom) (credit: Hamamatsu Photonics K.K).

### A.1.1 Photodetector electrical drawings

## A.2 Chapter 3 Appendix

This appendix is used for additional supporting material relating to the diffraction grating test results work discussed in Chapter 3.5.3.

### A.2.1 Grating drawing

The mechanical drawing for the MR3 (H-band) grating is shown in A.2.

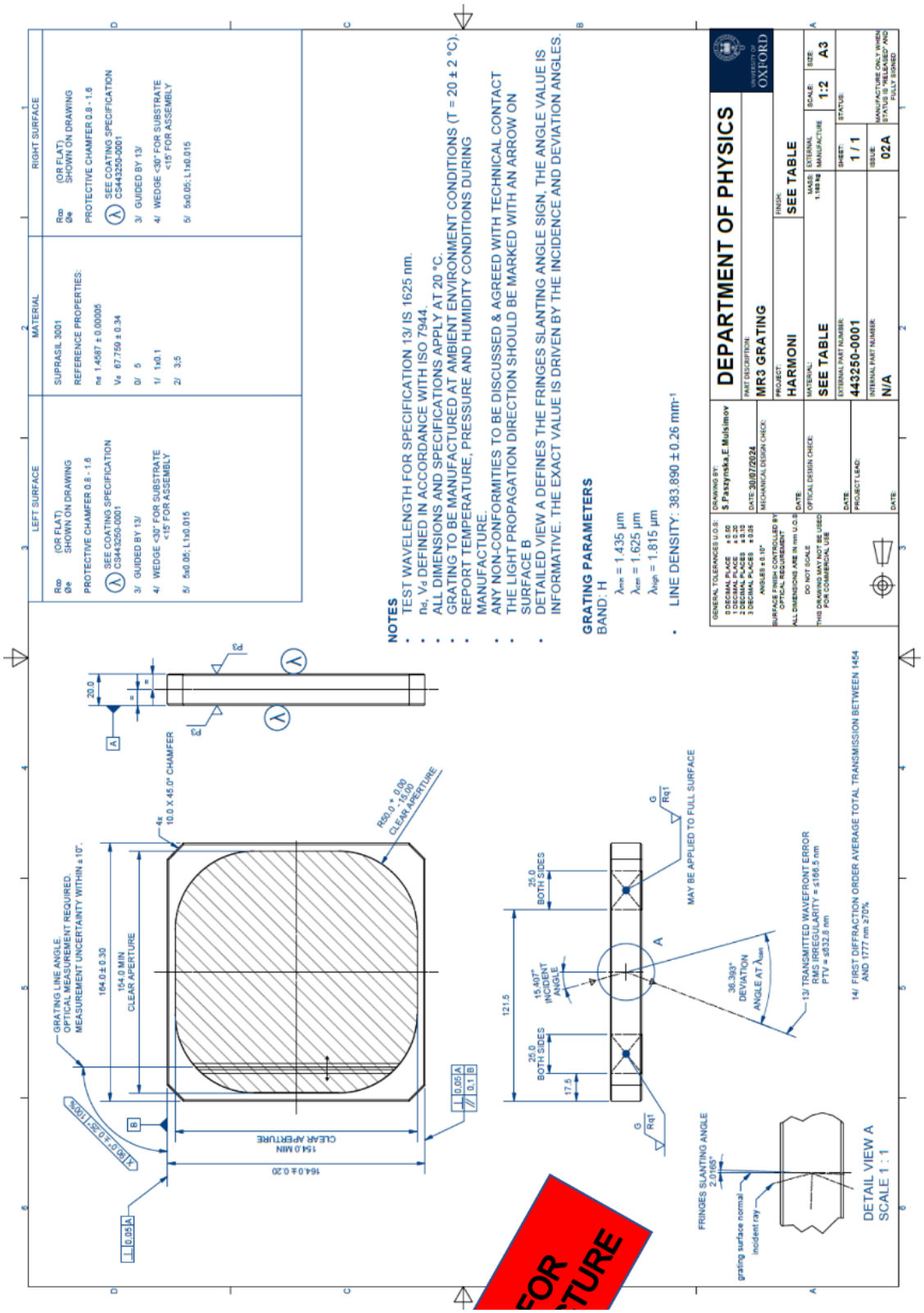


**Figure A.2:** The mechanical drawing of the MR3 grating which was sent to suppliers to assess manufacturability and receive quotations (credit: Oxford HARMONI team).

### A.2.2 Software masks for spaxel scale footprints

Figure A.3 shows the sizes and shapes of the software masks used to approximate the beam footprints on the grating for different spaxel scales.

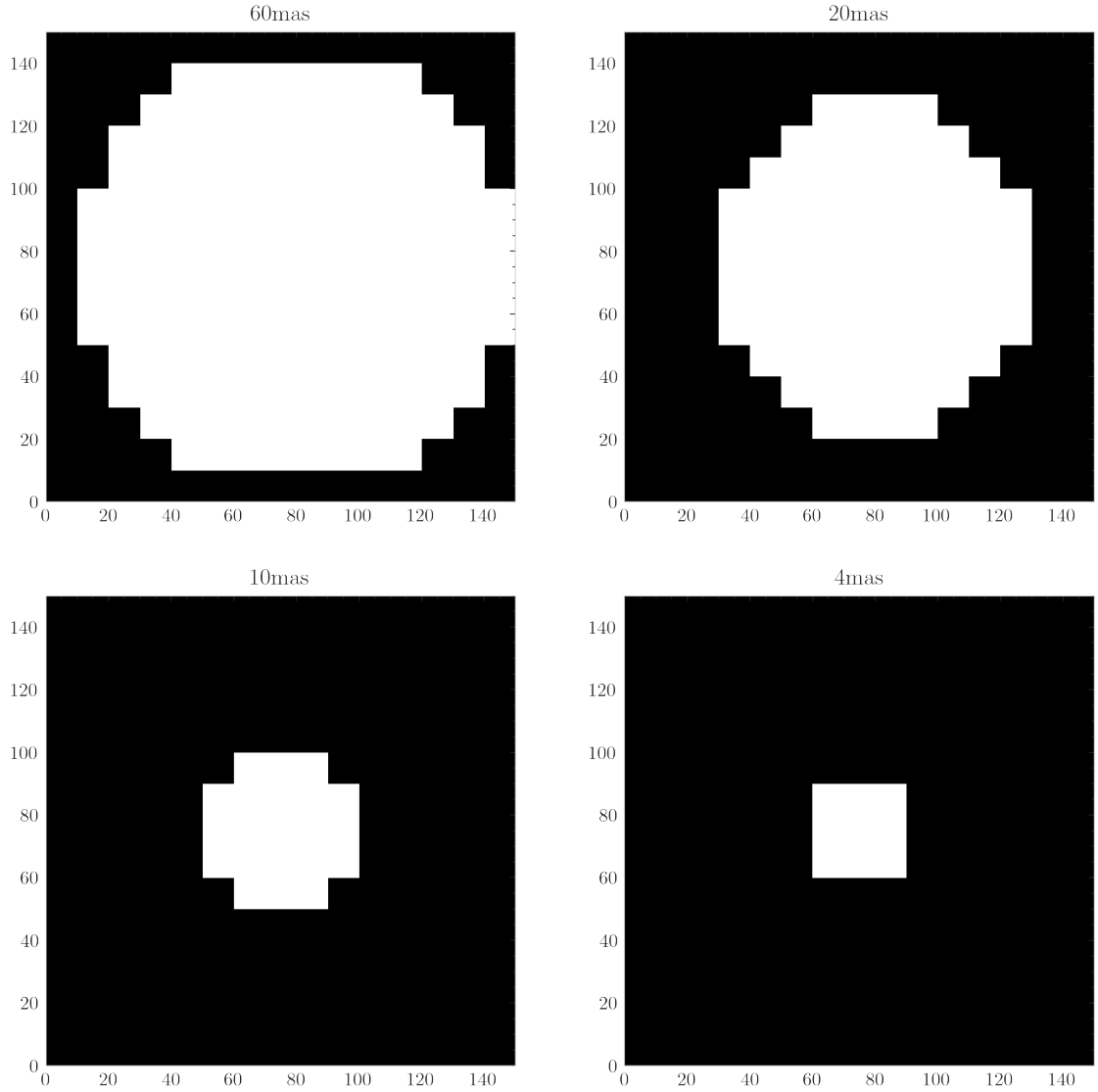


**Figure A.3:** Masks used to approximate beam footprints at the grating for different spaxel scales. The X and Y axes here are in millimetres.

### A.2.3 Incoming inspection process

I implemented an incoming inspection process that is applicable to lenses and gratings which aids quality control and traceability for the AIT phase of the instrument. The example, configured for gratings, in Figure A.4 shows a scanned

copy of a completed document for one of the MR3 prototype gratings. Upon receiving the part from the supplier the engineer/technician documents the details of the part, and follows the procedure ensuring photographs are taken of each step. Surface features and blemishes are marked in the diagram at the bottom.

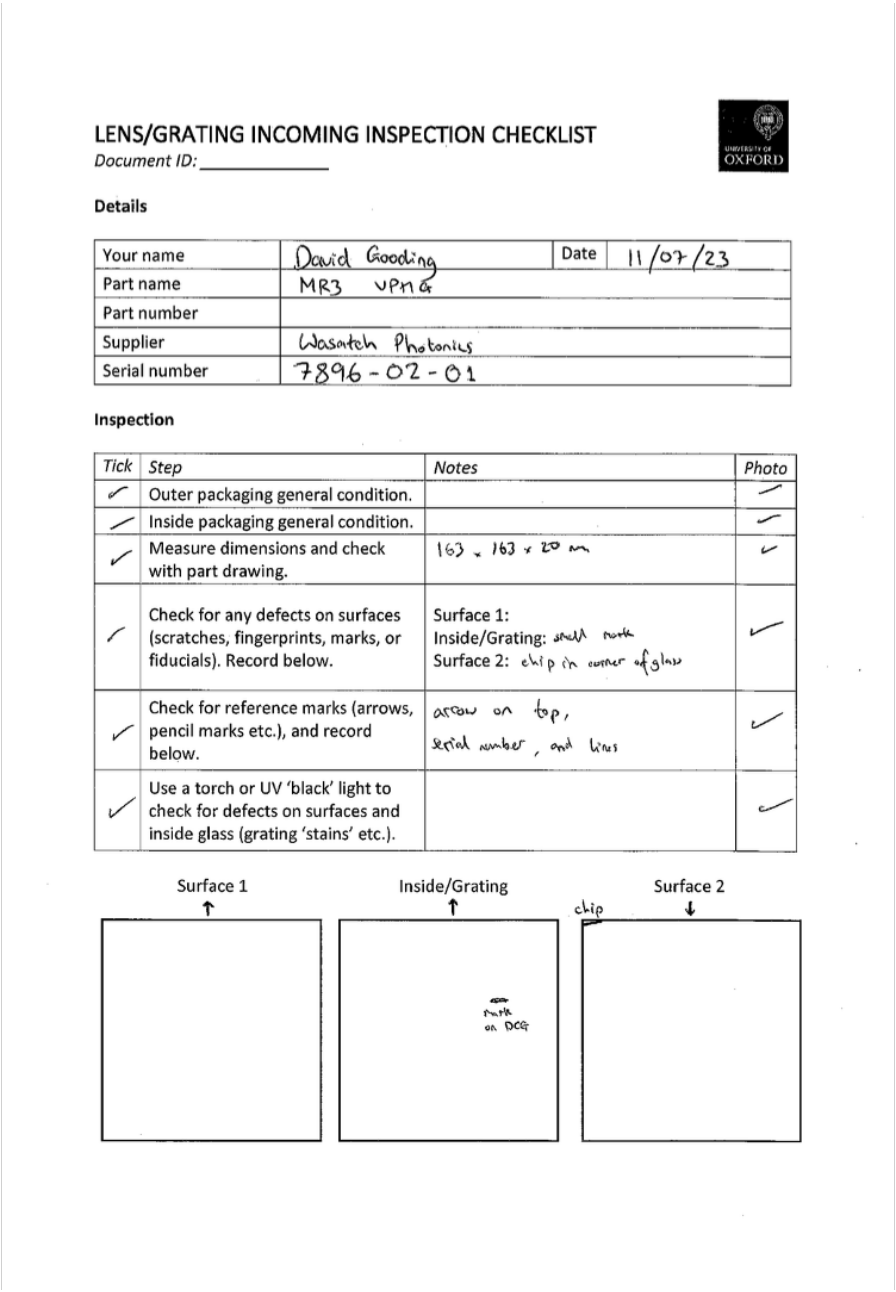

**LENS/GRATING INCOMING INSPECTION CHECKLIST**

*Document ID:* _____

UNIVERSITY OF OXFORD

**Details**

| | | | |
|---|---|---|---|
| Your name | David Gooding | Date | 11/07/23 |
| Part name | MR3 VPH G | | |
| Part number | | | |
| Supplier | Wasatch Photonics | | |
| Serial number | 7896-02-01 | | |

**Inspection**

| *Tick* | *Step* | *Notes* | *Photo* |
|---|---|---|---|
| ✓ | Outer packaging general condition. | | ✓ |
| ✓ | Inside packaging general condition. | | ✓ |
| ✓ | Measure dimensions and check with part drawing. | 163 × 163 × 20 mm | ✓ |
| ✓ | Check for any defects on surfaces (scratches, fingerprints, marks, or fiducials). Record below. | Surface 1:<br>Inside/Grating: small mark<br>Surface 2: chip in corner of glass | ✓ |
| ✓ | Check for reference marks (arrows, pencil marks etc.), and record below. | arrow on top,<br>serial number, and lines | ✓ |
| ✓ | Use a torch or UV 'black' light to check for defects on surfaces and inside glass (grating 'stains' etc.). | | ✓ |



**Figure A.4:** An example incoming inspection form, completed for one of the MR3 prototype gratings.

### A.2.4 Glass substrate transmission

Here is shown a plot from Edmund Optics which compares the transmission of a 5 mm thick sample of each of the two glass substrate materials used for different HARMONI gratings.

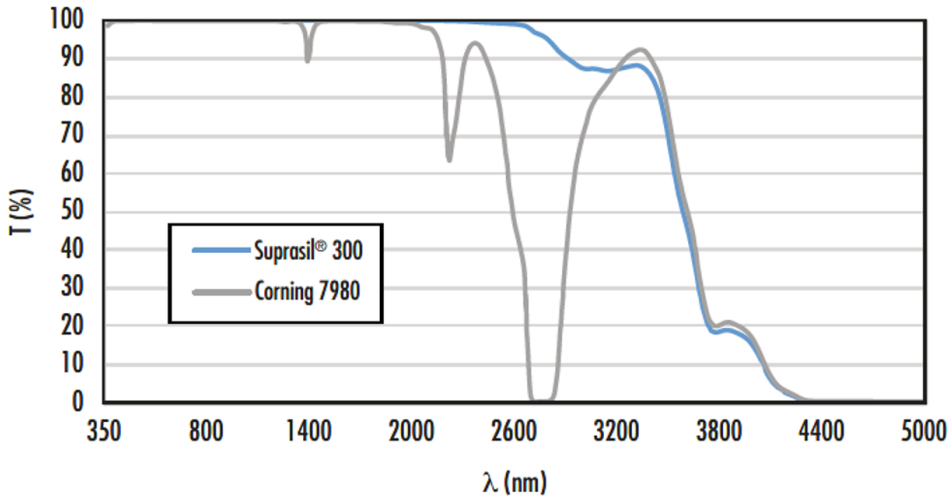


**Figure A.5:** Comparing the transmission of 5 mm thick samples of Corning 7980 and Suprasil glass (credit: Edmund Optics).

## A.3 Chapter 4 Appendix

This appendix is used for additional supporting material relating to the IMBH work discussed in Chapter 4.5.5.

### A.3.1 Raw datacube maker Python file

One of the Python programmes developed in Chapter 4.5.5 is called "`create_marcs_datacube.py`", and its key active functions are summarised in Table A.1.

### A.3.2 HSIM configuration file

Figure A.6 shows a screenshot of a .ini file which is used as a configuration file when running HSIM from the command line.

**Table A.1:** Summary of active functions in `create_marcs_datacube.py`.

| Module Name | One-Line Description | Lines |
|---|---|---|
| `create_harmoni_datacube` | Creates an empty datacube with the specified dimensions, wavelength range, and FITS header | 28 |
| `open_marcs_spectra` | Opens MARCS spectrum in a `.flx` file from a directory | 23 |
| `rebin_spectrum_bspline` | Rebins a spectrum to a constant spectral sampling using interpolation | 21 |
| `scale_vega` | Scales a spectrum to match a target magnitude in the H band using Vega as reference | 79 |
| `apply_spectra_from_file` | Loads source coordinates, applies MARCS spectra to a datacube, and scales them to Vega | 158 |
| `redshift_star` | Applies a combined LMC + stellar radial velocity redshift to the input wavelengths | 33 |
| `add_stellar_spectrum` | Inserts a stellar spectrum into the specified spaxel of the datacube | 40 |
| `crop_spectrum` | Crops the input spectrum to the chosen HARMONI band | 37 |
| `harmoni_band` | Returns the start and end wavelengths in Angstroms for the specified HARMONI band | 52 |
| `load_config` | Loads parameters from a config file (ignoring inline comments) | 61 |
| `load_json_config` | Loads parameters from a JSON configuration file | 7 |
| `split_fits_datacube` | Splits the datacube along the spectral axis into multiple overlapping parts | 47 |
| `marcs_condition` | Calculates the MARCS wavelength step size in the middle of the selected HARMONI band | 39 |
| `main` | Main routine creating and populating a datacube with MARCS spectra, then saving to FITS | 88 |
| `__main__` block | Parses command line interface arguments, loads config, and calls `main` | 26 |

### A.3.3 FITS file header

Figure A.7 shows a screenshot of the header of a raw input HSIM datacube produced with the code "`create_marcs_datacube.py`". QFitsView is used to display the datacube and the header.

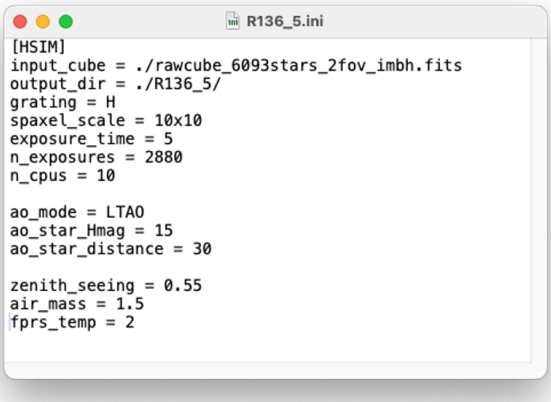


**Figure A.6:** An example configuration file used as an input to HSIM.

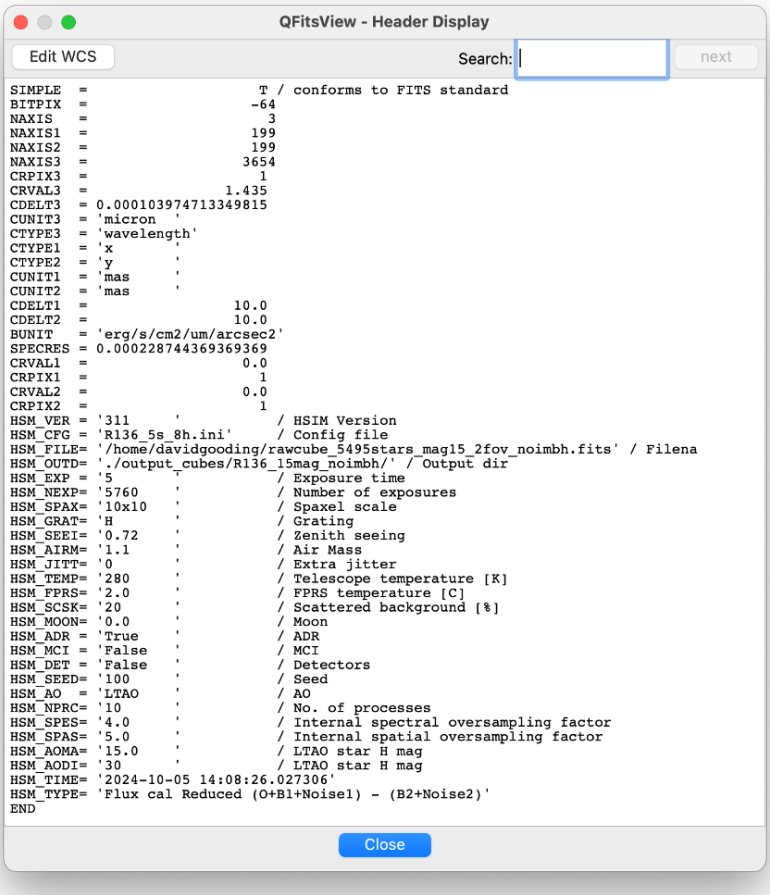


**Figure A.7:** The header information of an example HSIM output datacube.

### A.3.4 HSIM simulated background and transmission

Both Figure A.8 and A.9 are outputs from HSIM and they show the background emission and system transmission, used in the simulation, respectively.

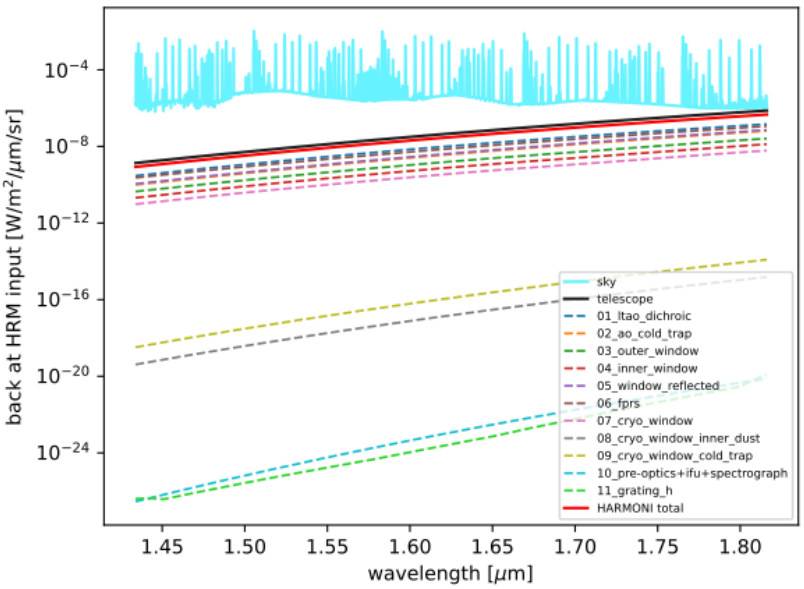


**Figure A.8:** Plot of the background emission broken up into the individual modelled components. The total HARMONI instrument total is also indicated.

### A.3.5 Velocity comparison

Figure A.10 shows a comparison between the input N-body velocity and the extracted velocity of each detected star coloured by the SNR of the spectrum.

### A.3.6 Velocity difference vs SNR

Figure A.11 shows the difference between the input and output velocity of each detected star plotted against the SNR of the spectrum, and coloured by the expected magnitude of each source.

### A.3.7 PSF contamination effect on LOSV determination

Figure A.12 shows the analysis undertaken to prove the impact of PSF contamination on the LOSV determination.

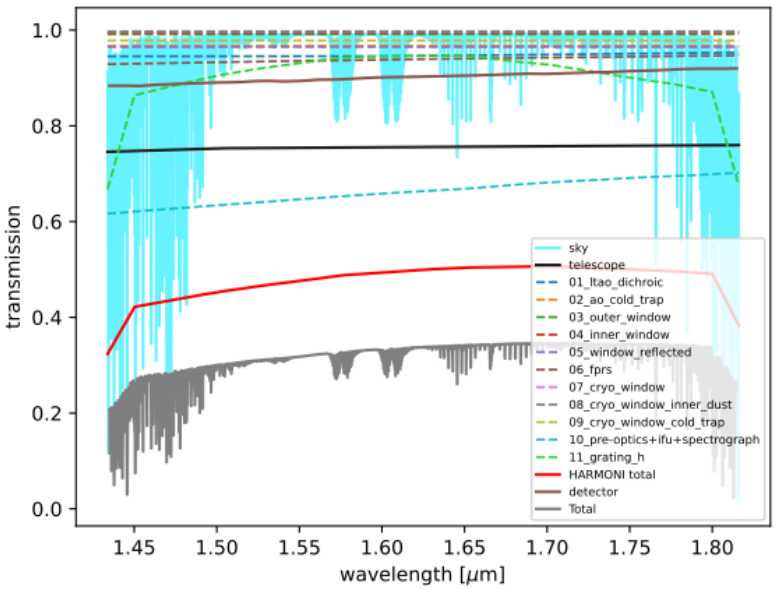


**Figure A.9:** Plot of system transmission broken up into the individual modelled components. The average HARMONI, sky, and telescope backgrounds are also indicated.

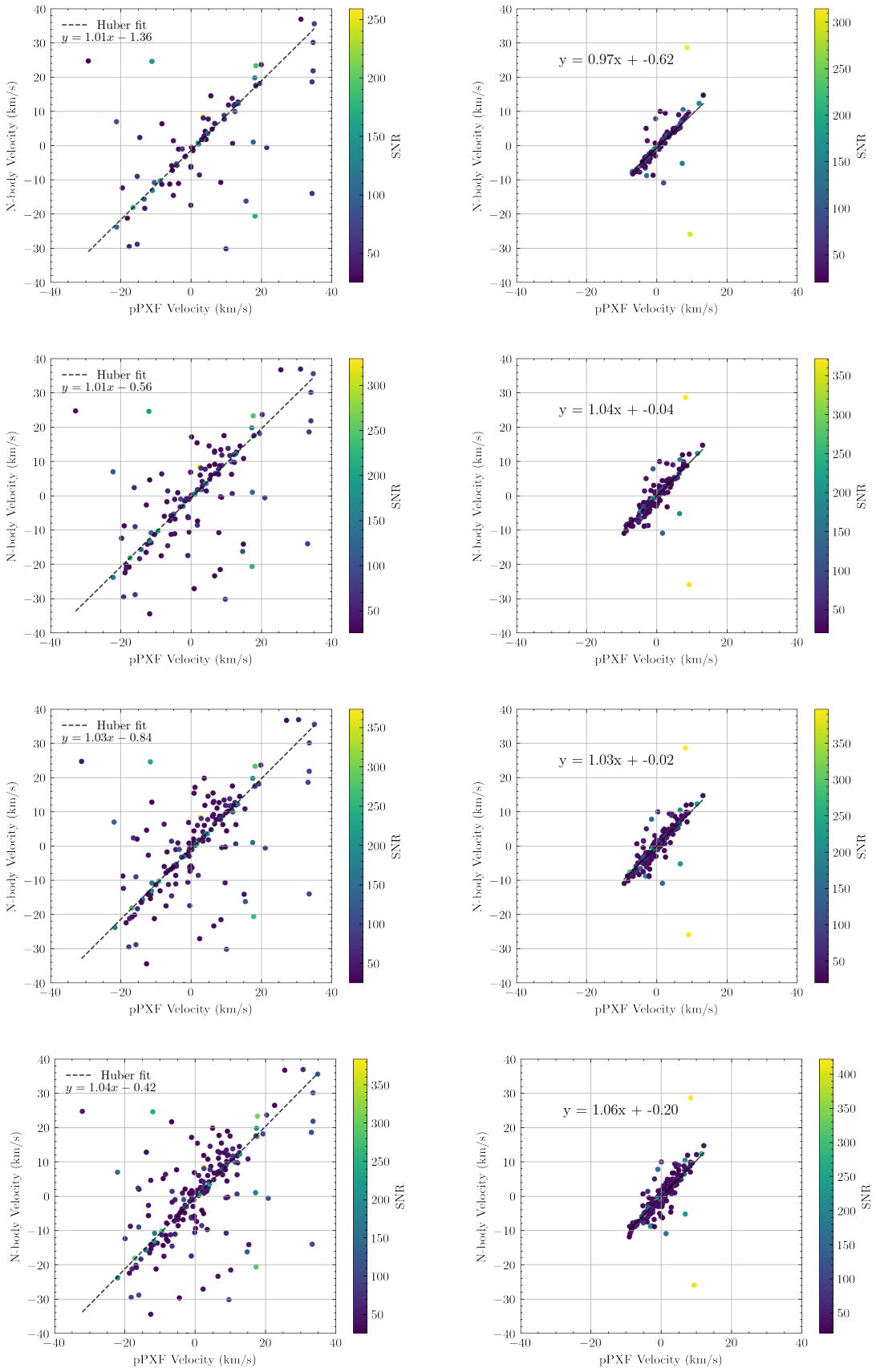


**Figure A.10:** These plots show the input N-body LOSV vs. the detected LOSV with pPXF. The left column is for the with-IMBH case, and the right column is without an IMBH. The rows are for different integration times, from the top 2, 4, 6, and 8 hours. A linear best fit is achieved using a Huber loss function [50] which is robust to outliers.

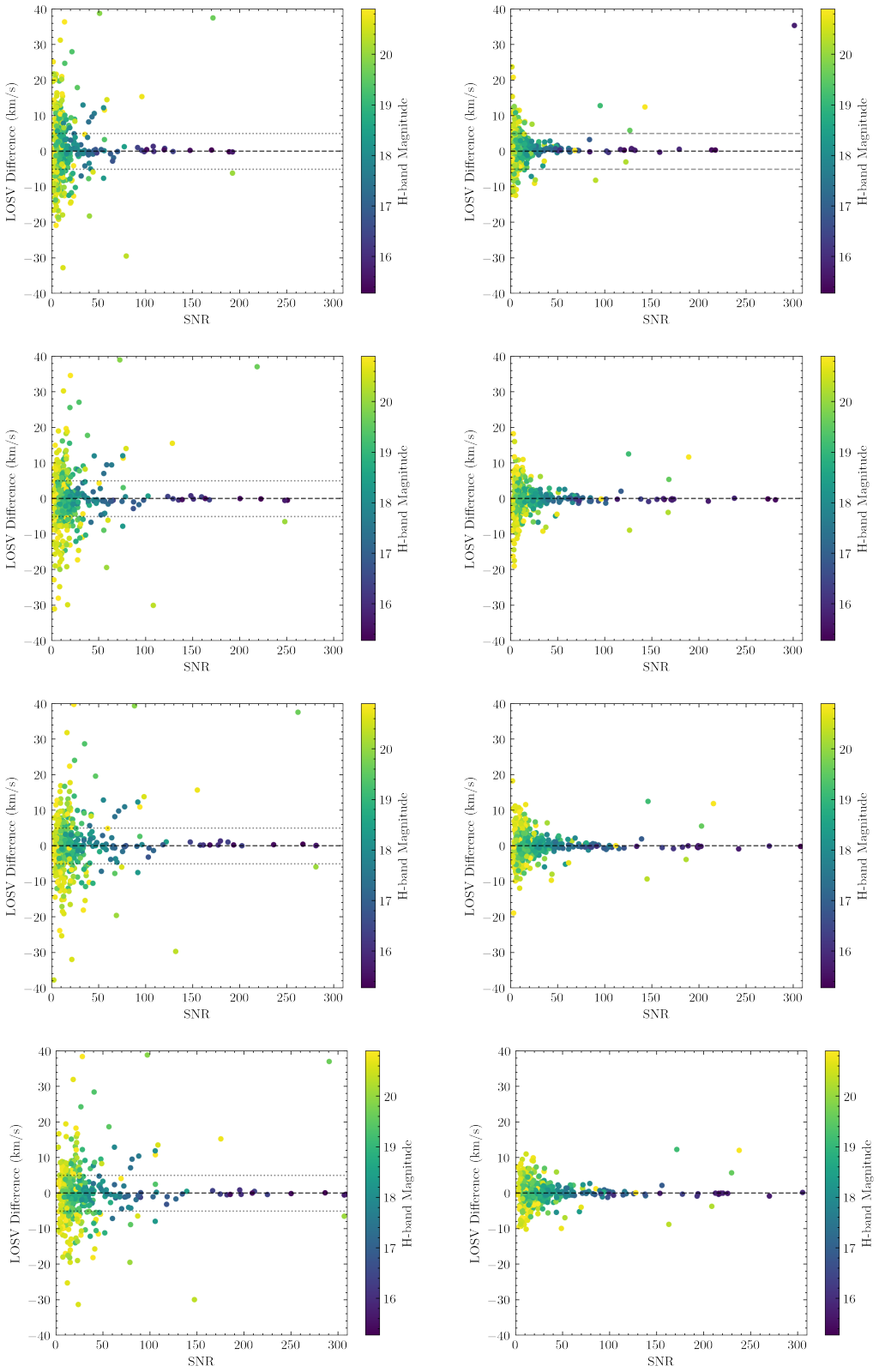


**Figure A.11:** These plots show the difference between the input N-body LOSV and the detected LOSV with pPXF vs. the SNR of the pPXF fit. The left column is for the with-IMBH case, and the right column is without an IMBH. The rows are for different integration times, from the top 2, 4, 6, and 8 hours. The grey dashed lines show the ±5 km/s regime where it is considered to be a good estimation.

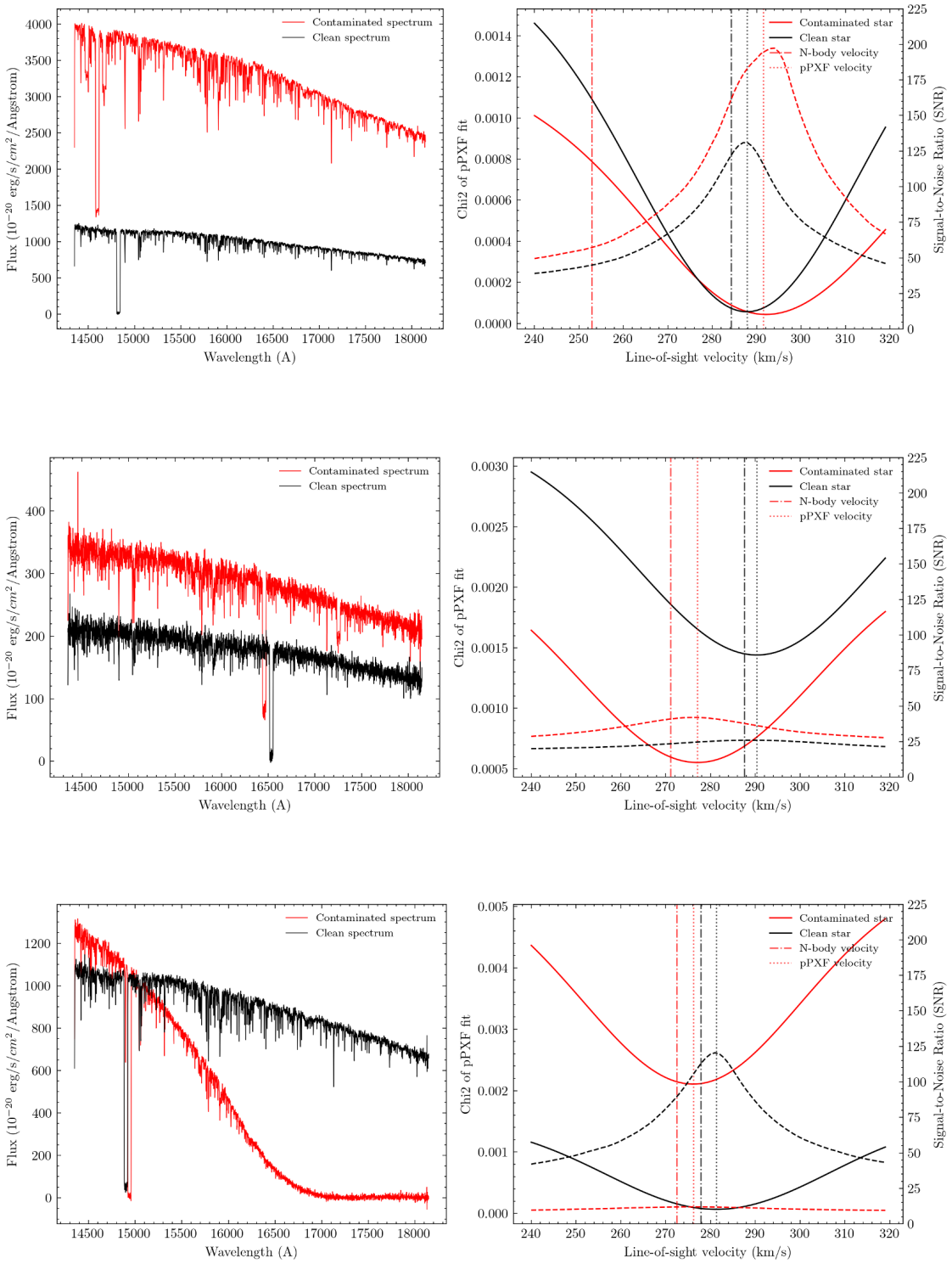


**Figure A.12:** Three more examples of spectrum comparison, as in Figure 4.28. A similarly contaminated spectrum is shown from one of the stars in the three-star group from the original plot (top). Next, a low SNR example with minor contamination is shown by a small secondary notch at around 1725 nm (middle). Finally, a different example which may be a faint star contaminated heavily by a wavelength-dependent discrete PSF feature.

# References


[1] Pau Amaro-Seoane et al. “Laser Interferometer Space Antenna (LISA L3 mission proposal)”. In: *arXiv preprint, arXiv:1702.00786* (2017). URL: http://arxiv.org/abs/1702.00786.

[2] Jay Anderson and Ivan R. King. “The Rotation of the Globular Cluster 47 Tucanae in the Plane of the Sky”. In: *The Astronomical Journal* 126.2 (2003), pp. 772–777.

[3] R Bacon. “The integral field spectrograph TIGER: results and prospects”. In: *International Astronomical Union Colloquium* 149 (1995), pp. 239–249.

[4] R Bacon et al. “The SAURON project - I. The panoramic integral-field spectrograph”. In: *mnras* 326.1 (Sept. 2001), pp. 23–35.

[5] Roland Bacon and Guy Monnet. *Optical 3D-Spectroscopy for Astronomy*. Wiley-VCH, 2018.

[6] Roland Bacon et al. “The second-generation VLT instrument MUSE: science drivers and instrument design”. In: *Ground-based Instrumentation for Astronomy* 5492.October 2019 (2004), p. 1145.

[7] Eduardo Bañados et al. “An 800-million-solar-mass black hole in a significantly neutral Universe at a redshift of 7.5”. In: *Nature* 553.7689 (2018), pp. 473–476.

[8] Samuel C. Barden, James A. Arns, and Willis S. Colburn. “Volume-Phase Holographic Gratings and Their Potential for Astronomical Applications”. In: *Optical Astronomical Instrumentation* 3355.July 1999 (1999), pp. 866–876.

[9] Holger Baumgardt, Junichiro Makino, and Piet Hut. “Which Globular Clusters Contain Intermediate-Mass Black Holes?” In: *The Astrophysical Journal* 620.1 (Feb. 2005), p. 238. URL: https://dx.doi.org/10.1086/426893.

[10] Mitchell C. Begelman, Marta Volonteri, and Martin J. Rees. “Formation of supermassive black holes by direct collapse in pre-galactic haloes”. In: *Monthly Notices of the Royal Astronomical Society* 370.1 (2006), pp. 289–298.

[11] Jillian Bellovary et al. “Where are the Intermediate Mass Black Holes?” In: (2019). URL: http://arxiv.org/abs/1903.08144.

[12] Bentham Instruments. *Bentham Monochromator FTMc50-SCL*. 2024. URL: https://www.bentham.co.uk/products/components/tuneable-light-sources/compact/ftmc50-scl-159/.

[13] Andrea Bianco et al. “VPHGs for WEAVE: design, manufacturing and characterization”. In: (2018), p. 190.

[14] J Binney and G. A. Mamon. “M/L and velocity anisotropy from observations of spherical galaxies, or must M87 have a massive black hole ?” In: *mnras* 200 (July 1982), pp. 361–375.

[15] James Binney and Scott Tremaine. *Galactic Dynamics: Second Edition*. 2008.

[16] W S Boyle and G E Smith. "Charge coupled semiconductor devices". In: *The Bell System Technical Journal* 49.4 (1970), pp. 587–593.

[17] Larry Bradley et al. *astropy/photutils: 1.13.0*. June 2024. URL: https://doi.org/10.5281/zenodo.12585239.

[18] H Bragg W and L Bragg W. "X-rays and Crystal Structure". In: *Science* 44.1126 (1915), pp. 137–138. URL: https://www.science.org/doi/abs/10.1126/science.44.1126.137.

[19] B Brandl et al. "METIS: The Mid-infrared ELT Imager and Spectrograph". In: *The Messenger* 182 (Mar. 2021), pp. 22–26.

[20] Kevin Bundy et al. "Overview of the SDSS-IV MaNGA Survey: Mapping nearby Galaxies at Apache Point Observatory". In: *\apj* 798.1 (Jan. 2015), p. 7.

[21] Annie J Cannon and Edward C Pickering. "Spectra of bright southern stars photographed with the 13-inch Boyden telescope as part of the Henry Draper Memorial". In: *Annals of Harvard College Observatory* 28 (Jan. 1901), 129–P.6.

[22] John I. Capone et al. "Near infrared throughput and stray light measurements of diffraction gratings for ELT-HARMONI". In: 44.0 (2018), p. 152.

[23] Michele Cappellari. "Improving the full spectrum fitting method: Accurate convolution with Gauss-Hermite functions". In: *Monthly Notices of the Royal Astronomical Society* 466.1 (2017), pp. 798–811.

[24] Michele Cappellari and Eric Emsellem. "Parametric Recovery of Line-of-Sight Velocity Distributions from Absorption-Line Spectra of Galaxies via Penalized Likelihood". In: *Publications of the Astronomical Society of the Pacific* 116.816 (2004), pp. 138–147.

[25] B W Carroll and D A Ostlie. *An Introduction to Modern Astrophysics*. Pearson Addison-Wesley, 2007. URL: https://books.google.co.uk/books?id=M8wPAQAAMAAJ.

[26] N. Castro et al. "Mapping the core of the Tarantula Nebula with VLT-MUSE: I. Spectral and nebular content around R136". In: *Astronomy and Astrophysics* 614 (2018), pp. 1–50.

[27] A. J. Cenarro et al. "Empirical calibration of the near-infrared Ca II triplet - I. The stellar library and index definition". In: *Monthly Notices of the Royal Astronomical Society* 326.3 (2001), pp. 959–980.

[28] Taylor S. Chonis et al. "Mass production of volume phase holographic gratings for the VIRUS spectrograph array". In: *Advances in Optical and Mechanical Technologies for Telescopes and Instrumentation* 9151 (2014), 91511J.

[29] Martin Cohen, Wm. A. Wheaton, and S. T. Megeath. "Spectral Irradiance Calibration in the Infrared. XIV. The Absolute Calibration of 2MASS". In: *The Astronomical Journal* 126.2 (2003), pp. 1090–1096.

[30] M Coleman Miller and E J M Colbert. "Intermediate-Mass Black Holes". In: *International Journal of Modern Physics D* 13.01 (2004), pp. 1–64. URL: https://doi.org/10.1142/S0218271804004426.

[31] M. Coleman Miller and E. J.M. Colbert. "Intermediate-mass black holes". In: *International Journal of Modern Physics D* 13.1 (2004), pp. 1–64.

[32] Jeffrey Crane et al. "NFIRAOS adaptive optics for the Thirty Meter Telescope". In: *Adaptive Optics Systems VI*. Ed. by Laird M Close, Laura Schreiber, and Dirk Schmidt. Vol. 10703. Society of Photo-Optical Instrumentation Engineers (SPIE) Conference Series. July 2018, p. 107033V.

[33] Scott M Croom et al. "The Sydney-AAO Multi-object Integral field spectrograph". In: *mnras* 421.1 (Mar. 2012), pp. 872–893.

[34] Paul A. Crowther et al. "The R136 star cluster dissected with Hubble Space Telescope/STIS. I. Far-ultraviolet spectroscopic census and the origin of He II $\lambda$1640 in young star clusters". In: *Monthly Notices of the Royal Astronomical Society* 458.1 (2016), pp. 624–659.

[35] R. Davies et al. "The Enhanced Resolution Imager and Spectrograph for the VLT". In: *A&A* 674 (2023), A207. URL: https://doi.org/10.1051/0004-6361/202346559.

[36] Richard Davies et al. "MICADO: the E-ELT adaptive optics imaging camera". In: *Ground-based and Airborne Instrumentation for Astronomy III*. Ed. by Ian S McLean, Suzanne K Ramsay, and Hideki Takami. SPIE, July 2010. URL: http://dx.doi.org/10.1117/12.856379.

[37] Laurent Drissen et al. "SITELLE: an Imaging Fourier Transform Spectrometer for the Canada-France-Hawaii Telescope". In: *mnras* 485.3 (May 2019), pp. 3930–3946.

[38] G. Fiorentino et al. "Deep into the core of dense star clusters: An astrometric and photometric test case for ELT". In: *Monthly Notices of the Royal Astronomical Society* 494.3 (2020), pp. 4413–4425.

[39] Giacomo Fragione et al. "Gravitational-wave Captures by Intermediate-mass Black Holes in Galactic Nuclei". In: *The Astrophysical Journal* 897.1 (2020), p. 46.

[40] Michiko S. Fujii et al. "Simulations predict intermediate-mass black hole formation in globular clusters". In: *Science* 1488 (2024), pp. 1–40.

[41] Karl Gebhardt, R. M. Rich, and Luis C Ho. "A 20,000 M$_{solar}$ Black Hole in the Stellar Cluster G1". In: *apjl* 578.1 (Oct. 2002), pp. L41–L45.

[42] Joris Gerssen et al. *Hubble Space Telescope Evidence for an Intermediate-Mass Black Hole in the Globular Cluster M15-II. Kinematical Analysis and Dynamical Modeling 1*. Tech. rep. 2002.

[43] David Gooding et al. "HARMONI at ELT: characterizing spatial variations in transmission efficiency of volume phase holographic diffraction gratings". In: *Advances in Optical and Mechanical Technologies for Telescopes and Instrumentation VI*. Ed. by Ramón Navarro and Ralf Jedamzik. Vol. 13100. Society of Photo-Optical Instrumentation Engineers (SPIE) Conference Series. Aug. 2024, 131001T.

[44] Jenny E Greene and Luis C Ho. "Active Galactic Nuclei with Candidate Intermediate-Mass Black Holes". In: *apj* 610.2 (Aug. 2004), pp. 722–736.

[45] Jenny E. Greene, Jay Strader, and Luis C. Ho. "Intermediate-Mass Black Holes". In: *Annual Review of Astronomy and Astrophysics* 58 (2020), pp. 257–312.

[46] B. Gustafsson et al. “A grid of MARCS model atmospheres for late-type stars I. Methods and general properties”. In: *Astronomy and Astrophysics* 486.3 (2008), pp. 951–970.

[47] Hamamatsu. “Infrared detector module with preamp, TEC cooled data sheet”. In: (2024).

[48] V. Hénault-Brunet et al. “The VLT-FLAMES Tarantula Survey : VII. A low velocity dispersion for the young massive cluster R136”. In: *Astronomy and Astrophysics* 546.case i (2012), pp. 1–18.

[49] Gary J. Hill et al. “The HETDEX Instrumentation: Hobby–Eberly Telescope Wide-field Upgrade and VIRUS”. In: *The Astronomical Journal* 162.6 (2021), p. 298. URL: http://dx.doi.org/10.3847/1538-3881/ac2c02.

[50] Peter J. Huber. “Robust Estimation of a Location Parameter”. In: *The Annals of Mathematical Statistics* 35.1 (1964), pp. 73–101. URL: https://doi.org/10.1214/aoms/1177703732.

[51] William Huggins. “On the Spectra of Some of the Chemical Elements”. In: *Philosophical Transactions of the Royal Society of London* 154 (Apr. 1864), pp. 139–160. URL: http://www.jstor.org/stable/108865.

[52] Yuzo Ishikawa et al. “Comprehensive Measurements of the Volume-phase Holographic Gratings for the Dark Energy Spectroscopic Instrument”. In: *The Astrophysical Journal* 869.1 (2018), p. 24. URL: http://dx.doi.org/10.3847/1538-4357/aaebfb.

[53] P Jakobsen et al. “The Near-Infrared Spectrograph (NIRSpec) on the James Webb Space Telescope. I. Overview of the instrument and its capabilities”. In: *aap* 661 (May 2022), A80.

[54] S. Kamann, L. Wisotzki, and M. M. Roth. “Resolving stellar populations with crowded field 3D spectroscopy”. In: *Astronomy and Astrophysics* 549 (2013), pp. 1–19.

[55] S. Kamann et al. “A stellar census in globular clusters with MUSE: The contribution of rotation to cluster dynamics studied with 200 000 stars”. In: *Monthly Notices of the Royal Astronomical Society* 473.4 (2018), pp. 5591–5616.

[56] Zeinab Khorrami et al. “High-contrast and resolution near-infrared photometry of the core of R136”. In: *Monthly Notices of the Royal Astronomical Society* 503.1 (2021), pp. 292–311.

[57] Ivan R. King. “The structure of star clusters. III. Some simple dvriamical models”. In: *The Astronomical Journal* 71.1 (1966), p. 64.

[58] Kirchhoff and Bunsen. “XXIV.—On chemical analysis by spectrum-observations”. In: *Q. J. Chem. Soc.* 13.3 (1861), pp. 270–289. URL: http://dx.doi.org/10.1039/QJ8611300270.

[59] Bülent Kızıltan, Holger Baumgardt, and Abraham Loeb. “An intermediate-mass black hole in the centre of the globular cluster 47 Tucanae”. In: *Nature* 542.7640 (2017), pp. 203–205.

[60] Herwig Kogelnik. "Coupled Wave Theory for Thick Hologram Gratings". In: *Bell System Technical Journal* 48.9 (1969), pp. 2909–2947. URL: https://onlinelibrary.wiley.com/doi/abs/10.1002/j.1538-7305.1969.tb01198.x.

[61] Pavel Kroupa. "On the variation of the initial mass function". In: *Monthly Notices of the Royal Astronomical Society* 322.2 (2001), pp. 231–246.

[62] James Larkin et al. "OSIRIS: a diffraction limited integral field spectrograph for Keck". In: *Ground-based and Airborne Instrumentation for Astronomy*. Ed. by Ian S McLean and Masanori Iye. Vol. 6269. Society of Photo-Optical Instrumentation Engineers (SPIE) Conference Series. June 2006, 62691A.

[63] Oliver Le Fèvre et al. "Commissioning and performances of the VLT-VIMOS instrument". In: *Instrument Design and Performance for Optical/Infrared Ground-based Telescopes*. Ed. by Masanori Iye and Alan F. M. Moorwood. Vol. 4841. Society of Photo-Optical Instrumentation Engineers (SPIE) Conference Series. Mar. 2003, pp. 1670–1681.

[64] LEUKOS. "Electro IR – NIR Supercontinuum Laser Data Sheet". In: (2019).

[65] J Norman Lockyer. "Notice of an Observation of the Spectrum of a Solar Prominence, by J. N. Lockyer, Esq". In: *Proceedings of the Royal Society of London Series I* 17 (Jan. 1868), pp. 91–92.

[66] N Lützgendorf et al. "Limits on intermediate-mass black holes in six Galactic globular clusters with integral-field spectroscopy". In: *\aap* 552 (Apr. 2013), A49.

[67] N. Lützgendorf et al. "Kinematic signature of an intermediate-mass black hole in the globular cluster NGC 6388". In: *A&A* 533 (2011), A36. URL: https://doi.org/10.1051/0004-6361/201116618.

[68] N. Lützgendorf et al. "Central kinematics of the globular cluster NGC 2808: upper limit on the mass of an intermediate-mass black hole". In: *A&A* 542 (2012), A129. URL: https://doi.org/10.1051/0004-6361/201219375.

[69] Roeland P van der Marel et al. "New Understanding of Large Magellanic Cloud Structure, Dynamics, and Orbit from Carbon Star Kinematics". In: *\aj* 124.5 (Nov. 2002), pp. 2639–2663.

[70] D. Massari, H. H. Koppelman, and A. Helmi. "Origin of the system of globular clusters in the Milky Way". In: *A&A* 630 (2019), p. L4. URL: https://doi.org/10.1051/0004-6361/201936135.

[71] Peter J McGregor et al. "Gemini near-infrared integral field spectrograph (NIFS)". In: *Instrument Design and Performance for Optical/Infrared Ground-based Telescopes*. Ed. by Masanori Iye and Alan F. M. Moorwood. Vol. 4841. Society of Photo-Optical Instrumentation Engineers (SPIE) Conference Series. Mar. 2003, pp. 1581–1591.

[72] R Elliot Meyer et al. "HARMONI at ELT: chromatic dependence of wavefront error performance in volume phase holographic diffraction gratings". In: *Advances in Optical and Mechanical Technologies for Telescopes and Instrumentation VI*. Ed. by Ramón Navarro and Ralf Jedamzik. Vol. 13100. International Society for Optics and Photonics. SPIE, 2024, 131005K. URL: https://doi.org/10.1117/12.3019252.

[73] A. F. J. Moffat. "A Theoretical Investigation of Focal Stellar Images in the Photographic Emulsion and Application to Photographic Photometry". In: *\aap* 3 (Dec. 1969), p. 455.

[74] U. Munari et al. "An extensive library of 2500-10500 Å synthetic spectra". In: *Astronomy and Astrophysics* 442.3 (2005), pp. 1127–1134.

[75] Dieu D Nguyen et al. "Improved Dynamical Constraints on the Masses of the Central Black Holes in Nearby Low-mass Early-type Galactic Nuclei and the First Black Hole Determination for NGC 205". In: *The Astrophysical Journal* 872.1 (Feb. 2019), p. 104. URL: https://dx.doi.org/10.3847/1538-4357/aafe7a.

[76] Darragh O'Donoghue, Adam Anthony, and Christopher Clemens. *Curved Volume Phase Holographic (VPH) diffraction grating with tilted fringes and spectrographs using same*. URL: https://patents.google.com/patent/US20150168625A1/en.

[77] Zeynep Ozer. *HRM-01120 ISP Infrared Gratings Procurement – Statement of Work*. 2024.

[78] Cecilia Helena Payne-Gaposchkin. "Stellar atmospheres: A contribution to the observational study of high temperature in the reversing layers of stars". PhD thesis. Radcliffe College, United States, Jan. 1925.

[79] Ph Prugniel and C. Soubiran. "A database of high and medium-resolution stellar spectra". In: *Astronomy and Astrophysics* 369.3 (2001), pp. 1048–1057.

[80] B. Reinoso et al. "Collisions in primordial star clusters: Formation pathway for intermediate mass black holes". In: *Astronomy and Astrophysics* 614 (2018), pp. 1–9.

[81] Edgard Renault et al. "Efficiency measurements performed on the MUSE VPHG". In: *Modern Technologies in Space- and Ground-based Telescopes and Instrumentation* 7739.July (2010), 77394R.

[82] S P Rigaud et al. *Correspondence of Scientific Men of the Seventeenth Century: Including Letters of Barrow, Flamsteed, Wallis, and Newton, Printed from the Originals in the Collection of the Right Honourable the Earl of Macclesfield*. Correspondence of Scientific Men of the Seventeenth Century v. 2. University Press, 1841. URL: https://books.google.co.uk/books?id=0h45L_66bcYC.

[83] Martin M Roth, Peter M Weilbacher, and Norberto Castro. *Resolving stellar populations with integral field spectroscopy*. Tech. rep. URL: https://gitlab.gwdg.de/skamann/pampelmuse.

[84] H. A. Rowland. "On concave gratings for optical purposes". In: *American Journal of Science* 26.152 (Aug. 1883), pp. 87–98.

[85] P. Sánchez-Blázquez et al. "Medium-resolution Isaac Newton Telescope library of empirical spectra". In: *Monthly Notices of the Royal Astronomical Society* 371.2 (2006), pp. 703–718.

[86] Eleonora Sani. "KMOS: K-Band Multi-Object Spectrograph". In: *ESO Calibration Workshop: The Second Generation VLT Instruments and Friends*. Sept. 2017, p. 39.

[87] W. L. W. Sargent et al. "Dynamical evidence for a central mass concentration in the galaxy M87." In: *\apj* 221 (May 1978), pp. 731–744.

[88] Hermine Schnetler. *HRM-00180 IFS Spectrograph Requirements Specification*. 2021.

[89] Laura Schreiber et al. "Handling a highly structured and spatially variable Point Spread Function in AO images". In: *Second International Conference on Adaptive Optics for Extremely Large Telescopes. Online at <A href="http://ao4elt2.lesia.obspm.fr">http://ao4elt2.lesia.obspm.fr</A*. Sept. 2011, P57.

[90] Rob Sharp et al. "GMTIFS: The Giant Magellan Telescope integral fields spectrograph and imager". In: *Ground-based and Airborne Instrumentation for Astronomy VI*. Ed. by Christopher J Evans, Luc Simard, and Hideki Takami. Vol. 9908. Society of Photo-Optical Instrumentation Engineers (SPIE) Conference Series. Aug. 2016, 99081Y.

[91] ANDREW F SIEGEL. "Robust regression using repeated medians". In: *Biometrika* 69.1 (1982), pp. 242–244. URL: https://doi.org/10.1093/biomet/69.1.242.

[92] Britton D. Smith et al. "The growth of black holes from Population III remnants in the Renaissance simulations". In: *Monthly Notices of the Royal Astronomical Society* 480.3 (2018), pp. 3762–3773.

[93] American Philosophical Society. *Transactions of the American Philosophical Society*. Transactions of the American Philosophical Society v. 2. American Philosophical Society, 1786. URL: https://books.google.co.uk/books?id=OLgAAAAAYAAJ.

[94] Peter B. Stetson. "DAOPHOT - A computer program for crowded-field stellar photometry". In: *Publications of the Astronomical Society of the Pacific* 99 (Mar. 1987), p. 191.

[95] A. A. Strugatskaya. "The study of the rotation of the globular cluster 47 TUC". In: *Pisma v Astronomicheskii Zhurnal* 14 (Jan. 1988), pp. 31–36.

[96] Naoyuki Tamura et al. "Measurement of throughput variation across a large format volume-phase holographic grating". In: *Optics Express* 13.11 (2005), p. 4125.

[97] Naoyuki Tamura et al. "Cryogenic tests of volume-phase holographic gratings: Results at 100 K". In: *Applied Optics* 45.23 (2006), pp. 5923–5928.

[98] Niranjan A Thatte et al. "SINFONI: a near-infrared AO-assisted integral field spectrometer for the VLT". In: *Adaptive Optical System Technologies*. Ed. by Domenico Bonaccini and Robert K Tyson. Vol. 3353. International Society for Optics and Photonics. SPIE, 1998, pp. 704–715. URL: https://doi.org/10.1117/12.321638.

[99] Niranjan A Thatte et al. "HARMONI: the first light integral field spectrograph for the E-ELT". In: *Ground-based and Airborne Instrumentation for Astronomy V*. Ed. by Suzanne K Ramsay, Ian S McLean, and Hideki Takami. Vol. 9147. Society of Photo-Optical Instrumentation Engineers (SPIE) Conference Series. Aug. 2014, p. 914725.

[100] The LIGO Scientific Collaboration, the Virgo Collaboration, and the KAGRA Collaboration. "Search for intermediate mass black hole binaries in the third observing run of Advanced LIGO and Advanced Virgo". In: (2021). URL: http://arxiv.org/abs/2105.15120.

[101] Francisco Valdes et al. "The Indo-US Library of Coude Feed Stellar Spectra". In: *The Astrophysical Journal Supplement Series* 152.2 (2004), pp. 251–259.

[102] K. Verro et al. "The X-shooter Spectral Library (XSL): Data Release 3". In: *Astronomy and Astrophysics* 660 (2022), pp. 1–26.

[103] Marta Volonteri. "Formation of supermassive black holes". In: *The Astronomy and Astrophysics Review* 18.3 (2010), pp. 279–315. URL: https://doi.org/10.1007/s00159-010-0029-x.

[104] Wasatch Photonics. *Advantages of VPH Gratings*. Tech. rep. 2020.

[105] Laura L. Watkins et al. "Hubble space telescope proper motion (hstpromo) catalogs of galactic globular clusters. Ii. Kinematic profiles and maps". In: *Astrophysical Journal* 803.1 (2015), p. 29. URL: http://dx.doi.org/10.1088/0004-637X/803/1/29.

[106] L Weitzel et al. "3D: The new MPE near-infrared field imaging spectrometer". In: *Experimental Astronomy* 3.1 (1994), pp. 317–318. URL: https://doi.org/10.1007/BF00430185.

[107] Claudia Winge, Rogemar A Riffel, and Thaisa Storchi-bergmann. "The Gemini spectral library of near-IR late type stellar templates and its application for velocity dispersion measurements." In: (2004).

[108] Shelley A Wright et al. "The infrared imaging spectrograph (IRIS) for TMT: overview of innovative science programs". In: *Ground-based and Airborne Instrumentation for Astronomy V*. Ed. by Suzanne K Ramsay, Ian S McLean, and Hideki Takami. Vol. 9147. Society of Photo-Optical Instrumentation Engineers (SPIE) Conference Series. July 2014, 91479S.

[109] Renbin Yan et al. "SDSS-IV MaStar: A Large and Comprehensive Empirical Stellar Spectral Library—First Release". In: *The Astrophysical Journal* 883.2 (2019), p. 175.

[110] S. Zieleniewski et al. "HSIM: A simulation pipeline for the HARMONI integral field spectrograph on the European ELT". In: *Monthly Notices of the Royal Astronomical Society* 453.4 (2015), pp. 3754–3765.